KTH Numerical Analysis
and Computer Science

Hybrid Methods for Computational Electromagnetics in Frequency Domain

STEFAN HAGDAHL

Doctoral Thesis
Stockholm, Sweden 2005

TRITA-NA-0441
ISSN 0348-2952
ISRN KTH/NA/R-04/41-SE
ISBN 91-7283-932-5

KTH Numerisk analys och datalogi
SE-100 44 Stockholm
SWEDEN

Akademisk avhandling som med tillstånd av Kungl Tekniska högskolan framlägges till offentlig granskning för avläggande av filosofie doktorsexamen fredagen den 1 april 2005 klockan 13.00 i Kollegiesalen, Kungl Tekniska högskolan, Vallhallavägen 79 Entrepl, Stockholm.

Tryck: Universitetsservice US AB

Abstract

In this thesis we study hybrid numerical methods to be used in computational electromagnetics. The purpose is to address a wide frequency range relative to a given geometry. We also focus on efficient and robust numerical algorithms for computing the so called Smooth Surface Diffraction predicted by Geometrical Theory of Diffraction (GTD). We restrict the presentation to frequency domain scattering problems.

The hybrid methods consist in combinations of Boundary Element Methods and asymptotic methods. Three hybrids will be presented. One of them has been developed from a theoretical idea to an industrial code. The two other hybrids will be presented mainly from a theoretical perspective.

To be able to compute the Smooth Surface Diffracted field we introduce a numerical method that is to be used with surface curvature sensitive meshing, complemented with auxiliary data taken from a geometry database. By using two geometry representations we can show first order convergence and we then achieve an efficient and robust numerical algorithm. This numerical algorithm may be an essential part of an GTD implementation which in its turn is a component in the hybrid methods.

As a background to our new techiniques we will also give short introductions to the Boundary Element Method and the Geometrical Theory of Diffraction from a theoretical and implementational point of view.

Keywords Maxwell's equations, Geometrical Theory of Diffraction, Smooth Surface Diffraction, Boundary Element Method, Hybrid methods, Electromagnetic Scattering

Sammanfattning

Denna avhandling studerar numeriska hybridmetoder för elektromagnetiska beräkningar. Syftet med metoderna är att kunna behandla ett brett frekvensintervall för en given geometri. Avhandlingen tar också upp effektiva och robusta numeriska algoritmer för att beräkna det asymptotiska spridningsbidraget från glatta ytor. Vi begränsar vår presentation till spridningsproblem i frekvensdomän.

Hybridmetoderna består av kombinationer av randelementmetoder och asymptotiska metoder. Tre hybrider kommer att presenteras. En hybrid har utvecklats från en teoretisk idé till en industriell kod. De två andra hybriderna kommer i huvudsak att presenteras från ett teoretiskt perspektiv.

För att kunna beräkna spridningen från de krypvågor som asymptotiskt sett propagerar längs med glatta ytor kommer vi att använda oss av en numerisk metod applicerad på en ytkurvaturkänslig yttriangulering kompletterad med geometrisk data beräknad ur en geometrisk databas. Genom att använda två geometribeskrivningar är det möjligt att visa första ordningens konvergens och samtidigt erhålla en effektiv och robust numerisk algoritm. Algoritmen skulle kunna vara en del i en implementation av asymptotiska metoder vilken i sig är en komponent i hybrid metoderna.

Som en bakgrund till våra nya tekniker kommer vi också ge en kort introduktion till randelementmetoder och geometrisk diffraktionsteori från ett teoretiskt perspektiv och från ett implementationsperspektiv.

Nyckelord Maxwells ekvationer, Geometrisk diffraktionsteori, Krypvågor, Randelementmetod, Hybridmetoder, Elektromagnetisk spridning

Contents

Acknowledgments

I wish to thank my advisor, Prof. B. Engquist, for his enthusiasm, his remarkable talent to communicate and for his ability to make complicated problems simple. Furthermore, I want to mention my assistant supervisors at NADA Prof. J. Oppelstrup and Dr. O. Runborg as two people who has been invaluable for this thesis.

I am indebted to all my colleagues in the NA-group at NADA, who have accepted me as an equal even though I have an industrial perspective of my research. I especially want to mention E. Olsson and A. Attle for being so willing and easy to discuss numerical and mathematical problems with.

The work presented in the thesis has been carried out in a joint academic-industrial project. To make these projects successful, a great amount of information has to be communicated, both ideas and hard facts. Therefore I want to point out my collaboration with my friend and former colleague J. Hamberg as a cornerstone to this work.

Parts of my work in high frequency methods has been done in close collaboration with S. Sefi and Prof. F. Bergholm and I thank them for a prosperous collaboration. All the programming would have been very hard, if not even impossible to finish, without the help from A. Ålund and Dr. U. Andersson. Thank you for your humility in front of my questions.

Thanks to the successful CEM-projects, GEMS and SMART, I also got in contact with the TDB-group at the Department of Information Technology, Uppsala University. This helped me getting acquainted with two project colleagues, J. Edlund and Dr. M. Nilsson, which I have had many fruitful discussion with.

I thank my dear colleagues at AeroTechTelub AB. Especially H.-O. Berlin, Dr. B. Strand and Dr. U. Thibblin who supported me all the time. At the same time I want to thank my former manager H. Frennberg who initially believed in this collaboration.

This work was supported by the CEM program at the Parallel and Scientific Computing Institute (PSCI) through the General ElectroMagnetic Solvers project (GEMS) and the Signature Modeling And Reduction Tools (SMART) project. Financial support was provided by the National Aeronautical Research Program (NFFP), Vinnova, Saab AB and Ericsson Microwave Systems AB.

Finally, I want to thank Anneli, Lovisa, Alice and my parents who have been a great support for me all the time.

Chapter 1

Introduction

> *. . . Men solen stod över Liljeholmen och sköt hela kvastar av strålar mot öster; de gingo genom rökarna från Bergsund, de ilade fram över Riddarfjärden, klättrade upp till korset på Riddarholmskyrkan, kastade sig över till Tyskans branta tak, lekte med vimplarna på skeppsbrobåtarna, illuminerade i fönstren på stora Sjötullen, eklärerade Lidingöskogarna och tonade bort i ett rosenfärgat moln, långt, långt uti fjärran, där havet ligger. . . .*
>
> Röda rummet, August Strindberg

In many engineering disciplines and scientific branches, electromagnetic (EM) radiation is important to study. Often, the EM-phenomenon represent attractive possibilities such as storing and carrying energy and information. We see examples of this in modern cell phones where information is both stored in digital memories and transmitted via an antenna. It also helps us producing and relocating energy in fusion/nuclear power plants and hydroelectric power stations. A list can be made much longer. In other cases the EM-field may carry unwanted effects such as in electromagnetic incompatibility problems or by its ability to interact with human tissue.

This thesis is inspired by challenges in electromagnetic engineering where numerical techniques are mature enough to be applicable to real world problems. For EM-problems with a size of several hundreds times of a wave length, asymptotic methods are most often fast and sufficiently accurate to be useful. For EM-problems with a size of less than some hundred times of a wave length the algebraic problems generated by numerical techniques fits into modern computers of today.

There are a fundamental difference between asymptotic and numerical techniques. While, for numerical techniques with a given discretization, the error is proportional to some *negative* power of the wave length the opposite holds for asymptotic techniques. The errors are here proportional to some *positive* powers of the wave length!

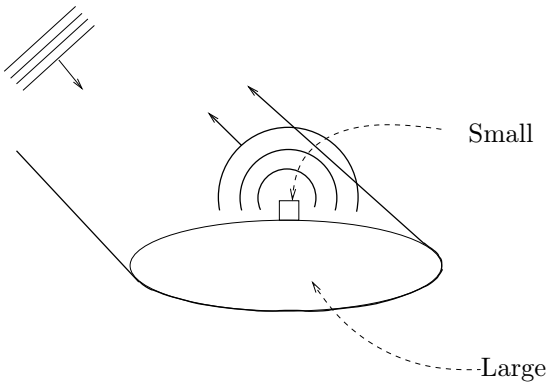

Figure 1.1: A perturbed scattering boundary value problem.

The objective of the thesis is to present numerical methods that can be applied to problems where large *and* small scales, or *only* large scales, are present. We could think of the problem schematically pictured in Figure 1.1. How should the small and the large scales, with respect to the wave length, be designed so that it achieve optimal performance for some of its electrical parameters. We will speak of how the small and the large features scatter or radiate electromagnetic energy. A small scale radiation problem, could be to design an antenna so that it maintain or achieve good coverage performance when installed on a large platform. The small scale scattering problem could be represented by the electromagnetic signature analysis done for a military vehicle when an antenna is to be installed. The large scale scattering problem could be exemplified by some shape optimization of the large platform to achieve a small electromagnetic signature.

Certainly, these question will not be answered by just solving the electromagnetic problem but technical, tactical and operational aspects have to be taken into account. We will however only focus on the EM-problem from a numerical point of view, i.e. develop numerical methods for computational electromagnetics. As an illustration on how an engineering problem can be condensed to a numerical let us consider the scattering problem.

A vehicle with an exterior design mainly developed with respect to signature analysis, i.e. reducing radar detection probability, is sometimes referred to a stealth vehicle. If radar waves are used to detect the vehicle then the probability of detection may be decreased by reducing the so called Radar Cross Section (RCS). The RCS is the logarithm of a number in unit square meters, and it is defined for a vehicle positioned in the origin, with a radar source positioned in $\mathbf{r}$, as

$$\sigma(\theta,\phi) = \lim_{|r|\to\infty} 10\,\log_{10}\left(\frac{4\pi r^2|\mathbf{E}(\mathbf{r})|^2_{scatt}}{|\mathbf{E}|^2_{inc}}\right). \tag{1.1}$$

Here, (θ,ϕ) is the Euler angles for the radar position and σ is sometimes generalized

to a matrix where each component represent different polarization of the incoming and scattered field. It tells us how much the vehicle scatter an incoming wave $\mathbf{E}_{inc}$, originating from the radar, back to the radar. With $\mathbf{E}$ we denote the electric field strength and it may be shown that for $|r| \to \infty$, $\mathbf{E}_{inc}$ will approach a plane wave, i.e. the equi-phase front is locally flat, the polarization of the magnetic field is orthogonal to the electric and their relative amplitude is directly proportional to each other via a physical real constant. It is natural to assume that the source currents, giving rice to the incoming field, is not dramatically influenced by the scattered field. In other words can the source currents on the radar, excited by for example a wave guide, be computed without knowing anything about the scatterer. To compute σ we therefore regard $\mathbf{E}_{inc}$ as given data and then let $\mathbf{E}_{scatt}$ become the unknown of our problem. In the literature these types of problems are referred to scattering problems.

To solve the EM scattering problem in the frame of computational electromagnetics we emanate from the Maxwell's equations. The equations containing time derivatives, the Ampere-Maxwell law and the Faraday lay, state that the electric $\mathcal{E}$ and magnetic $\mathcal{H}$ field strength in a piece wise homogeneous and isotropic media fulfill

$$\begin{aligned} \nabla \times \mathcal{H}(\mathbf{x},t) - \varepsilon \mathcal{E}_t(\mathbf{x},t) &= \sigma(\mathbf{x})\mathcal{E}(\mathbf{x},t) && (1.2)\\ \nabla \times \mathcal{E}(\mathbf{x},t) + \mu \mathcal{H}_t(\mathbf{x},t) &= 0. && (1.3) \end{aligned}$$

We have here introduced the material parameters electric conductivity σ, the electric permittivity ε and the magnetic permeability μ. The right hand side in equation (1.2) is sometimes called the volume current density $\mathcal{J}$. When the media is free space we have that $\varepsilon = \varepsilon_0 \approx 8.85 \times 10^{-12}$ [Farads/meter], $\mu = \mu_0 = 4\pi \times 10^{-7}$ [Henrys/meter] and $\sigma = 0$. Since Maxwell's equations is a type of wave equation one can derive a wave speed which tells us how fast information can propagate. The propagation speed in vacuum is $c_0 = 1/\sqrt{\varepsilon_0 \mu_0} \approx 3 \times 10^8$ [m/s] and more generally $c = 1/\sqrt{\varepsilon\mu}$.

The second two equations tells us about the divergence of the electric and magnetic field, i.e.

$$\begin{aligned} \nabla \cdot \mu \mathcal{H}(\mathbf{x},t) &= 0 && (1.4)\\ \nabla \cdot \varepsilon \mathcal{E}(\mathbf{x},t) &= \rho(\mathbf{x}). && (1.5) \end{aligned}$$

Here we identify ρ as the volume charge density.

If there are discontinuities in the electrical properties we can with mathematical analysis and equation (1.2-1.5) derive interface conditions at these discontinuities. Also, these discontinuities imply existence of surface current densities and surface charge densities.

By linearity of the equations we may suppress the time dependence by setting

$$\mathcal{E}(\mathbf{x},t) = \mathrm{Re}(e^{iwt}\mathbf{E}(\mathbf{x})) \text{ and } \mathcal{H}(\mathbf{x},t) = \mathrm{Re}(e^{iwt}\mathbf{H}(\mathbf{x})),$$

and look for time harmonic solutions $(\mathbf{E}, \mathbf{H})$. For non-conductive materials with no free charges it follows that

$$\nabla \times \mathbf{H}(\mathbf{x}) - i\omega\varepsilon\mathbf{E}(\mathbf{x}) = 0 \tag{1.6}$$

$$\nabla \times \mathbf{E}(\mathbf{x}) + i\omega\mu\mathbf{H}(\mathbf{x}) = 0. \tag{1.7}$$

We identify the wave length as $\lambda = 2\pi c/\omega$ [m]. For simple two dimensional problems equation (1.7) may be reduced to a scalar Helmholtz equation and an algebraic equation coupling the magnetic component to the electric.

During the last fifty years analytical, numerical and experimental studies have been performed to solve the RCS-challenges in the aircraft business. The crucial parameter which decides whether numerical or asymptotic methods can be used is the relative scale of the problem. With relative scale we mean the relation between the wave length and the characteristic length scales in the differential operator defined by equation (1.2) to (1.5) and in the boundary conditions. Some EM-problems may be defined as problems with a

Small Relative Scale where we can use direct numerical approximations of Maxwell's equations or having a

Large Relative Scale where we can use asymptotic approximations of Maxwell's equations,

to achieve *sufficient* accuracy. However, there are classes of problems that do not fit into any of the two *categories*, or problems that fit into both. We can also imagine that bounded parts of the boundary conditions are of small relative scale and other parts that are of large relative scale.

The reason for that we may want to use asymptotic methods is that the rigorous methods is not attainable because of computers' limited performance. To realize this let us consider the time independent scattering problem for a perfectly conducting sphere with radius r. Assume that we are able to solve a problem today for a sphere in $\mathbb{R}^d$ with a radius of n wave lengths producing $\mathcal{O}(n^{d-1})$ unknowns for a boundary element method and $\mathcal{O}(n^d)$ unknowns for finite element/difference/volume methods. For the complexity of the volume methods we assume that we apply a FDTD-scheme to a time harmonic problem during a fixed time. We then need, with direct methods, $\mathcal{O}(n^{3(d-1)})$ and $\mathcal{O}(n^{d+1})$ number of operations respectively to solve the problem. Let us assume that computers' performance is improved according to Moore's law each year y. The law is dependent on the time-span from which you take data. However, the exact definition of Moore's law is not crucial for the discussion. That is, assume that Moore's law is proportional to the number of transistors N per integrated circuit and

$$N(y) \sim 10^{\frac{y-1970}{6}+3}.$$

Moore's law now says that, with complexity number $p = 3(d-1)$ for boundary methods and $p = d+1$ for other methods, we need to wait $p \cdot 6 \cdot \log_{10} 2 \approx 2p$ years to expect the computers to be able to solve the problem with $r = 2n$.

Great progress has been achieved in decreasing the complexity for the boundary elements and volume methods. We will discuss the achievements for the boundary elements below. Note that we have left out all discussions on the coefficients in the complexity expressions, memory space demands and for that sake all other pre and cons for boundary and volume methods respectively.

Without access to powerful computers asymptotic methods where historically the only useful methods with respect to large scattering and radiation problems. Furthermore there have been many problems that did not have a unique small or large relative scale. This fact means that many problems were left to measurements and other analysis methods.

However during the last five to ten years the so called Fast Multilevel Multipole (FMM) method, which is a fast numerical boundary element method, has shown to be powerful enough on modern computers to solve problems only attainable by asymptotic methods previously. In other words we can say that, for the electromagnetic engineer, the FMM has filled the gap between large and small scales for certain applications. The complexity number p defined above can, for large n and a well conditioned problem, be shown to be proportional to 2, where we ignored the logarithmic factor in the complexity of FMM. Differently stated, with FMM we need to wait one third of the time compared to boundary element methods, solved with direct methods, to be able to solve a problem twice as big as the one which is state of the art today. Hence, even with the impressive Moore's law and the relatively low complexity of FMM in mind, we must realize that in the near future far from all relevant EM-problems can be solved with non-asymptotic methods.

With the discussion above in mind we realize that there are limits on the size of problems that we can solve with direct methods today. However, although specific problems are solvable with direct methods on computers of today, we may want to use other methods that are less expensive in terms of computer resources since then engineering time in general and depreciation cost will decrease. Hence, asymptotic techniques may be preferable although direct numerical methods are feasible.

This thesis addresses EM-computations on three types of problems:

1. Problems with boundary conditions given on smooth geometries that are of a relatively large scale. E.g. Figure 1.1 without the small scales, excited by a plane wave with a relatively small wave lengths. This type of problem fall into the category, problems of **Large Relative Scale**.

2. Problems which is mainly of a relatively large scale but contain parts with relatively small scales. E.g. Figure 1.1 excited by a plane wave with a relatively small wave lengths. This type of problem does not fall into any of the two categories.

3. Problems which is mainly of a relatively large scale but has been analyzed with rigorous methods before being retrofitted with parts of a relatively small scale. This problem address the fact that we may want to reduce the cost of computations by only discretizing the small scales. E.g. Figure 1.1 excited

by a plane wave with medium large wave lengths. This type of problem fall into the category, problems of **Small Relative Scale**.

There are two mayor contributions that will be presented in the thesis. The first one concerns problems of type 1 and 2. The second contribution concern problems of type 2 and 3. The first contribution will be summarized in Section 1.3 and presented more thoroughly in Chapter 4. The second contribution will be summarized in Section 1.4 and presented more thoroughly in Chapter 5.

The first contribution will address the electromagnetic wave that propagate tangentially and close to smooth surfaces. These waves are predicted by the Geometrical Theory of Diffraction (GTD). GTD can in general be used to compute the solution along stationary ray paths. These ray paths are trivial to find in homogeneous materials. However, in inhomogeneous or, as in our case, on smooth surfaces it is a non-trivial task. The corresponding method that we will present may be used in problems of type 1 and 2. More specifically we will focus on how the asymptotic surface wave are computed numerically with high efficiency, generality and robustness.

Since we have two different scales in the problems of type 2 and 3 we realize that it is quite natural to have two geometry representations. However, as we will see in Chapter 4, it is also practical to have a double representation of the geometry when we solve for the smooth surface diffracted waves. We say that we have a *hybrid geometry*.

The second contribution will address the small parts mentioned in 2 and 3. We will sometime refer to these parts as small perturbations of the original boundary conditions. Note that there are no a priori knowledge that tells us that small perturbations necessarily make a small impact on the scattered field. On the contrary we know that wave solutions may exhibit resonant behaviors and therefore may small perturbations contribute crucially to the scattered field. Also note we may speak of contributions to the scattered field from different parts as long as we approximate, or take into account, the interaction between the parts properly. Finally we want to remark that for these mixed problems our methods do not demand that there is a large scale separation between the large and the small scales.

Referring to problems of type 2 and 3 and with the definition of relative scale above it becomes natural to investigate the possibility to hybridize a numerical method with an asymptotic one. The challenge in the hybrid method is then to be able to design a numerical method which combines asymptotic theory with a so called boundary element method. The method's ability to properly take into account the interaction between the *small* and the *large* scales is crucial.

We want to stress that it is by no mean a unique approach to try to combine asymptotic techniques with numerical ones in computational electromagnetics. We see for example an asymptotic-numerical hybrid when we analyze perfectly matched layers or Mur boundary conditions for Finite Differences in Time Domain. Efficient solvers have also been developed by hybridizing finite element techniques with finite difference techniques.

We also would like to refer to Heterogeneous Multiscale Methods [1] for a more systematic treatment of multiscale methods in general. Our method fall into *Type A* problems in this reference. I.e. asymptotic techniques holds in the major parts of the computational domain but a more detailed Maxwell model is needed in small parts of the domain.

1.1 Boundary Element Method

As a background to our second contribution we will briefly discuss the Boundary Element Method (BEM).

Maxwell's differential equations may be rewritten into a Boundary Integral Equation (BIE) formulation. Assume that the discontinuities in the Maxwell differential operator coincide with a union of closed boundaries

$$\Gamma = \bigcup_{i=1\ldots j} \Gamma_i, \tag{1.8}$$

where each Γ_i bounds an open connected subset Ω_i in $\mathbb{R}^3$. Similarly we define $\Omega_j^+ = \mathbb{R}^3/\{\Omega_j^- \bigcup \Gamma_j\}$. Also assume that $\Omega_i^- \bigcap \Omega_k^- = 0$ when $i \neq k$. At the discontinuities the so called fundamental unknowns are defined as

$$\mathbf{J}_i(x) = \hat{\mathbf{n}}_i(x) \times \mathbf{H}(x) \text{ where } x \in \Gamma_i \tag{1.9}$$

and

$$\mathbf{M}_i(x) = \hat{\mathbf{n}}_i(x) \times \mathbf{E}(x) \text{ where } x \in \Gamma_i. \tag{1.10}$$

$\hat{\mathbf{n}}_i(x)$ is the normal to boundary Γ_i pointing into Ω_i^+. Here, $\mathbf{J}$ is the electric surface current and $\mathbf{M}$ the magnetic surface current. As the word *fundamental* indicate, may $(\mathbf{E}, \mathbf{H})$ in any point in space be derived from $(\mathbf{J}, \mathbf{M})$. If only discontinues in σ is present then only $\mathbf{J}$ is the relevant unknown for closed boundaries. In the thesis we will address a certain type of discontinuity in σ.

We consider perfect electric conducting infinitely thin sheets at $\bigcup_i \Gamma_i$ where $\sigma \to \infty$ holds. It can be deduced that we have a Dirichlet boundary condition on the tangential component of $\mathbf{E}$ at these interfaces, i.e.

$$\hat{\mathbf{n}}(x) \times \mathbf{E}(x) = 0 \text{ if } x \in \bigcup_{i=1\ldots j} \Gamma_i. \tag{1.11}$$

We can then formally write the electric surface currents in $\mathbb{R}^3$ as

$$\mathbf{J}(x) = \sum_{i=1}^{j} \delta_{\Gamma_i} \hat{\mathbf{n}} \times \mathbf{H}, \tag{1.12}$$

where we have smoothly extended $\hat{\mathbf{n}}$ to a tubular neighborhood around Γ which is sometimes called a lifting of $\hat{\mathbf{n}}$.

With $\mathbf{H} = \mathbf{H}_{inc} + \mathbf{H}_{scatt}$ we can define $\mathbf{J} = \hat{\mathbf{n}} \times \mathbf{H}$, $\mathbf{J}_{scatt} = \hat{\mathbf{n}} \times \mathbf{H}_{scatt}$ and $\mathbf{J}_{inc} = \hat{\mathbf{n}} \times \mathbf{H}_{inc}$.

If $\mathbf{H}_{scatt}$ and $\mathbf{E}_{scatt}$ fulfill specific radiation conditions [2], there exist two Fredholm integral equations of the first and second kind that, under certain regularity conditions, has a solution $\mathbf{J}$. Using Einstein's summation convention: If any index appears twice in a given term, once as a subscript and once as a superscript, a summation over the range of the index, i.e. $i = 1 \dots 3$ is implied. Let

$$E_{\mu\nu}(x, y^\alpha) = (I + \frac{1}{k^2}\frac{\partial}{\partial x^\mu}\frac{\partial}{\partial x^\nu})\frac{e^{ik\sqrt{\delta^{\beta\varepsilon}(x_\beta - y^\alpha_\beta)(x_\varepsilon - y^\alpha_\varepsilon)}}}{4\pi\sqrt{\delta^{\beta\varepsilon}(x_\beta - y^\alpha_\beta)(x_\varepsilon - y^\alpha_\varepsilon)}}, \tag{1.13}$$

define a tensor valued function (sometimes referred to the dyadic Green's function) in Euclidean metric, i.e. $g^{\mu\nu} = \delta^{\mu\nu}$, where $\delta^{\mu\nu}$ is Kronecker's delta symbol. Also define the wave number $k = 2\pi/\lambda$ and the free space wave impedance $Z = \sqrt{\mu_0/\varepsilon_0}$ and let $x \in \bigcup_i \Gamma_i$. The first kind integral equation then reads

$$ikZ \barint_{y_\alpha \in \bigcup_i \Gamma_i} E_{\mu\nu}(x, y^\alpha) J^\nu(y^\alpha) dy_\alpha = -C_{\mu\xi\beta} n^\xi E^\beta_{inc}(x), \tag{1.14}$$

where the third rank tensor $C_{\mu\xi\beta}$ represent the cross product and the bar over the integral sign indicate that it should be interpreted in a Cauchy principal value sense. The integral equation of second kind reads

$$C^\xi_{\mu\beta}\frac{\partial}{\partial x^\xi}\int_{y_\alpha \in \bigcup_i \Gamma_i} E^\beta_\nu(x, y^\alpha) J^\nu(y^\alpha) dy_\alpha = \frac{1}{2}J_\mu(x) - J^{inc}_\mu(x). \tag{1.15}$$

Equation (1.14) and (1.15) are sometimes referred to the Electric Field Integral Equation (EFIE) and the Magnetic Field Integral Equation (MFIE) respectively and they are based on the so called representation theorem [2].

BIEs have been mathematically analyzed during the last century and it is still an active subject of research. E.g. the well-posedness of equation (1.14) and (1.15) in problems where normals to Γ is discontinuous is still an open question. Also, there are values of k for which (1.14) is not uniquely solvable. Efficient and stable numerical methods are desirable and therefore are questions in what functional spaces that the solution should be searched in also very important to answer.

With the pioneering work of R. F. Harrington [3] thirty years ago these equations were opened up for numerical computations in the electromagnetic engineering society. The numerical method presented by Harrington is most often referred to the Method of Moments. However, mainly using point matching and piece wise constant basis functions one was confronted with numerical instabilities and non-satisfactory error estimates. With the work by J.-C. Nédélec [2], Rao et al. [4] and A. Bendali [5, 6] errors could be bounded by the residual error while the mathematical and numerical analysis were put on a more firm ground with Galerkin formulations.

The MFIE, since it is of second kind, is from a numerical point of view an attractive equation since you may straight forwardly use an iterative technique to solve the equation. You may also approximate the integro-differential operator and achieve fast asymptotic methods, called Physical Optics (PO) to solve large problems. However, it has a major drawback since it can not be used for open problems, i.e. Γ_i must be closed. This is not the case for the EFIE although the mathematical foundation for open problems is not as well analyzed as for closed ones.

The today standard numerical method to solve the EFIE and MFIE uses so called Rao, Wilton and Glisson [4] or Raviart and Thomas [7] finite elements. They are defined on a triangulation of Γ, i.e. $\Gamma \approx \sum_\ell T_\ell$. Each scalar complex valued unknown j_k in the discretized problem gives us the coefficient in front of the current basis function $\mathbf{B}_t^e$ corresponding to the triangle t and edge e. The current on each triangle is therefore decomposed into three vector basis functions each having an amplitude of one over their corresponding edge.

Having discretized the geometry and $\mathbf{J}$ we can apply the Galerkin method in a finite dimensional functional space. The EM-problem then reduces to a linear algebra problem where the impedance matrix is full and complex (sometimes also symmetric if special considerations are taken). Referring to the complexity discussion in the introduction and defining the discretization size $\Delta = \mathcal{O}(n^{-2})$ as the mean size of the triangle edges we know that we can expect a complexity of order Δ^{-6} arithmetic operations and a demand of order Δ^{-4} memory positions for direct methods. For properly chosen iterative methods we may achieve faster solvers and less memory needs. The state of the art iterative methods of today is based on the so called fast multilevel multipole method. In this method the number of floating point operations is proportional to $N\Delta^{-2}|\log\Delta|$ and memory storage to $\Delta^{-2}|\log\Delta|$, with N as the number of iterations.

1.2 Geometrical Theory of Diffraction

As a background to our first and second contribution we will briefly discuss Geometrical Theory of Diffraction (GTD).

In the first half of the last century, scientists managed to solve time harmonic EM boundary value problems for canonical or simple geometries. In some cases, though important ones, only asymptotic or high frequency solutions were achieved. At the same time people knew that given a Cauchy problem, i.e. an initial value problem, for a hyperbolic symmetric system of partial differential equations, a solution may be obtained with the method of characteristics. By combining method of characteristics and high frequency solutions J. B. Keller developed a theory called Geometrical Theory of Diffraction (GTD) [8]. First, Maxwell's time dependent hyperbolic equation had to be rewritten into its time harmonic form, i.e. vector Helmholtz equation. Since Helmholtz equation is elliptic the hyperbolicity was lost and the method of characteristics were not attainable. To remedy this, wave

propagation were studied at high frequencies and a new equation was achieved, the Eikonal equation, which was hyperbolic in its nature. We will call the class of solutions that GTD concerns Ray-field solutions or just Ray-fields. In a systematic manner J. B. Keller then solved initial value and boundary value problems for the Ray-fields. By combining solutions to initial value problems and solutions to boundary value problems a class of new problems were possible to solve analytically in the asymptotic regime.

Part from that analytical solutions where tractable numerical schemes are now, by using high frequency asymptotics, applicable to problems which previously were not reachable because of their large complexity. That is, with new types of numerical methods we will show that the complexity may be reduced substantially.

For time harmonic EM-problems and axi-symmetric problems it holds that Maxwell's equation may be rewritten into the reduced wave equation, which in its turn may be rewritten into scalar Helmholtz equation. We will therefore state that conclusions and results from a asymptotic analysis of Helmholtz equation is also applicable to Maxwell's equations.

Combining equation (1.6) and (1.7), while using standard vector identities, we can achieve

$$\nabla \times \nabla \times \mathbf{E} - i\omega\varepsilon\mathbf{E} = 0 \tag{1.16}$$

and

$$\nabla \times \nabla \times \mathbf{H} - i\omega\mu\mathbf{H} = 0. \tag{1.17}$$

Note that these equations are coupled via possible boundary conditions. However if μ and ε are axisymmetric, e.g. the x_3-axis, then it may be shown that we only need to solve a scalar equation, e.g.

$$\Delta E_3(x) + \frac{\omega^2}{c} E_3(x) = 0 \text{ where } x \in \mathbb{R}^3, \tag{1.18}$$

in problems with no free charges and currents. Let us denote $E_3 = u$ to the end of this section. For perfect electric conducting boundaries Γ_i we have a Dirichlet boundary condition on $u(x)$ and we may solve (1.18) as a boundary value problem. With no boundary condition, but a forcing f, it would be attractive to solve the problem as a Cauchy problem and apply method of characteristics. This problem is not well posed though. Let us assume that the transverse electric field fulfill the asymptotic expansion

$$u(x) \sim e^{ik\phi(x)} \sum_{m=0}^{\infty} (ik)^{-m} u_m(x). \tag{1.19}$$

Note that this assumption is only adequate for some simple wave problems where no boundary conditions are present and the wave speed profile $c(x)$ is of such a nature that $\phi(x)$ may be uniquely defined in any point. If we keep only the first term we get the so called Geometrical Optics approximation, c.f. equation (1.20) and (1.21) below.

If we plug this sum into (1.18) and collect terms of the same order of k we get the following infinite sequence of equations

$$|\nabla\phi(x)| = \eta(x) \quad O(k^2)\text{-equation} \tag{1.20}$$
$$2\nabla\phi(x)\cdot\nabla u_0 + u_0\Delta\phi(x) = 0 \quad O(k)\text{-equation} \tag{1.21}$$
$$\dots$$
$$2\nabla s\cdot\nabla u_m + u_m\Delta s = -\Delta u_{m-1} \quad O(k^{-m})\text{-equation}$$
$$\dots,$$

where $\eta = \frac{\omega^2}{c}$. Time t or position x can be used to parameterize the characteristic lines for time dependent hyperbolic problems. For time harmonic problems, in asymptotic form, the most natural parameter to use is the dependent phase variable ϕ, in (1.19). The Eikonal equation (1.20) tells us how this function ϕ depends on x. The amplitudes u_j is achieved by solving the sequence of so called transport equations in (1.21), ... Since the Eikonal equation is non-linear we potentially may encounter problems with non-unique solutions and in some cases we may even encounter infinitely many solutions. The manifolds where non-unique solutions exist is sometimes referred to *caustics*. There exist a uniqueness and existence theorem for a so called viscosity solution, developed by M. G. Crandall and P.-L. Lions in 1983 [9]. Since this solution is unique it does not have problems with multiple valued solutions. It is an active area of research to achieve numerical and analytic methods to treat these problems.

For certain problems the most efficient way to solve (1.20) is to rewrite it into a Lagrangian formulation. We then achieve a set of OEDs sometimes called the Ray-equations.

We call the curves of constant phase $\phi = \phi_0$ equi-phase fronts. Orthogonal to these wave fronts, rays can be defined and EM-energy propagates along the rays. In so called caustics either parts of the wave fronts collapses to a sub-manifold or the wave front normals build an envelope of rays.

As mentioned previously, GTD treats certain canonical initial value problems. Let us assume that we have initial values on a sub-manifold Γ in $\mathbb{R}^2$ or $\mathbb{R}^3$ (point, curve, surface). To be able to treat these problems correctly we need to be able to express the solution on a Ray-field format. E.g. an infinitely thin conductor with harmonic current I along the x_3-axis radiate according to

$$u(|\mathbf{x}|) = -\frac{kI}{4c\varepsilon}H_0^{(2)}(k|\mathbf{x}|), \tag{1.22}$$

where $H_0^{(2)}$ is the first order Hankel function of second type. This is not a Ray-field. However if the conductor, positioned in the origin, is in the center of a disc with radius $r = \sqrt{x_1^2 + x_2^2} >> \lambda$ of constant material then asymptotically the field at $|\mathbf{x}| \geq r$ look like

$$u(\mathbf{x}) = -ZI\sqrt{\frac{ik}{8\pi}}\frac{e^{-ikr}}{\sqrt{r}}. \tag{1.23}$$

Remark that $u_m = 0$ for $m > 0$ in (1.19) and that u_0 is direct proportional to $\sqrt{k}$ for this initial value problem. Since $u(x)$ solve (1.20) and (1.21), i.e. it is a Ray-field, we may use it as given data to a boundary value problem and in a second step solve the boundary value problem asymptotically. It also means that we may solve compound initial-boundary value problems as long as the boundary conditions is outside r. A question that is naturally raised and addressed in this thesis is: How to proceed if the initial value can not be written as a Ray field in the proximity of boundary condition? That is, how can we apply GTD to a general electric current close to a perfect electric conducting boundary? The research reported in [10] give new interesting ideas to solve such a problem.

We emphasis that the GTD, although only asymptotically accurate, is a very attractive solution method thanks to its complexity in terms of arithmetic operations. The scattering problems mentioned in the introduction typically contains the order of S=1000 NURBS elements. For the computation of some GTD-phenomenons, such as reflection and diffraction, one may achieve a complexity of the order of S or S^2. That is, to find all relevant rays, the complexity is independent of the frequency and the problem is much more of a logical nature than of a numerical one.

For smooth surface diffraction, that we will introduce in Section 1.3, we will see that it is a non-trivial numerical problem to find all relevant rays and it may be necessary to make the complexity wave length dependent.

1.3 Smooth Surface Diffraction, Hybrid Geometries

The work on hybrid geometries for GTD and the so called Smooth Surface Diffraction is inspired by challenges in electromagnetic engineering where numerical and asymptotic techniques are mature enough to be applicable to industrial and relatively complex problems. We have focused on the scattering problems induced by electromagnetic signature analysis and more specifically on plane wave back scattering problems, e.g. radar cross section computations mentioned previously, where only the scattered field propagating in the opposite direction of the exciting wave is studied. We will emphasize though that our numerical method is not restricted to the so called mono-static scattering problems but they may for example be used for bi-static scattering and radiation problems.

Geometrical Theory of Diffraction is today a well established theory used for analyzing wave phenomenons asymptotically, i.e. when the wave length is short compared to the characteristic sizes of the scales in the boundary conditions. The error in the asymptotic theory, as mentioned in the introduction, decreases as we decrease the wave length. In terms of errors there is a fundamental difference between the GTD and numerical methods. The errors in numerical methods used on the wave equation are typically proportional to some *negative* powers of the wave length. This fact is important to take into account when numerical methods are developed to solve the numerical problems induced by GTD. Our numerical method and the corresponding implementation have addressed both of the two

error contributions. Differently stated, we have developed a method that keep, if we perform the proper mesh refinement, the wave length proportionality of the error and we have therefore achieved a numerical method with a complexity that grows relatively slow with the frequency.

We have developed a numerical method for the so called smooth surface diffracted contributions predicted by GTD. Except for retaining the attractive feature with the direct asymptotic proportionality between wave length and error we have had two other major objectives when we have designed our numerical algorithm. The method should be efficient in predicting the scattered field in so called caustic regions and the algorithm should be able to predict smooth surface diffracted waves excited by edges in complex geometries. Putting all demands together we have implemented an algorithm that finds the smooth surface diffracted wave front solution in any point on a smooth surface by interpolation. The method is sometimes referred to a wave front construction technique [11] where the wave front is actually represented in phase space. Having access to the entire wave front in phase space, makes it possible to integrate the total field along the so called shadow line boundaries and therefore be able to evaluate the field in points/directions where infinitely many GTD-rays contribute (caustic points). C.f. [12] [13] and [14] for other approaches.

To be able to detect and treat non-smooth surfaces, e.g. edges, a meshed representation of the scatterer is not enough, but we need to be able to interpolate from exact geometry data. We say that we have a hybrid geometry and we consider the well established formats based on Non-Uniform Rational B-Splines (NURBS) as an exact representation of the geometry [15]. NURBS can be seen as a parametrical representation of the geometry. We could in principle formulate our wave front propagation algorithm in the surface parametrical space but since the NURBS representation is not optimized for numerical computations we have chosen to use a triangular mesh for the propagation. To make the numerical algorithm as efficient as possible we assume that the mesh has been produced by limiting the distance between the mesh and the exact geometry. If this distance is bounded by the wave length λ, one can show that the elements are of size order $1/\sqrt{\lambda}$ and that number of elements in the mesh therefor is of order $1/\lambda$.

Our solver has been developed from a Boundary Element solver presented in [16] and a GTD-solver presented in [17]. To be able to represent the geometry and the wave fronts efficiently we found it necessary to implement the algorithm in an object oriented fashion. To run our code on high performance computers we found it practical to write the code in Fortran 90.

If boundary conditions are present in the EM-problem we must use an expansion that distinguish from (1.19). In fact we can not assume that ϕ may be uniquely defined in all points and we must therefore assign several expansion corresponding to different waves. It may be shown that, if the scatterer is smooth, one of the waves in the expansion describe the so called smooth surface diffracted field. The phase of the asymptotic solution then also solves a type of Eikonal equation. J. B. Keller, c.f. [18], found the first amplitude function for the special case of a

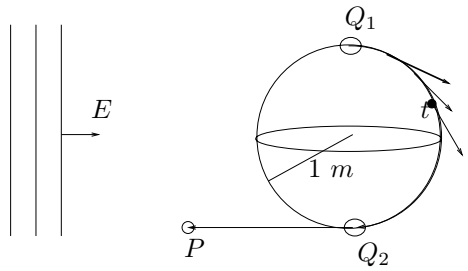

Figure 1.2: Plane wave scattering by a sphere.

sphere and indicated a solution method for a general convex smooth scatterer. For pedagogical reasons let us consider a simple example when discussing the Smooth Surface Diffracted solution. We refer to figure 1.2. The so called soft ($\mathcal{S}$) and hard ($\mathcal{H}$) components of the smooth surface diffracted electric field in P is according to [18]

$$\begin{aligned} E_{scatt}^{\mathcal{S},\mathcal{H}}(P) &= E_{inc}^{\mathcal{S},\mathcal{H}}(Q_1)\sqrt{\frac{\partial\eta(Q_1)}{\partial\eta(Q_2)}}\sqrt{\frac{\rho}{r(\rho+r)}} \\ &\cdot \sum_{p=1}^{N} D_p^{\mathcal{S},\mathcal{H}}(Q_1)\exp\left(-i\frac{2\pi}{\lambda}\int_{Q_1}^{Q_2} 1+\sigma_p^{\mathcal{S},\mathcal{H}}(t')\,dt'\right) D_p^{\mathcal{S},\mathcal{H}}(Q_2), \end{aligned} \tag{1.24}$$

with

$$\sigma_p^{\mathcal{S},\mathcal{H}} = \lambda^{2/3}\rho_g^{-2/3}c_1^{\mathcal{S},\mathcal{H},p}$$

and

$$D_p^{\mathcal{S},\mathcal{H}} = \lambda^{1/12}\rho_g^{1/6}c_2^{\mathcal{S},\mathcal{H},p}.$$

Here $c_j^{\mathcal{S},\mathcal{H},p}$ are given constants, ρ_g the radius of curvature of a geodesic line, ρ the radius of curvature of the so called geodesic wave front, $r = |P - Q_2|$ and t' the arc length parameter of the geodesic line. The square root of $\partial\eta(Q_1)/\partial\eta(Q_2)$ describes the geometrical spreading of the wave as it propagates along the surface. The soft component is the scattered electrical field that are parallel to the surface normal $\hat{n}$ at Q_1/Q_2 and the hard component is the scattered electrical field that are parallel to $\hat{p}\times\hat{n}$ where $\hat{p}$ is Poynting's vector of the wave at Q_1/Q_2. We see in (1.24) that, for propagation distances of $\mathcal{O}(\lambda^{1/3})$, the smooth surface diffracted field is proportional to $\lambda^{1/6}$. Hence this contribution may be significant for some scattering problems (c.f. edge diffraction [8] which is of $\mathcal{O}(\lambda)$). To be able to evaluate (1.24) numerically in a point P we need the geodesic line(s), i.e. the curves that are stationary with respect arclength, that ends in Q_2 and have a tangent, in the point P, that is parallel to $P - Q_2$. These lines, which are also characteristic curves to the so called surface Eikonal equation, can be found by solving a system of three ODEs. Let us

parameterize the geodesics with arc length in surface parametrical space (p, q), i.e. let $\dot{p} = \cos\alpha$ and $\dot{q} = \sin\alpha$. By differentiating $\alpha(s) = \arctan \dot{p}/\dot{q}$ we get

$$\dot{y} = \begin{pmatrix} \dot{p} \\ \dot{q} \\ \dot{\alpha} \end{pmatrix} = \begin{pmatrix} \cos\alpha(s) \\ \sin\alpha(s) \\ \ddot{p}(y(s))\sin\alpha(y(s)) - \ddot{q}(s)\cos\alpha(s) \end{pmatrix} = f(y). \tag{1.25}$$

The symbols $\ddot{p}(y)$ and $\ddot{q}(y)$ assign functions that can be found from the so called geodesic equations and will depend on local derivatives of the surface. This system has a unique solution under certain regularity conditions on the surface, and we may therefore interpolate between solutions that have initial conditions that are close in (p, q, α)-space. By solving (1.25) for a family of ODE-systems,

$$\begin{aligned} &\dot{y}^{(1)} = f(y^{(1)}) \text{ with } y^{(1)}(0) = \tilde{y}(\tau^{(1)}) \\ &\vdots \\ &\dot{y}^{(n)} = f(y^{(n)}) \text{ with } y^{(n)}(0) = \tilde{y}(\tau^{(n)}), \end{aligned} \tag{1.26}$$

where the initial conditions $\tilde{y}(\tau^{(j)})$ are parameterized with arclength and ordered along a smooth curve in (p, q, α)-space called

$$\tilde{y}(\tau) = (\tilde{p}(\tau), \tilde{q}(\tau), \tilde{\alpha}(\tau); s = 0) \text{ with } \tau_1 \leq \tau \leq \tau_n,$$

we may achieve the solution, by interpolation, in any point in (τ, s)-space. We call this approach a wave front construction method. Note that the name wave front indicates that the front is an equi-phase front, but the method itself does not insist on that, but just that the geodesic lines, corresponding to different initial conditions, are ordered such that neighboring initial conditions are close and that the geodesic lines are non-parallel to the front. To emphasize this, we call the fronts that we compute for generalized wave fronts. Also note that not only the solution to (1.25) may be interpolated along a generalized wave front but also the value of (1.24) may be achieved by interpolation if it is known on neighboring geodesics.

We have developed and implemented an algorithm that solve (1.25) on surface curvature sensitive triangular meshes. These meshes are characterized by a given boundedness, ϵ, on the distance between the mesh and the NURBS-geometry. More specifically for such a mesh, we have that the flat triangle nodes will coincide with the curved embedding geometry it is representing. The main idea with our algorithm rests on that we consider each triangle j, of size less than h, as a parametrical space (p_j, q_j) for a subset of the entire NURBS geometry. Each subset can be thought of a curved triangular patch given as a function $f_j(p_j, q_j)$ with an origin o_j that for example coincide with one of the triangle nodes.

In Chapter 4 we will explain how geodesics can be found on a hybrid geometry so that the smooth surface diffraction contribution can be estimated with sufficient accuracy and in an efficient manner. In our numerical algorithms we let straight line segments in the triangles approximate the geodesic curves in the true geometry.

By mathematical analysis we will then show how the small straight segments should be oriented, to build an open non-regular polygon in $\mathbb{R}^3$, so that the length of the polygon is an $\mathcal{O}(h)$ approximation of the true geodesic curve.

The error in $E_{scatt}^{\mathcal{S},\mathcal{H}}(P)$ will of course depend on the error in Q_1, Q_2, P, which will in its turn affect the geometrical spreading and $D_p^{\mathcal{S},\mathcal{H}}$. However, in the analysis we have focused on the error in the exponential factor which in its turn depends on the error in the numerical solution of (1.25). In fact we can expect that, as we decrease the wave length, it is the error in the first term in the exponent of expression (1.24) that are the dominant one since the corresponding integrand is proportional to λ^0. Consider Figure 1.2. Assume that the local radius of curvature can be computed exactly (It is in fact interpolated with an $\mathcal{O}(h^2)$ scheme in our implementation). If we mesh the sphere with triangles of size h then the geodesic line, indicated in the figure, will pass $\mathcal{O}(1/h)$ triangles. If we have a local error of the arc length of $\mathcal{O}(h^\gamma)$ then the exponential factor can, since we have constant radius of curvature, be shown to be

$$\exp\left(i2\pi\frac{(1+\alpha_p^{\mathcal{S},\mathcal{H}}(\lambda^{2/3}))(\ell+\mathcal{O}(h^{\gamma-1}))}{\lambda}\right) =$$
$$e^{i2\pi\frac{(1+\alpha_p^{\mathcal{S},\mathcal{H}})\ell}{\lambda}}\left[1+\lambda^{-1}\mathcal{O}(h^{\gamma-1})\right]\left[1+\mathcal{O}(\lambda^{-1/3})\mathcal{O}(h^{\gamma-1})\right].$$

If we choose $h\sim\mathcal{O}(\lambda^\delta)$ we get that the integral will be numerically estimated to

$$e^{i2\pi\frac{(1+\alpha_p^{\mathcal{S},\mathcal{H}})\ell}{\lambda}}(1+\mathcal{O}(\lambda^{\delta(\gamma-1)-1})). \tag{1.27}$$

That is the dominant error will decrease as we increase the frequency if we pick δ and γ properly. For example, if we manage to construct a scheme with a local error of order $\gamma=3$ then we need to pick $\delta\geq 1/2$ to have a non-increasing error with increasing frequency. If we, for a surface curvature sensitive mesh, bound the maximum distance between the mesh and the scatterer by a distance of $\mathcal{O}(\lambda)$ then one can show that $\delta=1/2$.

We have tested the major part of the algorithm on different geometries and achieved satisfactory results. We refer to Figure 1.3 for a quite complex geometry where we have tested the larger part of the algorithm. That is, finding the initial generalized wave front, propagating the front and applying the proper stopping criteria.

The main innovative features with our numerical method is that we have applied the *wave front construction technique* to Smooth Surface Diffraction by using a *hybrid geometry*. In this way we have achieved high accuracy and robustness.

1.4 Integral equations and Asymptotics, Hybrid Methods

We will present three hybrid methods in Chapter 5. To summarize them here we define an *asymptotic boundary* as a boundary where asymptotic techniques approximate the boundary conditions well. The over all focus of the hybrids are their

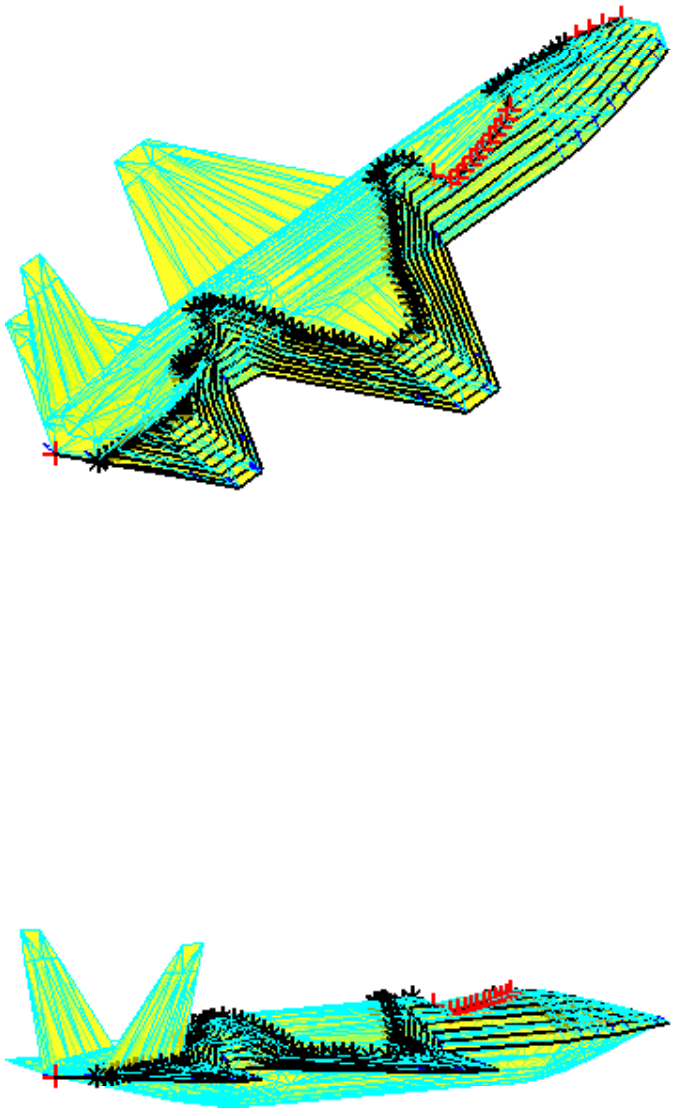

Figure 1.3: Example of wave fronts on a low signature vehicle meshed with a surface curvature sensitive mesh which is perceptible in the figure. The stars indicates where we interrupt the front propagation. I.e at edges or when corresponding markers have moved a specific length.

ability to represent currents on boundary elements *independently* of their distance to asymptotic boundaries and *independently* of the regularity of the asymptotic boundary in contrast to existing methods which mainly are designed for problems where the boundary element currents are *far* from asymptotic boundaries or *close* from smooth asymptotic boundaries. The first method is applicable to problems with a *smooth* asymptotic boundary, close or far from the boundary elements currents, which are *smooth*. The other two methods tries to remove this regularity condition on the asymptotic boundary.

The most basic hybrid technique that, in fact has been widely used in frequency domain, is the technique of separating the small scales from the large scales totally. This can be done for example by doing measurements with only the small scales present and then in a second step use this as given data in an asymptotic solver. Such methods and techniques were further investigated and improved in the seventies and eighties but they were not widely used by the electromagnetic society, until the last decade because of their loss of generality. Also, an obstacle to make them more popular in the electromagnetic society is that you need to have an experience and understanding both in numerical and asymptotic methods. Our numerical method aims at broadening the domain of applicability and therefore obtain a numerical solver which can form a part of general electromagnetic solvers designed for industrial use. Since the standard type of boundary elements used by industrial codes are triangles the hybrid method has to be able to represent these type of elements. The boundary conditions in the asymptotic domain needs to be defined by CAD data which today means Non-Uniform Rational B-Splines (NURBS). The kernel of such a hybrid solver then constitutes of algorithms that approximately compute currents on triangles close to boundary conditions defined on NURBS. We will restrict the discussion and the results to perfect electric conducting materials and just note that generalizations are most often straight forward.

The over all picture of our method can be seen for a scattering problem in Figure 1.4. The key feature of our algorithm is how we treat the scattered field originating from the excitation and the currents in the BEM-domain. In some cases it is a good approximation to assume that the field behaves as a Ray-field, i.e. J. B. Keller's GTD is applicable, in other cases we have to apply RBI (defined below), and finally we sometimes need to apply a linear combination of the methods. Let us analyze the methodology indicated in Figure 1.4 by generalizing the most simple scattering problem in a few steps.

Plane wave on a infinite (flat/non-flat) ground. Given an excitation, e.g. a plane wave $\mathbf{E}^{exc} = \mathbf{E}_0 e^{i\mathbf{k}\cdot\mathbf{x}}$, impinging on an infinite perfectly conducting plane, let us say the x_1x_2-plane with normal $\hat{\mathbf{n}} = (0, 0, 1)$, the so called image theory provide us with an exact analytic solution for the total field. The theory says that for $\{\mathbf{x} \in \mathbb{R}^3 : x_3 \geq 0\}$ the electric field is

$$\mathbf{E}(\mathbf{x}) = \mathbf{E}_0 e^{i\mathbf{k}\cdot\mathbf{x}} + (2\hat{\mathbf{n}} \cdot \mathbf{E}_0\hat{\mathbf{n}} - \mathbf{E}_0)e^{i(\mathbf{k}+2\hat{\mathbf{n}}\cdot\mathbf{k}\hat{\mathbf{n}})\cdot\mathbf{x}} \tag{1.28}$$

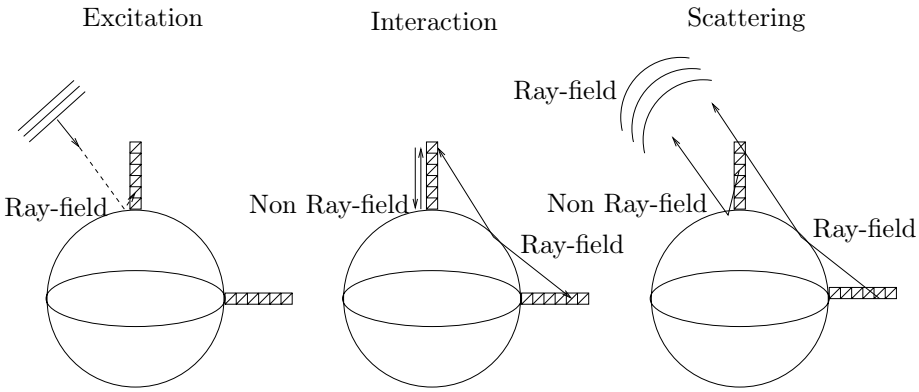

Figure 1.4: Each triangle contains a smooth union of infinitely small dipoles building a boundary element. When a triangle is too close to the sphere then the interaction can not be taken into account with GTD since then there is no Ray-field at the reflection/interaction point but RBI has to be used instead. If the triangles are too far then RBI is unappropriate and GTD has to be used instead.

and magnetic field is

$$\mathbf{H}(\mathbf{x}) = \mathbf{H}_0 e^{i\mathbf{k}\cdot\mathbf{x}} + (\mathbf{H}_0 - 2\hat{\mathbf{n}}\cdot\mathbf{H}_0\hat{\mathbf{n}})e^{i(\mathbf{k}+2\hat{\mathbf{n}}\cdot\mathbf{k}\hat{\mathbf{n}})\cdot\mathbf{x}}. \tag{1.29}$$

This solution fulfill the Dirichlet type of boundary condition $\hat{\mathbf{n}}\times\mathbf{E} = 0$ in the x_1x_2-plane and the surface current in the ground plane is $\mathbf{J} = \hat{\mathbf{n}}\times\mathbf{H} = 2\hat{\mathbf{n}}\times\mathbf{H}^{exc}$. Since a plane wave is a Ray-field GTD also provide us with a method to compute the solution $\mathbf{E}$ and $\mathbf{H}$ in the upper half space when the ground plane is non-flat.

An infinitely small dipole above an infinite (flat/non-flat) ground. Similar formulas/rules, as for plane waves, holds for infinitely small electric dipoles, i.e. $\mathbf{D}(\mathbf{x}) = \delta(\mathbf{x}-\mathbf{x}_0)\mathbf{J}$, above a perfectly conducting flat ground plane. However, unlike the plane wave, is the field from a infinitely small electric dipole only asymptotically a Ray-field as $|\mathbf{x}-\mathbf{x}_0|\to\infty$. Hence when the dipole is close to the ground plane GTD is not applicable to compute $\mathbf{E}$ and $\mathbf{H}$.

An infinite union of infinitely small dipole above an infinite (flat/non-flat) ground. We once more refer to Figure 1.4. An infinite smooth union of dipoles $\bigcup_{i=1\ldots\infty}\mathbf{D}_i$, e.g. defining a surface current density $\mathbf{J}_T$ on a triangle T, converges to a Ray-field, in general slower, as $|\mathbf{x}-\mathbf{x}_0|\to\infty$, compared to a single dipole. The image theory is however applicable for the smooth union above a flat ground plane but if we modify the flat ground, e.g. so that it becomes a perfect electric conducting sphere with radius R that fulfill $\lambda R >> 1$, then the image theory will not, in principle, be applicable any more. However we may, as we will motivate

in Chapter 5, apply the so called *Ray Based Image method* (RBI-method), which is a kind of modified image method.

It is hard to inspect the errors for the RBI-method. It is done by numerical experiments in this thesis and we have not tried to develop formal error estimates. However we can compare with other numerical and asymptotic methods to get a qualitative apprehension of the errors we do when using the RBI-method. The most simple and relevant test case that capture the physical quantities, distance between source and scatterer, polarization, wavelength and radius of curvature for the scatterer is a dipole above a sphere and it will be investigated in Section 5.4.1. What we at least intuitively may expect is that RBI fails when the source and/or the receiver is far away from the non-flat ground plane since then we know that GTD is the proper approximate method to be used.

In the simple test case mentioned above, we only consider the problem with an impressed source, i.e. the dipole is not influenced by the currents in the ground plane. To test the method for a more relevant problem we inspect the method by applying it to a perfect electric conducting strip above a finite ground plane illuminated by a plane wave. The final test case is done with a small conducting semi-sphere electrically attached to a large conducting sphere.

Let us return to the more simple test case of a conducting strip above a ground plane. The interaction between the ground plane and the strip can either be done iteratively or by directly modifying the kernel in the integral equation. For pedagogical reasons we choose to consider only the *iterative* approach in the introduction and save the discussion on the *direct* approach to later.

Assume that we have discretized the entire geometry with boundary elements and that a boundary element either belongs to the large scale geometry or the small scale geometry. By using the proper numbering of the unknowns we get a matrix problem, introduced in Section 1.1, that can be written as

$$\begin{pmatrix} A_{11}A_{12} \\ A_{21}A_{22} \end{pmatrix} \begin{pmatrix} \mathbf{J}_1 \\ \mathbf{J}_2 \end{pmatrix} = \begin{pmatrix} \mathbf{E}_1^{exc} \\ \mathbf{E}_2^{exc} \end{pmatrix}. \tag{1.30}$$

Let elements in A_{11} represent the mutual coupling between the elements in the large scale geometry and A_{22} the mutual coupling between elements in the small scale geometry. The cross term represent the action and reaction between the large and the small scale. The vector $\mathbf{J}_1$ contains the complex numbers representing the currents in the large scale and $\mathbf{J}_2$ the currents in the small scale. Similar, does $\mathbf{E}_1^{exc}$ represent the excitation falling onto the boundary elements in the large scale and $\mathbf{E}_2^{exc}$ the excitation falling onto the small scale. We can write (1.30) on an iterative form

$$A_{22}\mathbf{J}_2 = \mathbf{E}_2^{exc} - A_{21}A_{11}^{-1}\mathbf{E}_1^{exc} + A_{21}A_{11}^{-1}A_{12}\mathbf{J}_2, \tag{1.31}$$

which sometimes may be solved with an iterative scheme as

$$A_{22}\mathbf{J}_2^{(n+1)} = \mathbf{E}_2^{exc} - A_{21}A_{11}^{-1}\mathbf{E}_1^{exc} + A_{21}A_{11}^{-1}A_{12}\mathbf{J}_2^{(n)}. \tag{1.32}$$

The second and third term in the right hand side contains large matrices and we would therefore like to avoid filling and inverting them. Both of the terms can be interpreted as impressed source terms that excite the currents, $\mathbf{J}_2$, in the small scale. By looking at the problem from a physical point of view, we realize that the impressed sources can be represented by a linear combination between RBI and GTD. We write schematically

$$A_{22}\mathbf{J}_2^{(n+1)} = \mathbf{E}_2^{exc} + \mathbf{E}_2^{GTD}(\alpha_{ij}) + \mathbf{E}_2^{RBI}(\beta_{ij}), \tag{1.33}$$

The α_{ij} and β_{ij} represent weighting factors with $\alpha_{ij} + \beta_{ij} = 1, \forall\ (i,j)$. For the impressed plane wave $\mathbf{E}_2^{exc}$ we may apply GTD directly since it is a Ray-field everywhere.

How is α_{ij}s and the β_{ij}s going to be decided. As we mentioned earlier, if the currents in the small scale is far from the large scale geometry then RBI produce too large errors to be usable. We therefore apply GTD for these currents. More generally we apply a linear combination between GTD and RBI. The matrices represented by the α_{ij}s and β_{ij}s are not necessarily symmetric. By intuition the elements should be dependent on the distance between the basis, image basis and test function to the large scatterer. We will not try to derive the optimal expression for these dependencies but just note that it is probably dependent on specific properties of the geometry in both the small and the large scales.

We note that when (1.33) has converged we can with the help of the representation theorem, and a linear combination between GTD and RBI, compute the scattered field.

The method compactly described by equation (1.33) is applicable to problems where the small scales is introduced by

- *adding* boundary conditions *far* from large scale geometries which are represented by *smooth* and/or *non-smooth* boundaries.
- *adding* boundary conditions *close* to large scale geometries which are represented by *smooth* boundaries.

In Figure 1.4 we have attached two metal strips to a smooth boundary. If we want to introduce small scales by actually perturbing the large scales or adding small scales close to non-smooth boundaries the RBI-method is not applicable anymore. To solve these types of problems we suggest two types of methods. Either global basis and test functions are combined with functions with local support in the variational formulation or GTD edge diffraction is used to represent the currents in large scales.

1.5 Project Environment

The work reported in this thesis has been performed within research projects driven by industrial applications and motivated by academic research and industrial development. The industry mainly provided the project with user requirements, relevant

test cases and developed graphical user interfaces while academia and research institutes developed the algorithms and the core solvers. The funding were provided by the government and the industry.

The goal of the projects was to develop a state of the art software suite in computational electromagnetics and the generic term for the projects is The General ElectroMagnetic Solver project (GEMS).

The projects spans over the years 1998 to 2005. The industry are represented by Ericsson Microwave AB, Saab Ericsson Space AB and AerotechTelub AB. The research and the code developing were done by The Fraunhofer-Chalmers Research Center for Industrial Mathematics, The Swedish Defense Research Agency, Uppsala University (Department of Information Technology), The Royal Institute of Technology (Numerical Analysis and Computer Science) and The Chalmers University of Technology (Department of Electromagnetics). The aim of the projects where more specifically to provide the Swedish industry and academia with state of the art hybrid solvers in time and frequency domain which were able to solve industrial problems specified in the user requirements and to adapt the solvers to more specific engineering problems.

To follow the time schedule in the project specification, two solvers in the frequency domain where brought from other research establishments. A Boundary Integrals Equations (BIE) solver came from a research team lead by Prof. A. Bendali at CERFACS in Toulouse and a Geometrical Theory of Diffraction (GTD) solver came from a research team lead by Prof. M. F. Catedra then at Universidad de Cantabria. These two solvers where substantially modified so that they fulfilled the high project demands on portability and maintainability. Many new functionalities where also added.

Some of the test cases in the project where very large in terms of numerical unknowns and therefore asymptotic methods where implied. There where also rather restrict accuracy demands on these large problems. This fact where the main reason for developing hybrid methods in frequency domain. Both a Physical Optics (PO) - BIE hybrid and GTD-BIE hybrid where developed. These methods where expected to complement each other. The most straight forward way to rigorously couple PO with BIE is to use the same type of discretization elements in the two method domains. It makes the PO solver less powerful since unknown currents needs to be resolved with about ten elements per wavelength. That is the nice $O(1/\lambda)$-complexity for PO has been destroyed. This motivated a BIE-GTD hybrid solver development which achieve an $O(1)$-complexity in the asymptotic domain. The chosen type of GTD-implementation presented in [19] had problems around caustic points which motivated the BIE-PO-hybrid.

The aim of the projects following the initial one was mainly to further develop the frequency domain solvers for RCS applications and to optimize the time domain solvers for antenna applications. Some optimization tools were also developed during the later part of GEMS-project.

This thesis report on the research done while the GTD- and the GTD-BIE-solver were developed.

To develop a GTD-BIE hybrid solver and the improved GTD solver for industrial use, you necessarily need the main constituents, i.e. the GTD-solver and the BIE-solver, to be well written, stable and well adjusted to pre and post processing. Therefore the initial work in the hybridization was to adapt the main constituents for these needs. To be able to start the hybrid development at an early stage as possible the data flow between the solvers were done out-of-core and later on done by subroutine calls. The initial work on the GTD-solver where mainly done by F. Bergholm, L. Hellström, S. Hagdahl, U. Oreborn, S. Sefi. The work on the BIE-solver where mainly done by J. Edlund, A. Nilsson, B. Strand, M. Nilsson, L. Hellström, L. Lovius and A. Lei. Most of the work where supervised by B. Strand and A. Ålund.

All hybrid solvers are written in Fortran 90 with high demands on portability both to serial and parallel platforms. The GEMS-code, including both time and frequency domain solvers, contain today approximately 600 000 lines.

1.6 Publications

The results on hybrid methods are partly based on [20], [21], [22], and [23]. The results on Smooth Surface Diffraction are partly based on [17], [24], [23] and [25].

For convenience, we list all our publications below.

A) U. Andersson, F. Edelvik, J. Edlund, L. Eriksson, S. Hagdahl, G. Ledfelt and B. Strand, GEMS - A Swedish Electromagnetic Suite of Hybrid Solvers-Technical Aspects. In *AP2000 Millennium Conference on Antennas & Propagation*, 2000.

B) J. Edlund, S. Hagdahl and B. Strand, An Investigation of Hybrid Techniques for Scattering Problems on Disjunct Geometries. In *AP2000 Millennium Conference on Antennas & Propagation*, 2000.

C) F. Bergholm, S. Hagdahl and S. Sefi, A Modular Approach to GTD in the Context of Solving Large Hybrid Problems. In *AP2000 Millennium Conference on Antennas & Propagation*, 2000.

D) S. Hagdahl, Tracking Wavefronts with Lagrangian Markers. Royal Institute of Technology, Department of Numerical Analysis and Computer Science, TRITA-NA-0122. 2001.

E) B. Engquist and S. Hagdahl, Numerical Techniques for Mixed High-Low Frequency EM-Problems. In *Proceedings RVK02*, 2002.

F) S. Hagdahl and O. Runborg, Optimization of Flight Trajectories with Respect to Radar Signature. Poster at GO++ Winter School, INRIA, Rocquencourt, France, 2002.

G) S. Hagdahl, *Hybrid methods for computational electromagnetics in the frequency domain.* Royal Institute of Technology, Department of Numerical Analysis and Computer Science, Licentiate thesis No. 2003-018. 2003.

H) B. Engquist and S. Hagdahl, Computation of Smooth Surface Diffraction for Industrial Application, In *Proceedings EMB04*, 2004.

Chapter 2

Direct Numerical Approximations, Boundary Element Method

To be able to explain the hybrid methods in Chapter 5 we open our main presentation with a short introduction to the boundary element method continued with a more deep investigation of some specific details in the method.

The physics of the electromagnetic field is governed by Maxwell's equations which were stated in differential form by James Clerk Maxwell in 1864. To solve the equations numerically, in modern computers of today, two major techniques are used. Either discrete approximate differential or integral operators are deduced and used in finite volume, finite difference or finite element settings. Let us call them volume methods. The number of unknowns is proportional to the wave number powered by the number of independent variables. Alternatively we can solve the equations by first finding the fundamental solution to the problem and then by Green's theorem formulate the problem on a boundary integral equation form. After this is done integro- and differential-operators is defined in discrete form and solutions may be found in well chosen functional spaces. In this case the number of unknowns is proportional to the wave number powered by the number of independent variables.

There is a possibility to define a volume integral equation with the fundamental solution but this method is not computationally popular.

Notice that we gain at least one space dimensions by using the fundamental solution. However there is a price to be paid in doing this. Both methods end in systems of linear equations. For the boundary integral method we get a dense matrix in contrast to the volume methods which have sparse matrices. Problem to be solved often decide which method that is preferable.

Both methods mentioned above show up in time dependent and time harmonic form. We will however only focus on the boundary element method in the time harmonic form and we will mainly borrow results from a book written by J.C. Nédélec [2]. Rather briefly, we discuss how to transform Maxwell's time dependent

equations to a boundary integral equation in spectral domain. While introducing numerical approximations of the integro- and differential-operators, we also present the boundary element solver used in later chapters for numerical experiments.

2.1 Time Harmonic Maxwell Equations

We state Maxwell's equations in M.K.S. units as

$$\begin{aligned} &\nabla \times \mathcal{H}(\mathbf{x},t) - \varepsilon(\mathbf{x})\mathcal{E}_t(\mathbf{x},t) = \sigma\mathcal{E} \\ &\nabla \times \mathcal{E}(\mathbf{x},t) + \mu(\mathbf{x})\mathcal{H}_t(\mathbf{x},t) = 0 \\ &\nabla \cdot (\mu\mathcal{H}(\mathbf{x},t)) = 0 \\ &\nabla \cdot (\varepsilon\mathcal{E}(\mathbf{x},t)) = \rho(\mathbf{x},t). \end{aligned} \tag{2.1}$$

The electric $\mathcal{E}$ and magnetic $\mathcal{H}$ field is dependent on time t and the space variable $\mathbf{x}$. The dielectric constant ε and the magnetic permeability μ is assumed to be piecewise constant. ρ is the electric charge density and σ is the conductivity. Maxwell's equations are equations describing a wave phenomena. It is therefore natural to define a wave speed c and we can show that information travels with the speed $c = 1/\sqrt{\varepsilon\mu}$. If $\sigma(\mathbf{x}) = 0$ and, at $t = 0$, $\nabla \cdot (\varepsilon\mathcal{E}(\mathbf{x},t)) = 0$ it may be shown that the solution to

$$\begin{aligned} &\nabla \times \mathcal{H}(\mathbf{x},t) - \varepsilon\mathcal{E}_t(\mathbf{x},t) = 0 \\ &\nabla \times \mathcal{E}(\mathbf{x},t) + \mu\mathcal{H}_t(\mathbf{x},t) = 0, \end{aligned} \tag{2.2}$$

coincide with the solution to (2.1). Restricting solutions to time harmonic fields

$$\begin{aligned} \mathcal{E}(\mathbf{x},t) &= \mathrm{Re}(\mathbf{E}(\mathbf{x})e^{-i\omega t}) \\ \mathcal{H}(\mathbf{x},t) &= \mathrm{Re}(\mathbf{H}(\mathbf{x})e^{-i\omega t}), \end{aligned} \tag{2.3}$$

in source free points of zero conductivity, the complex field $(\mathbf{E}, \mathbf{H})$ fulfill the following two equations,

$$\nabla \times \mathbf{E} = i\omega\mathbf{H} \tag{2.4}$$

$$\nabla \times \mathbf{H} = -i\omega\mathbf{E}. \tag{2.5}$$

We will later indicate how we can rewrite these two PDE:s on a boundary integral equation form. Depending on which engineering problem that is to be solved, sources or data, can be given on different forms for boundary integral equations. They can for example consist of

- data on the integration boundary with surface normal $\hat{\mathbf{n}}$ in the form of impressed electric surface currents $\mathbf{J}^{imp} \equiv \hat{\mathbf{n}} \times \mathbf{H}$ or magnetic currents $\mathbf{M}^{imp} \equiv \hat{\mathbf{n}} \times \mathbf{E}$,
- data in the form of $\mathcal{J} = \sigma\mathbf{E}$ defined far away from the integration boundary giving rise to impinging approximate plane waves,

- data in the form of $\mathcal{J}$ at a finite distance from the integration boundary giving rise to more general impinging waves and
- data in the form of impressed **E** and/or **H** on the integration boundary,

where we assumed that **E** and **H** fulfills Maxwell's equations.

These types of data are more or less artificial since electromagnetic energy interact over finite distances. However, the errors can quite often be made sufficiently small in engineering problems. The important thing is that we, by rewriting the data, can specify it on the integration boundary where the unknowns will be defined. This also imply that the lack of free sources assumption in equation (2.4) and (2.5) is not a severe restriction since the excitation of the problem is done with the help of the boundary conditions. For a so called perfect electric conducting boundary, the tangential component of the **E**-field should be zero which corresponds to a Dirichlet type of boundary condition. There are also materials that calls for boundary conditions that resembles Neumann boundary conditions. Since we assumed that the material properties, ε and μ, were piece-wise constant we may also indicate interfaces between materials, i.e. data in the differential operator, with unknown electric and magnetic surface currents at these interfaces. To proceed, let us search the fundamental solution to the time harmonic Maxwell's equations.

2.2 Fundamental Solution

To be able to formulate the fundamental solution to (2.4) and (2.5) we introduce the tensor notation. While the distinction between covariant and contravariant indices must be made for general tensors, the two are equivalent for tensors in three-dimensional Euclidean space. Therefore we make no distinction between lower and upper indices. For the reason of symmetry between **E** and **H** in (2.4) and (2.5), we confine ourself to search for solutions to

$$\begin{aligned} i\omega\varepsilon_0 E^{\mu\nu}(x^\varepsilon) + \partial_\mu H^\nu(x^\varepsilon) &= \delta(x^\varepsilon)\delta^\mu_\nu & (2.6)\\ -i\omega\mu_0 H^{\mu\nu}(x^\varepsilon) + \partial_\mu E^\nu(x^\varepsilon) &= 0, & (2.7) \end{aligned}$$

where the Greek letters admit the values 1, 2 and 3. This would correspond to an infinitesimal electric current in x^ε with polarization δ^μ_ν, i.e. δ^μ_ν is Kronecker's delta symbol. Let us introduce the fundamental solution to Helmholtz equation, satisfying outgoing radiation condition, i.e. the Green function , as

$$G(x^\mu) = \frac{1}{4\pi}\frac{e^{ik_\mu x^\mu}}{\sqrt{x_\alpha x^\alpha}}, \tag{2.8}$$

where k_μ is the wave vector. That is, if have $exp(ikr)/r$ as the outgoing fundamental solution then we used $exp(-i\omega t)$ to achieve the harmonic equation. Then by defining the scalar potential V^ν and the vector potential $A^{\mu\nu}$ as

$$\begin{aligned} E^{\mu\nu} &= \partial_\mu V^\nu + A^{\mu\nu}\\ 0 &= \partial_\beta A^{\beta\nu} - k_\gamma k^\gamma V^\nu, \end{aligned} \tag{2.9}$$

we can show that a fundamental solution to our problem is

$$E^{\mu\nu}(x^\varepsilon) = i\omega G(x^\varepsilon)\delta^\nu_\mu + \frac{i}{\omega\varepsilon_0}\partial_\mu\partial_\nu G(x^\varepsilon) \tag{2.10}$$

and

$$H^{\mu\nu}(x^\varepsilon) = C^{\alpha\beta\mu}\partial_\alpha\delta^\nu_\beta G(x^\varepsilon), \tag{2.11}$$

where the third rank tensor $C^{\alpha\beta\mu}$ represent the cross product. Furthermore, it may be shown that $(E^{\mu\nu}, H^{\mu\nu})$ is a unique fundamental solution if we demand that the solution fulfill an extra radiation condition named by Silver-Müller, i.e.

$$\begin{array}{l} |\sqrt{\varepsilon_0}E^\mu - \sqrt{\mu_0}C^{\alpha\beta\mu}H_\alpha r_\beta/r| \leq \frac{const}{r^2} \\ |\sqrt{\varepsilon_0}C^{\alpha\beta\mu}H_\alpha r_\beta/r + \sqrt{\mu_0}H^\mu| \leq \frac{const}{r^2}, \end{array} \tag{2.12}$$

for sufficiently large r. Note that some of the components in $E^{\mu\nu}$ and $H^{\mu\nu}$ are non-integrable functions.

More specifically, will the E^μ-field in x^ε from an electric dipole positioned in x_0^β in free space with strength $I^\nu = I^\alpha\delta^\nu_\alpha$ be $E^\mu = I^\nu E_{\mu\nu}$. It can be shown that with $k = \sqrt{k^\alpha k_\alpha}$, $r^\alpha = x^\alpha - x_0^\alpha$ and $r = \sqrt{(x^\alpha - x_0^\alpha)(x_\alpha - x_{0,\alpha})}$,

$$\begin{array}{l} E^\mu(x^\varepsilon) = \\ r^\mu\delta^\alpha_\beta I^\alpha r_\beta \frac{i\omega\mu_0 e^{ik^\alpha r_\alpha}}{4\pi r^2}(-1 - \frac{3i}{kr} + \frac{3}{(kr)^2}) + \\ I^\mu \frac{e^{ik^\alpha r_\alpha}}{r}(1 + \frac{i}{kr} - \frac{1}{(kr)^2}) \end{array} \tag{2.13}$$

and

$$H^\mu(x^\varepsilon) = C^{\alpha\beta\mu}\partial_\alpha G(x^\varepsilon)I_\beta, \tag{2.14}$$

holds. For large r the dominating term is of order r^{-1} and after expressing the E^μ-field in a curve linear coordinate system we get, with standard spherical vector notation $(\hat{\mathbf{e}}_r, \hat{\mathbf{e}}_\theta, \hat{\mathbf{e}}_\phi)$,

$$\mathbf{E} \sim \hat{\mathbf{e}}_\theta \frac{i120|\mathbf{k}||\mathbf{I}|}{4}\frac{e^{i\mathbf{k}\cdot\mathbf{r}}}{|\mathbf{r}|}\sin\theta \tag{2.15}$$

and

$$\mathbf{H} \sim \frac{\mathbf{r}\times\mathbf{E}}{r}, \tag{2.16}$$

for $I^\mu = (0, 0, 1)$. In Chapter 1 we introduced something called Ray-field which is relevant for the GTD. It can be shown that the field from an infinitesimal dipole approaches a Ray-field as $r \to \infty$. One can also show that the asymptotic solution fulfill the Silver Müller radiation condition.

For later reference we will shortly discuss a continuous union of electric dipoles, i.e. a current in a domain Ω of $\mathbb{R}^3$. One can actually expand the radiated field into so called Vector Spherical Harmonics, where each term has an amplitude variation of $1/r^n$, c.f. [26]. If we evaluate the expansion in the far field, or far away from the dipoles, then it is the $1/r$ term that is the dominant one. In fact the $\hat{\mathbf{e}}_r$-component has no $1/r$-term and therefore it is only the $\hat{\mathbf{e}}_\theta$- and $\hat{\mathbf{e}}_\phi$-terms that are dominating. That is, for finite but large r and small, relative to the wave length, Ω the field behaves similar to a dipole but with different dependence on θ and ϕ.

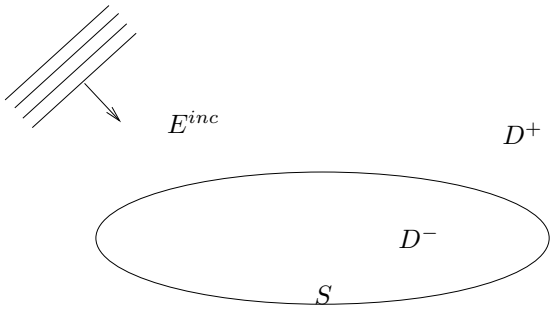

Figure 2.1: An unperturbed scattering boundary value problem.

2.3 Integral Representation

In previous sections we have discussed the scattered field in an unprecise way. Let us define it more sharp. The homogeneous Maxwell's equations admit some different type of solutions. For example a plane wave in a homogeneous dielectric material and the fundamental solutions defined above. Let us call such known analytic solutions $(\mathbf{E}_{exc}, \mathbf{H}_{exc})$. Call a solution to a certain boundary value problem $(\mathbf{E}, \mathbf{H})$. Now since Maxwell's equations are linear we may subtract any $(\mathbf{E}_{exc}, \mathbf{H}_{exc})$ from $(\mathbf{E}, \mathbf{H})$ and achieve a new solution. Let us call this solution $(\mathbf{E}_s, \mathbf{H}_s)$ or the scattered solution.

Consider Figure 2.1, where S represent a smooth boundary, bounding a closed simply connected region D^-, with a certain boundary condition. Define the surface normal $\hat{n}^\mu$ to S as the vector pointing into D^+. Let us also define the surface electric and magnetic current densities as the *tangent* field to the surface S, i.e.

$$j^\mu = C^{\alpha\beta\mu} H_s^\alpha \hat{n}^\beta + C^{\alpha\beta\mu} H_{exc}^\alpha \hat{n}^\beta$$

and

$$m^\mu = C^{\alpha\beta\mu} E_s^\alpha \hat{n}^\beta + C^{\alpha\beta\mu} E_{exc}^\alpha \hat{n}^\beta.$$

Before discussing the boundary integral equation and its well posedness some integral representations of the solution will be presented. It is relatively straight forward to show that the solution to Maxwell's equations admits an integral representation for E^μ and H^μ. One can show with tools from differential geometry that it is possible to uniquely and in a consistent manner define the divergence of a vector or gradient of a scalar surface field. The definitions rest on the fact that, with certain restriction on the surface, we can define surface fields u or u^μ and a surface normal n^μ in a tubular region in the neighborhood of a surface and then apply differential operators to these *lifted* fields $\tilde{u}$, $\tilde{u}^\mu$ or $\tilde{n}^\mu$. Let us indicate the

surfacic derivative as $\tilde{\partial}_\mu$. For the scattered electric and magnetic fields we have

$$\begin{aligned} E^\mu_{scatt}(y^\varepsilon) &= i\omega\mu_0 \int_S G(x^\varepsilon - y^\varepsilon) j^\mu(x^\varepsilon)\, ds(x^\varepsilon) \\ &+ \tfrac{i}{\omega\varepsilon_0}\partial_\mu \int_S G(x^\varepsilon - y^\varepsilon)\tilde{\partial}_\alpha j^\alpha(x^\varepsilon)\, ds(x^\varepsilon) \\ &+ C^{\alpha\beta\mu}\partial_\alpha \int_S G(x^\varepsilon - y^\varepsilon) m_\beta\, ds(x^\varepsilon), \end{aligned} \tag{2.17}$$

and

$$\begin{aligned} H^\mu_{scatt}(y^\varepsilon) &= i\omega\varepsilon_0 \int_S G(x^\varepsilon - y^\varepsilon) m^\mu(x^\varepsilon)\, ds(x^\varepsilon) \\ &+ \tfrac{i}{\omega\mu_0}\partial_\mu \int_S G(x^\varepsilon - y^\varepsilon)\tilde{\partial}_\alpha m^\alpha(x^\varepsilon)\, ds(x^\varepsilon) \\ &+ C^{\alpha\beta\mu}\partial_\alpha \int_S G(x^\varepsilon - y^\varepsilon) j_\beta\, ds(x^\varepsilon), \end{aligned} \tag{2.18}$$

when $y^\varepsilon \notin S$. The fundamental solution G is defined as in previous sections. More specifically for the vector field $C^{\alpha\beta\mu}\hat{n}^\alpha E^\beta$ letting $y^\varepsilon \in D^+ \to S$ we have

$$\begin{aligned} &(C^{\alpha\beta\mu}\hat{n}_\alpha E^{scatt}_\beta)(y^\varepsilon) = \\ &-\tfrac{m^\mu(y^\varepsilon)}{2} + \textstyle\int_S \hat{n}_\alpha \partial^{(y)}_\alpha G(x^\varepsilon - y^\varepsilon) m^\mu\, ds(x^\varepsilon) \\ &-\textstyle\int_S \partial^{(y)}_\mu G(x^\varepsilon - y^\varepsilon) m^\alpha(x^\varepsilon)(n_\alpha(y^\varepsilon) - n_\alpha(x^\varepsilon))\, ds(x^\varepsilon) \\ &+i\omega\mu_0 \textstyle\int_S G(x^\varepsilon - y^\varepsilon) C^{\alpha\beta\mu} j_\alpha \hat{n}_\beta(y^\varepsilon)\, ds(x^\varepsilon) \\ &+\tfrac{i}{\omega\varepsilon_0} \textstyle\int_S C^{\alpha\beta\mu}\partial^{(y)}_\alpha G(x^\varepsilon - y^\varepsilon)(n_\beta(y^\varepsilon) - n_\beta(x^\varepsilon))\tilde{\partial}_\alpha j^\alpha(x^\varepsilon)\, ds(x^\varepsilon) \\ &+\tfrac{i}{\omega\varepsilon_0} \textstyle\int_S G(x^\varepsilon - y^\varepsilon) C^{\beta\xi\mu}\tilde{\partial}_\beta\tilde{\partial}_\alpha j^\alpha(x^\varepsilon)\hat{n}_\xi(x^\varepsilon)\, ds(x^\varepsilon). \end{aligned} \tag{2.19}$$

The superscript (x) in the operator $\partial^{(x)}_\mu$ indicate that we operate the derivative on the x^ε-variable.

By using the boundary condition on S we have now obtained the searched integral equations. However, uniqueness and existence is not straightforward to show. I.e. functional spaces has to be defined and analysis has to be performed to see whether the integral operator is uniquely invertible.

2.4 Boundary Integral Equation

Let us consider the scattering problem for the Dirichlet type of boundary condition applied to Figure 2.1. That is, we search a Boundary Integral Equation (BIE) for the currents excited on a perfectly conducting sphere, $\mathbf{n} \times \mathbf{E} = 0$, by a plane wave illumination. Equation (2.19), by keeping only the three last terms in the right hand side, now reduces to

$$\begin{aligned} &(C^{\alpha\beta\mu}\hat{n}_\alpha E^{exc}_\beta)(y^\varepsilon) = \\ &+i\omega\mu_0 \textstyle\int_S G(x^\varepsilon - y^\varepsilon) C^{\alpha\beta\mu} j_\alpha \hat{n}_\beta(y^\varepsilon)\, ds(x^\varepsilon) \\ &+\tfrac{i}{\omega\varepsilon_0} \textstyle\int_S C^{\alpha\beta\mu}\partial^{(y)}_\alpha G(x^\varepsilon - y^\varepsilon)(n_\beta(y^\varepsilon) - n_\beta(x^\varepsilon))\tilde{\partial}_\alpha j^\alpha(x^\varepsilon)\, ds(x^\varepsilon) \\ &+\tfrac{i}{\omega\varepsilon_0} \textstyle\int_S G(x^\varepsilon - y^\varepsilon) C^{\beta\xi\mu}\tilde{\partial}_\beta\tilde{\partial}_\alpha j^\alpha(x^\varepsilon)\hat{n}_\xi(x^\varepsilon)\, ds(x^\varepsilon), \end{aligned} \tag{2.20}$$

since $(C^{\alpha\beta\mu}\hat{n}_\alpha E_\beta)(y^\varepsilon) = 0$. By singular integral operator analysis one can show that the kernel is integrable. However, there are second order derivatives of the unknown j^μ, which make the integrand very singular. By introducing a variational

formulation of (2.20) we can achieve a formulation, by using the so called Rumsey reaction, with only first order derivatives of the unknown. Introducing the test function j_t^μ one achieve, by using the Stokes formula on the surface,

$$\begin{aligned} &-\int_S E^\mu_{exc}(y^\varepsilon) j^t_\mu(y^\varepsilon)\, ds(y^\varepsilon) \\ &= i\omega\mu_0 \int_S \int_S G(x^\varepsilon - y^\varepsilon) j^\alpha(x^\varepsilon) j_{t,\alpha}(y^\varepsilon)\, ds(x^\varepsilon)\, ds(y^\varepsilon) \\ &-\tfrac{i}{\omega\varepsilon_0} \int_S \int_S G(x^\varepsilon - y^\varepsilon) \tilde\partial^{(x)}_\alpha j^\alpha(x^\varepsilon) \tilde\partial^{(y)}_\beta j^\beta_t(y^\varepsilon)\, ds(x^\varepsilon)\, ds(y^\varepsilon), \end{aligned} \tag{2.21}$$

for any j^t_μ in the proper functional space.

Up until now we have mainly focused on scattering problems, i.e. we search the field exterior to the scatterer. However, though equal to zero for a perfect electric conductor, it is useful to consider the interior problem also. In conformity with elliptic theory, i.e. the Laplace operator have Eigenvalue solution for boundary value problems, may the interior Maxwell problem contain spurious solutions for certain wave lengths λ (eigenvalues). This would have been surmountable if it did not corrupt the exterior solution, but it can be shown, that the spurious interior solutions will also corrupt the exterior problem and therefore make this problem ill posed for specific wave lengths.

We have the following fundamental result, taken from [2], which mainly rests on uniqueness of the solution and Fredholm's alternative. Let us decompose j^μ as

$$j^\mu = g^\mu + C^{\alpha\beta\mu} \tilde\partial^{(x)}_\alpha p(x^\varepsilon) \hat n_\beta,$$

then we have:

Proposition 2.1. *If $(2\pi/\lambda)^2$ is not an eigenvalue of the interior problem and if $C^{\alpha\beta\mu} n_a E^{exc}_\beta \in H^{-1/2}_{curl}(S)$ then equation (2.21) has a unique solution and*

$$j^\mu \in H^{-1/2}_{div}(S).$$

If also $C^{\varepsilon\gamma\mu}\tilde\partial_\varepsilon C^{\alpha\beta\gamma} n_\alpha E^{exc}_\beta \in H^{-1/2}_{curl}(S)$ then,

$$j^\mu \in TH^{1/2}(S).$$

If also $\tilde\partial_\beta E^{exc}_\beta \in H^{-1/2}_{curl}(S)$ then,

$$\tilde\partial_\mu j^\mu \in H^{1/2}(S).$$

Finally, if also $C^{\alpha\beta\mu} n_a E^{exc}_\beta \in H^{1/2}_{curl}(S)$ then,

$$j^\mu \in H^{1/2}_{div}(S).$$

T indicate that the function spaces concerns the vector components in the tangential plane to the scatterer and $H^{\cdots}_{\cdots}$ are Sobolev spaces putting regularity conditions on the functions. We will not further define the Sobolev spaces used in the theorem, and analyze there implications on S and E^{μ}_{exc}, but just refer to [2] and [5]. Equation (2.20) is sometimes referred to the Electric Field Integral Equation (EFIE), because it originates from the integral representation of the electric field. Since the unknown currents only are present in the integrand it can be classified as a Fredholm integral equation of *the first kind*. There is also an integral equation called MFIE, which is of *the second kind*, that rest on an integral representation of the magnetic field. The MFIE for a smooth perfect conducting body can schematically be written as

$$j_\alpha = 2C^{\alpha\beta\mu} n_\beta H^{exc}_\mu + L(j_\alpha), \tag{2.22}$$

where L is a linear integral operator, containing double integrals, representing the mutual coupling between the currents on the scatterer. The unknown currents are here also present outside the integral which suggest that an iterative solver can be used to solve the discrete problem. The MFIE, when numerically implemented, normally produce more well conditioned problems than the EFIE. However, the MFIE is only applicable to problems where S is closed.

Sometimes the MFIE and the EFIE is linearly combined into a so called Combined Field Integral Equation (CFIE). Numerical experience shows that the CFIE restrain the spurious solutions in the exterior domain and improve the condition number compared to EFIE.

Later we will numerically compare the so called RBI-method with some different approximate methods. One of these reference methods are based on an approximate version of equation (2.22). It is called the Physical Optics approximation and by referring to Figure 2.1 and using classical vector notation it can be written as

$$\mathbf{J}(x) = I\left[2\left(\hat{\mathbf{n}}(x) \times \mathbf{H}^{exc}(x)\right)\right] \text{ for } x \in S, \tag{2.23}$$

where $I = 1$ if x is illuminated by the wave $\mathbf{H}^{exc}$ or $I = 0$ otherwise. That is, if the exciting wave is not occluded, from an optical point of view, by S the approximation consists of neglecting the mutual interaction term. If the excitation wave is occluded then both terms on the right hand side of (2.22) is neglected.

2.5 Numerical Approximations

To be able to solve (2.21) we need to approximate the integral operator numerically and specify the finite dimensional spaces for j^μ and j^μ_t approximating the spaces given in Theorem (2.1).

2.5.1 Local Boundary Elements

Using finite elements [7, 4] as boundary elements for both basis and testing functions of the unknown current on a triangulated boundary we get a Galerkin type of

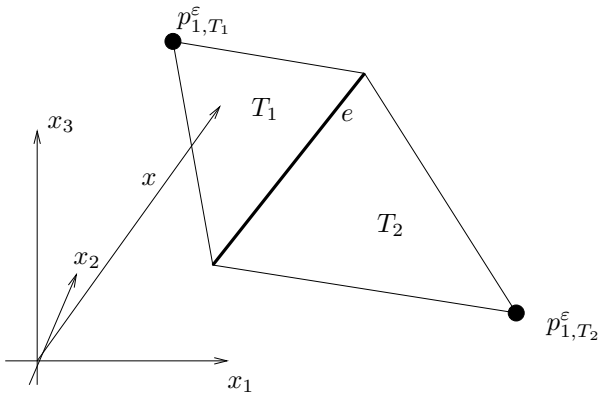

Figure 2.2: Two triangles sharing on edge with an associated basis function

method and it may be shown that j^{μ}_{approx} will approximate $H^{p}_{div}(\cdot)$ properly. A mathematical work analyzing numerical errors for this choice of elements is given in [5] and [6].

Let us present the numerical approximation of (2.21) in a very concise outline. For a more thorough description of the numerical implementation used in the numerical experiments presented below we refer to [16] and [27]. Using the notation introduced in Figure 2.2 let the boundary S be discretized with a number of triangles, each mathematically described by three nodes $p^{\varepsilon}_{j,T}$ ($j = (1 \dots 3)$ and $T = (1 \dots N_{tri})$). Let the triangle nodes coincide with S. The current in a point x^{ε} is given by a linear combination between three basis functions where each function is defined with a triangle edge and its two opposite nodes p^{ε}_{1,T_1} and p^{ε}_{2,T_2}. Let us consider the simplest case where a triangle edge e is shared by two triangles T_1 and T_2. Consider Figure 2.2. Call the area of T_1 A_1 and the area of T_2 A_2, we then have for the basis function matching edge e,

$$\begin{aligned} j^{\mu}_{e}(x^{\varepsilon}) &= \tfrac{l(x^{\varepsilon} - p^{\varepsilon}_{1,T_1})}{2A1} \text{ if } x^{\varepsilon} \in T_1 \\ j^{\mu}_{e}(x^{\varepsilon}) &= \tfrac{l(-x^{\varepsilon} + p^{\varepsilon}_{1,T_2})}{2A2} \text{ if } x^{\varepsilon} \in T_2 \\ j^{\mu}_{e}(x^{\varepsilon}) &= 0 \text{ if } x^{\varepsilon} \notin T_1 \text{ or } T_2, \end{aligned} \tag{2.24}$$

where l is the length of edge e. The current $j^{\mu}_{T}(x^{\varepsilon})$ on triangle T can now be written, not summing over T, as

$$j^{\mu}_{T}(x^{\varepsilon}) = J^{e}_{T} j^{\mu}_{T,e}(x^{\varepsilon}), \tag{2.25}$$

where $e = 1 \dots 3$ and J^{e}_{T}, $T = 1 \dots N_{tri}$, is to be decided by numerically solving equation (2.21). It can be shown that the total surface charge, by using the continuity equation $\tilde{\partial}_{\alpha} j^{\alpha}_{e} = -ik\rho$, is equal to zero which was assumed in (2.3). That is, by our choice of elements, we conserve surface charges to zero.

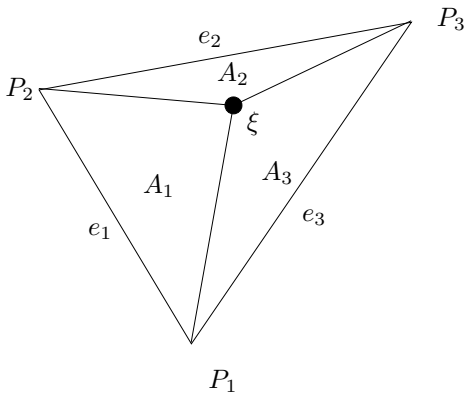

Figure 2.3: Simplex coordinates for one triangle. A_i is the are of each sub triangle of triangle T.

Let us now explicitly write down the discrete version of (2.21) by using Galerkin's method. Expand j^μ and j_t^μ in N_{edge} basis and test functions and let J^e be the complex scalar unknowns for the N_{edge} linear equations. We use the notation $T(e)$ for the 2 triangles sharing edge e and basis function e,

$$\begin{aligned}
&\textstyle\int_{T(e)} E_\mu j_e^{\mu,t}\, ds(x^\varepsilon) = \\
&i\omega\mu_0 J^{e'} \textstyle\int_{T(e')} \int_{T(e)} G(x^\varepsilon - y^\varepsilon) j_{e'}^\mu(x^\varepsilon) j_{\mu,e}^t(y^\varepsilon)\, ds(x^\varepsilon)\, ds(y^\varepsilon) - \\
&\tfrac{i}{\omega\varepsilon_0} J^{e'} \textstyle\int_{T(e')} \int_{T(e)} G(x^\varepsilon - y^\varepsilon) \tilde{\partial}_\alpha^{(x)} j_{e'}^\alpha(x^\varepsilon) \tilde{\partial}_\beta^{(y)} j_e^{\beta,t}(y^\varepsilon)\, ds(x^\varepsilon)\, ds(y^\varepsilon),
\end{aligned} \tag{2.26}$$

where $e' = 1 \ldots N_{edge}$. From a data-logical point of view it easier/faster to numerically evaluate the integrals, i.e. during the assembly of the matrix, by passing through the boundary S_{approx} triangle-wise. In a numerical implementation we therefore have integrals over single triangles and not triangle pairs as $T(e)$ indicate. By defining simplex coordinates, using notation introduced in Figure 2.3, as

$$\xi_\alpha = \frac{A_\alpha}{A_T}, \quad \alpha = 1 \ldots 2 \tag{2.27}$$

with $x^\varepsilon = \xi^\alpha P_\alpha^\varepsilon$, $\varepsilon = 1 \ldots 3$, most of the double integrals can be computed by numerical integration over $\xi_1 = [0,1]$ and $\xi_2 = [0,1]$. Some quadruple integrals are too singular for direct numerical integration and they therefore demand some analytical integration. We will not go into that here but just refer to [28]. Let us indicate the integration variables ξ^κ and ζ^κ, where κ is 1 or 2. In our specific case (EFIE for perfect conducting boundary) the integrals are

$$\int_0^1 \int_0^1 E(\xi^\kappa) j_e^t(\xi^\kappa) d\xi^1 d\xi^2, \tag{2.28}$$

$$\int_0^1 \int_0^1 \int_0^1 \int_0^1 G(\xi^\kappa - \zeta^\kappa) j_{e'}(\xi^\kappa) j_e^t(\zeta^\kappa) d\xi^1 d\xi^2 d\xi^1 d\xi^2 d\zeta^1 d\zeta^2, \tag{2.29}$$

and

$$\int_0^1 \int_0^1 \int_0^1 \int_0^1 G(\xi^\kappa - \zeta^\kappa) \frac{\partial j_{e'}}{\partial \xi}(\xi^\kappa) \frac{\partial j_e^t}{\partial \zeta}(\zeta^\kappa) d\xi^1 d\xi^2 d\zeta^1 d\zeta^2, \tag{2.30}$$

where the tilde on the derivatives have been removed since the geometry is now locally flat. In our implementation Gaussian quadrature have been used to evaluate (2.28), (2.29) and (2.30).

When all integrals are evaluated, we have a linear system of equations to be solved, in short notation we have

$$A\mathbf{J} = \mathbf{E}^{exc}. \tag{2.31}$$

In the numerical examples presented below we solve for $\mathbf{J}$ by LU factorization using the LAPACK routine ZGETRF. This algorithm has an $\mathcal{O}(N_{edge}^3)$ complexity in terms of arithmetic operations and $\mathcal{O}(N_{edge}^2)$ in terms of memory positions.

To compute the scattered field in a point z^ε, when we have solved the linear system, we use a numerical approximation of (2.17) and (2.18). To compute the scattered field in a direction, i.e. $\lim_{x\to\infty} E_\theta(x^\varepsilon)$ using polar coordinates, we use the numerical approximation of (2.17) by first taking the integral to the limit $x \to \infty$ while multiplying it by x.

2.5.2 Non-Local Boundary Elements

For some problems that we will consider later it may be more favorable to approximate the integral operator and the unknowns numerically by using basis functions with non-local support, or spectral elements. The theory for such basis functions in the context of BIE is not as well developed as for basis functions with local support.

2.6 Image Theory for Boundary Elements

In Chapter 5, when we are going to present the hybrid method, we need the solution to equation (2.6) and (2.7) for a very special type of boundary value problem. Namely $\hat{\mathbf{n}}(x^\varepsilon) \times \mathbf{E}(x^\varepsilon) = 0$ where x^ε is in an infinite plane chosen for simplicity to coincide with the $\hat{x}_1\hat{x}_2$-plane. Can we modify the right hand side in (2.6) with a function having support only for $x_3 < 0$ so that $\hat{\mathbf{n}} \times \mathbf{E}^\nu(x^\varepsilon) = 0$ for all x^ε with $x_3 = 0$?

First let us generalize the right hand side to $\delta(x^\varepsilon - x_s^\varepsilon)\delta_\alpha^\nu$ with $x_{s,3} > 0$, i.e. move the Dirac mass to x_s^ε in the upper half space. By inspection it can be shown that the change

$$\delta(x^\varepsilon - x_s^\varepsilon)\delta_\alpha^\nu \to \delta(x^\varepsilon - x_s^\varepsilon)\delta_\alpha^\nu - \delta(x^\varepsilon - x_s^\varepsilon + 2\hat{n}^\varepsilon(\hat{n}_\xi x_s^\xi)) \left[\delta_\gamma^\nu - 2\hat{n}^\nu \hat{n}_\gamma\right] \delta_\alpha^\gamma \tag{2.32}$$

do the job. The second rank tensor inside the brackets can be seen as a π radians rotation around $\hat{n}^\varepsilon$. With the new right hand side we no longer have any boundary values to fulfill but the solution is, by linearity, the sum of two fundamental solution. For the electric field we use expression (2.7) and get

$$\begin{aligned}\bar{E}^{\alpha\nu}(x^\varepsilon) &= i\omega G(x^\varepsilon - x_s^\varepsilon)\delta_\alpha^\nu + \frac{i}{\omega\varepsilon_0}\partial_\alpha\partial_\nu G(x^\varepsilon - x_s^\varepsilon) \\ &- i\omega G(x^\varepsilon - x_s^\varepsilon + 2\hat{n}^\varepsilon(\hat{n}_\xi x_s^\xi))(\delta_\gamma^\nu - 2\hat{n}^\nu\hat{n}_\gamma)\delta_\alpha^\gamma \\ &+ \frac{i}{\omega\varepsilon_0}\partial_\alpha\partial_\nu G(x^\varepsilon - x_s^\varepsilon + 2\hat{n}^\varepsilon(\hat{n}_\xi x_s^\xi)).\end{aligned} \tag{2.33}$$

Note that $\bar{E}^{\mu\alpha}(x^\varepsilon)$ is only valid for $x_3 \geq 0$. The solution given in (2.33) is sometimes referred to the image solution.

What we need in the next section is the solution to the boundary values problem described above but for three infinite union of infinitesimal dipoles over a triangular surface approximating the surface current j^μ in (2.24). That is, we search the image solution for one boundary element supporting at the most three basis functions described in Section 2.5.1 according to

$$j_\Delta^\mu(x^\varepsilon) = J^e j_e^\mu(x^\varepsilon). \tag{2.34}$$

As we know j_e^μ is linear in x^ε so by applying image theory to each infinitesimal current in triangle Δ we retrieve a triangular patch $\bar{\Delta}$ on opposite side of the boundary condition according to

$$j_\Delta^\mu(x^\varepsilon) + j_{\bar{\Delta}}^\mu(x^\varepsilon) = J^e j_e^\mu + \bar{J}^e \bar{j}_e^\mu. \tag{2.35}$$

Naturally we can define an image basis function, with support on the image triangle. Can we use this image basis function or the expression corresponding to (2.24) to represent $j_{\bar{\Delta}}^\mu$? Yes, since the basis function is linear in the geometry coordinates, we realize by inspection that $J^e = -\bar{J}^e$.

To compute the scattered field in $\bar{y}^\varepsilon$ from an image triangle becomes even simpler from an implementation point of view. We may use the true triangle in (2.17), but the field should be evaluated in an Image Field Point (IFP), rotated according to $(\delta_\gamma^\alpha - 2\hat{n}^\alpha\hat{n}_\gamma)$ and with a shift of sign. Let us define the IFP.

Definition 2.2. We search the field in $\bar{y}^\varepsilon$ from the current on an image triangle positioned in $\bar{x}_0^\gamma$. The true triangle is positioned in x_0^ε then the IFP y^ε is defined as follows

$$y^\varepsilon = x_0^\varepsilon - (\delta_\gamma^\varepsilon - 2\hat{n}^\varepsilon\hat{n}_\gamma)(\bar{y}^\gamma - \bar{x}_0^\gamma).$$

Note that the minus sign in front of the parenthesis is crucial to get the proper field. We realize that the field in the IFP is actually the same as in $\bar{y}^\varepsilon$ after transformation by noting that the $\bar{y}^\gamma - \bar{x}_0^\gamma$-vector should be transformed exactly as the basis function is transformed since they are directly linked by (2.17). Finally we note that the conclusions in this section entirely rests on the fact that the basis function is *linearly* represented by x^ε. There are generally no unique IFP for non-linear basis functions.

Chapter 3

Asymptotic Method, Geometrical Theory of Diffraction

A well known technique to solve or learn about solutions to differential equations is to consider the equations' differential operator or boundary condition under certain restricted conditions. For the wave equation, or its time harmonic counter part, it is quite natural to put restrictions on the wave length. Either it can be restricted to very long wave lengths or very short. In any cases, it is often possible to simplify the mathematical analysis so that an asymptotic numerical solution method may be achieved. We will consider Maxwell's equations in the short wave length limit or the so called high frequency regime. It is achieved by applying an asymptotic ansatz on the solution to the harmonic Maxwell's equations. We will by way of introduction assume that the total **E**-field fulfill

$$\mathbf{E}(x) \sim e^{ik\phi(x)} \sum_{m=0}^{\infty} (ik)^{-m} \mathbf{E}_m(x), \tag{3.1}$$

where $k = \omega/v$ is the wave number, ω the pulsation of the wave and v the wave speed in the medium. The **H**-field is assumed to fulfill a similar expansion. A theoretical systematic pioneering work was done by J. B. Keller to solve boundary value problems in the high frequency regime during the 1950s to 1960s. The theory he developed is called Geometrical Theory of Diffraction (GTD) and can be seen as a theory for solving initial boundary value problems asymptotically.

We want to point out, already at this stage, that it is very hard to say anything about the convergence of the infinite sum in (3.1) for finite values of k. We can only be sure that if all $\mathbf{E}_m$'s are bounded then $(ik)^{-m}\mathbf{E}_m \to 0$ as $k \to \infty$.

Remark that an asymptotic study can be done for the time dependent Maxwell's equations also. We will only briefly mention the time dependent problem for pedagogical reasons though. The reason for suppressing the time is that we aim at using analytically computed time independent solutions, so called diffraction and reflection coefficients, to time harmonic boundary value problems. Note though,

that we may in principle apply the inverse Fourier transform to these coefficients and apply them to time dependent solutions. To read more about time dependent asymptotics for the wave equation we refer to [29], [30] and [31].

The asymptotic study of Maxwell's equations will end up in non-linear equations. The most straight forward way to solve and analyze such equations is by the method of characteristics. We will therefore initially in section 3.1 demonstrate the main ideas in the method of characteristics, by analyzing a quasi linear and a non linear equation. To define the main constituents and understand the main ideas with the asymptotic method the scalar problem will be analyzed in Section 3.2.1. In Section 3.2.2 the Maxwell case will be mentioned. Section 3.3 and 3.4 treats the initial value problem and the boundary value problem correspondingly.

The presentation in this chapter is mainly based on [32], [33] and [34].

3.1 Method of Characteristics

We start with a definition.

Definition 3.1. Let

$$u_1(x), \dots u_n(x)$$

with $x \in \mathbb{R}^n$ be the scalar family of solutions to a first order partial differential equation then we define the solution u_γ to a Cauchy problem as the following. Given a curve $\Gamma(s) \in \mathbb{R}^{n+1}$ find the solution u_γ whose graph contains Γ.

Consider the Cauchy problem for the following first order quasi-linear equation

$$a(x, y, u)u_x + b(x, y, u)u_y = c(x, y, u), \tag{3.2}$$

where a, b and c depend continuously on x, y and u. For a function $u = u(x, y)$ we have, by using vector products, that $(u_x, u_y, -1)$ is normal to the surface $u(x, y)$. By equation (3.2) we then see that the vector (a, b, c) is tangent to u. In other words, does the vector (a, b, c) lie in the tangential plane to the graph $u(x, y)$. u is therefore sometimes referred to the integral surface to the vector field (a, b, c). Let us parameterize the curve $\Gamma(s)$ as

$$[f(s), g(s), h(s)] := \{s \in \mathbb{R} : g(s) = 0\}.$$

Let us interpret y as time and the Cauchy problem as an initial value problem, i.e. the initial curve or front, $(f(s), h(s))$, at $y = 0$ will propagate into positive time space. Alternatively, as we will see later on for the time harmonic Maxwell problem, we can interpret the independent variable as the phase. In the latter case it will be quite natural to talk about an initial equi-phase front.

Similarly, we say that the curve starting in a point $r_0 = (x_0, y_0, u_0)$ at a curve

$$r(t) = [x(t), y(t), u(t)],$$

with the tangent $(a(r_0), b(r_0), c(r_0))$ is an integral curve to the vector field. Parameterizing the integral curve with t, it will solve

$$\frac{dx}{dt} = a \tag{3.3}$$
$$\frac{dy}{dt} = b \tag{3.4}$$
$$\frac{du}{dt} = c. \tag{3.5}$$

The solution $r(t)$ is sometimes referred to a characteristic curve and its projections to the xy-plane are referred to characteristic base curves. By the existence and uniqueness theorem of ODEs, we can speak of a solution surface given by the two parameter surface $u(x, y)$ containing the curve $\Gamma(s)$ as long as Γ is compatible with the PDE. That is, if Γ is parallel to the vector field in the integral surface we must make sure that $h(s)$ is compatible with the PDE. Differently stated, if we want to allow for arbitrary $h(s)$ then we have to have a Γ that is non-tangential to the vector field in the integral surface. We say that Γ is non-characteristic if it fulfills the criteria. This criteria is fundamental for the Cauchy problem for high frequency wave propagation.

We see above that the uniqueness of (3.2) is based on well posedness of ODEs. What about the case when the PDE is not quasi-linear but non-linear, i.e. there are non-linear terms in the highest order derivative?

As we will see later, can Helmholtz equation in two dimensions, in the high frequency regime, be rewritten as an infinite sequence of first order non-linear PDEs. The lowest order equation tells us how the phase function ϕ depends on the spatial coordinate (x, y). That equation reads

$$\phi_x^2 + \phi_y^2 = \eta^2. \tag{3.6}$$

Because of the non-linearity we can not apply the same techniques as above to analyze existence and uniqueness.

Instead we do a trick by increasing the number of independent variables for ϕ. Note that the tangent to the characteristic curves are (ϕ_x, ϕ_y, η^2) and the tangent to the characteristic base curves are (ϕ_x, ϕ_y) in (3.6). We know that Helmholtz equation describes a time harmonic wave phenomena and, as we will see, equation (3.6) describes these waves in the high frequency regime. It is therefore quite natural to speak about equi-phase fronts $\phi(s, t) \to \phi_{const}(t)$. If these fronts are smooth enough we may uniquely define normals to them in (x, y, ϕ)- or (x, y)-space, and they will be parallel to the tangent of the characteristic curves or the characteristic base curves respectively.

Let us define an angle $\alpha(t)$ and a parameterization such that

$$[\cos\alpha, \sin\alpha]\,\eta = \nabla\phi, \tag{3.7}$$

where the brackets indicate a vector. Assume that there exist a unique function $\tilde{\phi}(x, y, \alpha) \in \Omega_1$ for each $\phi(x, y) \in \Omega_2$, where Ω_1 and Ω_2 are properly chosen functional spaces. Note that we do not demand vice versa. Are there functions f and g such that we can write

$$\eta \cos\alpha \tilde{\phi}_x + \eta \sin\alpha \tilde{\phi}_y + f(x, y, \alpha)\tilde{\phi}_\alpha = g(x, y, \alpha, \phi)? \tag{3.8}$$

With the parameterization given in expression (3.7) we have

$$[\dot{x}, \dot{y}] = \nabla\phi. \tag{3.9}$$

Differentiating once more we, by using the Eikonal equation, can prove that

$$[\ddot{x}, \ddot{y}] = \eta\nabla\eta. \tag{3.10}$$

Let us compute $\partial\alpha$ by noting that with the geometrical interpretation of a cross product in $\mathbb{R}^3$, we have

$$\frac{\delta\alpha}{\delta t} \approx \frac{\hat{e}_\phi \cdot [(\cos(\alpha(t)), \sin\alpha(t), 0) \times (\cos(\alpha(t + \delta t)), \sin\alpha(t + \delta t), 0)]}{\delta t}. \tag{3.11}$$

Hence, after some computations using

$$[\cos\alpha, \sin\alpha] = [\dot{x}, \dot{y}]/\eta$$

, the Eikonal equation and equation (3.10) we get by letting $\delta t \to 0$,

$$\dot{\alpha} = \eta_y \cos\alpha - \eta_x \sin\alpha. \tag{3.12}$$

I.e. we define the characteristic base curves in $(x, y, \alpha, \tilde{\phi})$-space as the curves solving the following ODE:

$$\begin{aligned} \dot{x} &= \eta\cos\alpha \\ \dot{y} &= \eta\sin\alpha \\ \dot{\alpha} &= f(x, y, \alpha) = \eta_y\cos\alpha - \eta_x\sin\alpha. \end{aligned} \tag{3.13}$$

With

$$g(x, y, \alpha) = \dot{x}^2 + \dot{y}^2 + \dot{\alpha}^2 = \eta^2 + (\eta_x \sin\alpha - \eta_y \cos\alpha)^2, \tag{3.14}$$

we have found the unknowns in the quasi-linear Equation (3.8) and we may apply the method of characteristics as was done before. That is, equation (3.8) has a unique solution provided that $\Gamma(x, y, \alpha)$ are non-characteristic, or if not, $\tilde{\phi}$ is chosen properly. We refer to Figure 3.1 where projected characteristic base curves are drawn for problem (3.6) and (3.8) for a special type of Cauchy problem, i.e. Γ coincide with $\hat{e}_\alpha$-axis. The method of characteristics has now been introduced in a setting as general as possible. Let us proceed to the wave equation and Maxwell's equations.

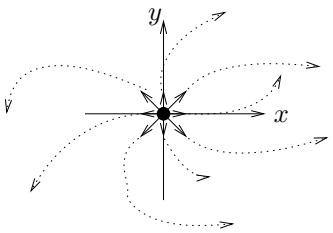

Figure 3.1: Characteristic base curves, projected down to xy-space, for equation (3.6). The curves starts in a so called caustic in x, y-space and the solution is non-unique in $(x, y) = (0, 0)$.

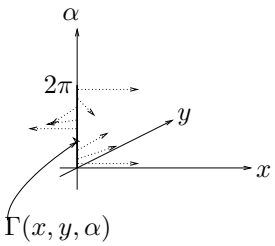

Figure 3.2: Characteristic base curves for equation (3.8). The curves starts along a line Γ in x, y, α-space and the solution is unique along Γ.

3.2 Eikonal and Transport Equation

Below we will present both the Eikonal and the Transport equation but we will focus on the Eikonal equation when we discuss the solutions. We refer to [33] and [31] when it comes to solving the Transport equations.

3.2.1 Scalar Case

The electromagnetic (EM) field is governed by Maxwell's equations. They decouple into scalar wave equations when boundary conditions and the differential operators are constant along one dimension. We can treat the magnetic and electric field strength individually if physical attributes are constant along the z-axis. Let us call the z-component of the electric field strength $U(\mathbf{x}, t)$. One can then show that $U(\mathbf{x}, t)$ must satisfy

$$U_{tt}(\mathbf{x}, t) - v^2(\mathbf{x})\Delta U(\mathbf{x}, t) = 0, \tag{3.15}$$

where $v(\mathbf{x})$ is the wave speed. If we assume a time harmonic solution, $U(\mathbf{x}, t) = u(\mathbf{x})e^{i\omega t}$ where $\omega = \frac{2\pi v(\mathbf{x})}{\lambda(\mathbf{x})}$, (3.15) will transform to Helmholtz equation

$$\Delta u(\mathbf{x}) + \left(\frac{2\pi}{\lambda(\mathbf{x})}\right)^2 u(\mathbf{x}) = 0, \tag{3.16}$$

where $\frac{2\pi}{\lambda(\mathbf{x})}$ is the wave number k at point $\mathbf{x}$. For later purpose we can define an index of refraction by $\eta(\mathbf{x}) = \frac{c}{v(\mathbf{x})}$ where c is the speed of an EM-wave in vacuum. For short wavelengths, it can be shown that the solution under certain conditions, asymptotically behave as

$$u(\mathbf{x}) = z(\mathbf{x}, k) \cdot e^{ik\phi(\mathbf{x})}, \tag{3.17}$$

while the amplitude function z reads

$$z(\mathbf{x},k) \sim \sum_{m=0}^{\infty} z_m(\mathbf{x})(ik)^{-m} + o(k^{-m}). \tag{3.18}$$

Notice that we have not included k in the argument of z_m or ϕ. This is not inconsistent with the result for the line source in the introduction. It just means that we should use another expansion for the line source problem to exclude the linear k-dependence in z_0. However, if the wave length of the Fourier components of the z_m:s would depend on k then the scale reduction would be lost. If this is not the case only the scales in the boundary conditions and the spatial variations of the wave speed have to be resolved in a numerical method applied to the corresponding PDEs. Differently stated it means that if we, with a numerical method, search the solution to our problem, i.e.

$$(\phi(\mathbf{x}), z_1(\mathbf{x}), z_2(\mathbf{x}), \ldots),$$

we are not obliged to resolve the wavelength.

If expansion (3.18) is put into (3.15) and we collect, into partial sums, terms of equal power of k we can achieve a sequence of homogeneous equations by equalize each partial sum to zero. That is,

$$|\nabla\phi(\mathbf{x})| = \eta(\mathbf{x}) \qquad \mathcal{O}(k^2)\text{-equation} \tag{3.19}$$

$$2\nabla\phi(\mathbf{x})\cdot\nabla z_0 + z_0\Delta\phi(\mathbf{x}) = 0 \qquad \mathcal{O}(k)\text{-equation} \tag{3.20}$$

$$2\nabla\phi\cdot\nabla z_m + z_m\Delta\phi = -\Delta z_{m-1} \qquad \mathcal{O}(k^{(-m)})\text{-equation.} \tag{3.21}$$

The non linear equation (3.19) is called the *Eikonal equation*. Equations (3.20) and (3.21) are called the *Transport equations* and may be solved sequentially when $\phi(x)$ is known.

Let us try to interpret the Eikonal equation by comparing with the corresponding time dependent problem! If we, instead of (3.16), start out with (3.15) and assume

$$u(\mathbf{x},t) = z(\mathbf{x},t)e^{i\omega\phi(\mathbf{x},t)}, \tag{3.22}$$

we get, by recognizing the highest order $\phi(\mathbf{x},t)$-terms,

$$\phi_t(\mathbf{x}) = v(\mathbf{x})|\nabla\phi(\mathbf{x})|. \tag{3.23}$$

Equation (3.23) is a Hamilton-Jacobi type equation and it is analyzed for example in [35] and numerical schemes can for example be found in [36], [37] and [38].

Equation (3.23) can also be deduced from the definition of a Level-Set function [39]. Let the zero Level-Set contour $\Gamma(t)$ define the propagating wave front at time t. Identify a marker on the contour and let it draw a line or a Ray along its path, $\mathbf{x}(t)$, with t as its curve parameter. Its speed will be $\dot{\mathbf{x}} = \mathbf{v}(\mathbf{x})$. If we

differentiate the Level-Set function at the zero contour, $\phi(\mathbf{x}(t), t) = 0$, with respect to t, we get

$$\phi_t(\mathbf{x}, t) - \mathbf{v}(\mathbf{x}) \cdot \nabla\phi(\mathbf{x}, t) = 0, \tag{3.24}$$

which becomes (3.23) if we notice that $\mathbf{v} \cdot \nabla\phi(\mathbf{x}) = v|\nabla\phi(\mathbf{x})|$ for a propagating EM-wave.

In conclusion, we can say that (3.19) is an equation which describe the phase function $\phi(\mathbf{x})$ in the harmonic solution (3.18). $\phi(\mathbf{x}) = C$ defines constant phase contours, i.e. wave fronts and if we want to look at these as time evolves we have to solve (3.23) and consider the zero contour.

The Eikonal equation is a first order non-linear partial differential equation. Hence it can, as we saw in section 3.1, be solved by applying the general theory of characteristics. Let us do it more carefully by doing the following observations.

A wave front is defined as $\phi(\mathbf{x}) = const$. Let us also define rays, or characteristics, as the orthogonal curves, $\mathbf{x}(s)$, to the wave fronts. Choosing the parameterization of $\mathbf{x}(s)$ accordingly we have,

$$\frac{d\mathbf{x}}{ds} = \nabla\phi. \tag{3.25}$$

If we differentiate with respect to s we get

$$\frac{d}{ds}\frac{d\mathbf{x}}{ds} = \frac{1}{2}\nabla|\nabla\phi(\mathbf{x})|^2, \tag{3.26}$$

and by using (3.19) we end up with

$$\frac{d}{ds}\frac{d\mathbf{x}}{ds} = \frac{1}{2}\nabla\eta^2(\mathbf{x}). \tag{3.27}$$

In addition, if we use (3.25) in (3.19), we get

$$|\frac{d\mathbf{x}}{ds}|^2 = \eta^2(\mathbf{x}). \tag{3.28}$$

Equations (3.27) and (3.28) are sometimes called the Ray equations. To solve the Eikonal equation for $\phi(\mathbf{x})$ we note that by using (3.25), (3.19) and differentiating $\phi(\mathbf{x})$ along a Ray give us

$$\frac{d\phi(\mathbf{x}(s))}{ds} = \nabla \cdot \frac{d\mathbf{x}}{ds} = (\nabla\phi(\mathbf{x}))^2 = \eta^2(\mathbf{x}). \tag{3.29}$$

Integrating (3.29) we get

$$\phi(\mathbf{x}(s)) = \phi(\mathbf{x}(s_0)) + \int_0^s \eta^2(\mathbf{x}(s'))ds'. \tag{3.30}$$

The validity of the asymptotic assumptions in (3.18) and (3.22) have been discussed and investigated in [33] and [29]. We will call a solution that fulfill (3.18) a *Ray-field*.

In (3.30) we have an explicit formula for the phase function along the rays defined by the ODEs in (3.27) and (3.28). If $\eta(\mathbf{x}) = const$ one can see in (3.27) that the rays are straight, which means that it is straight forward to fill the computational domain with rays and then achieve arbitrary accuracy on ϕ by interpolation. We recognize the method as a shooting method, or method of characteristics. However with non-homogeneous $\eta(\mathbf{x})$, this may demand some extra effort since the number of rays in certain domains may deplete which will make it hard to attain sufficient accuracy.

As we saw in section 3.1, may the solution to (3.8) be multi-valued in $\mathbf{x}$-space. Let us write ODE (3.27) as a first order system. Define $\dot{\mathbf{x}} = \mathbf{p}$ then

$$\begin{aligned} \dot{\mathbf{x}} &= \mathbf{p} \\ \dot{\mathbf{p}} &= \frac{\nabla \eta^2}{2} \\ |\dot{p}| &= \eta, \end{aligned} \tag{3.31}$$

which sometimes are referred to the Lagrangian equations. Comparing with equation (3.8) we see that, by defining a $\mathbf{p}$, we have the same number of dependent variables. Namely three for the case $\mathbf{x} \in \mathbb{R}^2$. That is, if we want to find the phase function ϕ with method of characteristics, then we automatically find the unique

$$\tilde{\phi}(x, y, \alpha) = \tilde{\phi}\left(x, y, \arcsin \frac{p_y}{\sqrt{p_x^2 + p_y^2}}\right).$$

Since the rays are unique in $(\mathbf{x}, \mathbf{p})$-space we may solve (3.31) for many initial conditions simultaneously starting along an initial curve $\Gamma(t)$ with

$$\tilde{\phi}_0(t) = \tilde{\phi}(\Gamma(t)), \tag{3.32}$$

c.f. last section, and thereby facilitate interpolation when depletion in $(\mathbf{x}, \mathbf{p})$-space occurs. In principle, we may obtain arbitrary accuracy on $\tilde{\phi}$ using this solution method. Later on, we will refer to each particle moving along a trajectory as a marker on an equi-phase front parameterized with t according to $\mathbf{y}(t) = (\mathbf{x}(t), \mathbf{p}(t))$. $\mathbf{p}$ and $\mathbf{x}$ is sometimes referred to Lagrangian coordinates and therefore, occasionally, solving a PDE with method of characteristics is referred to a Lagrangian method. Their advantage is that they are easy to implement as soon as the Lagrangian equations are known but the efficiency, especially when the solution is searched in many points, may in some cases be very low. In such cases, an Eulerian method may be more favorable. E.g. if we apply a finite difference scheme directly to (3.23), we achieve an Eulerian scheme. One drawback of the Eulerian approaches is that we will not straightforwardly catch the multi-valuedness in ϕ. In some cases the viscosity solution [9], or first arrival solution, will be achieved. This may be remedied by proper modifications [30]. Remark that it is not surprising that only one solution can be retrieved, since we assumed that only one exists in (3.22). If this is not the

case, a unique solution seize to exist in the classical sense. A nice overview of Lagrangian and Eulerian methods for computational high frequency wave propagation can be found in [31].

To conclude, we note that if ϕ gets multi-valued we can solve a system of transport equations for each ϕ. In some cases there will be infinite many solutions and it will be even more tricky to get the total amplitude since the sum of amplitudes will approach an integral. Sometimes this phenomena is referred to focusing or caustic formation. For future reasons we therefore present a qualitative definition of a geometrical object that may form in ray methods: A caustic is a manifold that is formed by an envelope of Rays. Furthermore will a more rigorous analysis of the solution to the transport equation show that the phase of the amplitude along a ray change with $\pm\pi/2$ when it goes trough a caustic. The sign depends on the sign convention in the Fourier transform when making the time dependent problem time harmonic.

3.2.2 Maxwell Case

Up to this point we have only treated the scalar Helmholtz equation. To be able to present the hybrid methods in next chapter we need the asymptotic solutions to the time harmonic Maxwell system. It is quite easy to show that the phase function ϕ in (3.1) solves the same Eikonal equation as for the scalar case. To achieve the Transport equations, describing how $\mathbf{E}$ and $\mathbf{H}$ changes along the characteristic base curves, we would need some further definitions and some more evolved analysis. The important thing we need to bring with us in the future presentation is that there are transport equations, explicit expressions exist for simple cases and they apply to the E- and H-components that lies in the orthogonal plane to $\nabla\phi$. To see how this and other results can be deduced we refer to [33].

3.3 Cauchy Problem

For the Eikonal equation in $\mathbb{R}^3$ there are three non-exotic manifolds from which we can specify Cauchy data. A point, a curve and a surface. In $\mathbb{R}^2$ we can choose between a point and a curve. In Figure 3.1 we see an example of a point manifold in $\mathbb{R}^2$.

To be able to specify $\tilde{\phi}_0$ in (3.32) arbitrarily we have to put restrictions on

$$\Gamma := \{\mathbf{x}(t) : [x(t), y(t), \alpha(t)] \in \mathbb{R}^3\}. \tag{3.33}$$

As we said previously, Γ is called non-characteristic if we are allowed to choose $\tilde{\phi}_0$ arbitrarily (we assume that $\tilde{\phi}_0(t)$ is continuous in t). I.e. if Γ where parallel to $\hat{e}_\alpha$, as in Figure 3.1, then $\tilde{\phi}_0(t)$ need to be compatible with (3.8). The same holds for Cauchy data along lines in $\mathbb{R}^2$ (surface in (x, y, α)-space), points in $\mathbb{R}^3$ (a 2 parameter sub-manifold in (x, y, z, α, β)-space), lines in $\mathbb{R}^3$ (a 2 parameter sub-manifold in (x, y, z, α, β)-space) and surfaces in $\mathbb{R}^3$ (a 3 parameter sub-manifold

in (x, y, z, α, β)-space). Although these manifolds sounds very "mathematical" they are directly applicable to problems already mentioned in Chapter 2. The phase of the asymptotic fundamental solution to Maxwell's equations, expression (2.15) in Chapter 2, solves the Eikonal equation for the point manifold case. Some wave length away from the point, $\mathbf{E}$ and $\mathbf{H}$ solves the Maxwell version of the Transport equations approximately. A plane wave that has been scattered/reflected by a large smooth surface has a phase-function that solves the Eikonal equation for the case of a 3 parameter sub-manifold in (x, y, z, α, β)-space. If the smooth surface is convex then the sub-manifold is *behind* the scatterer (Reflection) and if the vector $\nabla\phi_{plw}$ is tangential to the surface then parts of the sub-manifold coincide with the surface (Smooth Surface Diffraction defined below). For the case of a surface that contain an edge we will have a 2 parameter sub-manifold in (x, y, z, α, β)-space (Edge Diffraction) and for the grazing incidence case will the projection of the 2 parameter sub-manifold into (x, y, z)-space coincide with the edge.

In reference [33] the solution to the Eikonal and the Transport equation for a point X_P, a line $X_L(t)$ and surface $X_S(u, v)$ in free space is thoroughly investigated.

3.4 Boundary Value Problem

The solution to boundary value problems for the Eikonal and the Transport equations is, as already indicated in the end of section 3.3, deeply linked to the Cauchy problem. The key idea is to exploit the locality principle. That is, the Transport equation give us the solution along rays. There are no interaction between the solutions on different rays and energy only propagate in the $\nabla\phi$-direction. When a ray cross a boundary condition the local features, such as the shape of the geometry, is used to compute Cauchy data for the scattered ray. To explicitly compute the so called scattering coefficients, that is to compute $C^{\mu\nu}_{coeff}$ in

$$E^{\mu}_{scatt} = C^{\mu\nu}_{coeff} E^{\nu}_{inc}, \tag{3.34}$$

canonical problems needs to be solved and then taken to the asymptotic limit. In [40] the solution to a number of problems is presented and the coefficients are given explicitly for example in [34].

Below we focus on a specific type boundary value problem.

3.4.1 Smooth Surface Diffraction

The canonical boundary value problem for the so called Smooth Surface Diffraction was initially investigated by B. R. Levy and J. B. Keller in [18].

As a background to our presentation on smooth surface diffraction we, as a comparison, can think of that we split up numerical methods, used for solving the full wave Maxwell's equations, into two families. Those

1. where we try to solve the full wave problem in $(x, y, z) = \mathbf{x} \in \mathbb{R}^3$ with $(\mathbf{E}, \mathbf{H})(\mathbf{x}, t)$ as unknowns. Here, time t is sometimes suppressed. We call $(\mathbf{E}, \mathbf{H})$ for the electric and magnetic field strength.

2. where we solve the equations by first rewriting them as integral equations with the unknowns on the boundaries and then solve the problem with finite elements. For the $\mathbb{R}^3$ case we have $(p, q) = \boldsymbol{y} \in \mathbb{R}^2$, with $(\mathbf{J}, \mathbf{M})(\boldsymbol{y}, t)$ as unknowns.

In section 3.2.1 we saw that for high frequencies we may solve the Eikonal equation instead of the full wave problem to get one part of the asymptotic solution. Such solution can be compared and combined with solutions computed with numerical method 1. To get the asymptotic method that corresponds to numerical method 2 we need an Eikonal type of equation that have (p, q) as independent variables. In other words, what are the asymptotic solutions for $(\mathbf{J}(\boldsymbol{y}(t)), \mathbf{M}(\boldsymbol{x}(t)))$ for short wavelengths. In [33] a surface Eikonal equation is deduced for the fields in the neighborhood of the surface and we will follow parts of that outline.

Below we focus on the surface Eikonal equation, i.e. the geometrical problem, since this is the equation that one must analyze before we can solve the Transport equation (3.20).

Let $X = X(p, q)$ describe a surface in $\mathbb{R}^3$. We introduce the surface tangent vectors by using standard notation from differential geometry.

$$X_1 = X_p \tag{3.35}$$

and

$$X_2 = X_q. \tag{3.36}$$

The metric, used for defining a distance on the surface, is

$$g_{ij} = X_i X_j, \quad \text{for } i = 1|2 \text{ and } j = 1|2. \tag{3.37}$$

We can interpret the inverse of the metric by considering $g^{ki} g_{ij} = \delta_{kj}$ where, as in Chapter 2, δ_{kj} is Kronecker's symbol. Let us keep the notation ϕ for the wave front, although its gradient is only assumed to lie in the *tangential* plane to a surface and not in a flat plane as previously. We can define the surface gradient of the wave front as

$$\tilde{\nabla}\phi = g^{ki}\phi_i X_k. \tag{3.38}$$

To see that this is the proper definition, we set $dX = X_\nu d\tau_\nu$ and introduce $p = \tau_1$ and $q = \tau_2$. Now we observe that

$$\tilde{\nabla}\phi \cdot dX = g^{ki}\phi_i X_k \cdot X_\nu d\tau_\nu = \phi_i g^{ki} g_{k\nu}\tau_\nu = \phi_i \delta_{i\nu}\tau_\nu = \phi_\nu \tau_\nu = d\phi, \tag{3.39}$$

which tells us that definition (3.38) is well chosen since (3.39) reminds us of the Euclidean case. It follows that $(\tilde{\nabla}\phi)^2 = g^{ij}\phi_i\phi_j$. As usual we call the index of refraction $\eta(\tau_1, \tau_2)$. We can write the surface Eikonal equation as

$$(\tilde{\nabla}\phi)^2 = \eta^2(\tau_1, \tau_2). \tag{3.40}$$

or

$$H(\phi_1, \phi_2, \tau_1, \tau_2) \equiv g^{ij}(\tau_1, \tau_2)\phi_1\phi_2 - n^2(\tau_1, \tau_2) = 0. \tag{3.41}$$

We have deliberately named the function in (3.41) $H(\cdot)$ because we want to interpret it as a Hamiltonian. I.e. think of the characteristic lines as paths for particles (photons). The particles follows stationary (with respect to propagation time) paths $(\tau_1(s), \tau_2(s))$ and they should therefore fulfill Hamilton's equations

$$\dot{\tau}_i = \frac{\lambda}{2} H_{\phi_i} = \lambda g^{ij}\phi_j \tag{3.42}$$

and

$$\dot{\phi}_i = -\frac{\lambda}{2} H_{\tau_i} = -\frac{\lambda}{2}((g^{kj})_i\phi_k\phi_j - (\eta^2)_i). \tag{3.43}$$

We choose $\lambda = 1/\eta$ instead of $\lambda = 1$ as in (3.25). We name the characteristic curves surface rays and one can show, as in the free wave front case, that they are orthogonal to the wave fronts ϕ on the surface.

With a Dirichlet boundary condition for u on the entire surface we have for $\eta = const$ that (3.42) and (3.43) becomes

$$\dot{\tau}_i = \frac{1}{\eta} g^{ij}\phi_j \tag{3.44}$$

and

$$\dot{\phi}_j = -\frac{1}{2\eta}(g^{k\nu})_j\phi_k\phi_\nu. \tag{3.45}$$

This is a system of four first order ordinary differential equations and they correspond to (3.25) and (3.29) in the free wave front case. For practical reasons we do not want to have ϕ_i as unknowns. We therefore transform Hamilton's equations to system of two second order equations. This is done in the following way. Note that

$$\ddot{\tau}_r = \frac{1}{n} g^{rj}\dot{\phi}_j + \frac{1}{n}(g^{rj})_m\phi_j\dot{\tau}_m = -\frac{1}{2n^2} g^{rj}(g^{k\nu})_j\phi_k\phi_\nu + \frac{1}{n^2}(g^{r\nu})_m g^{mk}\phi_k\phi_\nu \tag{3.46}$$

and

$$\dot{\tau}_i\dot{\tau}_j = \frac{1}{n^2} g^{ik}\phi_k g^{j\nu}\phi_\nu. \tag{3.47}$$

Define the Christoffel symbol as

$$\Gamma_r^{ij} = \frac{1}{2} g^{rm}((g_{jm})_i + (g_{im})_j + (g_{ji})_m). \tag{3.48}$$

Then (3.47) and (3.48) give us

$$\Gamma_r^{ij}\dot{\tau}_i\dot{\tau}_j = \frac{1}{2n^2} g^{ik} g^{j\nu} g^{rm}((g_{jm})_i + (g_{im})_j + (g_{ji})_m)\phi_k\phi_\nu. \tag{3.49}$$

By differentiating equation (3.37)

$$(g^{ki})_\nu g_{ij} = -g^{ki}(g_{ij})_\nu, \tag{3.50}$$

we can simplify (3.49) to

$$\begin{aligned}\Gamma_r^{ij}\dot{\tau}_i\dot{\tau}_j &= \tfrac{1}{2n^2}(g^{ik}g^{rm}g_{jm}(g^{j\nu})_i + g^{j\nu}g^{rm}g_{im}(g^{ik})_j - g^{rm}g^{ik}g_{ji}(g^{j\nu})_m)\phi_k\phi_\nu \\ &= \tfrac{1}{2n^2}(g^{ik}(g^{r\nu})_i + g^{j\nu}(g^{rk})_j - g^{rm}(g^{k\nu})_m)\phi_k\phi_\nu.\end{aligned} \tag{3.51}$$

From (3.46) and (3.51) we get the differential equations for a surface geodesic

$$\ddot{\tau}_r + \Gamma_r^{ij}\dot{\tau}_i\dot{\tau}_j = 0. \tag{3.52}$$

To get a feeling for what kind of curves that solves (3.52) let $\mathbf{t}(s) = \mathbf{x}_s$ be the tangent to a curve $\mathbf{x}(s)$ confined to a surface. Then we can define a curvature vector $\mathbf{n}$ as

$$\mathbf{t}_s = \kappa\mathbf{n} = \mathbf{c}, \tag{3.53}$$

where κ is the curvature of the curve and $\mathbf{c}$ is perpendicular to $\mathbf{t}$. The curvature vector are only tangent to the surface if the surface is locally flat. Otherwise we can decompose it into one part that is tangent and one part which is normal to the surface. κ splits up correspondingly and we can define

$$\mathbf{c} = \mathbf{c}_n + \mathbf{c}_g, \tag{3.54}$$

where $\mathbf{c}_n$ is the normal curvature vector and $\mathbf{c}_g$ is the geodesic curvature vector. One can show that equation (3.52) finds the curve on the surface which has zero geodesic curvature. For a flat surface the normal curvature is naturally zero and zero geodesic curvature means straight curves.

We need to comment the scientific method used to deduce that the surface confined wave front given by (3.52) has anything to do with the searched asymptotic solution on a surface. Above we have not even tried to do this but just showed that we may define a surface Eikonal equation and that if we define characteristic curves on the surface we can find them by solving the surface geodesic equations. Whether these curves has anything to do with Maxwell's equations or can be used in a similar manner as for the free wave front case is an open question in our exposition. However, during the years of 1950-1970, analysis were performed by applying characteristic curves to different canonical geometries. At the same time explicit asymptotic expressions were at hand for the $(\mathbf{E}, \mathbf{H})$-fields. Using them on problems where Maxwell's equations had explicit solutions one saw that one could compute asymptotically correct solutions with GTD. Also, modern mathematical analysis shows that, on specific classes of problems where explicit solutions are unknown, the ray solutions are the proper asymptotic solutions. From a mathematical point of view it is of course not consistent to apply the formulas to other types of geometries than the ones they are deduced on. However, from a practical and an engineering point of view, especially since numerical solutions is tractable today and can confirm the validity of the formulas on an abundance of geometries, they are used with good results on smooth convex surfaces.

In the beginning of section 3.2.1 we said that Maxwell's equations decouple for certain 2D-problems into a scalar wave equation. E.g. it suffice that we consider

one component of the **E**-field. For the confined wave front case this is not the case. Without further comment we here state that we need to take care of two components, one that is tangential to the surface *and* orthogonal to the characteristic line and one component that is normal to the surface.

As we mentioned in section 3.2.1, we could regard the solution u as a solution to a Cauchy or an initial value problem. I.e. if we specify u on a initial manifold S, $\{S \subset \mathbb{R}^3\}$ (S can be a point, line or a surface for the $\mathbb{R}^3$-case), we may propagate the solution along the computed rays. In the free wave front case, an initial manifold is a subset of the space where we search the solution. For the confined wave front case we have two possibilities. Either we have an initial manifold on the surface (point or a line) or an initial manifold that is off the surface. We can for example think of a problem where the initial manifold is in $\mathbb{R}^3$ and that we propagate the wave front to the smooth surface and then use coefficients from the literature to quantify how the energy or solution behaves along the manifold defined by the surface. With the data on the manifold or surface we can think of a new initial value problem to be solved *on the surface*. With similar reasoning we may also detach the solution from the surface and propagate it out into $\mathbb{R}^3$ again. We can think of the entire problem as an initial-boundary value problem where boundary conditions are specified on the smooth surface.

As a conclusion, we said in the beginning of this section, that we searched asymptotic solutions corresponding to (3.20) and (3.21) for $(\mathbf{J}, \mathbf{M})$. Without writing out the explicit formulas we state that $(\mathbf{J}, \mathbf{M})$ can be computed when $(\mathbf{E}(\boldsymbol{y}), \mathbf{H}(\boldsymbol{y}))$ are known for perfectly conducting surfaces.

Chapter 4

Smooth Surface Diffraction

In this chapter we will present the first new contribution to the thesis. We will develop and analyze a numerical method to be used for the computation of the Smooth Surface Diffraction as predicted by the GTD. The core of the method consist in approximating the smooth surface geodesic curves on a surface Σ with a train of piece wise linear segments with support on a facetized approximation of Σ. By properly representing a family of such approximations along a wave front, we will show how to integrate the total smooth surface diffracted field in the mono-static direction achieving a certain order of accuracy.

Our Fortran 90 implementation of the numerical algorithm will also be presented and used to produce numerical results.

4.1 A Single Representation of the Geometry

4.1.1 An Example: The Sphere

As an introduction to this chapter we illustrate how the theory developed in the Chapter 3 can be used to numerically compute the smooth surface diffracted rays on a unit sphere parameterized with the Euler angles $x = x(\theta, \phi)$. That is, the entire scatterer is represented by **one** parameterization. Consider, as was done in chapter (1), the scattering example in Figure 4.1. Let us parameterize the surface rays with the arc length in the surface parameter space. I.e. let $\dot{\tau}_1 = \dot{p} = \cos\alpha$ and $\dot{\tau}_2 = \dot{q} = \sin\alpha$ corresponding to $\lambda = 1/\eta$ in (3.42) and (3.43). By differentiating $\alpha(s) = \arctan \dot{q}/\dot{p}$, we get

$$\begin{pmatrix} \dot{p} \\ \dot{q} \\ \dot{\alpha} \end{pmatrix} = G(p, q, \alpha) = \begin{pmatrix} \cos\alpha(s) \\ \sin\alpha(s) \\ \ddot{q}(s)\cos\alpha(s) - \ddot{p}(s)\sin\alpha(s) \end{pmatrix}. \tag{4.1}$$

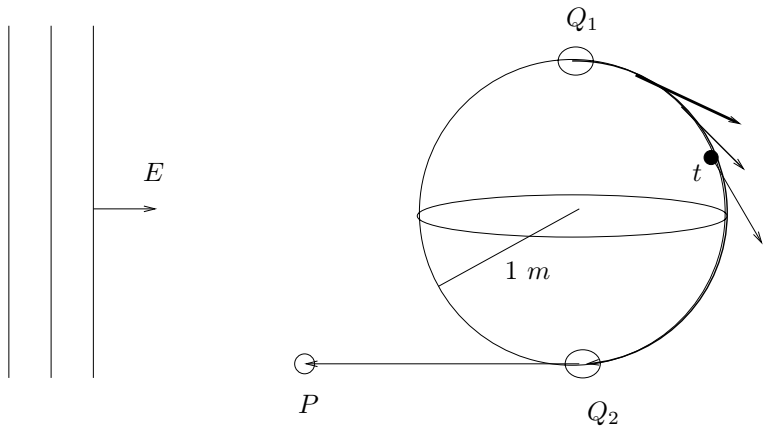

Figure 4.1: A plane wave $E = E_0 e^{ikx}$ scattered by a sphere.

More specifically for the sphere one can show, letting $\tau_1 = p = \theta$ and $\tau_2 = q = \phi$ in (4.1) and (3.52),

$$G_{sphere}(\theta, \phi, \alpha) = \begin{pmatrix} \cos\alpha \\ \sin\alpha \\ -\frac{\sin 2\theta \sin^3\alpha}{2} - \frac{\sin 2\alpha \cos\alpha}{\tan\theta} \end{pmatrix}. \tag{4.2}$$

For each vector in the family of initial conditions

$$(\tilde{\theta}^j, \tilde{\phi}^j, \alpha_{plw}) \text{ for } j = 1, \ldots n, \tag{4.3}$$

one can solve the three ODE:s with *ODE45* in Matlab®. In Figure 4.3 we have plotted the (θ, ϕ)-projected vector field, i.e. the ray-tangents in the parameter space.

When computing the mono-static scattered field one is interested in the boundary value problem

$$\begin{pmatrix} \dot{\theta} \\ \dot{\phi} \\ \dot{\alpha} \end{pmatrix} = G_{sphere}(\theta, \phi, \alpha) \text{ with } \begin{pmatrix} \theta(0) = \tilde{\theta}(t_0) \\ \phi(0) = \tilde{\phi}(t_0) \\ \phi(0) = \alpha_{plw} \end{pmatrix} \text{ and } \begin{pmatrix} \theta(s_1) = \tilde{\theta}(t_1) \\ \phi(s_1) = \tilde{\phi}(t_1) \\ \alpha(s_1) = \alpha_{plw} \end{pmatrix}, \tag{4.4}$$

for some (s_1, t_1). That is, the scalars (t_0, α_{plw}) and the curve $(\tilde{\theta}(t), \tilde{\phi}(t))$ is known, and the scalars (s_1, t_1) is considered to be unknown. When this boundary value problem has a unique solution standard iterative methods, developed from a linear theory, can be applied. Such a numerical method is sometimes referred to a shooting method and it can be quite efficient if the rays do not deplete too much and the linear assumption is reasonable. If this does not hold the convergence rate may be so slow, or the method may even diverge, that the method becomes inefficient or non-applicable.

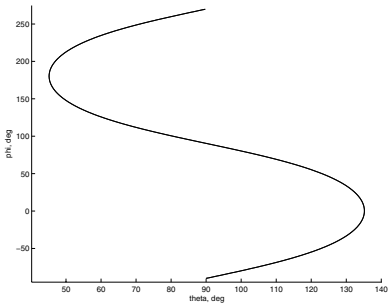

Figure 4.2: Shadow line for a sphere in (θ, ϕ)-space excited by a plane wave with $\hat{k} = (1/\sqrt{2}, 0, 1/\sqrt{2})$.

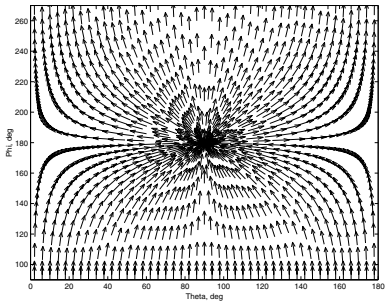

Figure 4.3: Plot of sampled points for one half of the wave front built up by a plane wave with $\hat{k} = (0, 1, 0)$.

4.1.2 Shadow lines

Let us generalize the concept of wave front in configuration space. In electromagnetics and in Chapter 3 a wave front assigns most often an equi-phase front. When GTD is applicable, we can also speak of rays and these are then orthogonal to the wave fronts. This definition is somewhat too restrictive for our purposes. Instead we will call any non-characteristic curve in configuration space a wave front. Below, in expression (4.5), we will mathematically define, a specific type of generalized wave front, called a *shadow line*. In words, is the shadow line a curve, represented in the parameter space, phase space or in configuration space, given by the boundary between light and shadow produced by some type of illumination. Hence, a shadow line can be used to define $(\tilde{\theta}(t), \tilde{\phi}(t))$ in (4.4) and sample points on the shadow line can be used to define the family of initial conditions in (4.3). We can also say that surface rays, defined as solutions to (4.1), are initiated at shadow lines.

To prepare for future analysis we will discuss the existence of unique shadow lines for smooth surfaces. Let us deduce a system of equations or ODEs that prescribe these lines. If there is a unique solution to the system, there is a unique shadow line in that point. Call the solution to the system of ODE:s, i.e. the shadow line, the initial wave front. For simplicity let us only consider monotone parameterizations of the shadow line and call the arc length parameter t. The normal $n(p, q)$, to a sufficiently smooth parameterized surface $X(p, q)$, can be computed with

$$n(p, q) = \pm X_p \times X_q.$$

More explicitly we have for the normal

$$n = \begin{pmatrix} \frac{\partial x_2}{\partial p}\frac{\partial x_3}{\partial q} - \frac{\partial x_3}{\partial p}\frac{\partial x_2}{\partial q}, \\ \frac{\partial x_3}{\partial p}\frac{\partial x_1}{\partial q} - \frac{\partial x_1}{\partial p}\frac{\partial x_3}{\partial q}, \\ \frac{\partial x_1}{\partial p}\frac{\partial x_2}{\partial q} - \frac{\partial x_2}{\partial p}\frac{\partial x_1}{\partial q} \end{pmatrix}.$$

For a point in parameter space $\xi(t) = (p(t), q(t))$ to be on a shadow line Γ, ξ must lie on

$$\Gamma := \{\xi \in \mathbb{R}^2 : N \equiv n(\xi) \cdot k = 0\}, \tag{4.5}$$

where we take k as Poynting's vector for a plane wave. Later, for general geometries, we will also demand that a point $X(\xi(t))$ on a shadow line should not, from an optical point of view (c.f. Physical Optics in Section 2.4), be occluded by the geometry. As we move along the shadow line, with a sufficiently smooth neighborhood, N must stay equal to zero, i.e.

$$\frac{\partial N}{\partial t} = 0. \tag{4.6}$$

Depending on the orientation of the curve parameterization we have two solutions which fulfill

$$\dot{X}^{(1)} = -\dot{X}^{(2)}.$$

We have

$$\begin{aligned} N &= \frac{\partial}{\partial p}\left[\sqrt{k_1}x_2, \sqrt{k_2}x_3, \sqrt{k_3}x_1\right] \cdot \frac{\partial}{\partial q}\left[\sqrt{k_1}x_3, \sqrt{k_2}x_1, \sqrt{k_3}x_2\right] \\ &- \frac{\partial}{\partial p}\left[\sqrt{k_1}x_3, \sqrt{k_2}x_1, \sqrt{k_3}x_2\right] \cdot \frac{\partial}{\partial q}\left[\sqrt{k_1}x_2, \sqrt{k_2}x_3, \sqrt{k_3}x_1\right] \\ &\equiv Y_p \cdot Z_q - Y_q \cdot Z_p, \end{aligned} \tag{4.7}$$

where Y and Z are defined accordingly. By the chain rule we also have for any vector $X(p(t), q(t))$

$$X_t = \dot{p}X_p + \dot{q}X_q. \tag{4.8}$$

By equation (4.8) and by interchanging the order of t-derivatives and p/q-derivatives in (4.6) we also have

$$\begin{aligned} \frac{\partial N}{\partial t} &= (\dot{p}Y_p + \dot{q}Y_q)_p Z_q + Y_p(\dot{p}Z_p + \dot{q}Z_q)_p \\ &- (\dot{p}Y_p + \dot{q}Y_q)_q Z_p - Y_q(\dot{p}Z_p + \dot{q}Z_q)_p. \end{aligned} \tag{4.9}$$

Finally, by rearranging the terms in (4.9) we get

$$A\dot{p} + B\dot{q} = 0, \tag{4.10}$$

where we defined

$$A = Z_q Y_{pp} + Y_p Z_{qp} - Z_p Y_{pq} - Y_q Z_{pp},$$

$$B = Z_q Y_{qp} + Y_p Z_{qq} - Z_p Y_{qq} - Y_q Z_{qp}.$$

If we, as before, let $\beta(t) = \arctan \dot{q}(t)/\dot{p}(t)$ and use equation (4.10) we get

$$\beta = \arctan\left(-\frac{A}{B}\right) \pm \pi, \tag{4.11}$$

where the sign should be picked so that $\dot{\xi}$ is continuous as we move along the curve.

Alternatively, to get a first order ODE, we can differentiate (4.11)

$$\dot{\beta} = Q_1 \dot{p} + Q_2 \dot{q},$$

where we defined

$$Q_1 \equiv \frac{AB_p - A_p B}{B^2 + A^2}$$

and

$$Q_2 \equiv \frac{AB_q - A_q B}{B^2 + A^2},$$

with

$$\begin{aligned} A_p &= Z_{qp}Y_{pp} + Z_q Y_{ppp} + Z_{qp}Y_{pp} + Z_{qpp}Y_p \\ &\quad -Z_{pp}Y_{pq} - Z_p Y_{pqp} - Z_{pp}Y_{qp} - Z_{ppp}Y_q, \end{aligned}$$

$$\begin{aligned} A_q &= Z_{qq}Y_{pp} + Z_q Y_{ppq} + Z_{qp}Y_{pq} + Z_{qpq}Y_p \\ &\quad -Z_{pq}Y_{pq} - Z_p Y_{pqq} - Z_{pp}Y_{qp} - Z_{ppq}Y_q, \end{aligned}$$

$$\begin{aligned} B_p &= Z_{qp}Y_{qp} + Z_q Y_{qpp} + Z_{qq}Y_{pp} + Z_{qpq}Y_p \\ &\quad -Z_{pp}Y_{qq} - Z_p Y_{qqp} - Z_{qp}Y_{qp} - Z_{qpp}Y_q, \end{aligned}$$

and

$$\begin{aligned} B_q &= Z_{qq}Y_{qp} + Z_q Y_{qpq} + Z_{qq}Y_{pq} + Z_{qqq}Y_p \\ &\quad -Z_{pq}Y_{qq} - Z_p Y_{qqq} - Z_{qp}Y_{qq} - Z_{qpq}Y_q. \end{aligned}$$

We now have a system of first order equations

$$\begin{pmatrix} \dot{p} \\ \dot{q} \\ \dot{\beta} \end{pmatrix} = \begin{pmatrix} \cos\beta \\ \sin\beta \\ Q_1 \cos\beta + Q_2 \sin\beta \end{pmatrix} = F(p, q, \beta), \tag{4.12}$$

where (4.11) can be used to set the initial condition for β with $(p(0), q(0))$ given. Here $p(0)$ and $q(0)$ needs to be given by other algorithms, c.f. [19] or discussion in Section 4.4.2.1. In Figure 4.2 we see a numerical solution to the algebraic equation (4.11) when applied to the unit sphere. To make a link to the boundary value problem discussed in Section 4.1.1 let us call the solution to (4.12) in parametrical space $(\tilde{p}, \tilde{q})(t)$.

4.1.3 Shadow Lines and Wave Fronts

If F in (4.12), and similarly G in (4.1), fulfill a Lipschitz condition in a domain $\Omega_G(p,q,\alpha)$ and $\Omega_F(p,q,\beta)$ respectively, then we know that there exist a unique solution to the systems in $\Omega_{F|G}$. Likewise since $\alpha(0)$ is a function of $(\hat{k},\tilde{p}(t),\tilde{q}(t))$, i.e.

$$\alpha(0,t) = f(\hat{k},\tilde{p}(t),\tilde{q}(t)),$$

we have that the two *coupled* ODE:s have a unique solution. Differently stated we can say that no rays will cross in (p,q,α)-space although they can of course cross in (p,q)-space.

If G fulfills a Lipschitz condition then we can represent the shadow line numerically by a discrete number of sample points, or markers, $[\tilde{p}(t_j),\tilde{q}(t_j),\alpha(t_j)]$ and we may order the markers with non-decreasing t by choosing a monotone parameterization of the shadow line. By propagating the initial shadow line as a generalized wave front we can, when depletion of markers occurs, interpolate new markers by using data from neighboring markers. Note that we can have depletion not only in parameter (p,q) space but also in phase space (p,q,α). I.e. to maintain sufficient accuracy of the propagating wave front we need to maintain the marker density in all dependent variables in (4.1). Since no rays cross we may even create, for a specific plane wave illumination $\hat{k}$ defining a unique $\tilde{p}(t),\tilde{q}(t)$, a one to one map,

$$(p,q,\alpha;\hat{k}) \leftrightarrow (s,t;\hat{k}), \tag{4.13}$$

where $(p,q,\alpha;\hat{k})$ is on a sub-manifold that the propagating wave front traces out in $\mathbb{R}^5$. With the new independent variables (s,t) we may interpolate any function $y(s,t;\hat{k})$.

The technique described above is sometimes referred to a wave front construction technique [11] and the solution is represented along a front. C.f. [12] and [13] for other types of ray methods. For electromagnetic linear wave problems, which is of our interest, will the wave front construction technique capture an essential property of the waves. I.e. different parts of a wave front, or rays, do not interact. For other type of moving front problems this quality may not be crucial or even not true. C.f. [41] for a fast method to find the solution to the Eikonal equation and [42] for fast method to find geodesics on a meshed geometry. Other fast techniques that capture multiple phases can be found in [14] and [43].

Later in the numerical examples we will see examples of how GTD-predicted smooth surface diffraction wave fronts may be initiated. It is not only shadow lines in smooth surfaces that excite surface rays but also edges, corners and discontinuities in the surface curvature. E.g. from a corner a fan of surface rays will build a surface wave front. The markers, in the initial wave front, will only be distinguishable in phase space and not in (p,q)-space. This is another reason to obtain high density in phase space for the shadow line and to retain sufficiently high density in the generalized moving wave fronts.

The numerical method implied by the discussion above is quite simple to implement if the entire geometry can be given with one parameterization. We also realize that since the independent variables is defined in parameter space the interpolation can be done efficiently since an interpolated marker in parameter space will stay on the manifold, i.e. on the surface. In addition we may integrate the solution to the transport equation with arbitrary accuracy since geometrical data is can be computed with the surface parameterization.

However, when it comes to industrial applications, there are three major drawbacks with the method mentioned above.

- The first drawback concerns solving equation (4.12). For a sphere there is only one shadow line and to find it, it is enough to get one pair of $(p(0), q(0))$, or one seed, along the shadow line. If the parameterized surface contain several shadow lines we need one seed from each shadow line. It may be hard to design an algorithm that discriminate two seeds if they come from two different shadow lines and to be sure that we find a seed from all shadow lines.

- The second drawback concerns solving equation (4.1). A general scatterer is commonly not given by one parameterization but several. These parameterizations or patches are glued together in a quite elaborate manner. Moving a marker from one patch to another, and to keep track of when the move should be done, can be very complicated. For similar reasons it is hard to interpolate between markers that belong to different patches.

- The third drawback is that when interpolation is done in surface parameter space the specific parameterization of the surface, that the designer has produced, will affect the accuracy of the interpolation.

In the next section we will show how the advantages with a parameterized geometry may be exploited when the geometry is used in conjunction with a triangular mesh.

4.2 Introduction to Fronts On a Hybrid Geometry

In this section we will discuss some of the implications of having access to a piecewise parameterization of the scattering geometry *and* a triangular mesh. When we have this double representation of the geometry we say that we have a *hybrid geometry*. We will show that a triangular mesh, with maximum edge length h, may be used to solve equation (4.12) and (4.1) numerically with fast and robust algorithms. If the triangle representation is completed by the underlying surfaces in parameterized form, then the front propagation may be done more efficiently and higher order GTD-effects may be included in the analysis.

In the introduction to this chapter the wave front had its representation in (p, q, α)-space. Of course we can easily compute its position in the five or six-dimensional space

$$[p, q, \alpha] \rightarrow [x_1, x_2, x_3, \sin\theta\cos\phi, \sin\theta\sin\phi, \cos\theta] \rightarrow [x_1, x_2, x_3, \theta, \phi)]$$

by using the surface parameterization and the definition of the Euler angles.

We want solve the ODE:s that corresponds to (4.1) and (4.12) in the six-dimensional space. This can be done by solving differential algebraic equations. However we propose that we search the rays on a triangularized approximation of the geometry with triangle nodes coinciding with the associated surface. The markers, and hence the surface rays or facet rays that the markers traces out, is always forced to be on the triangle facets by using algebraic expressions. We will see later that, to show sufficient accuracy for our type of meshes and applications, the rays given by (4.1) must be found by not only using data from the triangles (first order elements) but we also need to use geometrical data from the surface parameterization in the triangle nodes. More specifically, it concerns the surface normal. To be able to compute the electromagnetic field, the principal directions and the principal curvatures also have to be provided.

To be more precise we will show that, by completing the triangle node positions with the surface normals and computing the facet rays more accurate we can achieve, with h as the maximum size of largest triangle edge in the mesh, an $\mathcal{O}(h)$-approximation of the final position of the true geodesic line.

We have also developed an algorithm to solve (4.12) with an $\mathcal{O}(h)$ accuracy. To achieve a sufficiently high order representation of the shadow line, i.e. the initial conditions to equation (4.1), we project the front to the surface parameter space and run a Conjugate Gradient algorithm, c.f. [19]. However, we will only present the algorithm to find the shadow lines and not analyze the order of accuracy for it. We note that, by introducing a hybrid geometry we have retained the advantages with surface parameterized geometry, and

- we have solved the problem with finding all shadow lines for a general scatterer. It will not be shown from a mathematical point of view but just indicated, during the presentation of the computer implementation, that the shadow line algorithm on facets is relatively robust and efficient.
- we have removed the second drawback mentioned in the introduction since we reduced the marker moving, from one surface patch to another, to more trivial moves from one triangle patch to another.
- we will not be dependent on the specific type of parameterization of the surface since we will use an interpolation algorithm defined on the triangles.
- finally the advantage with having a hybrid geometry concerns the integration of expression (4.14) defined below. As we will see in 4.3.4.1, it is not straight forward to evaluate the GTD-expression with only the facetized geometry at hand, but we actually need both for non-smooth geometries.

4.3 Numerical Approximations

Our goal is to compute the so called soft ($\mathcal{S}$) and hard ($\mathcal{H}$) components of the smooth surface diffracted electric field in P

$$\begin{gathered} E_{scatt}^{\mathcal{S},\mathcal{H}}(P) = E_{inc}^{\mathcal{S},\mathcal{H}}(Q_1)\sqrt{\frac{\partial\eta(Q_1)}{\partial\eta(Q_2)}}\sqrt{\frac{\rho}{r(\rho+r)}}\cdot \\ \sum_{p=1}^{N} D_p^{\mathcal{S},\mathcal{H}}(Q_1)\exp\left(-i\tfrac{2\pi}{\lambda}\int_{Q_1}^{Q_2} 1+\sigma_p^{\mathcal{S},\mathcal{H}}(t')\,dt'\right)D_p^{\mathcal{S},\mathcal{H}}(Q_2) \end{gathered} \tag{4.14}$$

This section concerns the numerical approximations we do when we integrate and evaluate the smooth surface diffraction given in (4.14) where

$$\sigma_p^{\mathcal{S},\mathcal{H}} = \lambda^{2/3}\rho_g^{-2/3}C_1^{\mathcal{S},\mathcal{H},p} \tag{4.15}$$

and

$$D_p^{\mathcal{S},\mathcal{H}} = \lambda^{1/12}\rho_g^{1/6}C_2^{\mathcal{S},\mathcal{H},p},$$

where $C_j^{\mathcal{S},\mathcal{H},p}$ are given constants. ρ_g is the radius of curvature of a geodesic line and t' the arc length parameter of the geodesic line. Referring to Figure 4.1, the soft component of the scattered electrical field is parallel to the surface normal $\hat{n}$ at Q_1/Q_2. The hard component is the scattered electrical field that are approximately parallel to $\hat{p}\times\hat{n}$ where $\hat{p}$ is Poynting's vector of the wave at Q_1/Q_2. ρ is the radius of curvature of the geodesic wave front and $r = |P - Q_2|$.

Since expression (4.14) only applies to convex surfaces we have developed our theory only for such surfaces. However, we believe that it is straight forward to justify our contribution to concave surfaces also.

The investigation in this section will focus on three factors in expression (4.14) and an integration. Namely

$$F_1 = \exp\left(-i\frac{2\pi}{\lambda}\int_{Q_1}^{Q_2} 1\,dt'\right), \tag{4.16}$$

which has to do with the fact that the phase of the wave front must solve the surface Eikonal equation. It is mainly dependent on the arc length of the geodesic curve and it is investigated in Section 4.3.3.1. The second factor concerns intuitively the transport equation and, since $i\sigma_p^{\mathcal{S},\mathcal{H}}$ contains a real part, it will represent a so called exponential spreading of the energy. We define it as

$$F_2 = \exp\left(-i\frac{2\pi}{\lambda}\int_{Q_1}^{Q_2} \sigma_p^{\mathcal{S},\mathcal{H}}(t')\,dt'\right), \tag{4.17}$$

and it is investigated in Section 4.3.4.1. In Section 4.3.4.2, we will investigate the geometrical spreading represented in

$$F_3 = \sqrt{\frac{\partial\eta(Q_1)}{\partial\eta(Q_2)}}, \tag{4.18}$$

where $\partial\eta(Q_1)$ is the arc length of an infinitesimal segment of the wave front at Q_1 and $\partial\eta(Q_2)$ the arc length of this segment as it arrives at Q_2.

There is a final fourth factor that we evaluate numerically. Namely

$$\sqrt{\frac{\rho}{r(\rho+r)}}. \tag{4.19}$$

However, the approximation of it is based on some asymptotic assumptions which we have not addressed in our presentation. We will therefor avoid the corresponding analysis in the numerical approximation section.

Finally, if there are several t_0s or even a continuum of these that solve the boundary value problem in (4.4), we want to sum or integrate the contribution from all these smooth surface diffracted rays.

To be able to investigate the three factors and the integration we need an introductory discussion to surface curvature sensitive meshing in Section 4.3.1 and a short discussion on maps in Section 4.3.2.

4.3.1 Surface Curvature Sensitive Meshing

To achieve an efficient algorithm we have adapted our algorithm to surface curvature sensitive triangular meshes. They are characterized by a given bound, ϵ, on the distance between the mesh and the NURBS geometry Σ, c.f. [44]. More specifically for such a mesh Σ_T, we have that the triangle nodes will coincide with the curved embedding geometry it is representing. For a given meshed geometry we would like to associate a curved triangular patch $T_\Sigma^{(j)}$ to each triangle $T^{(j)}$. This partition of Σ can be done in several ways. To investigate surface curvature sensitive meshing we find the following definition practical, which is unique as long as we choose the triangle edges small enough. We have

$$\Sigma = \bigcup_{j=1}^{N_\Sigma} T_\Sigma^{(j)}$$

and

$$\Sigma_T = \bigcup_{j=1}^{N_{\Sigma_T}} T^{(j)}.$$

The union of all triangle edges in Σ_T forms a triangular web. We would like to map this web W_T to a web W_Σ in Σ such that $N_\Sigma = N_{\Sigma_T} = N$. Given a point $X_\Sigma \in \Sigma$ we can, by using the point X_{close} which solves

$$\min_{X\in\Sigma_T} |X_\Sigma - X|, \tag{4.20}$$

let $X_\Sigma \in W_\Sigma$ if $X_{close} \in W_T$. That is, we have, as long as (4.20) has unique solutions, defined a unique W_T. With W_Σ and W_T given, we can easily associate

each triangle $T^{(j)}$ to a curved triangular patch $T_\Sigma^{(j)}$. For each pair j we can define the following distance

$$D_T^j = \max_{X_\Sigma \in T_\Sigma^{(j)}} \left(\min_{X_T \in T^{(j)}} |X_T - X_\Sigma| \right).$$

We then define a surface curvature mesh as a mesh where

$$\max_{j=1\ldots N} D_T^j = D_T \leq \epsilon. \tag{4.21}$$

That is, the threshold ϵ controls the distance D_T between the geometry Σ and the meshed geometry Σ_T. Consequently, ϵ also controls the size of a triangle if its associated curved triangle is non-flat.

Call the triangle nodes for a specific triangle j

$$(x_1^{(j)}, x_2^{(j)}, x_3^{(j)}),$$

and define a local coordinate system $(\hat{\xi}_1', \hat{\xi}_2', \hat{\xi}_3')$, centered in $x_1^{(j)}$, as

$$\begin{aligned} \hat{e}_1^{(j)} &= \frac{x_2^{(j)} - x_1^{(j)}}{|x_2^{(j)} - x_1^{(j)}|} \\ \hat{e}_3^{(j)} &= \frac{\hat{e}_1^{(j)} \times (x_3^{(j)} - x_1^{(j)})}{|\hat{e}_1^{(j)} \times (x_3^{(j)} - x_1^{(j)})|} \\ \hat{e}_2^{(j)} &= \hat{e}_3^{(j)} \times \hat{e}_1^{(j)}. \end{aligned} \tag{4.22}$$

If, once again, ϵ is chosen small enough we may represent the curved triangular patch $T_\Sigma^{(j)}$ with a function $f^{(j)}$ in the jth coordinate system according to

$$T_\Sigma^{(j)} = \hat{e}_1^{(j)} \xi_1^{(j)} + \hat{e}_2^{(j)} \xi_2^{(j)} + \hat{e}_3^{(j)} f^{(j)}(\xi_1^{(j)}, \xi_2^{(j)}) + x_1^{(j)}. \tag{4.23}$$

Call the domain of definition of $f^{(j)}$ $\Omega_T^{(j)}$. Ω_T is exemplified in figure 4.4. For later reference we also define $\hat{\Omega}_T^{(j)}$ as the domain bounded by the triangle edges. Let Ω_T fit into a circle with diameter h_T. Call the maximum diameter, over all the patches in the geometry, h.

We assume that there is a coordinate system such that Σ can be written as *function*. If this does not exist we can always split up according to $\Sigma = \cup_{k=1}^M \Sigma_k$ and perform the analysis for each patch Σ_k. I.e. for any point X_Σ on Σ we have that

$$X_\Sigma = [\xi_1', \xi_2', F_\Sigma(\xi_1', \xi_2')].$$

Let us call the domain of definition of f_Σ Ω_Σ'. Similarly we have

$$X_T = \left[\xi_1', \xi_2', \sum_{j=1}^N F_j(\xi_1', \xi_2') \right],$$

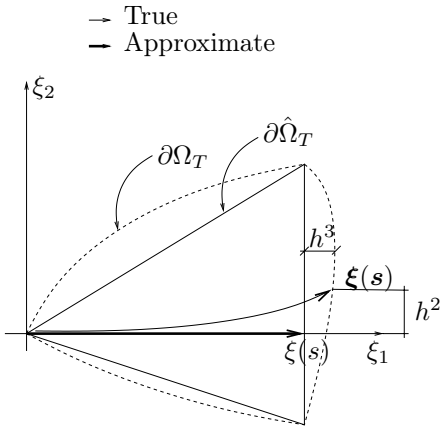

Figure 4.4: The local error of the marker position in (ξ_1, ξ_2)-space for an $\mathcal{O}(h)$-triangle. The dashed curve bounds the domain of definition, i.e. Ω_T, for the curved patch. Boldface indicate exact solution.

where F_j is a is a linear function on a linear Lagrange triangle j with a size bounded by h. Let us call the domain of definition of $\sum_{j=1}^{N} F_j(\xi_1', \xi_2')$ Ω_T'. From approximation theory, c.f. [45], we have that

$$\tilde{\epsilon} = \max_{j=1\ldots N} \|F_\Sigma - F_j\|_{W^0_\infty(\Omega_T')} \leq Ch^2 \|F_\Sigma\|_{W^4_1(\Omega_\Sigma')} \quad \forall\, F_\Sigma \in W^4_1(\Omega_{\Sigma'}), \tag{4.24}$$

where $W^k_p(\Omega')$ is a Sobolev space defined according to

$$W^k_p(\Omega') := \left\{ f \in L^1_{loc}(\Omega') : \left(\sum_{|\beta|\leq k} \|D^\beta f\|^p_{L^p(\Omega')} \right)^{1/p} \leq \infty \right\},$$

and $\|\cdot\|_{W^k_p(\Omega')}$ correspondingly. Here D^β is the βth weak derivative, $L^1_{loc}(\Omega')$ indicate that f_Σ should be locally integrable, the infinity norms will give the maximum value, p indicate that the L^p norm should be used and $|\beta| \leq k$ means that the sum should be taken over all (including mixed) derivatives up to the kth order. More specifically one can show, c.f. [46], that if we only consider the jth triangle with size $h^{(j)}$, i.e. instead of considering the entire geometry and Ω_T' as domain of definition we only consider a curved patch with $\hat{\Omega}_T^{(j)}$ as domain of definition, then

$$\epsilon^{(j)} = \|f^{(j)}\|_{L^\infty(\hat{\Omega}_T^{(j)})} \leq 2\left(h^{(j)}\right)^2 \max_{|\beta|=2} \|D^\beta f^{(j)}\|_{L^\infty(\hat{\Omega}_T^{(j)})}, \tag{4.25}$$

is the element wise error estimate. Let us call the norm on the right hand side $D^{(2)}(\hat{\Omega}_T^{(j)})$. It is a measure of the surface curvature for the specific patch $T_\Sigma^{(j)}$.

As said previously we will assume that the meshing algorithm is governed by a maximum distance, ϵ, between the mesh and the geometry. Hence, we assume that the meshing algorithm choose an $h^{(j)}$ for each triangle such that

$$\epsilon \approx 2\left(h^{(j)}\right)^2 D^{(2)}(\hat{\Omega}_T^{(j)}),$$

then the largest triangle in the mesh with size h will fulfill

$$h = C_1\sqrt{\frac{\epsilon}{\min\limits_{j=1\ldots N} D^{(2)}(\hat{\Omega}_T^{(j)})}}.$$

Referring to the discussion concerning expression (1.27) in the introduction we can pick $\epsilon = \mathcal{O}(\lambda)$, i.e $\delta = 1/2$, for an $\mathcal{O}(h^3)$-scheme to achieve

$$h = C_2\sqrt{\frac{\lambda}{\min\limits_{j=1\ldots N} D^{(2)}(\hat{\Omega}_T^{(j)})}}. \tag{4.26}$$

We want to make three remarks before we proceed.

- Equation (4.24) and (4.25) only holds for meshes were the triangle angles does not approach zero as $\epsilon \to 0$. When a surface, with zero curvature in some direction, is meshed this condition will not be fulfilled. However, then the mathematical and numerical problem presented later can be considered to be one dimensional and the one dimensional counterparts to (4.24) and (4.25) can be used.

- For a surface with zero curvature, $h = \infty$ in (4.26). This will not be a problem in the analysis below since our numerical algorithm will then represent the geodesics exactly. A geodesic line on a surface with zero curvature is a straight line.

- We note that since (4.21) holds and, as we will see later, (4.35) also holds we realize that the small surface stripes that are not covered by estimation (4.25) will not cause a problem in the analysis later.

By dropping the index j in (4.23) and Taylor expanding $f(\xi_1, \xi_2)$ around any point $({\xi_1}^{(0)}, {\xi_2}^{(0)}) \in \Omega_T$ we get

$$\begin{aligned} f({\xi_1}^{(0)} + h_{\xi_1}, {\xi_2}^{(0)} + h_{\xi_2}) &= f({\xi_1}^{(0)}, {\xi_2}^{(0)}) + \frac{\partial f}{\partial \xi_1}h_{\xi_1} + \frac{\partial f}{\partial \xi_2}h_{\xi_2} + 2\frac{\partial^2 f}{\partial \xi_1 \partial \xi_2}h_{\xi_1}h_{\xi_2} \\ &+ \frac{\partial^2 f}{\partial \xi_1^2}h_\xi^2 + \frac{\partial^2 f}{\partial {\xi_2}^2}h_{\xi_2}^2 + \mathcal{O}(h^3), \end{aligned} \tag{4.27}$$

where (h_{ξ_1}, h_{ξ_2}) must be chosen so that $({\xi_1}^{(0)} + h_{\xi_1}, {\xi_2}^{(0)} + h_{\xi_2})$ is inside Ω_T. Since, according to (4.25), the maximum should be of $\mathcal{O}(h^2)$ and we can choose $f(\xi_1^{(0)}, \xi_2^{(0)}) = 0$, then both

$$\frac{\partial f}{\partial \xi_1} = \mathcal{O}(h) \tag{4.28}$$

and

$$\frac{\partial f}{\partial \xi_2} = \mathcal{O}(h) \tag{4.29}$$

must hold.

4.3.2 Mapping Facets ↔ NURBS

To be able to derive the level of accuracy of our scheme we need to discuss the mapping between the triangles and the curved embedding geometry. The mapping can be chosen in several ways and each of them have pros and cons when it comes to proving the level of accuracy. However, as we will see later, will the selection not affect global error of convergence of the numerical scheme. We sketch three procedures that produce three different mappings. Let x be a point in a curved surface patch T_Σ in $\mathbb{R}^3$ and $(\xi_1, \xi_2) \in \hat{\Omega}_T$ the independent variables in the local coordinate system.

Bijection A one-to-one mapping that is onto. We need to define the general map

$$[\xi_1, \xi_2] \leftrightarrow x = \left[x^{(1)}(\xi_1, \xi_2), x^{(2)}(\xi_1, \xi_2), x^{(3)}(\xi_1, \xi_2)\right],$$

where $\hat{\Omega}_T \leftrightarrow x^T$. The curved surfaces patches introduced in Section 4.3.1 can be used to define a bijective map if we, for each triangle j, provide a map mapping points in $\hat{\Omega}_T^{(j)}$ to $T_\Sigma^{(j)}$.

Injection A one-to-one mapping that is not onto. Define a vector V going through (ξ_1, ξ_2) and that is parallel to $\hat{\xi}_1 \times \hat{\xi}_2$. Then

$$[\xi_1, \xi_2] \rightarrow \text{intersection}(V, T_\Sigma).$$

We have that $\hat{\Omega}_T \rightarrow x$, though not all point in T_Σ is covered.

Surjection An onto mapping that is not one-to-one. Map all point x in T_Σ to the closest point in $\hat{\Omega}_T$. We have a unique $\hat{\Omega}_T \leftarrow x$ but not a unique $\hat{\Omega}_T \rightarrow x$.

Note that for the surjection example a point may not, at least not in general, always be uniquely associated to only *one* triangle.

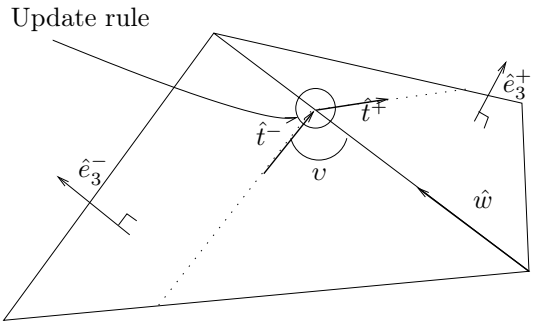

Figure 4.5: Figure defining variables used to update the approximate geodesic tangent.

4.3.3 Solution to Surface Eikonal Equation

In the convergence analysis that follows we will always assume a generic case as depicted in Figure 4.5. That is we will assume that the angle υ is strictly bounded away from 0 and π and that the geodesic ray is located away from the corners of the triangle by a distance larger than ch for some $c > 0$. Even if the analysis is restricted to this generic situation our extensive numerical test indicate convergence in general. The analysis covers the generic case and it gives an understanding of the size of the different components in the local truncation error.

4.3.3.1 Arc Length

We will now present a numerical scheme to compute geodesics and we will investigate the local order of accuracy of the scheme. That is, for a triangle of size h, how depends the error of some computed variable on h. In the end we want to make sure that the error of a computed variable decreases with $\mathcal{O}(\lambda^\mu)$, with $\mu > 0$, as long as h depends on λ according to some polynomial rule.

C.f. Figure 4.5. In short will our numerical scheme of moving markers along straight lines on the triangular elements, jumping to neighboring triangles and updating the arclength correspondingly.

The order of accuracy discussion we did in Section 1.3 concerned the approximate solution to the surface Eikonal equation, i.e. the phase. As already mentioned we find its solution by applying the method of characteristics and solve a set of ODEs approximately. In this section we will analyze the error of the numerically computed geodesics' final position, derivative and length.

As an introduction to the quite technical proofs on the order of accuracy done later, we will discuss geodesics on a cylinder, i.e a simply curved geometry. Consider a cylindrical patch and the corresponding unfolded patch, including the surface curvature sensitive mesh, in Figure 4.6. If the short edges on the triangles are of

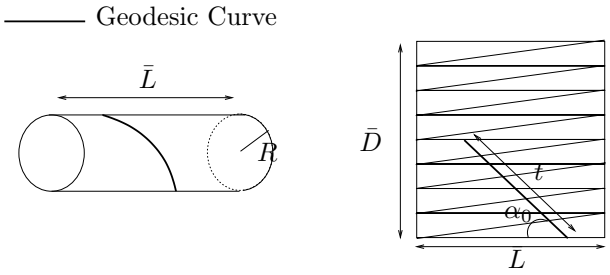

Figure 4.6: Schematic picture of a cylinder and the unfolded mesh.

size $\mathcal{O}(h)$ then one can easily show, using the notation in the figure and assuming α_0 is given exactly, that $\bar{D} = 2\pi R - \mathcal{O}(h^2)$. This means that the length of the straight line on the unfolded geometry, i.e. the approximate unfolded geodesic, is an $\mathcal{O}(h^2)$ approximation of the true geodesic length. Above suggest that a numerical scheme defined for a general surface curvature sensitive mesh, approximating a "doubly curved" surfaces, should produce straight lines when triangles are pairwise unfolded.

If we call the numerically computed geodesic tangent on triangle $T^{-|+}$ $\hat{t}^{-|+}$ and let $\hat{w}$ be a properly signed common edge vector, i.e. $(\hat{e}_z^+, \hat{t}^-, \hat{w})$ should form a right handed system, for triangle $+$ and $-$, then one can show that the following update rule, with notation as in Figure 4.5,

$$\hat{t}^+ = \frac{\hat{e}_3^+ \times \left(\hat{t}^- \times \frac{\hat{e}_3^+ + \hat{e}_3^-}{2}\right)}{\left|\hat{e}_3^+ \times \left(\hat{t}^- \times \frac{\hat{e}_3^+ + \hat{e}_3^-}{2}\right)\right|} = (\hat{w} \cdot \hat{t}^-)\hat{w} + \sqrt{1 - (\hat{w} \cdot \hat{t}^-)^2}(\hat{w} \times \hat{e}_3^+), \tag{4.30}$$

will produce the straight line pictured in Figure 4.6. Here $\hat{e}_3^{+|-}$ are triangle normals. The second equality can be shown with some algebra and calculus. We also realize that if we let $\upsilon = \arccos\left(\hat{w} \cdot \hat{t}^-\right)$, c.f. Figure 4.5, then

$$\hat{t}^+ = \cos(\upsilon)\hat{w} + \sin(\upsilon)(\hat{w} \times \hat{e}_3^+).$$

However, since update (4.30) is hard to analyze mathematically, and it is less evident that we get $\mathcal{O}(h^2)$ convergence experimentally, we will investigate a scheme based on a different but related update rule. It will however assume that we have access to information from the geometry which the mesh approximate.

Once more let us redefine our dependent variables in parameter space. Let $p \to \xi_1$ and $q \to \xi_2$ in (4.1). That is, we locally let the triangles and their coordinate systems, define the parameter space. Since ξ and α is coupled by the right hand side in (4.1) we realize that any local numerical error we do when we update ξ or α will affect the global error in both ξ and α. By moving the marker along straight lines we will introduce a local error in both ξ and α. By jumping from one triangle

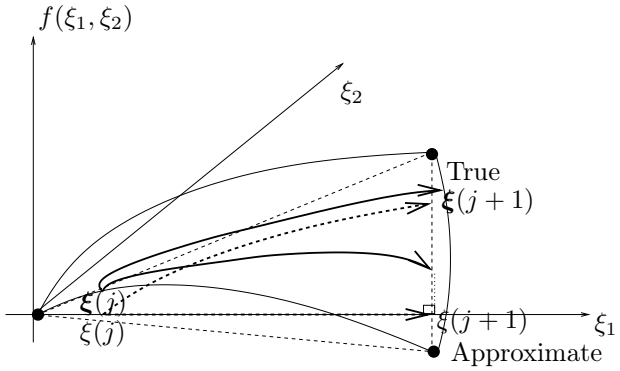

Figure 4.7: Schematic picture of a triangle and the associated curved patch. Boldface indicate exact solution.

to another we will also introduce errors, with a size depending on which mapping we use, in both ξ and α. That is, our scheme introduce four errors and all of them needs to be bounded by $\mathcal{O}(h^\gamma)$. Let us enumerate and quantify the numerical local truncation errors, which will be justified later, that are introduced in the numerical scheme. If we consider the local numerical error *triangle wise* (the tangent update is not included) we introduce the following errors:

Error 1 Since the marker is moved along straight lines in each triangle we introduce an $\mathcal{O}(h^3)$ error in ξ.

Error 2 Since the marker is moved along straight lines in each triangle we introduce an $\mathcal{O}(h^2)$ error in α.

However if we consider the local error *edge wise* (both tangent and position update included) we achieve

Error 3 an $\mathcal{O}(h^3)$ error in ξ and

Error 4 an $\mathcal{O}(h^3)$ error in α at a **specific position** after the jump.

Because of the reduction of the fourth local error, we believe that global error of the geodesic in $\mathbb{R}^3$ is actually the local error times the number of passed edges, i.e.

$$\mathcal{O}(h^{-1})\mathcal{O}(h^3) = \mathcal{O}(h^2).$$

Numerical evidence will also support this statement. Let us first define two updating procedures applied to our set of equations in (4.1). We apply the first one to the position variables (ξ_1, ξ_2) in parameter space and the second we apply to the direction variable α, also defined in the parameter space. Consider Figure 4.7 and 4.4. We define the triangle wise update,

$$\begin{aligned} &\xi(j) \in \hat{\Omega}_T \rightarrow \xi(j+1) \in \hat{\Omega}_T \\ &\alpha(j) \in [0, 2\pi] \rightarrow \alpha(j+1) \in [0, 2\pi], \end{aligned}$$

as

Update 4.1. *Given a direction $\alpha(j)$ and a position $\xi(j) = (\xi_1(j), \xi_2(j))$ in parameter space in the triangle T^-, update the position according to*

$$\xi(j+1) = \xi(j) + \Delta s_j(\cos(\alpha), \sin(\alpha)) \tag{4.31}$$

where $\Delta s_j = |\xi(j+1) - \xi(j)|$ is the Euclidean distance found by solving

$$\textit{intersection}\left[\xi(j) + \Delta s_j\left(\cos(\alpha), \sin(\alpha)\right), \partial\hat{\Omega}_T^-\right]$$

for $\xi(j+1)$. The angle is unaltered in a triangle, i.e.

$$\alpha(j+1) = \alpha(j). \tag{4.32}$$

We now have a numerical approximation of ξ and α in the points $j = 1 \dots n$. We will not call these mesh points *since they do not correspond to a fixed mesh but they are dependent on the numerical solution that we compute.*

Call the numerically computed geodesic tangent $\hat{t}^{-|+}(\alpha(T^-|T^+)) \in \mathbb{R}^3$, then we define a direction update, different from expression (4.30), when moving from one triangle T^- to a neighboring triangle T^+,

$$\alpha(T^-) \to \alpha(T^+),$$

where

$$\alpha(T^{-|+}) = \arccos\left(\hat{t}^{-|+} \cdot \hat{e}_1^{-|+}\right),$$

as

$$\hat{t}^+ = \frac{\hat{e}_z^+ \times (\hat{t}^- \times \hat{N}_s)}{|\hat{e}_z^+ \times (\hat{t}^- \times \hat{N}_s)|}. \tag{4.33}$$

$\hat{N}_s(\xi)$ is the surface normal, interpolated to some order in the solver, at the point where we do the jump. The surface normal is considered to be known exactly in the triangle nodes, we can therefore use standard linear interpolation, c.f. (4.25), to achieve a second order approximation of $\hat{N}_s$. Note that we have with update (4.30) and (4.33) forced the approximate tangent to be orthogonal to the triangle normals. Hence, by Update 4.1 and update (4.30) or Update 4.1 and update (4.33) the approximate geodesic will stay on the facetized geometry as we integrate it. Also note that $\hat{t}^-$ and $\hat{t}^+$ are the approximate geodesic tangent at the same approximate arc length or edge. That is, the numerical geodesic tangents is not well defined at the jumping points.

The numerical method where we use expression (4.30) minimizes the approximate arclength locally on two neighboring triangles and the final total approximate curve will therefore be an exact geodesic for the meshed geometry. Hence, since the approximate curve is a geodesic, will the scheme based on update (4.30), as we

refine the mesh and use exact initial conditions, intuitively be consistent with the ODE that we want to solve.

That this also holds for (4.33) is not as easy to realize. By noting that update (4.30) use an arithmetic mean of a piece wise constant approximations of the surface normals while update (4.33) use a piece wise linear approximation of the normal we once more get from approximation theory [46] that

$$\hat{e}_z^+ \xrightarrow{(4.30) \to (4.33)} 2N_s - \hat{e}_z^- = 2\left(\frac{\hat{e}_z^- + \hat{e}_z^+}{2} + \mathcal{O}(h)\right) - \hat{e}_z^- = \hat{e}_z^+ + \mathcal{O}(h).$$

That is, the local difference between update (4.30) and update (4.33) is of $\mathcal{O}(h)$, i.e. the global difference seems to be of $\mathcal{O}(1)$. We will see that this incomplete analysis does not imply that the scheme based on update (4.33) is inconsistent. Note that the use of an $\mathcal{O}(h)$ approximation of the surface normal in update (4.30) suggest the inconsiderate conclusion that the global error is of $\mathcal{O}(1)$.

We also note that update (4.33) takes explicitly into account the change in surface normal as we perturb the jumping point along the edge while for the simply curved surface in Figure 4.6 update (4.30) and (4.33) produce the same approximate geodesic line.

To further characterize update rule (4.33) we need a parameterization of two neighboring triangles as defined in Figure 4.8 and the union of their corresponding embedded geometry. By choosing such a parameterization we manage, if we let $\chi \in \hat{\Omega}_{TP}$, to design a bijective map while considering a triangle pair and their common edge. The normal projection, of the true geodesic lines, onto the $\hat{\chi}_1\hat{\chi}_2$-plane will therefore have a continuous tangent. Hence, both the projection of the approximate (defined in ξ-space) and the true tangent may be parameterized with χ_1. As mentioned in the last chapter can the geodesic curve be defined as a curve that have zero geodesic curvature. That is

$$c_g(t) = \ddot{x}(t) \cdot (\hat{N}_s(x(t)) \times \dot{x}(t)) = 0 \quad \forall\, t, \tag{4.34}$$

where $x(t) \in X_\Sigma$ is the true geodesic curve and t the geodesic arc length. The approximate geodesic has up until now only been defined on the triangles. However by using orthogonal projections from the $\chi_1\chi_2$-plane we can also define an approximate geodesic on Σ as long as $(\chi_1, \chi_2) \in \hat{\Omega}_{TP}$. Since, by Update 4.1, α is constant in each triangle we know that, at least in general, the approximate geodesic will violate (4.34). However, one realizes by inspection, that if we update α according to update (4.33), then the approximate $c_g(\chi_1)$ will be continuous when passing the edge.

Let us once more consider Figure 4.4 and 4.7. Schematically we have pictured a triangle with its associated curved patch. Indicate the exact geodesic curve in parametrical space with boldface. To be able to estimate $|\xi(\boldsymbol{\xi}_1) - \boldsymbol{\xi}(\boldsymbol{\xi}_1)|$ we need an estimation of the maximum distance between the projected surface patch boundary and the triangle. Below we therefore state and prove a lemma that tell us about

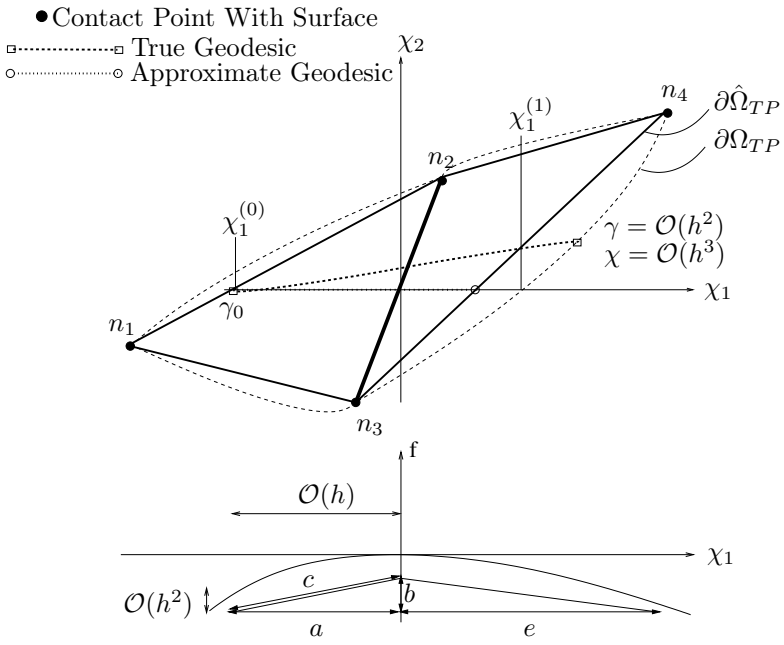

Figure 4.8: Parameter space for the surface associated to two neighboring triangles. Note that we have forced the interpolated surface normal $\hat{N}_s$ at the *jumping*-point, chosen to coincide with the origin, to be parallel to the $(\hat{\chi}_1 \times \hat{\chi}_2)$-axis. Also note that the true surface and the triangles, indicated by their boundary projected onto the $\hat{\chi}_1\hat{\chi}_2$-plane, are not necessary in this plane. In fact we assume that the normal has been chosen so that surface and the triangles are below the $\hat{\chi}_1\hat{\chi}_2$-plane.

the maximum distance between $\partial\hat{\Omega}_T$ and $\partial\Omega_T$ for a given triangle T. However, to formulate and prove the lemma we need to define three curved segments.

Consider edge j. Use expression (4.20) when defining the curved segment $\partial\Omega_\Sigma^j \in \Sigma$ associated to $\partial\Omega_T$. Also define the curved segments that corresponds to orthogonal projection of $\partial\hat{\Omega}_T^{j-}$ onto χ-space and $\partial\hat{\Omega}_T^{j+}$ and call them $\partial\hat{\Omega}_\Sigma^{j-}$ and $\partial\hat{\Omega}_\Sigma^{j+}$

By inspection for sufficiently small h we realize that any point $\chi \in \partial\Omega_\Sigma^j$ is in the closed domain

$$\partial\hat{\Omega}_\Sigma^{j-} \cup \partial\hat{\Omega}_\Sigma^{j+}.$$

Lemma 4.2. *Referring to Figure 4.4 and 4.9. Let $\bar{r}$ be a point on the boundary $\partial\hat{\Omega}_T$ and r be a point on the boundary $\partial\Omega_T$ then*

$$\Delta_1 = \max_{r\in\partial\Omega_T} \left(\min_{\bar{r}\in\partial\hat{\Omega}_T} |\bar{r} - r| \right) = \mathcal{O}(h^3).$$

Proof. As before call the triangle normals $\hat{e}_3^{-|+}$ and consider Figure 4.9. As before call the triangle normals $\hat{e}_3^-$ and $\hat{e}_3^+$ then we want to show that

$$\beta = \arccos\left(\hat{e}_3^- \cdot \hat{e}_3^+\right) = \mathcal{O}(h). \tag{4.35}$$

Call the four triangle nodes in Figure 4.8 n_1, n_2, n_3 and n_3. Then we evaluate

$$\sin\beta = \left| \frac{(n_4 - n_3) \times (n_2 - n_3)}{|(n_4 - n_3) \times (n_2 - n_3)|} \times \frac{(n_2 - n_3) \times (n_1 - n_3)}{|(n_2 - n_3) \times (n_1 - n_3)|} \right|.$$

By (4.27) we can choose a coordinate system such that $n_3 = 0$ and

$$\begin{aligned} n_1 &= \left[\mathcal{O}(h), \mathcal{O}(h), \mathcal{O}(h^2)\right] \\ n_2 &= \left[\mathcal{O}(h), \mathcal{O}(h), 0\right] \\ n_4 &= \left[\mathcal{O}(h), \mathcal{O}(h), \mathcal{O}(h^2)\right]. \end{aligned} \tag{4.36}$$

We have

$$\mathcal{O}(h^4)\sin\beta = \left|(n_4 \times n_2) \times (n_2 \times n_1)\right|.$$

By using a standard vector product rule we get

$$\mathcal{O}(h^4)\sin\beta = n_2\{(n_4 \times n_2) \cdot n_1\} - n_1\{(n_4 \times n_2) \cdot n_2\},$$

where the second term is zero since $(n_4 \times n_2) \perp n_2$. Finally, using (4.36) and the vector product definition, we get

$$\begin{aligned} &\mathcal{O}(h^4)\sin\beta = \\ &\Big| n_2 \Big(n_1^{(1)}(n_4^{(2)} n_2^{(3)} - n_2^{(2)} n_4^{(3)}) + \\ &n_1^{(2)}(n_4^{(3)} n_2^{(1)} - n_2^{(1)} n_4^{(3)}) + \\ &n_1^{(3)}(n_4^{(1)} n_2^{(2)} - n_2^{(2)} n_4^{(1)}) \Big) \Big| = \\ &\left| n_2 \left(\mathcal{O}(h)\mathcal{O}(h^3) + \mathcal{O}(h)\mathcal{O}(h^3) + \mathcal{O}(h^2)(\mathcal{O}(h^2) + \mathcal{O}(h^2)) \right) \right| \\ &= \left| \left[\mathcal{O}(h^5), \mathcal{O}(h^5), 0\right] \right|, \end{aligned}$$

which render in $\beta = \mathcal{O}(h)$. By referring to Figure 4.9 and expression (4.25), we have

$$\Delta_2 = \mathcal{O}(h^2)\mathcal{O}(h) = \mathcal{O}(h^3),$$

then we also realize by inspection that $\Delta_1 \sim \Delta_2 = \mathcal{O}(h^3)$. □

Corollary 4.3. *By Lemma 4.2 we know that using combinations of the injection and surjection exemplified in Section 4.3.2 will only introduce an $\mathcal{O}(h^3)$-error in the position and direction.*

Consider the bottom of Figure 4.8 then we have for later reference:

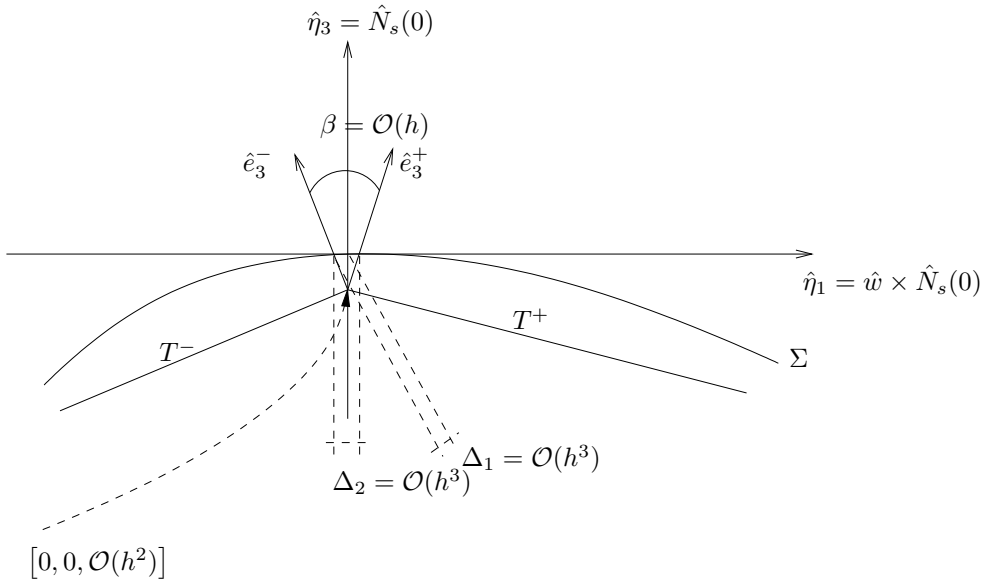

Figure 4.9: η-system showing how the maximum error of $|\partial\Omega_T - \partial\hat{\Omega}_T|$ can be bounded by $\mathcal{O}(h^3)$. By inspection we see that Δ_1 in Lemma 4.2 is proportional to the $\mathcal{O}(h^3)$-distance indicated in the figure. Note that $\hat{\eta}_2$ has been chosen such that it is parallel to the common edge.

Corollary 4.4. *By Lemma 4.2 we know that $\beta = \mathcal{O}(h)$ then, by the assumption in the introduction to Section 4.3.3, both $a \geq \mathcal{O}(h)$ and $c \geq \mathcal{O}(h)$ hence $b = \mathcal{O}(h^2)$. We then have since both $a > 0$ and $c > 0$*

$$(c-a)(c+a) = b^2 = \mathcal{O}(h^4),$$

and that $c - a = \mathcal{O}(h^3)$.

Let us consider the local error for a move in one triangle if the error in initial data in phase space is zero. Rotate the coordinate system defined in (4.22) to be in accordance with Figure 4.4 and let $[p, q] \to \xi$ in (4.1). We then define y as

$$y(s) = [\xi_1(s), \xi_2(s), \alpha(s)]\,,$$

for the marker position in phase space, and

$$x(s) = [x_1(\xi), x_2(\xi), x_3(\xi)]\,(s) \in \Sigma,$$

for the marker position on the sub-manifold Σ of $\mathbb{R}^3$. Since we only consider the local error in one triangle, c.f. figure 4.4, we assume that h has been chosen small enough so that locally

$$x(s) = x_1 + \xi_1(s)\hat{e}_1 + \xi_2(s)\hat{e}_2 + f(\xi(s))\hat{e}_3,$$

where we have dropped j in definition (4.22). Then

$$\frac{\partial y}{\partial s} = G^s(y)$$

and

$$G^s(\xi_1, \xi_2, \alpha) = \begin{pmatrix} \cos\alpha(s) \\ \sin\alpha(s) \\ -\Gamma^1_{ij}\dot{\xi}_i\dot{\xi}_j \sin\alpha(s) + \Gamma^2_{ij}\dot{\xi}_i\dot{\xi}_j \cos\alpha(s) \end{pmatrix}, \tag{4.37}$$

where s is the arc length parameterization in (ξ_1, ξ_2)-space, $\dot{\xi}_1 = \cos\alpha$ and $\dot{\xi}_2 = \sin\alpha$. Formally we may now write for $X(s) = [x(s), \dot{x}(s)]$

$$\dot{X} = H(X), \tag{4.38}$$

where we will assume that H is Lipschitz continuous for all arguments with

$$\Lambda := \{X = [x, \dot{x}] : x \in \bigcup_{j=1}^{N_\Sigma} T_\Sigma^{(j)}, \left(\frac{\partial\Sigma}{\partial\xi_1}, \frac{\partial\Sigma}{\partial\xi_2}, -1\right) \cdot \dot{x} = 0\},$$

where $x(s)$ is geodesic.

Once again if we choose our coordinate system properly and consider (4.37) for sufficiently small s then we can choose ξ_1 as a parameter for the geodesic. Then we have

$$G^\xi(\xi_1, \xi_2, \alpha) = \begin{pmatrix} 1 \\ \tan\alpha(\xi_1) \\ \frac{\Gamma_1^{22}\tan^3(\alpha) + (2\Gamma_1^{12} - \Gamma_2^{22})\tan^2(\alpha) + (\Gamma_1^{11} - 2\Gamma_2^{12})\tan(\alpha) - \Gamma_{11}^2}{1+\tan^2(\alpha)} \end{pmatrix}. \tag{4.39}$$

The Christoffel symbol are functions of ξ and α and may be written explicitly as

$$\begin{array}{rcl} \Gamma^1_{11} & = & \frac{CA_{,1} - 2BB_{,1} + BA_{,2}}{2(AC - B^2)} \\ \Gamma^1_{12} & = & \Gamma^1_{21} = \frac{CA_{,2} - BC_{,1}}{2(AC - B^2)} \\ \Gamma^1_{22} & = & \frac{2CB_{,2} - CC_{,1} - BC_{,2}}{2(AC - B^2)} \\ \Gamma^2_{11} & = & \frac{2AB_{,1} - AA_{,2} - BA_{,1}}{2(AC - B^2)} \\ \Gamma^2_{12} & = & \Gamma^2_{21} = \frac{AC_{,1} - BA_{,2}}{2(AC - B^2)} \\ \Gamma^2_{22} & = & \frac{AC_{,2} - 2BB_{,2} + BC_{,1}}{2(AC - B^2)}, \end{array} \tag{4.40}$$

where $A = x_{,1} \cdot x_{,1}$, $B = x_{,1} \cdot x_{,2}$, $C = x_{,2} \cdot x_{,2}$ and we used Einstein notation

$$\frac{\partial f}{\partial \xi_j} \to f_{,j}.$$

In the order of accuracy proofs below we will refer to a well known convergence theorem in numerical analysis for ODEs. To be able to state this fundamental theorem we define a discrete evolution operator Ψ and an increment function ψ as follows.

Definition 4.5. Let the continuous interval $[t_0, T]$ be divided by the $n+1$ discrete one dimensional points

$$t_0 < t_1 < \ldots < t_n = T.$$

These points form a mesh $\Delta = t_0, t_1, \ldots, t_n$ on $[t_0, T]$ with $\tau_p = t_{p+1} - t_p$. Call the state variable X, then the *discrete evolution operator* Ψ is defined by

$$X_\Delta(t_{p+1}) = \Psi^{t_{p+1},t_p} X_\Delta(t_p)$$

and the *increment function* $\psi(\cdot)$ as

$$\Psi^{t_{p+1},t_p} X_\Delta(t_p) = X + \tau\psi(t, X, \tau).$$

We here state as a proposition a version of a fundamental convergence theorem for ODEs given in [47].

Proposition 4.6. *Let Ψ be a given discrete evolution for which the increment function ψ is locally Lipschitz continuous with respect to the state variables. Assume further that along some trajectory $X \in C^1([t_0, T], \mathbb{R}^n)$ the consistency error of the numerical scheme satisfies*

$$X(t+\tau) - \Psi^{t+\tau} X(t) = \mathcal{O}(\tau^{k+1}).$$

Then for any mesh with sufficiently small τ, the discrete evolution Ψ defines a numerical approximation X_k defined in t_p with $p = 1, \ldots, n$ and with initial value $X_0(t_0) = X(t_0)$. This numerical approximation converges with order k to the trajectory X.

Remark that X is a vector. That is, if we have a local error of $\mathcal{O}(\tau^2)$ for element $X^{(j)}$ then we must assume that the global error in all elements in X is of $\mathcal{O}(\tau)$.

As stated previously will the update given in expression (4.30) not be analyzed here but we will just show some numerical results in the end of the chapter. Instead we will analyze the method implied by Update 4.1 and update (4.33). We therefore define the two numerical methods according to below.

Method 4.7. *Let $X_0 = (x_0, \dot{x}_0)$ be initial condition for (4.38). Map $X_0 \to y_0$ to the facetized geometry by using the surjective map given in Section 4.3.2. Update ξ and α according to Update 4.1 and update (4.30) consecutively with y_0 as initial data. Stop when stopping criteria has been fulfilled. Referring to Update 4.1 estimate the arclength with*

$$t \approx \sum_{j=1}^{n} \Delta s_j. \tag{4.41}$$

Method 4.8. *As in Method 4.8 but Update (4.30) replaced by (4.33).*

Remark that we can in principle map $y^n \to X_n$ according to the injection given in Section 4.3.2. However we will not assume this in the analysis below.

To be able to estimate the global convergence error, we will first analyze, mainly for pedagogical reasons, the local truncation error for the position and direction in one triangle, i.e. Update 4.1. In a second step we will analyze the error over two triangles to take into account angle updates, i.e. the compound update given by Update 4.1 and update (4.33). Finally we multiply this error with the number of edges that the geodesic cross, i.e. $\mathcal{O}(h^{-1})$, to get the convergence error of the numerical method given in Method 4.8.

Proposition 4.9. *Update ξ and α according to Update 4.1 and choose ξ_1 such that*

$$(\xi_1, \xi_2(\xi_1)) \in \Omega_T.$$

Then the local truncation error of ξ_2 and α are of $\mathcal{O}(h^3)$ and $\mathcal{O}(h^2)$ correspondingly.

Proof. According to expression (4.28) and (4.29), and by inspection of Γ^k_{ij}, we have that

$$\Gamma^k_{ij} \leq \mathcal{O}(h). \tag{4.42}$$

By rotating the coordinate system defined in (4.22) to be in accordance with Figure 4.4 we have $\alpha(0) = 0$ and since all terms in G^s but the Γ^2_{11}-term contain at least one sin-factor we realize that the Γ^2_{11}-term is the dominant one for the $\dot{\alpha}$-equation. For the ξ_1-parameterization we get more explicitly for sufficiently small h that

$$\dot{\alpha} = -\Gamma^2_{11} \cos^2 \alpha + \mathcal{O}(h^2) \tag{4.43}$$

or

$$\dot{\alpha} = -\frac{f_{,1,1} f_{,2}}{1 + f_{,1}^2 + f_{,2}^2} \cos^2 \alpha + \mathcal{O}(h^2) \overset{\text{Taylor}}{=} -f_{,1,1} f_{,2} \cos^2 \alpha + \mathcal{O}(h^2). \tag{4.44}$$

With initial condition $\alpha(0) = 0$ we can solve (4.44) and get $\alpha(\xi_1) = -\arctan(f_{,1,1} f_{,2} \xi_1)$. By Taylor expansion we therefore have

$$\alpha(\xi_1) = \mathcal{O}(h^2), \tag{4.45}$$

since ξ_1 is bounded by h and $f_{,2} = \mathcal{O}(h)$. For ξ_2 we have

$$\dot{\xi}_2 = \tan \alpha(\xi_1) \overset{\text{Taylor}}{=} \mathcal{O}(h^2)$$

and therefore

$$\xi_2 \leq \xi_1 \mathcal{O}(h^2) = \mathcal{O}(h^3).$$

□

To make use of the properties of coordinate system introduced for a pair of triangles we will show the following lemma.

Lemma 4.10. *The derivatives $f^{(0)}_{,1}$ and $f^{(0)}_{,2}$ in the origin of the coordinate system defined in figure 4.8 is bounded by $\mathcal{O}(h^2)$.*

Proof. The interpolated surface normal is by construction

$$N_s(\chi) = (0, 0, 1),$$

in the χ-system. Since we assume that the normal is computed by an $\mathcal{O}(h^2)$ interpolation of

$$\frac{\frac{\partial}{\partial\chi_1}(\chi_1, \chi_2, f(\chi_1, \chi_2)) \times \frac{\partial}{\partial\chi_2}(\chi_1, \chi_2, f(\chi_1, \chi_2))}{\left|\frac{\partial}{\partial\chi_1}(\chi_1, \chi_2, f(\chi_1, \chi_2)) \times \frac{\partial}{\partial\chi_2}(\chi_1, \chi_2, f(\chi_1, \chi_2))\right|} = \frac{(-f_{,1}, -f_{,2}, 1)}{\sqrt{f^2_{,1} + f^2_{,2} + 1}}, \tag{4.46}$$

we realize by Taylor expansion that $f^{(0)}_{,1} = \mathcal{O}(h^2)$ and $f^{(0)}_{,2} = \mathcal{O}(h^2)$ in the origin. □

We now want to prove that in the very specific coordinate system defined in figure 4.8 the angle γ will be unaffected by update (4.33).

Lemma 4.11. *Let*

$$\gamma^{-|+} = \arccos\left(NP\left[(\cos\alpha(T^{-|+}), \sin\alpha(T^{-|+}))\right] \cdot \hat{\chi}_1^{-|+}\right)$$

and $NP[\cdot]$ the projection and normalization of the approximate tangent onto the $\hat{\chi}_1\hat{\chi}_2$-plane. If α is updated according to update (4.33) and if $(\chi_1, \chi_2(\chi_1)) \in \hat{\Omega}_{TP}$ then

$$\gamma(\chi_1) \equiv 0,$$

as we move the marker along the approximate trajectory from T^- to T^+.

Proof. We want to show that

$$\arccos\left(NP\left[\hat{t}^-\right] \cdot NP\left[\frac{\hat{e}^+_z \times (\hat{t}^- \times \hat{N}_s)}{|\hat{e}^+_z \times (\hat{t}^- \times \hat{N}_s)|}\right]\right) = 0 \tag{4.47}$$

By construction we know that

$$\hat{N}_s = [0, 0, 1]$$

and from Lemma 4.2 ($\beta = \mathcal{O}(h)$) we see, using trigonometry, that

$$\hat{t}^- = \frac{[1, 0, \mathcal{O}(h)]}{\sqrt{1 + \mathcal{O}(h^2)}}.$$

Then

$$\hat{t}^+ = \frac{\hat{e}^+_z \times \frac{[0,1,0]}{\sqrt{1+\mathcal{O}(h^2)}}}{\left|\hat{e}^+_z \times \frac{[0,1,0]}{\sqrt{1+\mathcal{O}(h^2)}}\right|} = \frac{[-\hat{e}^+_z(3), 0, \hat{e}^+_z(1)]}{\left|[-\hat{e}^+_z(3), 0, \hat{e}^+_z(1)]\right|}.$$

and

$$NP\left(\frac{[-\hat{e}_z^+(3),0,\hat{e}_z^+(1)]}{|[-\hat{e}_z^+(3),0,\hat{e}_z^+(1)]|}\right) = N\left(\frac{[-\hat{e}_z^+(3),0]}{|[-\hat{e}_z^+(3),0,\hat{e}_z^+(1)]|}\right) = [1,0]\,.$$

We have now shown (4.47) since $NP[\hat{t}^-] = \hat{\chi}_1 = (1,0)$ by construction. □

We can now prove the following proposition in the χ-coordinate system.

Proposition 4.12. *Update ξ and α according to Update 4.1 and update (4.33), then the leading order error term for γ over a pair of triangles is*

$$\boldsymbol{\gamma}(\boldsymbol{\chi}_1) - \boldsymbol{\gamma}(\boldsymbol{\chi}_1^{(0)}) = \frac{1}{2} f_{,1,2}^{(\boldsymbol{o})} f_{,1,1}^{(\boldsymbol{o})} \left[\left(\boldsymbol{\chi}_1^{(0)}\right)^2 - \boldsymbol{\chi}_1^2\right], \tag{4.48}$$

where $\boldsymbol{\chi}_1^{(0)}$ is defined according to figure 4.8 and $f_{,i,j}^{(\boldsymbol{o})}$ are second order derivatives of the surface in the origin. The error is of $\mathcal{O}(h^2)$.

Proof. Let us drop the boldface for the exact solution and Taylor expand, c.f. Proposition 4.9, the dominating term on the right hand side of

$$\dot{\gamma} = -\Gamma_{11}^2 \cos^2\gamma + \mathcal{O}(h^2), \tag{4.49}$$

around the origin. We then get

$$\begin{aligned}\dot{\gamma} &= -\cos^2\gamma \left[f_{,1,1}^{(o)} + \chi_1 f_{,1,1,1}^{(o)} + \chi_2 f_{,1,1,2}^{(o)}\right] \\ &\cdot \left[2f_{,2}^{(o)} + 2\chi_1 f_{,1,2}^{(o)} + 2f_{,2,2}^{(o)}\chi_2 + \chi_1^2 f_{,1,1,2}^{(o)} 2\chi_1\chi_2 f_{,1,2,2}^{(o)} + \chi_2^2 f_{,2,2,2}^{(o)}\right] \\ &+ \mathcal{O}(h^2).\end{aligned} \tag{4.50}$$

The leading order term is $-2f_{,1,1}^{(o)}\chi_1 f_{,1,2}^{(o)}$ since

$$f_{,j} = \mathcal{O}(h) \Rightarrow \chi_2 = \mathcal{O}(h^3),$$

because of Proposition 4.9 and

$$f_{,j}^{(o)} = \mathcal{O}(h^2), \tag{4.51}$$

according to Lemma 4.10. That is, we have that

$$\dot{\gamma} = -2f_{,1,1}^{(o)}\chi_1 f_{,1,2}^{(o)} \cos^2\gamma + \mathcal{O}(h^2), \tag{4.52}$$

which can be solved and

$$\gamma(\chi_1) = -\arctan\left(f_{,1,1}^{(o)} f_{,1,2}^{(o)} \chi_1^2 - f_{,1,1}^{(o)} f_{,1,2}^{(o)} \left(\chi_1^{(0)}\right)^2\right) + \mathcal{O}(h^3). \tag{4.53}$$

Taylor expanding once more and using Lemma 4.11 we get (4.48). □

Solving for χ_2 in $\dot{\chi}_2 = \tan\gamma(\chi_1)$ we get

$$\chi_2(\chi_1) = -\frac{1}{3}f^{(o)}_{,1,1}f^{(o)}_{,1,2}\chi_1^3 + \left(\chi_1^{(0)}\right)^2 f^{(o)}_{,1,1}f^{(o)}_{,1,2}\chi_1 - \frac{2}{3}f^{(o)}_{,1,1}f^{(o)}_{,1,2}\left(\chi_1^{(0)}\right)^3 + \mathcal{O}(h^4). \quad (4.54)$$

We have tried to illustrate the polynomial behavior of $\chi_2(\chi_1)$ in Figure 4.8 and by inspection of (4.48) we directly realize

Corollary 4.13. *The local error in γ is of $\mathcal{O}(h^3)$ at $|\chi_1| = \chi_1^{(0)}$.*

The surface curvature sensitive mesh, for a specific geometry, is not uniquely defined from the discussion in Section 4.3.1. By inspection of the corresponding curvature sensitive mesh of a one dimensional function and the coordinate system illustrated in Figure 4.8 one realize that the following demands on the mesh elements is not unrealistic.

1. The meshing algorithm should try to make the elements as big as possible without violating a given mesh error parameter.

2. The triangles size relative to their neighbors, is not allowed to differ too much in terms of element size.

A curvature sensitive mesh of a one dimensional function will then be unique if either demand 1 or a combination of demand 1 and 2 are chosen while a surface curvature sensitive mesh needs to be further defined to become unique. With these reflections in mind we state the following.

Consider the bottom of Figure 4.8. If the triangles has been produced with a mesh algorithm that bound the difference in size according to

$$a^2 - e^2 = (a-e)(a+e) \leq \mathcal{O}(h)(c_1 h - (c_1 h + c_1 h\mathcal{O}(h))) = \mathcal{O}(h^3), \quad (4.55)$$

then the local error in γ is of $\mathcal{O}(h^3)$.

A proof of that the error in γ is of $\mathcal{O}(h^3)$ would consist in showing that if (4.55) holds, it will render in, that the same holds for χ in mean. That is, we know that the length of the segments does not directly depend on the size of the triangles and it is therefore not straight forward to achieve

$$|\xi(j) - \xi(j-1)|^2 - |\xi(j+1) - \xi(j)|^2 \approx \left(\chi_1^{(0)}\right)^2 - \chi_1^2 = \mathcal{O}(h^3).$$

However, if we manage to show this we get $\mathcal{O}(h^2)$-convergence globally.

Remark that it would probably be more complicated to show a proposition similar to Proposition 4.12 for update (4.30). We need to show that Σ in the corresponding coordinate system χ', which would produce a $\gamma' = 0$ for update (4.30), have derivatives in the origin that fulfills Lemma 4.10. The coordinate system we would search, i.e. $(\hat{\chi}'_1, \hat{\chi}'_2, \hat{\chi}'_3)$ solves the nonlinear problem

$$\begin{cases} P_{\hat{\chi}'_3}\left[\hat{t}^-\right] \times P_{\hat{\chi}'_3}\left[\hat{t}^+\right] = \left(\hat{t}^- - \hat{\chi}'_3(\hat{\chi}'_3 \cdot \hat{t}^-)\right) \times \left(\hat{t}^+ - \hat{\chi}'_3(\hat{\chi}'_3 \cdot \hat{t}^+)\right) = 0 \\ \left(\hat{t}^{-|+} - \hat{\chi}'_3(\hat{\chi}'_3 \cdot \hat{t}^{-|+})\right) \cdot \chi'_2 = 0 \\ \hat{\chi}'_2 \times \hat{\chi}'_3 = \hat{\chi}'_1 \\ \hat{N}_\Sigma(0,0) \times \hat{\chi}'_3 \leq \mathcal{O}(h^2), \end{cases} \quad (4.56)$$

where $\hat{t}^+$ is found with update (4.30), $P_{\hat{\chi}_3'}$ is the projection down to the $\hat{\chi}_1'\hat{\chi}_2'$-plane and $N_\Sigma(0,0)$ is the surface normal of Σ in the origin of the χ'-system. That is, we would need to show that (4.56) has a solution for sufficiently smooth surfaces.

To be able to show global order of convergence we need some further definitions and lemmas.

We will later compute the difference between the exact geodesic and the so called *interpolant* of the numerical solution. In contrast to the numerical solution, which is only defined in mesh points, is the interpolant a curve on Σ. We let the interpolant be a union of curve segments, where each curve segment is given by an orthogonal projection, along $\hat{\chi}_3$, of the numerical solution $[\chi_1, \chi_2]$ onto Σ. We realize that the union of curve segments implied by Figure 4.8 and 4.10 are not connected. However, one see by inspection, that it is possible fill out the gaps with even smaller curve segments, of $\mathcal{O}(h^3)$ length, such that the final interpolant has a continuous derivative. The important information that we will bring with us to the global convergence proof though, is that their length is only of $\mathcal{O}(h^3)$.

Instead of using the points $\xi(j)$ for $j = 1, \dots, n$, implied by Update 4.1, we will investigate convergence rate at the following *mesh points*.

Let $\boldsymbol{X}(\boldsymbol{t}) = (\boldsymbol{x}(\boldsymbol{t}), \dot{\boldsymbol{x}}(\boldsymbol{t})) \in \Lambda$ be the exact solution, where $\boldsymbol{t}$ is the arc length parameterization. Let $X(t) = (x(t), \dot{x}(t)) \in \Lambda$ be the interpolant of the numerical solution computed by applying Method 4.8 and projection according to Figure 4.8. Referring to Figure 4.10 pick a δ so that the maps

$$(\delta\xi(j) + (1-\delta)\xi(j+1)) \leftrightarrow \chi(j+\delta) \leftrightarrow x(j+\delta)$$

can be done orthogonally along $\hat{\chi}_1 \times \hat{\chi}_2$ without introducing an error, i.e. we avoid the domain close to the triangle edges where orthogonal projection is not a bijection. For notational simplicity $j+\delta$ will indicate an index somewhere between j and $j+1$ though it will be considered as an integer index. In a second step find the exact δ, for a well chosen $t(j+\delta)$, by solving

$$\min_\delta |x(j+\delta) - \boldsymbol{x}(t(j+\delta))| .$$

The interpolant of the numerical solution

$$X(j+\delta) = [x(j+\delta), \dot{x}(j+\delta)] ,$$

then approximate the exact solution in the mesh points

$$\{t(\delta), t(1+\delta), \dots, t(n-\delta)\}. \tag{4.57}$$

Lemma 4.14. *Compute the approximate arc length in the ξ- and the χ-system as*

$$t_\xi^{(j+1)} = t_\xi^{(j)} + |\xi(j+1) - \xi(j)| \tag{4.58}$$

and

$$t_\chi^{(j+1+\delta)} = t_\chi^{j+\delta} + |\chi(j+1+\delta) - \chi(j+\delta)|. \tag{4.59}$$

The local error in arc length in the mesh points is then bounded by $\mathcal{O}(h^3)$.

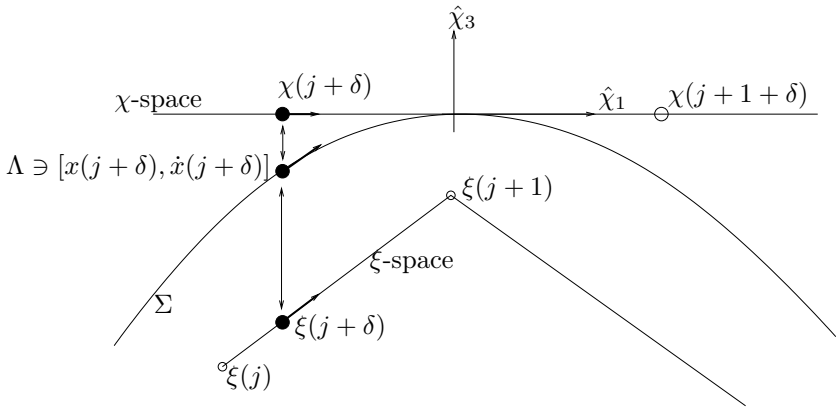

Figure 4.10: Mapping between three different spaces where $\xi(j)$, $j = 1, \ldots, n$ is computed with the numerical scheme given in Method 4.8. Note that the mapping is done along the χ_3-axis.

Proof. The arc length $\boldsymbol{t}$ of $\boldsymbol{x}(\boldsymbol{t})$ can be given as a function of $\boldsymbol{\chi}_1$ by

$$\boldsymbol{t}(\boldsymbol{\chi}(\delta+1)) = \int_{\boldsymbol{\chi}_1(\delta)}^{\boldsymbol{\chi}_1(\delta+1)} |\dot{\boldsymbol{x}}|\, d\boldsymbol{\chi}_1 = \int_{\boldsymbol{\chi}_1(\delta)}^{\boldsymbol{\chi}_1(\delta+1)} \sqrt{1+\tan^2\boldsymbol{\gamma} + (f_{,1} + f_{,2}\tan\boldsymbol{\gamma})^2}\, d\boldsymbol{\chi}_1$$

where we used (4.39) applied in the χ-system. By Lemma 4.10 and Proposition 4.12 we have that

$$\boldsymbol{t}(\boldsymbol{\chi}(\delta+1)) = \int_{\boldsymbol{\chi}_1(\delta)}^{\boldsymbol{\chi}_1(\delta+1)} \sqrt{1+\mathcal{O}(h^2)}\, d\boldsymbol{\chi}_1 = (\boldsymbol{\chi}_1(\delta+1) - \boldsymbol{\chi}_1(\delta)) + \mathcal{O}(h^3).$$

For similar reasons and Lemma 4.2 we also have that

$$\boldsymbol{t}(\boldsymbol{\xi}(1)) = \int_{\boldsymbol{\xi}_1(0)}^{\boldsymbol{\xi}_1(1)} \sqrt{1+\mathcal{O}(h^2)}\, d\boldsymbol{\xi}_1 = (\boldsymbol{\xi}_1(1) - \boldsymbol{\xi}_1(0)) + \mathcal{O}(h^3),$$

which also can be applied to the point $\xi(\delta)$. □

Proposition 4.15. *Assume that H in expression (4.38) fulfill a Lipschitz condition and let $\mathcal{T}$ assign the triangular mesh and $\mathcal{G}$ the surface geometry. We formally define the increment function ψ_χ as a function to be used in the following iterative scheme,*

$$X(t(j+\delta+1)) = X(t(j+\delta)) + |t(j+\delta+1) - t(j+\delta)|\, \psi_\chi(\mathcal{T}, \mathcal{G}, X(t(j+\delta)), t(j+\delta))$$

to achieve the approximate values in the mesh points defined in (4.57). The increment function is Lipschitz continuous in the state variables X and t.

We do not state a formal proof here but just note the following. The tangential plane in Figure 4.8 is based on surface normals achieved from a second order interpolation scheme and the surface is assumed to be sufficiently smooth. The interpolated normal is therefore Lipschitz continuous and by inspection we see that the operations we do in update (4.1), which we investigated in Lemma 4.11, are Lipschitz in the state variables X and t. The increment function is therefore Lipschitz continuous.

We believe that it is a little more complicated, if possible, to investigate the scheme based on update (4.30).

We have now reached the point where we are able to show the global convergence rate. The proof will be partly based on Proposition 4.15 which imply, c.f. Proposition 4.6, that it is sufficient to consider the local error when we search the global error.

Theorem 4.16. *Solve the ODE in (4.38) numerically up to a point $\boldsymbol{t}(n)$ by initializing and updating ξ and α according to Method 4.8. Let $o(j-\delta)$ be the origin for the coordinate system $(\hat{\chi}_1^{j-\delta}, \hat{\chi}_2^{j-\delta})$ defined in Figure 4.8. Let $o(j)$ be the origin for the $\hat{\xi}_1^j\hat{\xi}_2^j$-system. Then*

$$\left|\boldsymbol{x}(\boldsymbol{t}(n-\delta)) - \hat{\chi}_1^{n-\delta}\chi_1(n-\delta) - \hat{\chi}_2^{n-\delta}\chi_2(n-\delta) - o(n-\delta)\right| \leq \mathcal{O}(h), \tag{4.60}$$

$$\left|\dot{\boldsymbol{x}}(\boldsymbol{t}(n-\delta)) - \hat{\chi}_1^{n-\delta}\right| \leq \mathcal{O}(h). \tag{4.61}$$

We also have

$$\left|\boldsymbol{x}(\boldsymbol{t}(n)) - \xi_1(n)\hat{\xi}_1^n - \xi_2(n)\hat{\xi}_2^n - o(n)\right| \leq \mathcal{O}(h), \tag{4.62}$$

$$\left|\dot{\boldsymbol{x}}(\boldsymbol{t}(n)) - \hat{\xi}_1^n\right| \leq \mathcal{O}(h) \tag{4.63}$$

and

$$\left|\boldsymbol{t}(n) - \sum_{j=0}^{n}|\xi(j+1) - \xi(j)|\right| \leq \mathcal{O}(h). \tag{4.64}$$

Proof. We do the proof in three steps. We analyze the *initial* error when projecting down from Σ to χ-space, in a second step the *local* truncation error as we propagate the interpolant and finally the *final* error when we project once more the interpolant from Σ- to χ- and ξ-space.

By using a surjection for the initial condition the error in the initial condition for $x(0)$ will be bounded by $\mathcal{O}(h^3)$ because of Corollary 4.3. The error in $\dot{x}(0)$ is zero if we compute the tangent by an orthogonal projection down to ξ-space. Hence, we have an initial condition for the numerical scheme.

The bound on the global error of position x and direction $\dot{x}$ is by Proposition 4.6 and 4.15 given by the largest local error times the number of iteration steps. Hence we need to find the local error in position and direction. By Proposition 4.12,

Lemma 4.14 and some trigonometry the local error in *position* of the interpolant, in a mesh point defined according to (4.57), is bounded according to

$$\begin{aligned}\Delta x(t(\delta)) &= |\boldsymbol{x}(t(\delta+1)) - x(t(\delta+1))| \overset{\text{Pythagoras}}{=} \\ &\sqrt{(\mathcal{O}(h^3))^2 + (f(\boldsymbol{\chi}_1(\delta), \boldsymbol{\chi}_2(\boldsymbol{\chi}_1(\delta))) - f(\boldsymbol{\chi}_1(\delta), \chi_2(\boldsymbol{\chi}_1(\delta))))^2} \overset{\text{Taylor}}{=} \mathcal{O}(h^3),\end{aligned} \tag{4.65}$$

where the first square corresponds to the error in χ-space and the second square correspond to error in height and finally the last equality can be shown by Taylor expanding f at (χ_1, χ_2) and once more using Proposition 4.12 and Lemma 4.14.

To be able to compute the direction of the geodesic in mesh points, we need the surface tangent along the parameter space direction $\dot{\chi} = (\cos\gamma, \sin\gamma)$. The normalized surface tangent is

$$\hat{\dot{x}}(\chi, \gamma) = \frac{\frac{\partial}{\partial \chi_1}[\chi_1, \chi_2, f(\chi_1, \chi_2)]}{\left|\frac{\partial}{\partial \chi_1}[\chi_1, \chi_2, f(\chi_1, \chi_2)]\right|}.$$

Now we search

$$\Delta\hat{\dot{x}}(t(\delta+1)) = |\hat{\dot{\boldsymbol{x}}}(\boldsymbol{t}(\delta+1)) - \hat{\dot{x}}(\boldsymbol{t}(\delta+1))|.$$

We can Taylor expand $\hat{\dot{\boldsymbol{x}}}(\boldsymbol{\chi}_1)$ and $\hat{\dot{x}}(\boldsymbol{\chi}_1)$ around $o(\delta)$ and make use of Proposition 4.12, Lemma 4.14 and Lemma 4.10 to get

$$\hat{\dot{x}}(\boldsymbol{\chi}_1) = \frac{\left[1, \mathcal{O}(h^2), f_{,1}|_o + f_{,1,1}|_o\boldsymbol{\chi}_1 + \frac{1}{2}f_{,1,1,1}|_o\boldsymbol{\chi}_1^2 + \mathcal{O}(h^3)\right]}{\sqrt{1 + (f_{,1}|_o + f_{,1,1}|_o\boldsymbol{\chi}_1)^2 + \mathcal{O}(h^3)}}. \tag{4.66}$$

and

$$\hat{\dot{x}}(\boldsymbol{\chi}_1) = \frac{\left[1, 0, f_{,1}|_o + f_{,1,1}|_o\boldsymbol{\chi}_1 + \frac{1}{2}f_{,1,1,1}|_o\boldsymbol{\chi}_1^2 + \mathcal{O}(h^3)\right]}{\sqrt{1 + (f_{,1}|_o + f_{,1,1}|_o\boldsymbol{\chi}_1)^2 + \mathcal{O}(h^3)}}.$$

Most of the terms will cancel in $\Delta\hat{\dot{x}}$ and we get, by Lemma 4.14, that the local error in the *direction* variable is

$$\Delta\hat{\dot{x}} = \| \left[\mathcal{O}(h^3), \mathcal{O}(h^2), \mathcal{O}(h^3)\right] \| = \mathcal{O}(h^2). \tag{4.67}$$

Hence, the local maximum error, as suspected from Proposition 4.9 and 4.12 spring from the numerical approximation of the direction updates in Method 4.8.

By Proposition 4.6 we get that the global order of convergence is

$$\begin{aligned}&\|\boldsymbol{X}_{n-\delta}(1:3) - \hat{\chi}_1^{n-\delta}\chi_1(n-\delta) - \hat{\chi}_2^{n-\delta}\chi_2(n-\delta) - o(n-\delta) + \\ &\boldsymbol{X}_{n-\delta}(4:6) - \hat{\chi}_1^{n-\delta}\|^2 \\ &\leq \underbrace{\mathcal{O}(h^3)}_{\text{Init. Pos.}} + \underbrace{0}_{\text{Init. Dir.}} + \underbrace{\mathcal{O}(\frac{1}{h})\max(\mathcal{O}(h^2), \mathcal{O}(h^3))}_{\text{Local Error}} = \mathcal{O}(h)\end{aligned} \tag{4.68}$$

We must add the error at the final step (c.f. (4.60)) when we let

$$\boldsymbol{x}(n-\delta) \approx \hat{\chi}_1^{n-\delta}\chi_1(n-\delta) + \hat{\chi}_2^{n-\delta}\chi_2(n-\delta) + o(n-\delta),$$

and (c.f. (4.61))

$$\dot{\boldsymbol{x}}(n-\delta) \approx \hat{\chi}_1^{n-\delta}.$$

By Taylor expansion and Lemma 4.10 the orthogonal projection of $\boldsymbol{x}$ down to χ-space is bounded by $\mathcal{O}(h^2)$. Then by Pythagoras' theorem and (4.68) we get that

$$\|\boldsymbol{x}(n-\delta)-\hat{\chi}_1^{n-\delta}\chi_1(n-\delta)+\hat{\chi}_2^{n-\delta}\chi_2(n-\delta)+o(n-\delta)\| = \sqrt{\left(\mathcal{O}(h)\right)^2+\left(\mathcal{O}(h^2)\right)^2} \leq \mathcal{O}(h),$$

and (4.60) follows. With similar motivation as in (4.66) and Pythagoras' theorem we get that

$$\|\dot{\boldsymbol{x}}(n-\delta) - \hat{\chi}_1^{n-\delta}\| = \mathcal{O}(h),$$

and (4.61) follows.

(4.62) and (4.63) follows easily because of Proposition 4.9 and that naturally

$$\arccos\left(\hat{\xi}_3^n \cdot \hat{\chi}_3^{n-\delta}\right) = \mathcal{O}(h),$$

since expression (4.35) holds

The arc length can be found by solving

$$\dot{t} = \sqrt{1+\tan^2\gamma+\left(f_{,1}+f_{,2}\tan\gamma\right)^2},$$

between two mesh points in the associated coordinate system. Solving from

$$\chi^{(0)} = \left[\chi_1^{(0)}, 0\right],$$

with $t^{(0)} = 0$ we get since, $\tan\gamma = \mathcal{O}(h^2)$ and $f_{,1} + f_{,2}\tan\gamma = \mathcal{O}(h)$, that

$$t = |\chi_1 - \chi_1^{(0)}| + \mathcal{O}(h^3).$$

By Corollary 4.3 and 4.4 we also get

$$\Delta t(0) = \int_{x(0)}^{x(1)} |\dot{x}|\, d\xi_1 = |\xi(1)-\xi(0)| + \mathcal{O}(h^3). \tag{4.69}$$

Hence, the global error of the arc length computation is given by Proposition 4.12 because of Proposition 4.6 and the subsequent remark. Therefore bound (4.62) will follow. □

Referring to the discussion concerning expression (1.27) in the introduction we get that the numerical error contribution to (4.14), that stems from the approximation of expression (4.16), will be of

$$\mathcal{O}(h^{\gamma-1}) = \mathcal{O}(h^{2-1}) = \mathcal{O}(h^1). \tag{4.70}$$

4.3.4 Solution to Transport Equation

4.3.4.1 Exponential Attenuation

Let us discuss the numerical approximation in factor (4.17). We are tempted to compute this factor by just applying the existing GTD formulas for the edge diffraction in the facetized geometry. This would correspond to the attempt in expression (4.30) which make the approximate geodesic an exact geodesic on the facetized geometry. However we will dismiss this idea by the following illustrations.

In Keller's edge diffraction coefficients for hard/soft components and oblique incidence, c.f. [8], $E_{scatt}^{\mathcal{S},\mathcal{H}}$ is

$$-E_{inc}^{\mathcal{S},\mathcal{H}}\frac{e^{-i\pi/4}\sin\left(\frac{\pi}{1+\frac{\beta}{\pi}}\right)}{\left(1+\frac{\beta}{\pi}\right)\sqrt{2\pi k}}\left(\frac{1}{\cos\frac{\pi}{\left(1+\frac{\beta}{\pi}\right)}-\cos\frac{\phi-\phi'}{\left(1+\frac{\beta}{\pi}\right)}}\mp\frac{1}{\cos\frac{\pi}{\left(1+\frac{\beta}{\pi}\right)}-\cos\frac{\phi+\phi'}{\left(1+\frac{\beta}{\pi}\right)}}\right), \tag{4.71}$$

where ϕ and ϕ' is defined in Figure 4.11. In the figure we also see that

$$\beta = 2\arcsin\left(\frac{ds}{2\rho_g}\right).$$

We want to check if it is possible to approximate (4.17), with a product of factors similar to (4.71). For the special case when $\phi' = 0$, $\phi = \pi + \beta$ and the problem of a diffracted wave along a half circle according to Figure 4.11, we have for $m = \frac{\pi}{\beta}$ edges,

$$\left(\frac{2e^{-i\pi/4}}{\sqrt{2\pi k}}\frac{\sin\left(\frac{\pi}{1+\frac{\beta}{\pi}}\right)}{\left(1+\frac{\beta}{\pi}\right)\left(\cos\left(\frac{\pi}{1+\frac{\beta}{\pi}}\right)+1\right)}\right)^m \tag{4.72}$$

for the hard component. By inspection we see that this expression is non-uniform in the point $\beta \to 0$. In [48], [49] and [50] more generally applicable coefficients has been developed. However, with our knowledge, uniform coefficients, as $\beta \to 0$, for edges built up by flat faces has not yet been developed. Disregarding the lack of a complete GTD-description of edge diffraction we want to compare (4.72) with smooth surface diffraction. That is we want to compare (4.72) with

$$\left(\exp\left(C_1^{\mathcal{H},1}\beta\left(\frac{k\rho_g}{2}\right)^{1/3}\right)\right)^m, \tag{4.73}$$

where we used expression (4.15) and $dt'\rho_g^{-2/3} = \beta\rho_g^{1/3}$. We would like to show that at least asymptotically, as $\beta \to 0$,

$$\left(\frac{2e^{-i\pi/4}}{\sqrt{2\pi k}}\frac{\sin\left(\frac{\pi}{1+\frac{\beta}{\pi}}\right)}{\left(1+\frac{\beta}{\pi}\right)\left(\cos\left(\frac{\pi}{1+\frac{\beta}{\pi}}\right)+1\right)}\right)-\left(\exp\left(C_1^{\mathcal{H},1}\beta\left(\frac{k\rho_g}{2}\right)^{1/3}\right)\right)\sim\mathcal{O}(\beta^2), \tag{4.74}$$

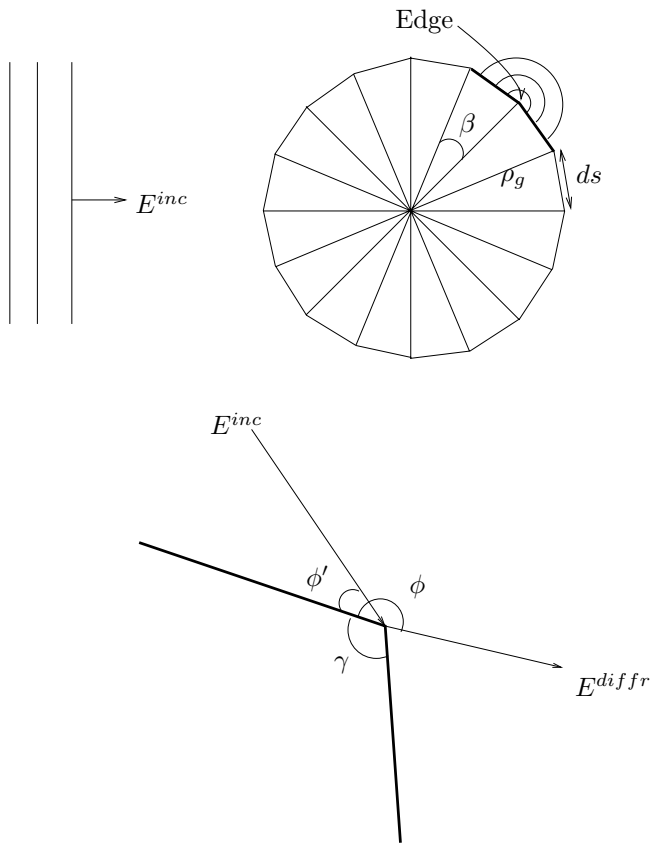

Figure 4.11: Smooth surface diffraction approximated by edge diffraction for a two dimensional circular geometry. That is, no geometrical spreading.

to get a second order scheme. Clearly there is no hope for this since the second term depends on the radius of curvature, ρ_g, in the ray direction and almost by definition there are no radius of curvature in the facetized geometry.

When we consider the two dimensional problem in Figure 4.11 we are also tempted, to be able to compute the radius of curvature approximately, to generalize the following theorem to three dimensions. Let x_i be the mesh points on a two dimensional curve $x(t)$, then we state, which is straight forward to prove, the following proposition:

Proposition 4.17. *An approximation of the radius of curvature ρ_i in a mesh point*

x_i can be computed with

$$Intersection_{\rho_i}\left(x_{i+\frac{1}{2}}+\rho_i\hat{n}_{i+\frac{1}{2}}, x_{i-\frac{1}{2}}-\rho_i\hat{n}_{i-\frac{1}{2}}\right)$$

where $x_{i\pm\frac{1}{2}}=\frac{x_{i\pm1}+x_i}{2}$, $\hat{t}_{i\pm\frac{1}{2}}=\frac{x_i-x_{i\pm1}}{|x_i-x_{i\pm1}|}$ *and* $\hat{n}_{i\pm\frac{1}{2}}=\left[\hat{t}_{i\pm\frac{1}{2}}(2),\hat{t}_{i\pm\frac{1}{2}}(1)\right]$.

However, we search an approximate formula for ρ_g on a meshed geometry along the geodesic. In Proposition 4.17 we have assumed that mesh points coincide with $x(t)$ which does not hold, along the geodesic, in the three dimensional case. C.f. Figure 4.10 for example. One can of course construct better schemes using more triangle nodes, c.f. [12], to compensate for this but it will make the approximation non-local which will be fatal for non-smooth surfaces. I.e. if there are true edges or corners close to the triangle edge e, we will get an $\mathcal{O}(1)$ error in the approximate scheme if there are no a priori knowledge about the discontinuities in the surface derivative in the neighborhood of e.

As can be seen above, it is hard to design a numerical method with a flat triangular mesh. One would need higher order triangular elements or, as in our case, access to some additional information in the triangle nodes. We will therefore analyze the numerical error, i.e. what order of convergence, that can be achieved by using a second order interpolation scheme of the radius of curvatures given in the triangle nodes.

We want to estimate the numerical error we do when we approximate the integral in factor (4.17), that is

$$I(t)=\int_0^t \lambda^{2/3}c^{2/3}(t')C_1^{\mathcal{S},\mathcal{H},p}\,dt', \tag{4.75}$$

where $1/\rho_g=c$. Let us approximate (4.75) with an integral over a straight segment by using the interpolated curvature at the middle of two triangle jumps. As before call the state vector $[x,\dot{x}]\,(t)$ $X(t)$. Let

$$m(X)=\lambda^{2/3}c^{2/3}(X)C_1^{\mathcal{S},\mathcal{H},p},$$

then by change of variables $t\to\xi_1$, c.f. Figure 4.4, we can study (4.75) locally

$$I(\xi_1)=\int_{\xi_0;\alpha_0}^{\xi_1}\lambda^{2/3}c^{2/3}(\xi_1',\xi_2(\xi_1'),\alpha(\xi_1'))C_1^{\mathcal{S},\mathcal{H},p}\frac{\partial t}{\partial\xi_1'}\,d\xi_1'+\mathcal{O}(h^3),$$

where $(\xi_2(\xi_1'),\alpha(\xi_1'))$ is given by the ODE with right hand side according to (4.39). The interchanging of integration limits from X to y-space and Corollary 4.3 motivates the $\mathcal{O}(h^3)$-term. As before we will study the numerical error as we integrate an ODE instead, i.e.

$$\begin{aligned}&\tfrac{\partial}{\partial\xi_1}I=\lambda^{2/3}c^{2/3}(\xi_1,\xi_2(\xi_1),\alpha(\xi_1))C_1^{\mathcal{S},\mathcal{H},p}\tfrac{\partial t}{\partial\xi_1}+\mathcal{O}(h^3)=\\&m(\xi_1,\xi_2(\xi_1),\alpha(\xi_1))+\mathcal{O}(h^2),\end{aligned} \tag{4.76}$$

where we have used Lemma 4.14 to approximate $\partial_{\xi_1} t$ by 1 locally. Since we will try to show local truncation error of $\mathcal{O}(h^3)$ for I the $\mathcal{O}(h^2)$-term will not bother us. If we can estimate $\boldsymbol{I} - I$, where boldface assign the exact solution, the global error estimate will follow by applying Proposition 4.6.

We will first give some formulas from differential geometry that relate the surface curvature to first and second order surface derivatives. Note that we have assumed that second order surface derivatives are of $\mathcal{O}(1)$ in the ξ-system.

According to Euler's theorem [51] we have, with arc length parameterization t, that

$$c(\xi, \alpha) = c_1(\xi)\cos^2(\beta(\xi, \alpha)) + c_2(\xi)\sin^2(\beta(\xi, \alpha)) \tag{4.77}$$

where

$$\beta(\xi, \alpha) = \arccos(\dot{x}(t) \cdot \hat{p}) \tag{4.78}$$

and $\hat{p}$ is the first principal direction defined below. Expression (4.77) can be simplified to

$$c = (\dot{x} \cdot \hat{p})^2(c_1 - c_2) + c_2. \tag{4.79}$$

Let $N_j(\xi)$ be the surface normal in a point ξ then we can define, with Einstein's summation convention,

$$\tilde{A} = x_{j,\xi_1,\xi_1} N_j = x_{j,1,1} N_j,$$
$$\tilde{B} = x_{j,\xi_1,\xi_2} N_j = x_{j,1,2} N_j$$

and

$$\tilde{C} = x_{j,\xi_2,\xi_2} N_j = x_{j,2,2} N_j.$$

According to differential geometry [51]

$$\hat{p} = \frac{\left[1, \frac{\tilde{A}-c_1 A}{c_1 B - \tilde{B}}, f_1 + f_2 \frac{\tilde{A}-c_1 A}{c_1 B - \tilde{B}}\right]}{\sqrt{1 + \left(\frac{\tilde{A}-c_1 A}{c_1 B - \tilde{B}}\right)^2 + \left(f_1 + f_2 \frac{\tilde{A}-c_1 A}{c_1 B - \tilde{B}}\right)^2}} \tag{4.80}$$

where (A, B, C) is defined in (4.40) and c_j are the principal curvatures solving

$$c_j^2 - 2\frac{A\tilde{C} - 2B\tilde{B} + C\tilde{A}}{2(AC - B^2)} c_j + \frac{\tilde{A}\tilde{C} - \tilde{B}}{(AC - B^2)} = 0.$$

Hence we have for the two principal curvatures

$$c_j = \frac{A\tilde{C} - 2B\tilde{B} + C\tilde{A}}{2(AC - B^2)} \pm \sqrt{\left(\frac{A\tilde{C} - 2B\tilde{B} + C\tilde{A}}{2(AC - B^2)}\right)^2 - \frac{\tilde{A}\tilde{C} - \tilde{B}}{(AC - B^2)}}. \tag{4.81}$$

By inspection of c_2 in (4.79) we see that c, and hence m, is not bounded by h. For example, we know that

$$A = 1 + f_{,1}^2 = 1 + \mathcal{O}(h^2),$$

$$B = f_{,1}f_{,2} = \mathcal{O}(h^2),$$

and

$$C = 1 + f_{,2}^2 = 1 + \mathcal{O}(h^2),$$

then the first term in c_2 will be

$$\frac{A\tilde{C}}{2(AC - B^2)} = \frac{1 + \mathcal{O}(h^2)}{2\left((1 + f_{,1}^2)(1 + f_{,2}^2) - (f_{,1}f_{,2})^2\right)} = \frac{f_{,2,2}}{2} + \mathcal{O}(h^2),$$

since

$$\tilde{C} = [0, 0, f_{,2,2}] \cdot \left(\frac{\partial}{\partial \xi_1}[\xi_1, \xi_2, f(\xi_1, \xi_2)] \times \frac{\partial}{\partial \xi_2}[\xi_1, \xi_2, f(\xi_1, \xi_2)]\right) = f_{,2,2}.$$

Hence, (4.79) and therefore also the right hand side of (4.76), is as we suspected of $\mathcal{O}(1)$.

Now we are prepared for the proposition concerning local truncation error for the numerical approximation of equation (4.76).

Proposition 4.18. *Let $c(\xi, \alpha) = c(y)$ be the $\mathcal{O}(h^2)$ interpolated surface curvature in y and*

$$m(y) = \lambda^{2/3} c^{2/3}(y) C_1^{\mathcal{S},\mathcal{H},p}.$$

Choose a coordinate system such that the point $\xi^{(0)} = [0, 0]$ coincide with an edge and such that $\alpha^{(0)} = 0$. Then we have $I(\xi^{(0)}) = I^{(0)} = \mathcal{O}(h^3)$ according to Corollary 4.3. Assume that we use Method 4.8 to compute $\xi^{(1)}$ which coincide with the following edge which the approximate geodesic cross. At $\xi_1 = \mathcal{O}(h)$ we have that the modified midpoint rule

$$I^{(1)} = I^{(0)} + \xi_1 m\left(\frac{\xi_1^{(1)}}{2}, 0, 0\right) = \mathcal{O}(h^2) + \xi_1 m\left(\xi_1^{(1/2)}, 0, 0\right), \tag{4.82}$$

introduce an $\mathcal{O}(h^3)$ local truncation error when used on

$$\frac{\partial}{\partial \boldsymbol{\xi}_1} \boldsymbol{I} = m(\boldsymbol{\xi}_1, \boldsymbol{\xi}_2(\boldsymbol{\xi}_1), \boldsymbol{\alpha}(\boldsymbol{\xi}_1)), \tag{4.83}$$

where

$$\boldsymbol{y} = [\boldsymbol{\xi}_1, \boldsymbol{\xi}_2(\boldsymbol{\xi}_1), \boldsymbol{\alpha}(\boldsymbol{\xi}_1)],$$

is the exact solution.

Proof. Taylor expand $I(\boldsymbol{\xi}_1^{(1)})$ around the origin. We then get by Corollary 4.3

$$I(\boldsymbol{\xi}_1^{(1)}) - I(0) + \mathcal{O}(h^3) = \boldsymbol{\xi}_1^{(1)} \left.\frac{\partial I}{\partial \boldsymbol{\xi}_1}\right|_{\boldsymbol{\xi}_1 = 0} + \frac{\left(\boldsymbol{\xi}_1^{(1)}\right)^2}{2} \left.\frac{\partial^2 I}{\partial \boldsymbol{\xi}_1^2}\right|_{\boldsymbol{\xi}_1 = 0} + \mathcal{O}(h^3). \tag{4.84}$$

Similarly we can Taylor expand $\boldsymbol{\xi}_1 \boldsymbol{m}(\boldsymbol{\xi}_1^{(1)}/2, 0, 0)$ around the origin and get, by using (4.83),

$$\boldsymbol{\xi}_1^{(1)} m\left(\frac{\boldsymbol{\xi}_1^{(1)}}{2}, 0, 0\right) = \boldsymbol{\xi}_1^{(1)} \left.\frac{\partial \boldsymbol{I}}{\partial \boldsymbol{\xi}_1}\right|_{\boldsymbol{y}=0} + \frac{\left(\boldsymbol{\xi}_1^{(1)}\right)^2}{2} \left.\frac{\partial^2 \boldsymbol{I}}{\partial \boldsymbol{\xi}_1^2}\right|_{\boldsymbol{y}=0} + \mathcal{O}(h^3), \tag{4.85}$$

where we assumed that $m(\xi_1^{(1)}/2, 0, 0)$ has been found by an $\mathcal{O}(h^2)$-scheme. By computing the difference between (4.84) and (4.85) we get that the truncation error of (4.82) is of $\mathcal{O}(h^3)$. □

Since the dominating error comes from the α update in the coupled ODE-system

$$\begin{pmatrix} \dot{\xi}_1 \\ \dot{\xi}_2 \\ \dot{\alpha} \\ \dot{t} \\ \dot{I} \end{pmatrix} = H(\xi, \alpha, t) \tag{4.86}$$

we have the following Corollary for the global error.

Corollary 4.19. *The numerical error when estimating factor (4.17) with the modified mid point rule is of $\mathcal{O}(h^\nu)\lambda^{-1/3}$, where ν is shown to be equal to 1 in Section 4.3.3.1.*

Proof. X in Proposition 4.6 is in our case

$$X = [\xi_1, \xi_2, \alpha, t, I]^T.$$

Because of the remark after Proposition 4.6 and Proposition 4.9 the error follows by Taylor expansion of the exponential function in factor (4.17). □

4.3.4.2 Geometrical Spreading

The geometrical spreading is contained in factor (4.18), c.f. Figure 4.12. In words it tells us how the distance between two neighboring rays on a generalized wave front, has changed as they pass from one shadow line part to another (c.f. $Q_1 \to Q_2$ in Figure 4.1. We are going to simplify the analysis by

Assumption 4.20. *We assume that we can compute the arc length distance between two exact neighboring rays, along a common wave front, with an $\mathcal{O}(h^2)$-scheme.*

Without this assumption we would need to analyze the algorithm we use to compute the distance between markers, generally not on the same triangle but on the same wave front, which is out of the scope in this analysis. Similarly for simplicity, we are going to assume that the final projected point $\boldsymbol{Q}_2$ for the exact solution will be on the same triangle as the approximate point Q_2. The assumption

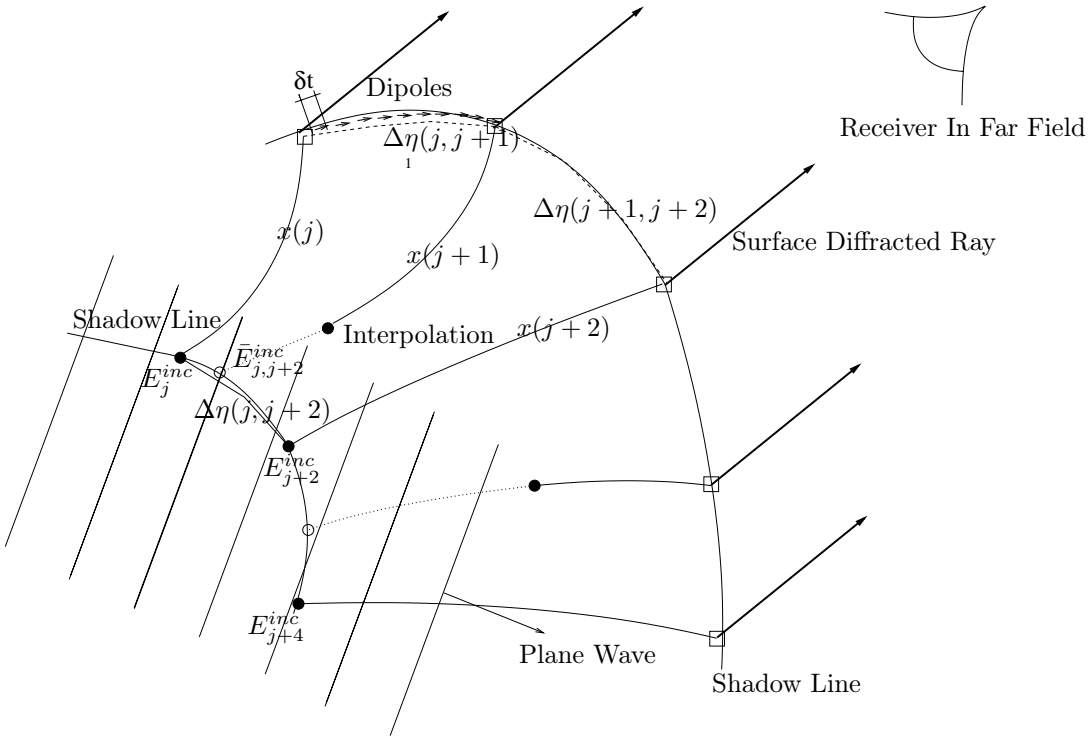

Figure 4.12: Schematic picture to illustrate variables or data used to interpolate and finally integrate the field in the monostatic direction.

above seems not to be consistent with Theorem 4.16. However, as we will see in the numerical experiments, Corollary 4.13 and/or expression (4.55) seems to induce second order convergence which will justify the assumption.

Call the exact arc length between two neighboring rays, $\boldsymbol{x}_k$ and $\boldsymbol{x}_{k+1}$, along the initial wave front, $\Delta\boldsymbol{\eta}_k(\boldsymbol{Q}_1|\boldsymbol{Q}_2)$. We need to know the error when we approximate (4.18) as

$$\lim_{\partial\boldsymbol{\eta}(\boldsymbol{Q}_1)\to 0}\sqrt{\frac{\partial\boldsymbol{\eta}(\boldsymbol{Q}_1)}{\partial\boldsymbol{\eta}(\boldsymbol{Q}_2)}} \approx \sqrt{\frac{\Delta\boldsymbol{\eta}_k(\boldsymbol{Q}_1)}{\Delta\boldsymbol{\eta}_k(\boldsymbol{Q}_2)}} \equiv \boldsymbol{S}(\Delta\boldsymbol{\eta}_k(\boldsymbol{Q}_1), \Delta\boldsymbol{\eta}_k(\boldsymbol{Q}_2)) = \boldsymbol{S}(\boldsymbol{d}_1, \boldsymbol{d}_2(\boldsymbol{d}_1)), \tag{4.87}$$

where we introduced $\boldsymbol{S}$ as a short hand notation for the square root and $\boldsymbol{d}_1$ and $\boldsymbol{d}_2$ for the finite distances. We assume that $\boldsymbol{S}(\boldsymbol{d}_1, \boldsymbol{d}_2(\boldsymbol{d}_1))$ may be Taylor expanded

around $\boldsymbol{d}_1$ to get

$$\boldsymbol{S}(0,0) = \boldsymbol{S}(\boldsymbol{d}_1, \boldsymbol{d}_2(\boldsymbol{d}_1)) - \boldsymbol{d}_1 \left(\frac{\partial \boldsymbol{S}}{\partial \boldsymbol{d}_1} + \frac{\partial \boldsymbol{S}}{\partial \boldsymbol{d}_2} \frac{\partial \boldsymbol{d}_2}{\partial \boldsymbol{d}_1} \right) \Bigg|_{\boldsymbol{d}_1 = 0} + \mathcal{O}(\boldsymbol{d}_1^2).$$

The use of approximation (4.87) will introduce an error that is proportional to

$$\boldsymbol{d}_1 = \Delta \boldsymbol{\eta}_k(Q_1),$$

i.e. inversely proportional to the density of the rays along the initial wave front.

We realize, having assumption 4.20 in mind, that the error in the numerical estimation of factor (4.18) is of the same order as the error in approximation (4.87). The numerical error when estimating factor (4.18) with the help of an algorithm defined later in Section 4.4.2.2, using a ray density that is proportional to $1/h$ where h is the characteristic element size, is then

$$S(d_1, d_2(d_1)) = \lim_{\partial \boldsymbol{\eta}(\boldsymbol{Q}_1) \to 0} \sqrt{\frac{\partial \boldsymbol{\eta}(\boldsymbol{Q}_1)}{\partial \boldsymbol{\eta}(\boldsymbol{Q}_2)}} + \mathcal{O}(h). \tag{4.88}$$

As mentioned in the introduction to this chapter, are the ODEs for the geodesics not unique in ξ-space. Hence, the rays may cross and the geometrical spreading factor can become infinite and the wave front will collapse. The analysis of the field in such points is beyond the scope of this presentation. However, engineering rules say that the field make a phase shift as it passes through such crossing point. We refer to [31] and [34] on this subject. However, we note that since we use wave front construction techniques we are able detect points where the wave front will collapse, since neighboring rays will change position on the wave front. With this knowledge we can apply the proper phase shift to the field.

4.3.5 Integration

The method that we are going to use to compute the scattered field is sometimes referred to the Equivalent Current Methods (ECM). We refer to [52], [53] and [54] and we do not claim that there is any mathematical rigour in our presentation below.

By inspection one see, with notation as in expression (4.15), that with $j > 1$,

$$-\mathrm{Re}(C_1^{\mathcal{H},1}) > -\mathrm{Re}(C_1^{\mathcal{S},1}) > -\mathrm{Re}(C_1^{\mathcal{S}|\mathcal{H},j}),$$

hence for relatively large propagation distances it suffices to study the contribution from the first hard term in expression (4.14). Let us therefor drop the superscript $\mathcal{H}$ below.

To be able to write down the total smooth surface diffracted field into a specific direction, specified by the two Euler angles (θ, ϕ) we need to define the unit vectors in the spherical polar coordinate system and know how they are transformed under

rotation. Let $(\hat{e}_1, \hat{e}_2, \hat{e}_3)$ be the Cartesian unit vectors. The polar unit vectors are then

$$\begin{aligned}\hat{r}(\theta,\phi) &= \hat{e}_1 \sin\theta\cos\phi + \hat{e}_2 \sin\theta\sin\phi + \hat{e}_3\cos\theta \\ \hat{\theta}(\theta,\phi) &= \hat{e}_1 \cos\theta\cos\phi + \hat{e}_2 \cos\theta\sin\phi - \hat{e}_3\sin\theta \\ \hat{\phi}(\theta,\phi) &= -\hat{e}_1 \sin\phi + \hat{e}_2\cos\phi.\end{aligned} \tag{4.89}$$

Under the unitary rotation $[\hat{e}_1, \hat{e}_2, \hat{e}_3] \rightarrow [\hat{e}'_1, \hat{e}'_2, \hat{e}'_3]$, where the Cartesian coordinates transforms as

$$x' = \begin{pmatrix} x'_1 \\ x'_2 \\ x'_3 \end{pmatrix} = \begin{pmatrix} \hat{e}_1\hat{e}'_1 & \hat{e}_1\hat{e}'_2 & \hat{e}_1\hat{e}'_3 \\ \hat{e}_2\hat{e}'_1 & \hat{e}_2\hat{e}'_2 & \hat{e}_2\hat{e}'_3 \\ \hat{e}_3\hat{e}'_1 & \hat{e}_3\hat{e}'_2 & \hat{e}_3\hat{e}'_3 \end{pmatrix} \begin{pmatrix} x_1 \\ x_2 \\ x_3 \end{pmatrix} = R_x x, \tag{4.90}$$

the polar polar coordinates $E = (E_r, E_\theta, E_\phi)$ transforms as

$$E' = \begin{pmatrix} E_{r'} \\ E_{\theta'} \\ E_{\phi'} \end{pmatrix} = \begin{pmatrix} \hat{r}R_x\hat{r} & \hat{r}R_x\hat{\theta} & \hat{r}R_x\hat{\phi} \\ \hat{\theta}R_x\hat{r} & \hat{\theta}R_x\hat{\theta} & \hat{\theta}R_x\hat{\phi} \\ \hat{\phi}R_x\hat{r} & \hat{\phi}R_x\hat{\theta} & \hat{\phi}R_x\hat{\phi} \end{pmatrix} \begin{pmatrix} E_r \\ E_\theta \\ E_\phi \end{pmatrix} = R_E(\theta,\phi)E. \tag{4.91}$$

4.3.5.1 The Infinitesimal Magnetic Current and Its Radiation

The electric far field from an infinitesimal magnetic dipole directed along the Cartesian $\hat{e}_3$-axis, c.f. [26], is in polar coordinates

$$\mathbf{E}^{far}_{zdip}(\theta) = \lim_{r\rightarrow\infty}\left[0, \frac{-i\delta\mathcal{M}\sin\theta}{2r\lambda}, 0\right] = \lim_{r\rightarrow\infty}\left[0, \frac{-ikI_m\delta t\sin\theta}{4\pi r}, 0\right], \tag{4.92}$$

where $\delta\mathcal{M} = I_m\delta t$ is the magnetic dipole moment, I_m the current in the dipole and δt the length of the dipole. By setting either polar coordinates or Cartesian coordinates in the argument we indicate whether the vector is given as a polar- or Cartesian vector. We see that asymptotically there are only a $\hat{\theta}$-directed component and this also holds if the dipole is moved a finite distance from the origin. It can be shown that the electric field propagating in the direction

$$\hat{P} = [\sin\theta\cos\phi, \sin\theta\sin\phi, \cos\theta],$$

from a magnetic dipole, oriented along $\hat{m}$ and positioned in x_0, is

$$\begin{aligned}\mathbf{E}^{far}_{dip}(\theta,\phi) &= R_E(\theta,\phi)\mathbf{E}^{far}_{zdip}(\arccos\left(\hat{P}\cdot\hat{m}\right))e^{ikx_0\cdot\hat{P}} \\ &= e^{ikx_0\cdot\hat{P}}R_E\left[0,1,0\right]\lim_{r\rightarrow\infty}\frac{-i\delta\mathcal{M}\sin\left[\arccos\left(\hat{P}\cdot\hat{m}\right)\right]}{2r\lambda} \\ &= e^{ikx_0\cdot\hat{P}}\left[\hat{r}R_x\hat{\phi}, \hat{\theta}R_x\hat{\phi}, \hat{\phi}R_x\hat{\phi}\right]E^{far}_\infty\left(\hat{P},\hat{m}\right) \\ &= e^{ikx_0\cdot\hat{P}}\left[0, \hat{\theta}R_x\hat{\phi}, \hat{\phi}R_x\hat{\phi}\right]E^{far}_\infty\left(\hat{P},\hat{m}\right) \\ &= e^{ikx_0\cdot\hat{P}}\left[0, p^E_\theta, p^E_\phi\right]E^{far}_\infty\left(\hat{P},\hat{m}\right),\end{aligned} \tag{4.93}$$

where R_E is defined according to (4.91) with

$$[\hat{e}_1', \hat{e}_2', \hat{e}_3'] = \left[\hat{m}^\perp, \hat{m} \times \hat{m}^\perp, \hat{m}\right],$$

and $\hat{m}^\perp$ is any unit vector orthogonal to $\hat{m}$. Above we have used the $\exp(-i\omega t)$-convention. The exponential factor therefore give us the proper phase shift when the dipole is not positioned in the origin but in x_0.

The electro-magnetic field far from a dipole behaves locally as a plane wave, e.g. the electric and magnetic field components are orthogonal. By using Z, the intrinsic wave impedance defined in Chapter 1, and by transforming the polarization of the H-field,

$$\hat{p}^H = \left(p_\theta^E \hat{\theta} + p_\phi^E \hat{\phi}\right) \times \hat{P},$$

into polar coordinates we get

$$\mathbf{H}_{dip}^{far}(\theta, \phi) = e^{ikx_0 \cdot \hat{P}} \frac{E_\infty^{far}\left(\hat{P}, \hat{m}\right)}{Z} \left[0, \hat{p}^H \hat{\theta}, \hat{p}^H \hat{\phi}\right] = e^{ikx_0 \cdot \hat{P}} \frac{E_\infty^{far}\left(\hat{P}, \hat{m}\right)}{Z} \left[0, p_\theta^H, p_\phi^H\right], \tag{4.94}$$

as the magnetic far field.

As mentioned previously, we are only going to present this analysis for the hard component, or hard surface ray mode, of the smooth surface diffracted field. Referring to [54], this ray mode propagate an electric field orthogonal to the so called binormal

$$\hat{b} = \frac{\dot{x} \times \ddot{x}}{|\dot{x} \times \ddot{x}|},$$

of the geodesic curve $x(t)$, and a magnetic field that is parallel to the binormal. We are going assume that the torsion is neglectable, i.e. the binormal can be approximated with $\hat{b} = \hat{n} \times \hat{x}$, where we assumed that the surface is uniquely convex and that the surface normal $\hat{n}$ is pointing in the convex direction. The reason for calling the mode hard is that the magnetic field asymptotically fulfills a hard boundary condition, c.f. acoustic boundary conditions, $\partial_n \hat{b} H = 0$ at the surface. We are going to make the following assumption.

Assumption 4.21. *Assume that, when the far field is computed, the hard component propagated along the geodesics may be replaced by a magnetic current, or infinitely many infinitesimal magnetic dipoles, directed along the shadow line. The amplitude of the current in the dipoles are set so that they radiate, c.f. expression (4.92), with the same strength and phase as the smooth surface diffraction formula predicts in the ray direction. I.e. the currents are* ***calibrated*** *so that the radiation is consistent with GTD in* one *radiation direction. However, when we integrate the currents, c.f. expression (2.17), the currents will of course scatter in* ***all*** *directions.*

For some problems the assumption above is totally consistent with GTD. If we for example consider the problem in Figure 4.1 for the mono-static case. All rays

along the shadow line, i.e. infinitely many, will contribute to the scattered field. The smooth surface diffraction contribution E_{ssd}^{tot} can asymptotically be computed by subtracting the reflected (Geometrical Optics) field from the total, asymptotically computed, scattered field. Equivalent currents can now be set along the shadow line so that they will radiate with the same strength as E_{ssd}^{tot} in the far field. A similar method can be applied to an infinitely long cylinder. However, the currents are calibrated on canonical problems, so to apply them to general scatterers and non-ray directions needs to be justified by numerical experiments, measurements or mathematical analysis. Numerical justifications can be found in for example [52] and [53] and measurements in [55]. Parts of the mathematical analysis in the literature concerns a stationary phase evaluation of (2.17) for a problem where only one GTD-ray contribute. It is then shown that the integral asymptotically reproduce the GTD-solution.

The magnetic far field from a smooth surface diffracted ray, originating from the first hard surface ray mode, leaving the smooth surface at x_0, can the be shown to be

$$\begin{aligned}\mathbf{H}_{ssd}^{far}(\theta,\phi) &= \lim_{r\to\infty} \hat{b}E_{inc}^{h}(Q_1)D_1^{\mathcal{H}}(Q_1)\exp\left(-i\frac{2\pi}{\lambda}\int_{Q_1}^{Q_2} 1+\sigma_1^{\mathcal{H}}(t')\,dt'\right)\\ &\quad\cdot\sqrt{\frac{\rho}{r(\rho+r)}}\sqrt{\frac{\partial\eta(Q_1)}{\partial\eta(Q_2)}}D_1^{\mathcal{H}}(Q_2)\frac{\exp\left(ikx_0\cdot\hat{P}\right)}{Z}\left[0,\hat{b}\hat{\theta},\hat{b}\hat{\phi}\right] \qquad (4.95)\\ &\equiv \lim_{r\to\infty}\sqrt{\frac{\rho}{r(\rho+r)}}\sqrt{\frac{\partial\eta(Q_1)}{\partial\eta(Q_2)}}\frac{T(\lambda)\exp\left(ikx_0\cdot\hat{P}\right)}{Z}\left[0,\hat{b}\hat{\theta},\hat{b}\hat{\phi}\right],\end{aligned}$$

where the phase factor compensate for moving Q_2 to the origin and where $\hat{\phi}$ and $\hat{\theta}$ are computed in the (θ,ϕ)-direction.

The field from a magnetic line source aligned with the $\hat{e}_3$-axis can be shown to radiate according to

$$\mathbf{H}_{ssd}^{far}(\theta,\phi) = \lim_{r\to\infty}\left[0,0,\frac{I_m e^{i\frac{\pi}{4}}}{Z\sqrt{\lambda r}}\right]\exp\left(ikx_0\cdot\hat{P}\right). \qquad (4.96)$$

If we apply (4.95) to the mono-static problem of the scattering by an infinite cylinder, where the plane wave propagate orthogonally to the cylinder axis, we realize that the wave front curvature of the smooth surface diffracted field will be zero. I.e. if we let the radius of curvature tend to infinity before we let the distance $r\to\infty$ the attenuation factor becomes

$$\lim_{r\to\infty}\lim_{\rho\to\infty}\sqrt{\frac{\rho}{r(\rho+r)}} = \lim_{r\to\infty}\sqrt{\frac{1}{r}}. \qquad (4.97)$$

The order which we take the limits is not set by anything that we have presented up until now so from a mathematical point of view the order is arbitrary. However, if we want that the smooth surface diffracted field should behave as a magnetic line

source according to (4.96) the order chosen in (4.97) is the proper one. Then if we equalize (4.96) to (4.95) for the cylindrical case and ϕ-polarization we can solve for I_m and get

$$I_m = \sqrt{\lambda} T(\lambda) e^{-i\frac{\pi}{4}} \sqrt{\frac{\partial \eta(Q_1)}{\partial \eta(Q_2)}}. \tag{4.98}$$

By combining (4.98), (4.92) and (4.94), a fraction δt of the smooth surface diffracted wave front, will radiate according to

$$\partial \mathbf{H}^{far}_{dip/ssd}(\theta,\phi) = \delta t e^{i\left(\frac{2\pi x_0 \cdot \hat{P}}{\lambda} - \frac{3\pi}{4}\right)} \frac{T(\lambda)\sin\left(\arccos\left(\hat{P}\cdot\hat{b}\right)\right)}{2Z\sqrt{\lambda}} \sqrt{\frac{\partial \eta(Q_1)}{\partial \eta(Q_2)}} \left[0, \hat{b\theta}, \hat{b\phi}\right], \tag{4.99}$$

where we suppressed the $1/r$ dependence. In the next section we will show how to sum up the contribution from all infinitesimal magnetic dipoles along the shadow line. Remark that by transforming the ray representation of the Smooth Surface Diffracted field to a current representation in (4.98) we see that a $\lambda^{-1/2}$ has shown up in the scattered field. That is, in caustics, where the entire wave front may contribute to the scattered field, the scattered field does not drop of with frequency as fast as in non-caustic cases.

4.3.5.2 The Integration of the Field

We will now show how to integrate over the dipoles exemplified in Figure 4.12. The a priori assumption will be that the arc length computation along the shadow line, already mentioned in assumption 4.20, will fulfill our needs of accuracy so that we achieve second order accuracy when using the Trapezoid Rule in the arc length space. To distinguish between the arc length parameterization of the shadow line, along which we will integrate, and the arc length parameterization of a geodesic ray, let us call the geodesic ray for $x(s) = x^s$ and the shadow line $x(t) = x^t$.

Let δt be an infinitesimal distance along the shadow line and let $\mathbf{H}_j(\theta,\phi)$ be the scattered field from the ray x^s_j into direction (θ,ϕ). Assume that we have a $\mathcal{O}(h^{-1})$ density (c.f. expression (4.88)) of the rays. By linear interpolation, between rays in t-space, we introduce an $\mathcal{O}(h^2)$ error as we compute the dipole currents I_m over small elements, let us say of length $\mathcal{O}(\lambda/10)$, centered in the points $x^s_{j,k}, k = 1,\dots n_j$. Each element (j,k) radiate a magnetic field according to (4.99). Call the distance between two neighboring points $x^t_{j,k}$ and $x^t_{j,k+1}$ $\delta t_{j,k}$ and assume that N rays arrives at the shadow line. The total radiated magnetic field, assuming a closed wave front, into the direction (θ,ϕ) is then

$$\mathbf{H}_{tot}(\theta,\phi) = \int_0^T \partial \mathbf{H}(\theta,\phi,t) = \sum_{j=1}^{N}\sum_{k=1}^{n_j} \mathbf{H}_{j,k}(\theta,\phi)\left(\frac{\delta t_{j,k-1} + \delta t_{j,k}}{2}\right). \tag{4.100}$$

For later reference we just mention that it is straight forward to extract the wave length dependent parts from (4.100) by taking

$$\begin{aligned}\log H_{j,k}^{(\theta)}(\theta,\phi,\lambda) &= A_{j,k}^{(\theta)}(\theta,\phi,\lambda) + a_{j,k}^{(\theta)}(\theta,\phi,\lambda)B_{j,k}^{(\theta)}(\theta,\phi)\\ \log H_{j,k}^{(\phi)}(\theta,\phi,\lambda) &= A_{j,k}^{(\phi)}(\theta,\phi,\lambda) + a_{j,k}^{(\phi)}(\theta,\phi,\lambda)B_{j,k}^{(\phi)}(\theta,\phi),\end{aligned} \tag{4.101}$$

where $B_{j,k}^{\theta|\phi}$ contain the major computational complexity. I.e. we need to compute the shadow line and the geodesic curve to be able to evaluate them. This enables us to make a more efficient algorithm when it comes to implementation and looping over frequencies.

4.3.6 Total Error

Disregarding the numerical error in expression (4.19), each term in the double sum contain three numerically computed factors. According to expressions (4.70), (4.88) and Corollary 4.19 we can write each term in the double sum in (4.100) as

$$\begin{aligned}&\partial\mathbf{H}_{j,k}(\theta,\phi)\left(\tfrac{\delta t_{j,k-1}+\delta t_{j,k}}{2}\right)\cdot\\ &F_1^{(j,k)}(\lambda)\left(1+\mathcal{O}_1(h^\mu,\lambda)\right)F_2^{(j,k)}(\lambda)\left(1+\mathcal{O}_2(h^\mu,\lambda)\right)\left(F_3^{(j,k)}+\mathcal{O}_3(h)\right),\end{aligned} \tag{4.102}$$

where $\partial\mathbf{H}_{j,k}$ has been defined correspondingly and we indexed the notation for the attenuation factors introduced in expression (4.16) to (4.18). At first sight it seems that the third error factor, for $\mu > 1$, dominate the error as we decrease λ and h correspondingly. However, by inspecting the λ dependence in F_1 and F_2, letting $\delta t = \mathcal{O}(\lambda)$, $h = \mathcal{O}(\lambda^\delta)$ and use expression (1.27) we can build the following error table for sufficiently small λ:

	$\upsilon = 2$	$\upsilon = 3$
F_1	$\mathcal{O}(\lambda^{\delta-1})$	$\mathcal{O}(\lambda^{2\delta-1})$
F_2	$\mathcal{O}(\lambda^{\delta-\frac{1}{3}})$	$\mathcal{O}(\lambda^{2\delta-\frac{1}{3}})$
F_3	$\mathcal{O}(\lambda^{\delta})$	$\mathcal{O}(\lambda^{\delta})$
$\max(F_1,F_2,F_3)$	$\mathcal{O}(\lambda^{\delta-1})$	$\mathcal{O}(\lambda^{2\delta-1})$
Integral	$\mathcal{O}(\lambda^{\delta-1})$	$\mathcal{O}(\lambda^{2\delta-1})$

(4.103)

Where we have chosen υ as the local error in the ODE-solver given in Method 4.8 and *Integral* assigns the total numerical error in (4.100).

More generally for a local error of γ we realize that if we want to integrate over $\mathcal{O}(1/\lambda)$ infinitesimal dipoles according to expression (4.100), we are only allowed to have a mesh which fulfill

$$\delta(\gamma-1)-1 \geq 0,$$

i.e. the element size should fulfill

$$h \sim \mathcal{O}(\lambda^{\frac{1}{\gamma-1}}),$$

to get a non-increasing error as we increase the frequency. If we choose to fulfill the equality sign we must assure by numerical test that the error for a moderate wave length is sufficiently small.

4.4 Implementation

In this section we are going to present the key constituents of our implementation. Some components of the implementation have support in the analysis done in Section 4.3 other components are just inventions that seems to work satisfactory.

We have developed and implemented the wave front solver in Fortran 90. Imagine that we have a mathematically exact representation of the geometry. Let us call this representation the true geometry. The true geometry is represented both with triangle data structure and a NURBS (Non-Uniform Rational B-Splines) data structure. We use the same data structure for the triangles as in [16] and we build the hybrid geometry by picking data from the NURBS data structure present in a GTD-solver called MIRA, c.f. [17] and [19]. Since we use routines from MIRA to check for occlusion we refer the reader to [19] for presentation of these algorithms.

As discussed in Section 4.3.1 we will assume that the geometry, or the scatterer, is meshed with a surface curvature sensitive meshing.

Our wave front solver can only treat bodies which, when they are meshed, only have edges that is shared by exactly two triangles.

The surface patches of the scatter is provided via a well defined file-format. The file is built from a geometrical data base defined in a software product called CADfix® designed to translate and repair engineering product data [56]. In MIRA a surface is defined by its *shape* given by NURBS parameterized with $(u, v) \in \Omega$, where

$$\Omega := \{(u, v) : 0 \leq u \leq 1, 0 \leq v \leq 1\}.$$

The surface, or the material, does not always exist though in the entire Ω but only *inside* of closed, so called, trim curves defined in Ω. Inside is defined with the help of the orientation of the trim curve. If there are no other trim curves in the exterior to a trim curve then we will assume that its representation in $\mathbb{R}^3$ coincide with another trim curve's, defined in another surface patch, representation in $\mathbb{R}^3$. The word coincide should though be interpreted as close within a tolerance since the two trim curves have two different representations and are not the same curves mathematically speaking. In the wave front solver we have access to curve pointers and surface pointers making it possible to compute geometrical quantities in any point. We may for example compute how smooth the transition between two surfaces are. Below we will speak of $G0$, $G1$ and $G2$-points which the surface rays passes trough. That is, the classification of a point in a surface depends not only on which point it is but also in which direction the ray go through the point. Differently stated it is the point in the *phase space*, introduced in the introduction, that we classify according to below:

G0 The ray through a G0-point is continuous.

G1 The tangent $\dot{x}(s)$ to a ray going through a G1-point is continuous. A G1 point is also G0.

G2 The curvature $c(s) = \frac{\dot{x}(s)\times\ddot{x}(s)}{|\dot{x}(s)|^3}$ to a ray, going through a G2-point, is continuous. A G2 point is also G1.

Remark that $\dot{x}(s)$ is not uniquely defined in a $G0$-point. C.f. an edge, built by two faces, where the surface derivative at the edge depends on which face we use to define it with. We assume that all points in phase space with (u, v) off the trim curves are G2. A trim curve that describe a boundary between two surfaces with all its phase space points, where the directions are non-tangential to the trim curve, in G0 but not in G1 is referred to a true surface edge.

In the presentation of the implementation below we will mention the most relevant and crucial parts of the wave front solver. Especially we will focus on the algorithms that achieve the proper level of accuracy and produce unique solutions (robust algorithms).

Below we will speak of smooth shadow lines, having its representation in both parameter space and in $\mathbb{R}^3$, and polygonal shadow lines only having a representation on the facet geometry. Given a plane wave illumination with a Poynting's vector $\hat{k}$ the smooth shadow lines divide the illuminated parts from the non-illuminated ones.

In the present implementation we have focused on finding four types of smooth surface diffracted rays. Initially the rays belongs to an initial wave front that are

1. Edge excited: The initial wave front coincide with a true surface edge.
2. Shadow line excited: All points in the initial wave front are G1.

For the edge excited wave fronts either one or both of the surfaces defining the edge can be illuminated.

The field associated to a marker or a ray will contribute to the scattered field if it reaches an illuminated edge, or a shadow line which is not occluded. Hence there are four categories of wave fronts.

1. Shadow line → Shadow line
2. Shadow line → Illuminated true surface edge
3. Illuminated true surface edge → Illuminated true surface edge
4. Illuminated true surface edge → Shadow line.

GTD predict of course other asymptotic phenomenons but from an asymptotic point of view these are the strongest ones. For specific applications and scatterers it is hard to say a priori which ones that contribute the most to the scattered field.

According to the discussion in the introduction, the wave front propagation problem is well posed if F and G is Lipschitz continuous in Ω_F and Ω_G. Since we

search shadow lines and propagating wave fronts on a facet approximation of the true geometry we should analyze the well posedness of this problem also. However, to avoid this quite complicated problem we will justify our method by noting that as long as the problem with the true geometry or true problem is well posed then it is correct to design a numerical method that predict unique solutions. When the true problem contain edges or corners, i.e. G is not Lipschitz continuous, then we must adjust our numerical method on faceted geometry so that it mimic the rules for the true problem predicted by GTD. We will exemplify this in Section 4.6.

4.4.1 Data Structure

When we search initial wave fronts, on shadow lines and true surface edges, and propagate markers on the faceted geometry we need surface normals, surface curvatures and principal directions (geometrical quantities) to get the proper order of accuracy as seen previous sections. To be able to compute these, we need geometrical information for the triangle edges and triangle nodes. The data structures storing the geometry information are exemplified in Figure 4.13. When the data structure for the geometry is set, we are able to compute geometrical quantities and link these to the triangles. Remark that these links are not trivial to build since we do not demand that the scatterer is smooth. When the geometrical quantities for each node in a triangle are stored we can do second order interpolation in a linear Lagrange triangle of the geometrical quantities.

To be able to design efficient and well traceable algorithms for the wave front propagation we need to store the fronts in a dynamic and well organized data structure. For each plane wave excitation we dynamically allocate a list of so called wave sheets. The structure of a wave sheet is presented in Figure 4.14.

4.4.2 Algorithms

The main objectives we had when we designed the solver was to separate three building blocks. Namely

1. Data structure for geometry.
2. Computations of wave fronts.
3. Computation and integration of scattered fields.

Since these blocks are well separated, block 1 can be called outside the loop over excitations and block 2 can be called outside the loop over frequencies. In figure 4.15 we present an overview of the algorithm.

4.4.2.1 Creation of Initial Wave Fronts

An initial wave front either coincide with a true surface edge or a shadow line and they are constructed in `GetShadowlines` referred in Figure 4.15.

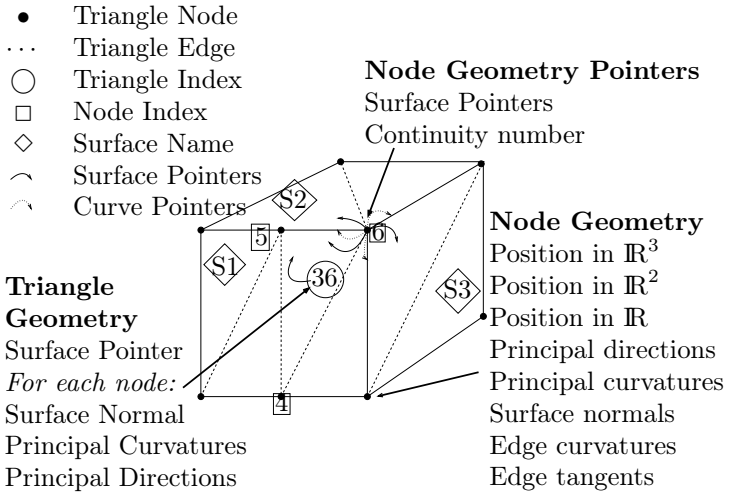

Figure 4.13: Above we see an illustration of the geometrical data structure stored for, in this example, a cube. Initially, in the solver, we build the node geometry telling us where the triangle nodes are positioned: At the end points of a trim curve, on a trim curve but off the endpoints or finally on a surface but off the set of trim curves. In the node geometry we store pointers to the trim curves and surfaces associated to the node. Node 6 in the illustration, is on the end point of a trim curve and for this type of corner 3 curve pointers and 3 surface pointers are stored. After the node geometry is built we build the node geometry. It contains node position in $\mathbb{R}^3$, in parameter surface space $\mathbb{R}^2$ and in parameter trim curve space $\mathbb{R}$. Principal directions and curvatures together with surface normals, edge curvatures and edge tangents are also stored in the node geometry. When the node geometry is built we can complement the node geometry with a matrix telling us the level of smoothness between surfaces associated to the trim curve end point, trim curve or interior node. For node 6 it is a 3 by 3 matrix. Finally we obtain the main data structure for triangles enabling us to do linear interpolation of principal directions and curvatures and surface normals. The nodes associated to triangle 36 have one surface common, $S1$, and hence the normals and principal directions/curvatures for this surface $S1$ (at the node points) are stored in the data structure for triangle 36.

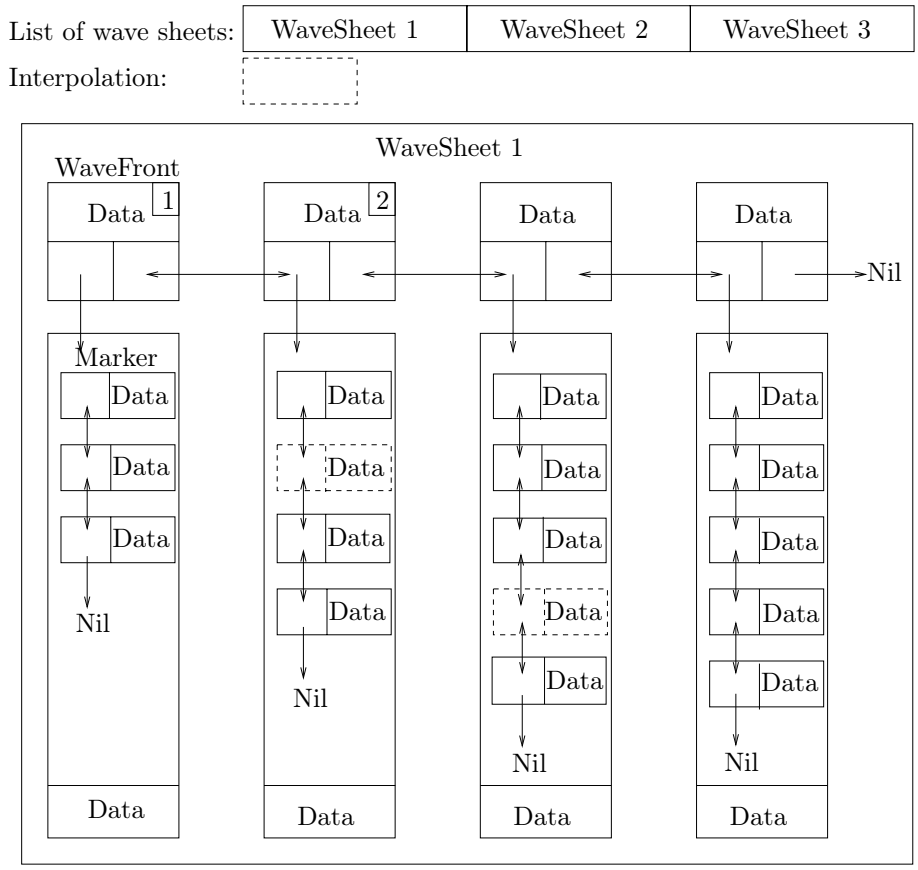

Figure 4.14: The dynamically allocated data structure for one exciting wave. In this example (WaveSheet 1) four wave fronts are stored. When a wave front is moved the previous front is stored in a linked list called a wave sheet. Each wave front consist of a linked list where each element represent a marker on the wave front containing a set of data. Above we see that wave front 1, for example, contain 3 markers and wave front 2 contain 4 markers. The data stored at the marker level is the Incoming Electric field E at the initial front, how much it is attenuated D, the position x, the direction the marker is moving p, the distance it has moved along the ray s_1, the distance to one of its neighbors s_2 and which on which triangle it is positioned on. Finally it contain information if it has reached a shadow line and if it is a direct off spring from a marker in the initial wave front (i.e. not introduced by interpolation). Note that not all data has to be applicable for all markers. The list of wave sheets is an allocatable and it is deallocated for each new excitation.

```
call ReadProblem()
call AllocateNURBSGeometry(MyScene)
call AllocateTriangleGeometry(Triangles)
call BuildGeometry(Geometry)
EXCITATIONLOOP: do jj=1,NumberOfExcitation
 call GetShadowlines(Shadowlines)
 call AllocateListOfWaveSheets(Shadowlines,LOWS)
 DISTRIBUTELOOP: do ll=1,NrOfShadowLines
  nullify(WaveFrontSheet)
  call GetFront(ShadowLines,ll,WaveFront)
  call AddFront(WaveFrontSheet,WaveFront)
  LOWS(ll)%Sheet=>WaveFrontSheet
  call ImproveDiscreteShadowLine(WaveFront,ll)
 end do DISTRIBUTELOOP
 FRONTLOOP: do jj=1,NrOfShadowLines
   WaveFrontSheet=>LOWS(jj)%Sheet
   call GetFront(WaveFrontSheet,WaveFront)
   MOOVELOOP: do while (.not.ReachedSadowLine)
    call MoveFront(WaveFront,ReachedSadowLine)
    call Interpolate(WaveFront)
    call AddFront(WaveFrontSheet,WaveFront)
   end do MOOVELOOP
 end do FRONTLOOP
 call ComputeDivFactor(WaveFrontSheet)
 INTEGRATIONLOOP: do ll=1,NrOfShadowLines
  WaveFrontSheet=>LOWS(jj)%WFL
  FREQUENCYLOOP: jj=1,NumberOfFrequencies
   call ComputeScatteredField(WaveFrontSheet)
   call PrintField(WaveFrontSheet)
  end do FREQUENCYLOOP
 end do INTEGRATIONLOOP
 call Deallocate(LOWS)
end do EXCITATIONLOOP
call Deallocate(MyScene,Triangles,Geometry)
```

Figure 4.15: Algorithm for the front solver.

Let us introduce some simple definitions to investigate the success and robustness of the algorithm presented below. A *Shadow Line Triangle Edge* (STE) candidate is an edge where exactly one of its associated triangles are illuminated, i.e. the scalar product between the triangle normal and the Poynting's vector is negative, and the other triangle is non-illuminated, i.e. the scalar product between the triangle normal and the Poynting's vector is positive. A *Shadow Line Surface Edge* (SSE) candidate is an edge which coincide with a true surface edge. Note that no occlusion is taken into account in these definitions.

Call the nodes, to shadow line triangle edge candidates and shadow line surface edge candidates, that build simply connected graphs, *Initial Wave Front* (IWF) candidates. With a *Simply Connected Graph* (SCG) we mean that exactly two edges share a node accept for graphs which are open where the end point nodes are allowed to be connected to only one edge.

The success of the method that we will use to approximate (4.12) depends on the well posedness of the true shadow line problem and the stability of the approximate problem. Our numerical experience say that there are meshes that will produce graphs that are not simply connected. However we have removed these anomalies by changing the scalar product sign for triangles with neighbors that have a different product sign. E.g. if triangle T is illuminated, and therefore have scalar product less than zero, and all its three neighbors has a scalar product larger than zero then we flip the sign for triangle T and consider it as non-illuminated. We have no rigorous proof that all anomalies will be removed with these logical tests but we have yet not seen it fail. This empirical conclusion needs of course to be investigated further in future work.

For initial wave front candidates that are built up by SSE-candidates we can make sure that the graphs are simply connected if we see to that all nodes in a SSE-IWF candidate points to the same trim curve.

The routine `GetShadowlines` is built up by a number of algorithms. Initially we store, in a linked list L, the triangle edges that are candidates to coincide with the shadow line or coincide with true surface edges. Only the true surface edge candidates that are non-occluded by the NURBS-geometry are stored. The occlusion test for the shadow line candidates is postponed to later.

As we saw in the introduction to this chapter, we have at least for a sufficiently smooth scatterer (all derivatives in F exist), existence of a unique shadow line if a Lipschitz condition is fulfilled.

Having the assumption above in mind we generate an ordered number of markers along the shadow line with the following algorithm.

1. Pick one edge E_1 from the list L, remove this element from L and add the element to a list l.

2. Search in the triangle data base, in a clock wise sense, with one of the nodes of E_1 in the center (c.f. Figure 4.16), after next shadow line candidate E_2 that are of the same type as in 1 (STE/SSE).

3. Find E_2 in L and repeat 1.

4. Repeat until no neighbors found. Then save l as either a STE-IWF or SSE-IWF in a WaveSheet (c.f. Figure 4.15 and 4.14).

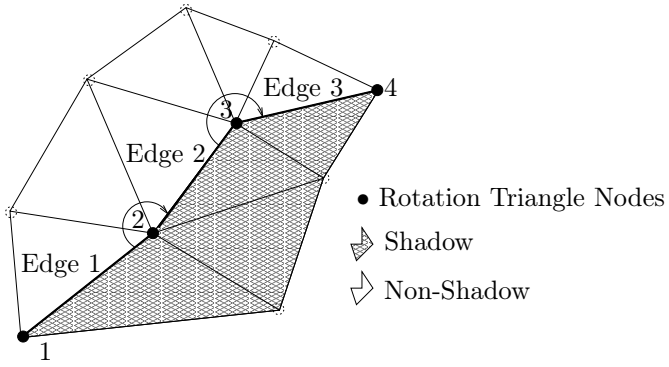

Figure 4.16: Algorithm to generate a discrete number of ordered markers along a shadow line. By searching in clock wise sense after STEs at each node we get a demarcation polygon between shadow and non-shadow.

After all the graphs of Initial Wave Front candidates are stored we increase the accuracy of the STE-IWF's by running a Conjugate Gradient algorithm [19] in parameter space minimizing (4.5). As initial conditions for the CG-solver we use the position of the edge nodes in parameter space stored in the geometry data structure (c.f. 4.13). Since the edge nodes coincide with the curved embedding geometry no projection is needed and therefore no error is introduced in this step. After a stationary point is found in the CG-solver we check for occlusion of the refined STE-IWF candidates and split the STE-IWF and SSE-IWF candidates if they are partly occluded. Finally we project the STE-IWF markers back to the faceted geometry.

4.4.2.2 Interpolation

In the subroutine `Interpolate` we add new markers so that a satisfactory density is reached. Since the markers are in $\mathbb{R}^5$ ($(x, \hat{n})$-space) we have two interpolation conditions. If the distance in $|x_j - x_{j+1}|$ is larger than a threshold or if $n_1 \cdot n_2$ is smaller than another threshold. The position of the new marker is found with the following algorithm.

Let marker x_j belong to triangle $T^{(j,0)}$ propagating in direction n_j and similarly let x_{j+1} belong to triangle $T^{(j+1)}$ propagating in direction n_{j+1}. Now we want to find a point $x_{j,j+1}$ on the meshed geometry that is, in some sense, in the middle of x_j and x_{j+1}.

Our algorithm rests on the assumption that the interpolated marker should be positioned on a geodesic line between marker x_j and x_{j+1}. Since we believe that it would be to expensive to find the geodesic line, with for example the algorithm presented in section *Front Propagation* below, we have invented an algorithm that produce an approximate geodesic line. Differently stated, when we form the polygonal line between x_j and x_{j+1} we try to make $\mathbf{c}_g$ (at least point wise, c.f. discussion on page 69) as small as possible.

Let $p^{(0)} = x_{j+1} - x_{j,0}$ and $n^s_{j,0}$ be the first order interpolated surface normal in $x_{j,0}$. Define a plane $P^{(j,0)}$ with the same normal as the triangle $T^{(j,0)}$ has and another plane $P_{j,j+1,0}$ with the normal $n^s_{j,0} \times p^{(0)}$. Also define a direction $\hat{t}^0$ as the vector parallel to line that the intersection between the two planes $P^{(j,0)}$ and $P_{j,j+1,0}$ build. The interpolation algorithm now reads as follows.

1. Project the point $x_{j,0}$ to the triangle edge of $T^{(j,0)}$ along $\hat{t}^0$. Call this point $x_{j,1}$.

2. Jump to neighboring triangle $T^{(j,1)}$ and build $p^{(1)}$, $n^s_{j,1}$ and $\hat{t}^1$ correspondingly.

3. Go to 1 until there is a point $x^{(middle)}_{j,j+1}$ along the approximate geodesic line that fulfill
$$|x_j - x^{(middle)}_{j,j+1}| = |x_{j+1} - x^{(middle)}_{j,j+1}|.$$
Call the triangle that host $x^{(middle)}_{j,j+1}$, $T^{(middle)}_{j,j+1}$.

4. Build the wave front normal $n^{(middle)}_{j,j+1}$ by least square projection of the arithmetic mean $\frac{n_j+n_{j+1}}{2}$ onto $T^{(middle)}_{j,j+1}$.

4.4.2.3 Shadow Line Representation

Since flat surfaces may exist will the maximum triangle edge length only be partly controlled by the engineer, i.e. the STEs can not be used for stopping criteria. Therefore to have an accurate stopping criteria for category 1 and 4 mentioned in the introduction to Section 4.4 we create a more dense polygonal representation, i.e. the polygon connecting the markers coincide with the faceted geometry, of the illuminated STE-IWFs. This is done in `ImproveDiscreteShadowLine` referred in Figure 4.15.

The markers in the SSE-IWFs do not necessarily belong to neighboring triangles, since the markers are projected from the NURBS-geometry, but there may be *gaps* in the polygon train. We use the interpolation described above to find the shadow line position in the triangles that are left out in the SSE-IWFs. When the gaps are filled, line segments are saved for each triangle that lies on a shadow line.

The stopping criteria for category 2 and 3 is more straight forward to implement. A ray is stopped if it reaches an illuminated SSE.

4.4.2.4 Front Propagation

`MoveFront` contain the central part of the wave front propagation algorithm. It moves the markers on the faceted geometry such that they trace out an approximate geodesic line.

The algorithm implement four rules to update position $x^p(s)$, $\dot{x}^p/|\dot{x}^p| = n$ and the arc length s^p of $x^p(s)$ of marker p.

- A marker inside a triangle, i.e. associated to triangle T_j, is moved along a straight line, i.e. $x^p_{k+1} = x^p_k + \Delta s n^p_k$ until it reaches a triangle edge.
- The arc length is updated according to $s^p_{k+1} = s^p_k + |x^p_{k+1} - x^p_k|$.
- The exponential attenuation is updated according to the modified midpoint rule presented in Proposition 4.18.
- When a marker has reached a triangle edge of triangle T_j the marker is associated to the triangle neighbor T_i, and n^p_{k+1} is computed according to the update rule (4.33).

The front propagation routine apply the four rules above for each marker in a front until all markers has propagated a fixed length. I.e. for each marker p that has passed $m^p - 1$ triangle edges update the arc length according to

$$s^p \to s^p + \sum_{t=1}^{m^p} \Delta s^p_t$$

and the frequency independent part of the exponential attenuation

$$\tilde{I}^p \to \tilde{I}^p + \sum_{t=1}^{m^p} \Delta \tilde{I}^p_t.$$

If a marker reaches a shadow line then it is also stopped.

4.4.2.5 Integration

In `ComputeScatteredField` the total smooth surface diffracted field is computed by implementation of the numerical approximations suggested under *Integration and evaluations* in Section 4.3.

To compute the geometrical spreading we do the following. Let (x^j_0, x^{j+1}_0) be neighbors on the initial wave front and (x^j_1, x^{j+1}_1) there positions on the final wave front. Compute the distance between x^j_0 and x^{j+1}_0 by integrating the distance while using the interpolation algorithm all the way from x^j_0 to x^{j+1}_0, i.e. stop when

$$|x_{j+1} - x^{(final)}_{j,j+1}| = 0.$$

Each marker has an *orientation* set initially. It is defined as follows.

Once more let, (x_0^j, x_0^{j+1}) be two neighboring points and $n^s(x_0^j)$ be the first order interpolated surface normal in x_0^j then we define the initial orientation o_0^j for a marker j as

$$o_0^j = \text{sgn}\left[\left((x_0^{j+1} - x_0^j) \times n^s(x_0^j)\right) \cdot n_0^j\right]. \tag{4.104}$$

In each loop `ll` in `MOOVELOOP`, before interpolation is done, we compute o_{ll}^s for each marker s if $o_{ll}^s - o_{ll+1}^s \neq 0$ then the marker has went through a caustic and the phase of the amplitude is changed $\pi/2$ radians.

To evaluate the terms in (4.100), each corresponding to a magnetic dipole along the final wave front, we interpolate the arc length, incoming field, attenuation etc. separately and in a second step we evaluate the frequency independent functions. The summation in (4.100) of the dipoles is done straight forwardly by evaluating the frequency independent $B_{j,k}^{\theta|\phi}(\theta, \phi)$ in (4.101) and finally loop over all frequencies and evaluate the frequency dependent terms in (4.101). We do correspondingly for (4.87).

4.5 Improvements on the Implementation

We see several possibilities of improvements in our implementation and we list some of them below.

1. Since triangle edges can be arbitrarily large in number of wave lengths we should use a refinement algorithm for SSEs also. I.e. we should run a 1D Conjugate Gradient algorithm along the edge.

2. Present implementation only test occlusion on the markers stored in the STE-IWFs and SSE-IWFs. Once more, since triangles can be arbitrarily large, we should run the occlusion algorithm on the refined, with proper marker density, initial shadow line.

3. Concave surfaces are today treated as flat. Even though the asymptotic theory is not as well developed for concave surfaces as for convex ones, the amplitude may be estimated more consistently than today.

4. Analyze the interpolation conditions and step sizes discussed in section *Interpolation* and *Front Propagation* better. Try to find optimal conditions with respect to numerical errors and even try to develop adaptive algorithms. One can for example try to compute the wave front curvature and use this as an indicator when interpolation is needed. We refer for example to [57].

5. The wave front data structure needs to be modified to facilitate the representation of higher order effects.

6. The interpolation algorithm fails if surface normal is parallel to p in the interpolation algorithm presented at page 105. This may happened if we pass a surface edge. In this case one can reverse the algorithm, i.e. let $x_j \rightarrow x_{j+1}$ and vice versa.

4.6 Numerical Results

We have tested the ODE solvers, based on Method 4.7 and Method 4.8, in `GetShadowlines` and `MoveFront` together with `Interpolate` and `ImproveDiscreteShadowLine` on a sphere, a cylinder, a torus and two quite complex low signature vehicles. The numerical results on the complex objects has only been checked qualitatively where a plot of the induced wave fronts for one angle of incidence can be seen in Section 1.4. Quantitatively and satisfactory results have been produced for the canonical objects. In the level of accuracy experiments we focus on the dominant error term in F_1, c.f. table (4.103). That is, the computation of the arc length.

We present the level of accuracy of the ray propagation algorithm on a torus because of its simplicity, and since it is doubly curved with two different radius of curvatures (c.f. cylinder and the sphere). The torus we use is given by the following parameterization,

$$\begin{aligned} x &= (7.5 + 2.5\cos v)\cos(u) \\ y &= (7.5 + 2.5\cos v)\sin(u) \\ z &= 2.5\sin(v), \end{aligned} \tag{4.105}$$

where $u, v \in [0, 2\pi)$ and Poynting's vector for the exciting plane wave is

$$\left[\cos\left(\frac{\pi}{10}\right), \sin\left(\frac{\pi}{10}\right), 0\right].$$

Since it is hard to compute the geodesics analytically for a torus we do this numerically with our solvers for a geometry with very small triangles. It will of course introduce errors in the analysis which will produce approximate order of accuracy levels. However, since the solvers converges for the cylinder and the sphere, where analytical results are known, we believe that the errors in the convergence analysis is bounded by the triangle size in the highly resolved torus. Also, both the previous order of accuracy analysis and the similarity between numerical results based on Method 4.7 and the consistent Method 4.8 imply consistency of Method 4.7. Mathematically, we use the following method to estimate the convergence rate.

Let us call any of the numerical computed variables for ζ then we assume that the numerical error fulfill

$$\text{error} = |\boldsymbol{\zeta} - \zeta| = Ch^{\gamma}.$$

We refine the mesh four times and we therefore have 5 estimations of $\boldsymbol{\zeta}$, i.e.

$$[\zeta_1, \ldots \zeta_5] \leftrightarrow [h_1, \ldots h_5],$$

then we estimate γ by assuming $\zeta_5 = \boldsymbol{\zeta}$ and therefore

$$\gamma \approx \frac{\log(|\zeta_5 - \zeta_1|) - \log(|\zeta_5 - \zeta_4|)}{\log h_1 - \log h_4}. \tag{4.106}$$

In Figure 4.18 and 4.19 we show the convergence rate of x (c.f. (4.62)), $\dot{x}$ (c.f. (4.63)) and t (c.f. (4.64)), for one of the rays building a family of generalized wave fronts indicated in Figure 4.17. Hence, the interpolation algorithm is not included in the test.

If we use a surface curvature sensitive mesh, where the mesh error is bounded by a parameter h^2, the variation in element size h will be quite large. In the order of accuracy analysis we need meshes where the element size can be changed linearly or similar. Hence, for practical reasons we have used a triangular mesh with bounded edge lengths. However, for canonical objects with constant radius of curvature we have seen good convergence results for surface curvature sensitive meshes also.

In Figure 4.18 we use the numerical method based on Method 4.7. It is clear that not all variables show global $\mathcal{O}(h^2)$ convergence for this geometry. This is not surprising, since as we refine the mesh, the shape of the $\mathcal{O}(h)$ triangles will change which for example will make a direct $\mathcal{O}(h)$ impact on the final update of α in update (4.30). For some reason is this direction error not apparent for our specific geometry. However, the direction error may have influenced the position error.

In Figure 4.19 we use the numerical method based on Method 4.8. It is clear that for the torus we have $\mathcal{O}(h^2)$-convergence for x, $\dot{x}$ and t.

In Figure 4.20 we try to illustrate the quite complex family of smooth surface diffracted wave fronts that can be excited by a plane wave impinging on a cylinder.

4.7 Discussion

We have analyzed and developed a wave front construction technique [11] applied to Smooth Surface Diffraction. To be able to get an implementation that can compute the smooth surface diffracted field in a robust, efficient and convergent way we have implemented a wave front solver in a hybrid geometry setting. The algorithm consist of the following steps

- Find approximate shadow line according to Section 4.4.2.1.
- Refine the approximate shadow line according to Section 4.4.2.1.
- Consider the first shadow line as an initial wave front represented in a data structure described in Section 4.4.1. Propagate it by moving a discrete number of markers, representing the front, a certain length Δs. Each marker is moved according to the following.

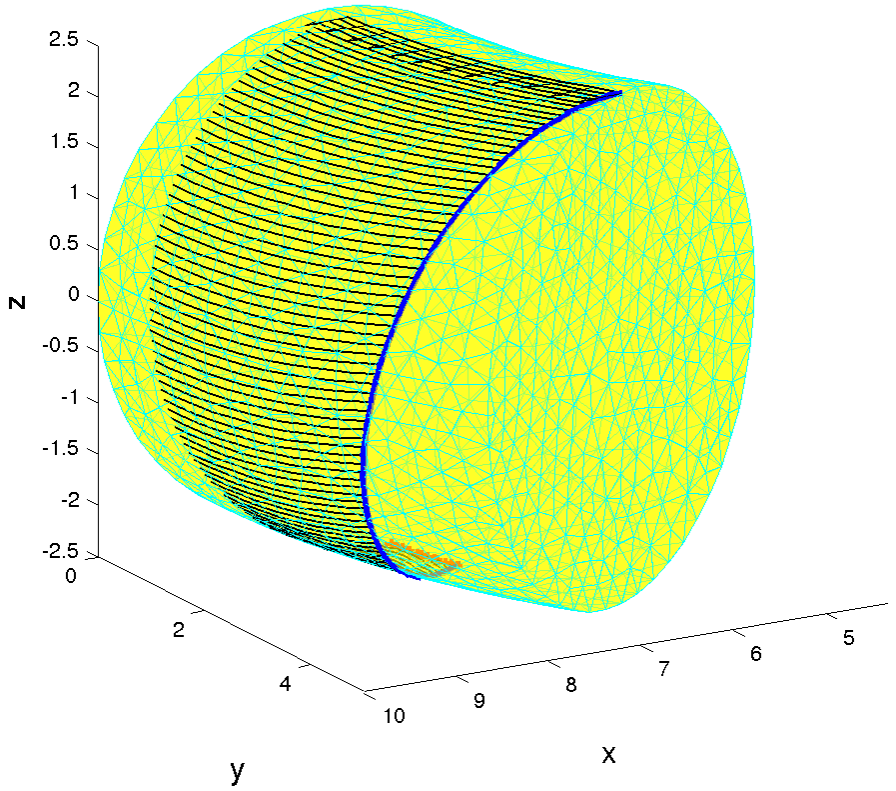

Figure 4.17: A segment of a meshed torus. The segment is closed by two flat surfaces and for viewing purposes we have made the triangles transparent. The smooth surface diffracted generalized wave front that we consider is excited on the shadow side of the torus, indicated by black arrows, by a plane wave and we only consider the wave sheet on the shadow side of the torus (the propagation is stopped at the red stars). We analyze the accuracy of the blue ray in Figure 4.18 and 4.19.

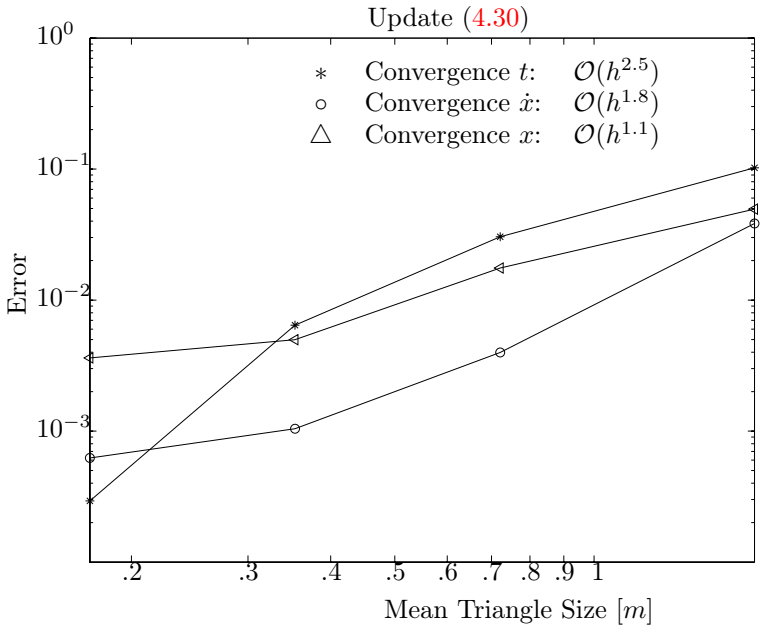

Figure 4.18: The convergence rate for update (4.30), as we refine the mesh, of the final direction and length for one ray is seen to be approximately of $\mathcal{O}(h^2)$. The error in the final position is of $\mathcal{O}(h)$. Depending on the direction of the plane wave relative to the geometry will the position error contaminate the arclength estimation. The numerical experiment therefore indicate that the arclength error also should be considered to be of $\mathcal{O}(h)$ for Method 4.7. If the coarsest mesh where to be omitted in the analysis the convergence rate for $\dot{x}$ would have reduced to approximately $\mathcal{O}(h)$.

1. Propagate each marker Δs according to Update 4.1 and update (4.33). We let Δs approximate the true arc length according to (4.41).
2. If the markers along a wave front is too depleted in phase space then interpolate by using the interpolation technique described in Section 4.4.2.2.
3. Stop the propagation of a marker if the marker pass a shadow line edge and refine its position by using a conjugate gradient algorithm applied to the NURBS.

- Interpolate the field by using linear interpolation along the initial and final wave front according to Figure 4.12 and integrate the field into a direction according to Section 4.3.5.2.

By having access to a triangular mesh we have solved the problems with gaps between NURBS by just jumping between triangles instead of NURBS. That is,

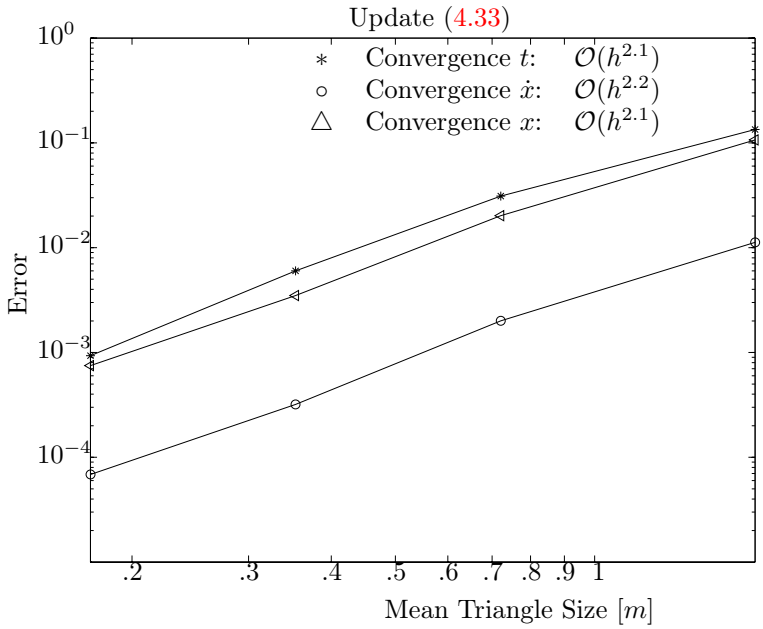

Figure 4.19: The convergence rates for update (4.33), as we refine the mesh, of the final position and direction for one ray is seen to be approximately of $\mathcal{O}(h^2)$. We also get the same convergence rate for the arc length of one ray. We believe that the numerical results indicate that the numerical scheme based on update (4.33) has a local error of exactly $\mathcal{O}(h^3)$.

instead of passing over complicated curves (trim curves) in $\mathbb{R}^3$ we pass over straight triangle edges with the marker. By combining NURBS and triangles we are also able to find all shadow lines by using shadow line data from the triangles as seeds to the shadow line algorithm applied to the NURBS setting. Combinations of edge diffraction and Smooth Surface Diffraction for non-smooth geometries can also be taken into account by using both geometry representations.

The NURBS enables us to propagate the field over geometries that contain true edges and corners. We also achieve an almost mesh independent accuracy of the shadow line which includes occlusion. The NURBS data also enables us to assign geometrical data to the triangle nodes. The interpolated surface normals can then be used to update the geodesic ray direction in such a manner that it is possible to do a proper order of convergence analysis. With interpolated surface curvatures we are able to evaluate the GTD formulas with sufficient accuracy.

By actually representing the solution along wave fronts we are able to use standard techniques to compute the field in caustics, to keep track of phase shifts as the wave front passes through caustics and, by interpolation, achieve high efficiency as

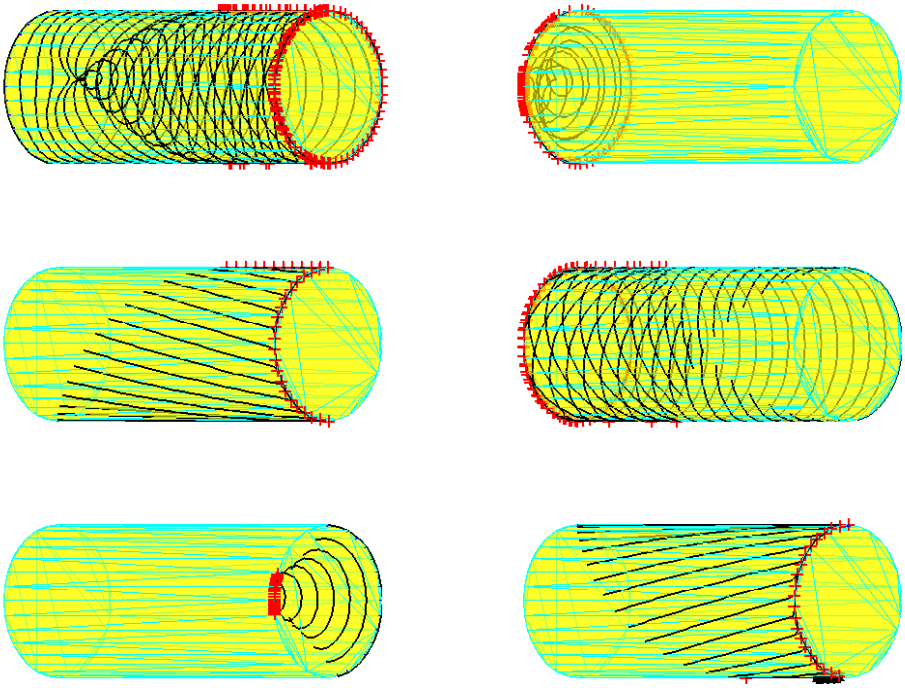

Figure 4.20: Example of generalized wave fronts on a cylinder meshed with a surface curvature sensitive mesh. The mesh can be perceived in the figure. Four fronts are edge excited and two fronts are excited by smooth surfaces. The stars indicate where we interrupt the front propagation. I.e at edges or shadow boundaries. In upper left figure one can see how a caustic forms and the orientation of the wave front changes. C.f. expression (4.104)

depletion of rays occurs.

Mathematical analysis suggest that the numerical error of the scattered field (c.f. (4.100)), while using Method 4.8, is of $\mathcal{O}(h)$. However, numerical results c.f. Figure 4.19, expression (4.55), Corollary 4.13 and mathematical analysis in Section 4.3.5 indicate that the method is actually convergent with an error proportional to $\mathcal{O}(h^2)$. Expressed in wave lengths, with element size is of $\mathcal{O}(\sqrt{\lambda})$, the error is bounded by a number, independent of λ, as we decrease λ and refine the mesh. Remark that it is then natural to use a surface curvature sensitive mesh, bounding the distance between the geometry and the mesh by an $\mathcal{O}(\lambda)$-parameter. If we necessarily want to have decreasing errors as we decrease λ we can for example use a classical mesh, where the element size is bounded by λ, to get an error that is of the order λ.

It may also be interesting to compare the complexity of our method with the Fast Multilevel Multipole (FMM) method. Assume that we want to compute the scattered field from a sphere. Using asymptotic techniques the complexity of computing the reflection contribution is negligible. Hence, the complexity of computing the smooth surface diffraction is the dominant one. In a boundary element method there are $\mathcal{O}(\lambda^{-2})$ unknowns and with FMM it takes $\mathcal{O}(\lambda^{-2}\log\lambda)$ time to solve the numerical problem. Assuming $\mathcal{O}(h^2)$ error in our method and a mesh with element size is of $\mathcal{O}(\sqrt{\lambda})$ we need $\mathcal{O}(\lambda^{-1})$ floating point operations to propagate a front over a surface curvature sensitive mesh of a sphere. With a global $\mathcal{O}(h)$ error we get approximately the same complexity as for FMM, i.e. $\mathcal{O}(\lambda^{-2})$. Remark, that we have disregarded the differences in constants of proportionality in the complexity analysis. E.g. since we can use surface curvature sensitive meshing in the asymptotic method, may the constant of proportionality be very small for geometries that contain large flat surfaces. In FMM the elements need to resolve the wave length.

To be able to apply the wave front construction technique we had to invent, an interpolation scheme for rays on faceted geometries, and a routine that find all shadow lines.

When it comes to implementational issues of the wave front construction technique, dynamic allocation of data and well organized data structure was crucial for the success of the method. This also enables efficient routines for engineering problems where many frequencies are studied for one specific problem.

During the presentation of the method and implementation above we had a scattering problem in focus. We emphasize however that it is quite easy to adapt the method to a radiation problem. The wave vector k in (4.5) will then be ξ-dependent and a modified diffraction coefficients, $D_p^{\mathcal{S},\mathcal{H}}(Q_1)$, has to be used in (4.14).

Chapter 5

Hybrid Methods

In this chapter we will present the second contribution in the thesis. Hybrid methods, combining Boundary Element Methods (BEM) and asymptotic methods, are studied. These hybrids are meant to be used on large problems where both small and large scales are present. The solution in the small scales will be represented by using boundary element methods while the solution in the large scales will be represented by using asymptotic methods. The numerical method presented in Chapter 4 could be an asymptotic method in the hybrid. However, we will consider more lower order asymptotic methods in our presentation.

Let us modify Figure 2.1 to Figure 5.1. We are interested in hybrid methods

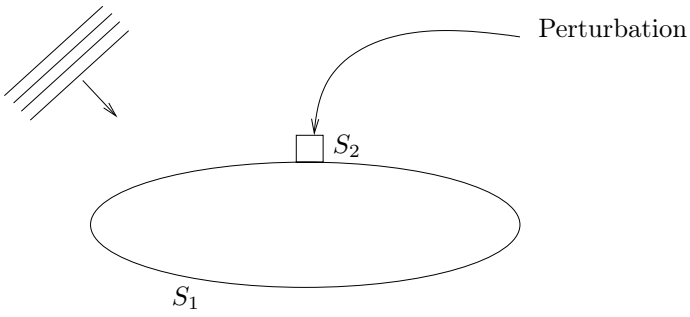

Figure 5.1: A perturbed scattering boundary value problem.

to be used for wave propagation problems where both relatively short and long wavelengths, λ, are present. Short and long wavelengths is referred to the characteristic sizes of the scales in the boundary conditions (BC), material properties (MP) and forcing. Depending on properties of the given data, one of three methodologies are used to hybridize the BEM with GTD. One of them is implemented and tested numerically.

We will only consider the scattering problem here since, from our method point of view, the radiation problem is then implicitly treated. We want to emphasis that the methodology we use is also applicable to antenna analysis such as antenna performance- and antenna-to-antenna isolation computations. A quite different discipline, where both large and small scales in the BC are present, are the photographic cards used by the integrated circuit manufacturers. Wavelength size notches are present in a ground plane of hundreds or thousands of wavelengths.

Sometimes the electromagnetic engineer needs to know how a small size feature, e.g. a small perturbation of the BC, affects scattering parameters. We indicate the original Scatterer by an upper case S and the small scatterer, i.e. the perturbation, with lower case s. If the perturbation together with the Scatterer is small, BEM will serve as an excellent tool for numerical computations. However, when the complexity of the problem overcome the computer resources, other methods must be used. It is well known that it is hard to say, ad hoc, that geometrically small sized features necessarily make a relatively small impact on electromagnetic parameters. In extreme cases, such as if small sized features in the order of wavelength size, are installed on stealth fighter aircraft they can actually affect the electromagnetic signature tremendously in specific sectors. The engineer thereby have to include all small features of $\mathcal{O}(\lambda)$ when the signature analysis is done. This means of course great demands on computer resources and engineering time.

In contrast to the rather intricate and complicated geometries, that are present in the engineering applications mentioned above, we will focus on very simple geometries in the discussion below. We do not think though, that there are any difference of principle between the true applications and the simplified boundary value problems, in terms of the applicability of our methods.

As an illustration of what type of boundary value problems that can arise in signature analysis we can think of two types of antennas. Exterior antennas, objects that actually are attached to a smooth part of the geometry and therefore leave the initial geometry unaffected, and structure integrated antennas, objects that we integrate in the skin. We have implemented one method that can be used to solve the first type of problem, represented by the exterior antenna, and we propose two other methods that can be applied to the more general case. To be able to relate the three methods to the two type of problems, exemplified above, let us consider Figure 5.2. It is not clear from our presentation up to this point why case A should be more representative for an exterior antenna than case B. However, let us postpone this discussion until we define our methods more thoroughly. If the perturbation only consist in an addition of a geometrical detail far from a boundary, i.e. the Scatterer's BC and MP is unaffected by the perturbation, the perturbation can be discretized with local boundary elements and the impact on scattering parameters can be taken into account with GTD. How this is done will later be shown more explicitly. If a boundary element is close to a Scatterer, hence does not illuminate the Scatterer with a Ray-field, we propose to use a linear combination of a flavor of the image method, and the GTD to model the interaction between large and small scales. Below will refer to this method as Method 1.

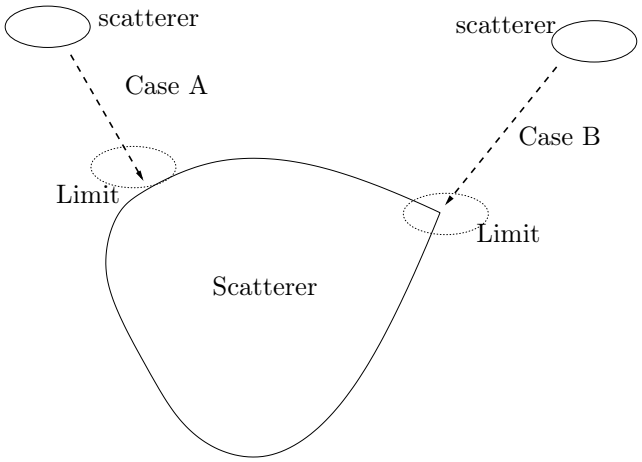

Figure 5.2: The limit of case A represents the exterior antenna and the limit of case B, will as we will show, the structure integrated antenna. In case A we are able to use method 1 independently of how close the scatterer is to the Scatterer. In case B method 1 will be less and less accurate as the scatterer and the Scatterer is approaching each other.

If the perturbation actually consist of a modification of the Scatterer or, as in Figure 5.2 the scatterer is close to non-smooth part of the Scatterer, we need as will be shown later, to solve a problem reminiscent to the limiting case of B. That is, the case when the perturbation is attached or close to the scatterer at a point where the surface normal is discontinuous. What we will propose is to actually incorporate the part of the Scatterer that contains the edge into the scatterer. This means that we will redefine both scatterers and we will introduce, what we call artificial edges, along the curve that indicate the common boundary of the two new scatterers. To treat the artificial edges, we propose that GTD edge diffraction is applied together with a new type of field transformation presented in [10]. Below will refer to this method as Method 3.

A final method is introduced and it reminds us of Method 3. We refer to this method as Method 2. It can be used for both case A and case B and we then suggest that mixed local and global boundary elements in the BEM-domain is used to model the interaction more rigorously. More specifically, we will discuss how to formulate the boundary integral problem for a small change in a infinite electric perfect conducting ground plane.

This thesis is by no mean the first work on hybrid methods between BEM and GTD. We therefore refer the reader to the early work reported in [58] and [59]. More later work are presented in [60], [61], [62] and [63]. A nice overview of hybrid methods can also be found in [64].

As mentioned earlier, we only investigate methods in the frequency domain. For hybrid methods in time domain we refer to the work performed in the GEMS-project [65] and [20], especially [66].

Chapter 2 treated the BEM method and Chapter 3 treated the asymptotic method GTD. We can therefore open the chapter by directly show how we can approximate substantial numerical work, i.e. solving Maxwell's equations by direct numerical method, e.g. by using explicit solutions to the Eikonal and Transport equations.

5.1 Hybrid Method 1, Theory

Consider the time harmonic Maxwell boundary value problem pictured in Figure 5.1. According to the boundary element technique presented in Chapter 2, we can numerically approximate the integral equation in (2.21) by using the Galerkin method. Let us write the linear system of equations in (2.26) as

$$A\mathbf{J} = \mathbf{E}^{exc}. \tag{5.1}$$

$\mathbf{J}$, the electric surface current density, is now a large unknown complex vector and A is full, complex, sometimes symmetric, matrix. For many engineering cases, will the size of vector $\mathbf{J}$ be too large to be found numerically even with the most modern numerical techniques implemented on state of the art super computers. Some approximations have to made! By splitting up S as in Figure 5.2 and calling the Scatterer for S_1 and the scatterer for S_2 we can manipulate (5.1) as follows.

The interaction between the Scatterer and the scatterer can either be done *iteratively* or by *directly* modifying the kernel in the integral equation. The iterative approach generally fails for the limiting case of both A and B since it is then hard to achieve sufficient accuracy in the numerical integrations done for equation (2.17) and (2.18). The direct approach only fails in the limit of Case B. However, for pedagogical reasons, we will present and investigate both methods.

5.1.1 Iterative Approach

Decompose (5.1) into a block matrix as

$$\begin{pmatrix} A_{11} & A_{12} \\ A_{21} & A_{22} \end{pmatrix} \begin{pmatrix} \mathbf{J}_1 \\ \mathbf{J}_2 \end{pmatrix} = \begin{pmatrix} \mathbf{E}_1^{exc} \\ \mathbf{E}_2^{exc} \end{pmatrix}, \tag{5.2}$$

where $\mathbf{J}_1 \in S_1$, $\mathbf{J}_2 \in S_2$ and we disregard for the moment the fact that there may exist basis functions that are non-zero both in S_1 and S_2. Then A_{jj} represent the impedance matrix of S_j and A_{ij} represent the coupling between S_1 and S_2. Solving (5.2) for $\mathbf{J}_1$ we can write

$$A_{22}\mathbf{J}_2 = \mathbf{E}_2^{exc} - A_{21}A_{11}^{-1}\mathbf{E}_1^{exc} + A_{21}A_{11}^{-1}A_{12}\mathbf{J}_2. \tag{5.3}$$

We will assume that this linear system can be solved with the iterative scheme

$$A_{22}\mathbf{J}_2^{(n+1)} = \mathbf{E}_2^{exc} - A_{21}A_{11}^{-1}\mathbf{E}_1^{exc} + A_{21}A_{11}^{-1}A_{12}\mathbf{J}_2^{(n)}. \tag{5.4}$$

The convergence of of (5.4) is mathematically investigated in [67].

Since we assumed that $dim(A_{11}) \gg dim(A_{22})$ we would like to compute the influence of $\mathbf{J}_1$ on $\mathbf{J}_2$ with a fast method and then solve for $\mathbf{J}_2$ rigorously. I.e. we want to avoid filling and inverting the large matrices in term two and three on the right hand side. Some physical intuition and results from the literature is now needed to proceed. Literature suggest that if the Scatterer is an infinite ground plane then image theory could be used to compute term two and three exactly. If the scatterer is far from the Scatterer, and asymptotic techniques are applicable to S_1, we can use GTD for the non-limiting cases of A and B to estimate the terms. What to do if the scatterer is close to a smooth Scatterer, i.e. the limit of A? We propose the following method to be used.

Given an EM point source x_s (c.f. Section 2.2), and an arbitrary point x above a scatterer then we can, if the scatterer $X(\xi_1, \xi_2)$ is convex, define a so called Geometrical Optics (GO) reflection point $X_{rp}(\xi_{rp})$ where ξ_{rp} solves

Definition 5.1.

$$\min_{\xi} \left(|x_s - X(\xi)| + |X(\xi) - x|\right) \equiv \min_{\xi} \left(s_{br}(\xi) + s_{ar}(\xi)\right) = \min_{\xi} f(x_2, x, \xi).$$

For non-convex boundaries we actually have to generalize the definition by searching for stationary points, i.e. $\nabla_\xi f = 0$. For later reference we also define

Definition 5.2. the closest point X_c as the vector solving

$$\min_{\xi} \left(|x_s - X(\xi)|\right).$$

With Einstein notation of derivatives we can compute the surface normal in X_{rp} as

$$\hat{n}_{rp} = \left.\frac{X_{,1} \times X_{,2}}{|X_{,1} \times X_{,2}|}\right|_{\xi=\xi_{rp}},$$

and a unique infinite ground plane P_{RBI}, going through X_{rp} and having a normal $\hat{n}_{rp}$, can be defined. The corresponding closest point definition can be used to define P_c. We are now able to define the so called *Ray Based Image method* (RBI-method), applied to a source $E(x; x_s)$.

Method 5.3. *Apply the image theory presented in Section 2.6 to P_{RBI} and $E(x; x_s)$, to get an image source $E^{img}(x; x_s^{img})$. Let the total scattered field from the Scatterer and the source be approximated by*

$$E^{tot}(x) = E(x; x_s) + E^{img}(x; x_s^{img}).$$

For later reference we also define the following method

Method 5.4. *Apply the image theory presented in Section 2.6 to P_c and $E(x;x_s)$, to get an image source $E_c^{img}(x;x_s^{img})$. Let the total scattered field from the Scatterer and the source be approximated by*

$$E^{tot}(x) = E(x;x_s) + E_c^{img}(x;x_s^{img}).$$

If we are not in the limiting case of A or B we can also compute the total field by using GTD. Let us just call it the GTD-method. Referring to Chapter 3 we know that the electromagnetic field along a GTD ray is assumed to be orthogonal to the ray direction, the electric and magnetic field to be in phase and $|E|/|H| = Z$. Assume that the point source is an electric or magnetic dipole, then we can use the formulas in Section 2.2 to compute $E(X_{rp};x_s)$ and $H(X_{rp};x_s)$. If the source is a surface current in a domain with a size much less than a wave length, c.f. the end of Section 2.2, we can use the integrals (2.17) and (2.18) to compute $E(X_{rp};x_s)$ and $H(X_{rp};x_s)$. In neither case we know a priori that $E(X_{rp};x_s)$ and $H(X_{rp};x_s)$ can locally be well approximated by one Ray-field. What actually can be done is to numerically compute a sum of Ray-fields and ray directions which asymptotically in the high frequency limit approximate the electromagnetic field. This is done by using electromagnetic field data in the neighborhood of X_{rp} (c.f. [10]). We will not pursue this idea any further but our GTD-method will be based on the following a priori assumption.

Assumption 5.5. *Let*

$$\hat{k} = \frac{X_{rp} - x_s}{|X_{rp} - x_s|},$$

then the electromagnetic field E and H in X_{rp} is well approximated by the spherical Ray-fields, centered in x_s,

$$\tilde{E}(X_{rp};x_s) = E(X_{rp};x_s) - \hat{k}(E(X_{rp};x_s)\cdot\hat{k})$$

and

$$\tilde{H}(X_{rp};x_s) = \frac{\hat{k}\times\tilde{E}(X_{rp};x_s)}{Z},$$

where Z is the free space wave impedance.

Below we will mainly discuss GTD-reflection. A similar discussion could be done on GTD-diffraction. X_{rp} is then replaced by a diffraction point which we could call X_{dp}.

Let $(\tilde{E},\tilde{H})$ be a Ray-field propagating in direction $\hat{k}$ then the total field in an arbitrary point x along the ray can be approximated with the GTD-method.

Method 5.6. *Let the total scattered field from the Scatterer and the source be approximated by*

$$E^{tot}(x) = E(x;x_s) + GTD(\tilde{E},\hat{k},x,X_{rp},G;x_s),$$

where $GTD(\cdot)$ indicate that the field should be reflected/diffracted and propagated according to formulas from GTD [33] and G represent geometrical data computed at the reflection/diffraction point. We assume that the source is point like and it will therefore produce a spherical wave front of radius $|X_{rp} - x|$ at X_{rp} (c.f. end of Section 2.2).

To understand the RBI- and the GTD-method applied to the iterative scheme in (5.4), let us consider Figure 5.3. It represents one triangle element of the scatterer, its image and a small part of the Scatterer. We exemplify the method by considering the ground plane-triangle interaction for one triangle element, i.e. half of a boundary element, and disregard the other triangles in the scatterer. At iteration level $n = 0$ we compute the plane wave excitation represented by term one in (5.4) directly. Term two we compute by using GTD (a plane wave is a Ray-field, c.f. Chapter 3). Finally we solve the linear system by setting $\mathbf{J}_1^{(0)}$ to zero. At next step we need to compute the coupling term, i.e. the third term, between the Scatterer and the scatterer. This can be done with the GTD-method if the triangle is far from the Scatterer or by computing the field from the image triangle, c.f. RBI, if it is close to the Scatterer. Using the GTD-method we just compute the field from $\mathbf{J}_2^{(0)}$ at the reflection point according to Assumption 5.5 and Method 5.6 (source and receiver in the same point). This field can then be reflected and propagated back to the triangle according to GTD formulas. The field from the image triangle can be computed by using the technique implied by the discussion in Section 2.6. That is, we can estimate (2.17) and (2.18) for the image triangle by numerically compute the field in an Image Field Point from the (non-image) triangle and then apply a rotation operator to this field. Now all three terms is known at level $n = 1$ and we can solve the system to get $\mathbf{J}_2^{(1)}$. The self illumination can be repeated until convergence has been reached. The scattered field can be computed by using the same technique as for the self illumination but the field point is then not a point any more but a specified direction.

It is hard to say something general about the convergence of the iterative scheme discussed above because only A_{22} is known explicitly, since the other terms on the right hand side is only estimated with the GTD- and RBI-method. The convergence rate will of course depend on the errors we do by approximating term two and three with the GTD- and RBI-method but also the specific geometry for the Scatterer and the scatterer. However, as we will see in the numerical result, the convergence is rather fast if the Scatterer is convex close to the perturbation and if the perturbation does not trap waves between itself and the Scatterer. Naturally no correct convergence is reached if the numerical errors is too big when computing (2.17) and (2.18). Note that the right hand side is computed by using numerical quadrature applied to a limited number of points (in our implementation only one or three points) on each triangle and then numerically estimate, by a plane wave assumption, an integral over each triangle. If the field is rapidly changing over the triangle it is unwise to use this iterative technique since it will be very costly to evaluate the field in sufficiently many points to get sufficient accuracy. In the extreme case,

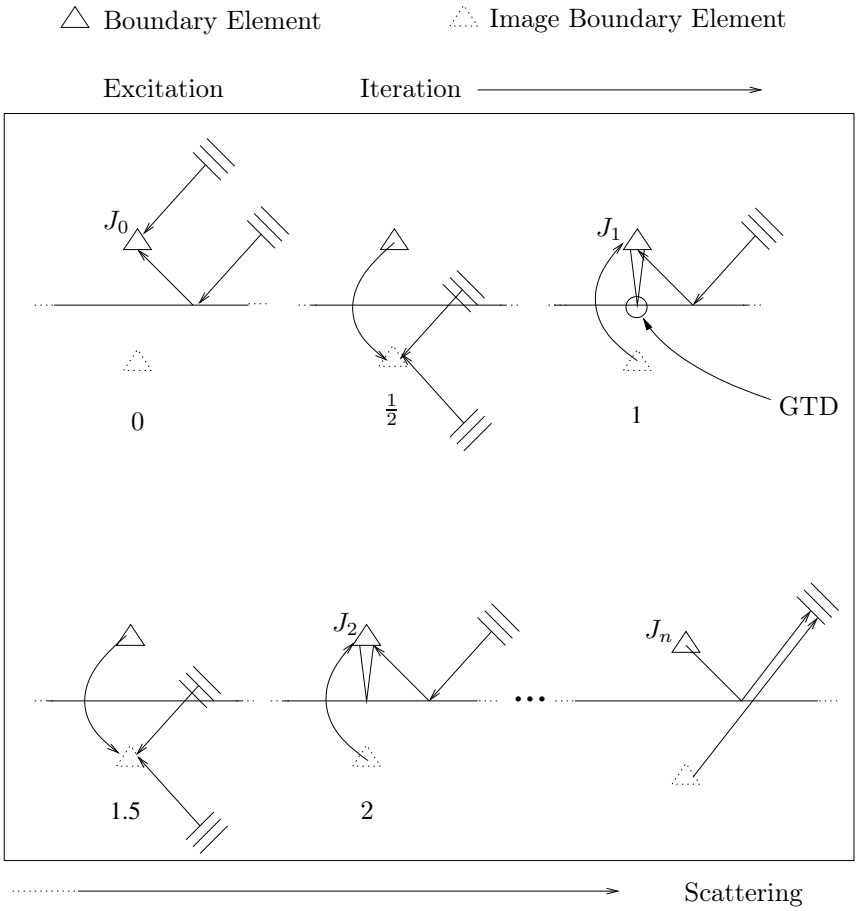

Figure 5.3: Excitation and Scattering with only Direct and Reflected contributions present. The horizontal line represent the Scatterer and the triangle indicated by a continuous line represent the a part of the small scatter. The dotted triangle represent the image of the triangle.

when the triangle is attached to a non-flat Scatterer, probably no convergence can be reached since the integration partly needs to be done analytically. The direct method will address this drawback.

We remind the reader that if a boundary element triangle edge is only shared by one triangle no current is allowed to pass over that edge, i.e. for a PEC triangle there is no degree of freedom on that edge. However, triangles edges in the scatterer that have electrical contact with the Scatterer should have at least one degree of freedom.

As already mentioned, the RBI-method is intended to be used for problems where the Scatterer is smooth in the proximity of the scatterer, i.e. in the limiting case of A. RBI is not a good approximation when the receiver triangle is far away from a non-flat Scatterer. We realize this by considering GTD, which we know is asymptotically correct. It is clear that the attenuation factor, from a propagating reflected GTD-field, and the diffraction coefficient is strongly dependent on first and second order surface derivatives at the reflection/diffraction point. This dependence is not explicitly present in RBI. The derivatives are only implicitly present when the point P is searched. Differently stated, the phase may be rather well taken into account by RBI in field points far from the Scatterer but the amplitude will be less accurate. A similar discussion can be done for a source triangle by a reciprocity argument.

We have now presented the RBI-method which we assume is successful in the limiting case of A and the GTD-method which we assume is successful in the non-limit case of A and B. It is apparent that we would like to have a method that is a combination between the GTD method and the RBI method so that we get a more generally applicable method. We suggest a method that can be used to compute the second and third term on the right hand side of (5.4) by using a linear combination of the GTD- and RBI-method. The exact appearance of the optimal combination is naturally dependent on the problem at hand and we will not investigate this thoroughly but postpone it to the numerical experiments. Consider (5.4) and let us define

$$Y = A_{21}A_{11}^{-1}A_{12},$$

and a star $*$-operator as element wise multiplication of matrices (c.f. the Matlab® operator $.*$). Then we can *split* Y in (5.4) as

$$A_{22}\mathbf{J}_2^{(n+1)} = \mathbf{E}_2^{exc} - A_{21}A_{11}^{-1}\mathbf{E}_1^{exc} + (\alpha * Y + \beta * Y)\mathbf{J}_2^{(n)}, \tag{5.5}$$

where α and β are matrices fulfilling

$$\alpha_{ij} + \beta_{ij} = 1 \ \forall \ (i,j). \tag{5.6}$$

For the impressed plane waves, represented by term one and two, we may apply GTD directly since a plane wave is a Ray-field.

5.1.2 Direct Approach

Let us now consider the *direct* approach. Even though we have a non-flat ground plane in the general case let us consider an infinite perfect electric ground plane as the Scatterer. Then we know from the symmetry of the Green function (image theory) that we may solve the problem by replacing the ground plane with an image of the small scatterer and an image of the impressed sources. Let us call currents in the small scatterer $\mathbf{J}_2^D$ and the currents on the image for $\mathbf{J}_1^D$. In the discrete case

$\mathbf{J}_1^D$ and $\mathbf{J}_2^D$ are vectors of scalar numbers and the coupling between the currents are represented by the D_{ij} in the following matrix problem

$$D_{11}\mathbf{J}_1^D + D_{12}\mathbf{J}_2^D = \mathbf{E}_1^{exc}(\mathbf{x}) + \bar{\mathbf{E}}_1^{exc}(\mathbf{x}) \quad (5.7)$$
$$D_{21}\mathbf{J}_1^D + D_{22}\mathbf{J}_2^D = \mathbf{E}_2^{exc}(\mathbf{x}) + \bar{\mathbf{E}}_2^{exc}(\mathbf{x}), \quad (5.8)$$

where the bar sign assigns the image excitation. By profiting on the linearity of the basis functions, c.f. Chapter 2, and by enumerating the unknown scalar numbers $\mathbf{J}^D$ properly, we realize that $\mathbf{J}_1^D = -\mathbf{J}_2^D$. We can therefore write

$$(D_{22} - D_{21})\mathbf{J}_2^D = \mathbf{E}_2^{exc} + \bar{\mathbf{E}}_2^{exc}(\mathbf{x}). \quad (5.9)$$

D_{22} is a standard impedance matrix for the currents in the small scatterer above the ground plane. Up to this point the only errors we made are of numerical nature by discretizing the geometry and the currents. To solve the true problem with a non-flat ground plane we use the RBI-method to compute D_{21} approximately. I.e. for each element in D_{22}, representing the coupling between the basis functions and test functions, we have an additional element in D_{12} representing the coupling between the image of the basis function and the test function. The position of the image is computed by using RBI. Since $D_{22} = A_{22}$ in (5.2) and approximately $\mathbf{J}_1 = \mathbf{J}_1^D$ we can compare the direct RBI approach with the iteration (5.5) by writing

$$(A_{22} - D_{21})\mathbf{J}_2 = \mathbf{E}_2^{exc} + \bar{\mathbf{E}}_2^{exc}(\mathbf{x}). \quad (5.10)$$

We realize that the second term on the right hand side, i.e. the image of the excitation, can be estimated with GTD as was done for the iterative case. If the scatterer is close to a smooth Scatterer then we believe that (5.10) is an efficient way to solve the sub-scattering problem pictured in Figure 5.1, i.e. the limiting case of A. However, if parts of the scatterer can be considered to be close to the Scatterer and other parts to be far from the scatterer we suggest a method that combines (5.5) and (5.10).

5.1.3 Combination of Direct and Iterative Approach

By using the same notation as in (5.5) we can split D_{12} in (5.10) as

$$\left(A_{22} - (\alpha * D_{12} + \beta * D_{12})\right)\mathbf{J}_1 = \mathbf{E}_1^{exc} + \bar{\mathbf{E}}_1^{exc}(\mathbf{x}),$$

which can be solved with an iterative scheme as

$$(A_{22} - \beta * D_{12})\mathbf{J}_1^{n+1} = \mathbf{E}_1^{exc} + \bar{\mathbf{E}}_1^{exc}(\mathbf{x}) + \alpha * D_{12}\mathbf{J}_1^n, \quad (5.11)$$

where we have assumed that $A_{22} - \beta * D_{12}$ is non-singular. If all BEM-triangles are relatively close to a smooth Scatterer all α_{ij}:s may be put to zero and we get a direct method. By comparing with the iterative method we realize that $D_{12}\mathbf{J}_1^n$ may be estimated by either the GTD-method or the RBI-method. If all BEM-triangles

are relatively far from the Scatterer all β:s may be put to zero and we can use the GTD-method to estimate the third term on the right hand side. If parts of the scatterer is far and other parts is close the α_{ij}s and β_{ij} should be chosen so that we achieve as small asymptotic errors as possible.

The matrices represented by the α_{ij}s and β_{ij}s are not necessarily symmetric. By intuition the elements should be dependent on the distance between the basis function and the Scatterer, and the distance between the test function and the Scatterer.

We note that when (5.5) or (5.11) has converged, we can with the help of the representation theorem and a linear combination between the GTD- and RBI-method, compute the scattered field.

5.2 Hybrid Method 1, Complexity

5.2.1 Complexity Analysis

Let us consider a somewhat artificial but illustrating scattering problem where we escape from the inherent problem with non-smooth boundaries by only having disjunct sub-scatterers S_j well distanced from each other, with $j = 1 \dots q$. Also assume that all S_j is approximately of the same size in number of unknowns n and that $N \approx qn$ is the the total number of unknowns. Could we put the method in the last section in a more general setting by considering it as domain decomposition method?

Assume that we use the Fast Multipole Method (FMM) to solve for the currents on each S_j and use N_{iter}^{hybrid} iterations to include the GTD interaction with the other scatterers

$$S_1, \dots, S_j, S_{j+1}, \dots, S_q.$$

The largest complexity in the hybrid method is then found in the computation of the image impedance, that is, a complexity of $\mathcal{O}(\frac{N}{n} n^2 N_{iter}^{hybrid}) = \mathcal{O}(NnN_{iter}^{hybrid})$ in terms of arithmetic operations. Compared to FMM, $N_{iter} N \log N$, this complexity number looks rather disappointing and the success will be strongly dependent on q. Especially if you take into account that, in our implementation, the constant in front of the complexity expression must be considered to be rather large for implementations developed for quite general problems with large focus on robustness. For each element in the impedance matrix a number of rays must be found by passing through logics and several calls to a Conjugate Gradient algorithm. There are also $\mathcal{O}(Nn)$ algorithms in the solver such as the excitation and scattering represented by rays.

However a more advantageous comparison, from a hybrid point of view, with other methods is achieved if we split up the $\mathcal{O}(NnN_{iter}^{hybrid})$ complexity in two terms

$$C_{geo}\mathcal{O}(Nn) + C_{field}\mathcal{O}(NnN_{iter}^{hybrid}).$$

The *geometrical* computations has a much larger coefficient, C_{geo}, than the frequency specific *field* computations represented by the second term. Note though, that the geometrical computations are frequency independent and we can therefore achieve the solution for a large number frequency, i.e. a broad band solution, with a relatively efficient algorithm.

The memory requirements are of $M_{geo}\mathcal{O}(qn^2) + M_{field}\mathcal{O}(qn^2)$ to be compared with the Fast Multipole Multipole (FMM) which is of $M_{FMM}\mathcal{O}(qn\log qn)$.

Finally we would like to point out that the hybrid method is mainly designed for engineering problems mentioned in the introduction where only a few sub-scatterer is meshed which make the following Hybrid/FMM-ratio

$$\frac{C_{geo}n^2 + C_{field}n^2 N_{iter}^{hybrid}}{C_{FMM}N_{iter}^{FMM} N\log N} \tag{5.12}$$

more relevant.

5.2.2 Partition of Unity

With the complexity discussion in the last section in mind, we theoretically investigate the possibility to reduce the size of C_{geo}. We propose that a type of partition of unity method is applied to speed up the ray calculations. For simplicity we only discuss the excitation computations.

Assume that the scatterer is N_λ wave lengths large which will, especially for many plane wave computations, make the ray computations for the first term in equation (5.11) quite time consuming. More specifically, will the complexity be of $\mathcal{O}(N_\lambda^2 N_{rh})$, where N_{rh} is the number of right hand sides, or plane waves.

Let us use equation (4.21) to define the mesh error, ϵ. Assume that we may approximate the geometry with triangles that are of size $\mathcal{O}(\sqrt{\lambda})$ and fulfill $\epsilon < \lambda/10$, then by using this mesh during the geometrical computations we would achieve an algorithm of $\mathcal{O}(N_\lambda N_{rh})$. That is, we have decreased the C_{geo}-term with a factor N_λ.

To be able to approximate, i.e. finding all GTD-rays and evaluate all matrix and vector elements, the right hand side in equation (5.11) we need two meshes. One to resolve the geometry represented by the N_λ and one to resolve the incoming field $\mathbf{E}_{exc}^1 + \bar{\mathbf{E}}_{exc}^2$ to all $\mathcal{O}(N_\lambda^2)$ elements. As an example, let us consider figure 5.4. We see how each super triangle (bold lines), T, is subdivided into four triangles, t_j. Rays can be computed to each three super nodes X_ξ^ε, $\xi = 1\ldots 3$. Knowing the rays, $E_{exc}^\mu(X_\xi^\varepsilon)$ can also be computed by local plane wave assumption. To compute the incoming field in each field point one can for example use interpolation, i.e. the field in a point x^ε is approximated to be

$$E^\mu(x^\varepsilon) = \delta_\nu^\mu P^{\nu\xi}(x^\varepsilon) E_{exc}^\nu(X_\xi^\varepsilon), \tag{5.13}$$

where $P^\mu(x^\varepsilon)$ is a vector valued Partition of Unity function fulfilling

$$P_T^{1\nu}(x^\varepsilon) + P_T^{2\nu}(x^\varepsilon) + P_T^{3\nu}(x^\varepsilon) = 1, \tag{5.14}$$

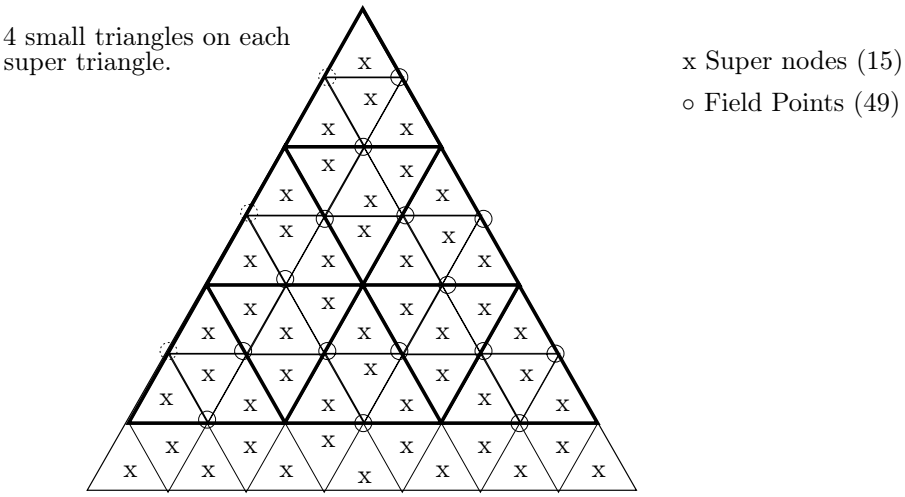

Figure 5.4: One patch of a sphere meshed with small triangles and super triangles.

for any x^{ε} and polarization ν in a super triangle T.

We see an example of a double mesh in figure 5.5. Each initial triangle is refined with 4, 16 and 64 smaller ones. Since we use like sided triangles the finest subdivision will give us super triangles that have edges that are around λ long (assume that we resolve the wave with 10 elements).

The reason for that we do not start with a fine grid and then make it coarser is double folded. It may be hard to define the partition of unity function, with support on a surface, which fulfill (5.14) if the small triangles do not lie in the same plane as the large triangles. That is, the small triangles does not generally have support on the super triangles in this case. Of course we could use partition of unity functions defined off the triangulated surface but that would be unphysical since the fundamental unknowns are only defined on the surface. Secondly, it may be hard to find a robust meshing algorithm starting out with a fine mesh and then create a coarser mesh within certain accuracy limits on ϵ.

Partition of unity methods can be used for all ray tracing parts in the hybrid solver. For example may the plane wave excitation be speeded up by only computing rays for every tenth angle and then use the plane wave assumption when the rest of the angles are treated [27]. Also, the impedance computation can be speeded up clustering starting points or ending points for all rays. In this case a circular wave assumption should be used instead of a plane wave assumption. Finally we point out that, for the case of impedance computation speed up, if some elements in the scatterer is close to the Scatterer then the partition of unity approximation discussed above will probably produce too large errors and adaptive methods must be used instead.

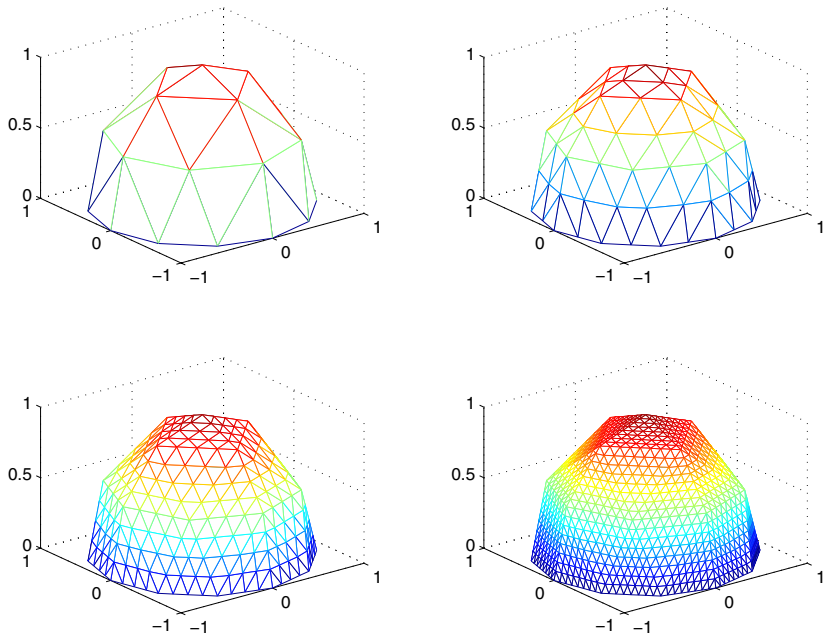

Figure 5.5: A hemisphere discretized at four levels. Note that the geometrical accuracy in the meshed geometry is held constant. The hemispheres are discretized with 16, 64, 256 and 1024 triangles.

5.3 Hybrid Method 1, Implementation

The computer implementation of the hybrid discussed in Section 5.1 was done by combining two existing solvers. A boundary element solver [16] and a GTD solver [17]. The original requirements on the GTD-solver where designed, among other things, for a hybrid implementation. Three geometries is used by the hybrid solver.

1. A NURBS-description of the Scatterer (GTDGeo1) to be used for the computation of rays for $\mathbf{E}^1_{exc}$ in equation (5.11).

2. A NURBS-description of the Scatterer (GTDGeo2) to be used for the computation of GTD/RBI rays in D_{12} for equation (5.11).

3. A triangle mesh of the scatterer (BEM) to be used for the computation of A_{22} in the boundary element solver.

The reason for that we have two NURBS geometries in the ray computation is that we believe that the experienced engineer know how to remove less important part

```
call ReadProblem
call ReadGTDGeo1
call CreateExcEvents
call DeallocateGTDGeo1
call ReadGTDGeo2
call CreateIterationEvents
call DeallocateGTDGeo2
call ReadBemGeometry
FreqLoop: do jj=1,FreqList%items
  call ExcitationAttenuation
  call ModifyImpedanceMatrix
  IterationLoop: do ii=1,NrOfIterations
    call RunRandolph
    call ComputeGTDWaves
    call IterationAttenuation
    call ComputeExcField
  end do IterationLoop
  call ComputeGTDWaves
  call ScatteringAttenuation
  call PrintResult
end do FreqLoop
call deallocate
```

Figure 5.6: Algorithm for Hybrid method 1.

of the geometry when the image impedance D_{12} is computed. Roughly speaking, geometrical details that are far away from the scatterer make a small impact on the image impedance matrix. The two NURBS geometries must be processed in a CAD software so that it fulfills certain design rules [68].

The triangle mesh, which must be compatible with GTDGeo1 and GTDGeo2, is a standard boundary element mesh [69] with the extra information indicating which, if any, nodes that are attached to the Scatterer.

The main program, intended for mono-static scattering problems, is schematically described in Figure 5.6.

In `CreateExcEvents` a list of excitation events, describing rays starting from a direction and stopping at a boundary element center of gravity, is created and saved for later use (a copy of the reversed events are also created representing the scattering events). In `CreateIterationEvents` a list of iteration events, describing rays starting at a boundary element and stopping at a boundary element, is created and saved for later use. The exciting field is computed with a GTD-routine called `ExcitationAttenuation` by using excitation events as argument. The image impedance D_{12} is added to A_{22} in `ModifyImpedanceMatrix`. In `RunRandolph` the currents on the scatterer is computed. The scattered field at event points (reflection/diffraction) is computed by the numerical approximation of

equation (2.17) and Method 5.6 in `ComputeGTDWaves`. The fields at the event points is attenuated in `IterationAttenuation` with the iteration events as argument. A new right hand side to $A\mathbf{J}^{n+1} = E^n$ is computed in `ComputeExcField`. When a user defined convergence is attained, scattered fields at scattering event points is computed in `ComputeGTDWaves`. The scattered field is computed/attenuated with the RBI- or GTD-method with the scattering events in argument to subroutine `ScatteringAttenuation`.

We emphasis that the computer time consuming routines `CreateIteration-Events` and `CreateExcEvents` is done outside the `FreqLoop`. This is advantageous when the problem is investigated for many frequencies.

5.4 Hybrid Method 1, Numerical Examples and Results

In this section we will compare the hybrid method described in Section 5.1 with a boundary element solution. In some examples it is possible to compare the currents computed with the hybrid with currents from the boundary element solver. For some other problems we think that it is more illustrative to compare the scattered fields. For the current computations we use the following error estimates

Definition 5.7.

$$e_c(j) = 10\log_{10}\left(\frac{1}{n}\sum_{e=1,n}\left|\frac{J^e_{apprx} - J^e_{bem}}{J^e_{bem}}\right|\right), \tag{5.15}$$

where n is the number of unknowns in the scatterer, j the iteration number and J^e is the complex scalar defined in equation (2.25). For the field computations we use

Definition 5.8.

$$e^{\mu\nu}_f(x_s, x) = \log_{10}\left(\left|\frac{E^{\mu\nu}_{BEM}(x_s, x)) - E^{\mu\nu}_{approx}(x_s, x)}{E^{\mu\nu}_{BEM}(x_s, x))}\right|\right). \tag{5.16}$$

This error depends on four vectors. μ indicate the polarization of the source in a point x_s and ν the polarization of the field in a point x. Addressing the discussion on Ray-field in the end of Section 2.2 it is sometimes more illustrative to plot the field errors in the *Ray coordinates*, (s_1, s_2). Referring to Definition 5.1 we define, for a source in x_s and a field point/receiver in x, the wave length dependent Ray coordinates (s_1, s_2) as

Definition 5.9.

$$s_1 = \frac{s_{br}}{\lambda}$$

and

$$s_2 = \frac{s_{ar}}{\lambda},$$

where λ is the wave length we solve for. Note that for a convex Scatterer $(x_s, x) \leftrightarrow (s_1, s_2)$ is a bijection.

5.4.1 Error for Approximate Fundamental Solution Above a Truncated Sphere

We start the error analysis by computing the scattered field from an infinitesimal electric dipole placed at three different positions x_s, with three different polarizations ($\nu = 1 \dots 3$), just above the north pole of a truncated sphere. The reason for merging the error plots was to reduce computational cost for the test cases, i.e. by moving the source properly we can achieve error plots in a larger (s_1, s_2)-space with less computational cost. The parametrical space is explained by Figure 5.7.

It is natural to initiate the error analysis of the hybrid method by testing the method on an *infinitesimal dipole* above a non flat ground plane since, in the more composite problem, with currents defined over triangle edges, we have an infinite union of these. If RBI fails in this simple case it will in general fail for the more complex case to. It is also interesting to not only compare the scattered solution with a numerically converging method but also with other asymptotic/approximate methods. Our four approximate solutions are the following.

PO The unknown currents on the truncated sphere is computed with Physical Optics (PO), c.f. equation (2.23), and then scattered by applying numerical quadrature to (2.17).

RBI The scattered field is computed with the RBI method described in Method 5.3.

GTD The scattered field is computed with the GTD method using Method 5.6 and using field expressions in Section 2.2 at the reflection point.

IMG The scattered field is computed with image theory according to Method 5.4.

The relative error in definition 5.8 has been used in the plots. The four approximate solutions are compared with the boundary element solution (approximately 80000 unknowns) in Figure 5.8 to 5.12. Since the asymptotic solutions in e_f^{12}, e_f^{21}, e_f^{23} and e_f^{32} are so small, that it is hard to interpret the errors, we choose to omit these plots in our presentation. Note that we have truncated the color bar scale so that values less than -2 are approximated to be -2 and values larger than 1 are approximated to be 1.

Each sub-figure is a superposition of three runs, each having the dipole placed at three different positions. The truncated sphere is meshed with care. Not, only the scale in the differential operator needs to be resolved by the boundary elements but also the incoming field, i.e. $\mathbf{E}_1^{exc}$ in equation (5.11). The incoming field changes faster than the characteristic scale, represented by λ, do. We have therefore decreased the element size just below the dipole, c.f. end of Section 2.2.

Some important observations on the numerically converging solution must be made before the errors in the asymptotic/approximate solutions can be discussed. What we really would like to compare our asymptotic solutions with is an infinite convex body, since then asymptotically all currents on the Scatterer would be outgoing and only the local currents will make the main contribution to the scattered

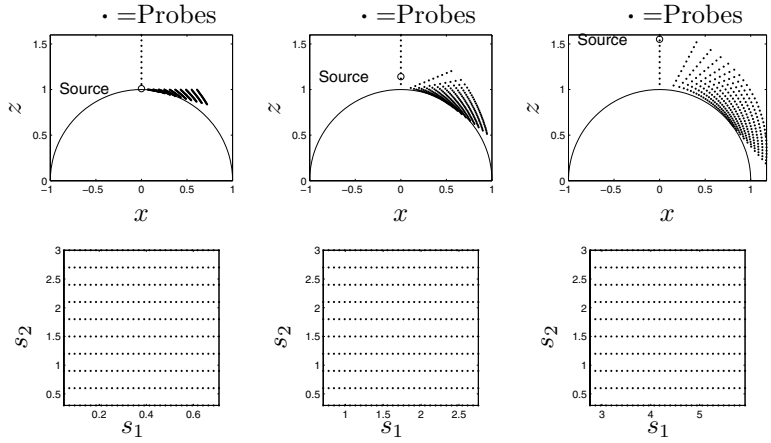

(a) Parameter space case 1.

(b) Parameter space case 2.

(c) Parameter space case 3.

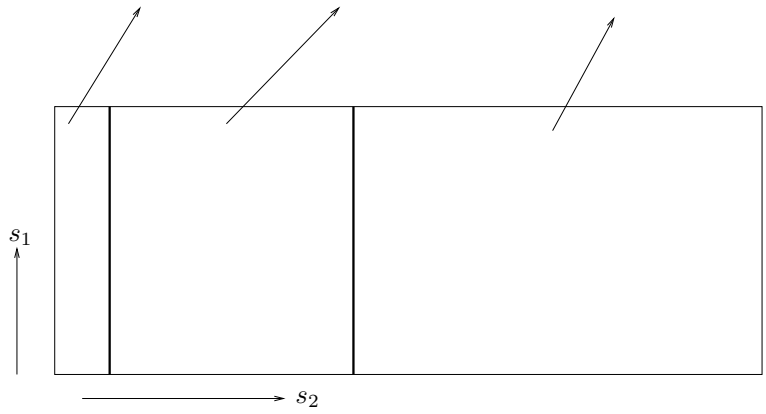

(d) Blank illustration of error plots

Figure 5.7: The probe points lies in the x_1x_3-plane and the dipole is positioned some distance above the north pole of a truncated sphere. The truncation plane coincide with the x_1x_2-plane.

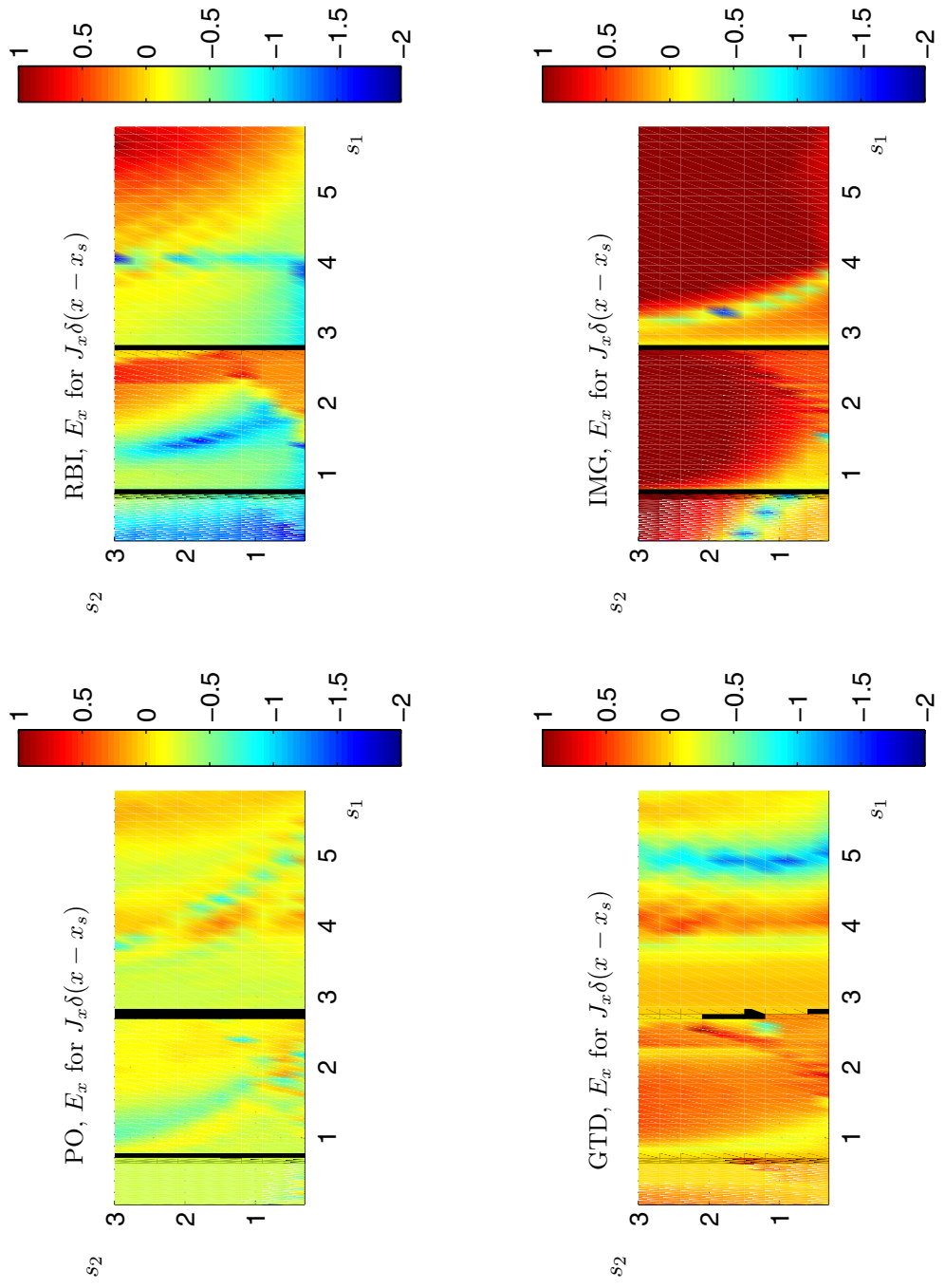

Figure 5.8: Co-polar measure. Logarithm of relative error for the J_x- and E_x-polarization.

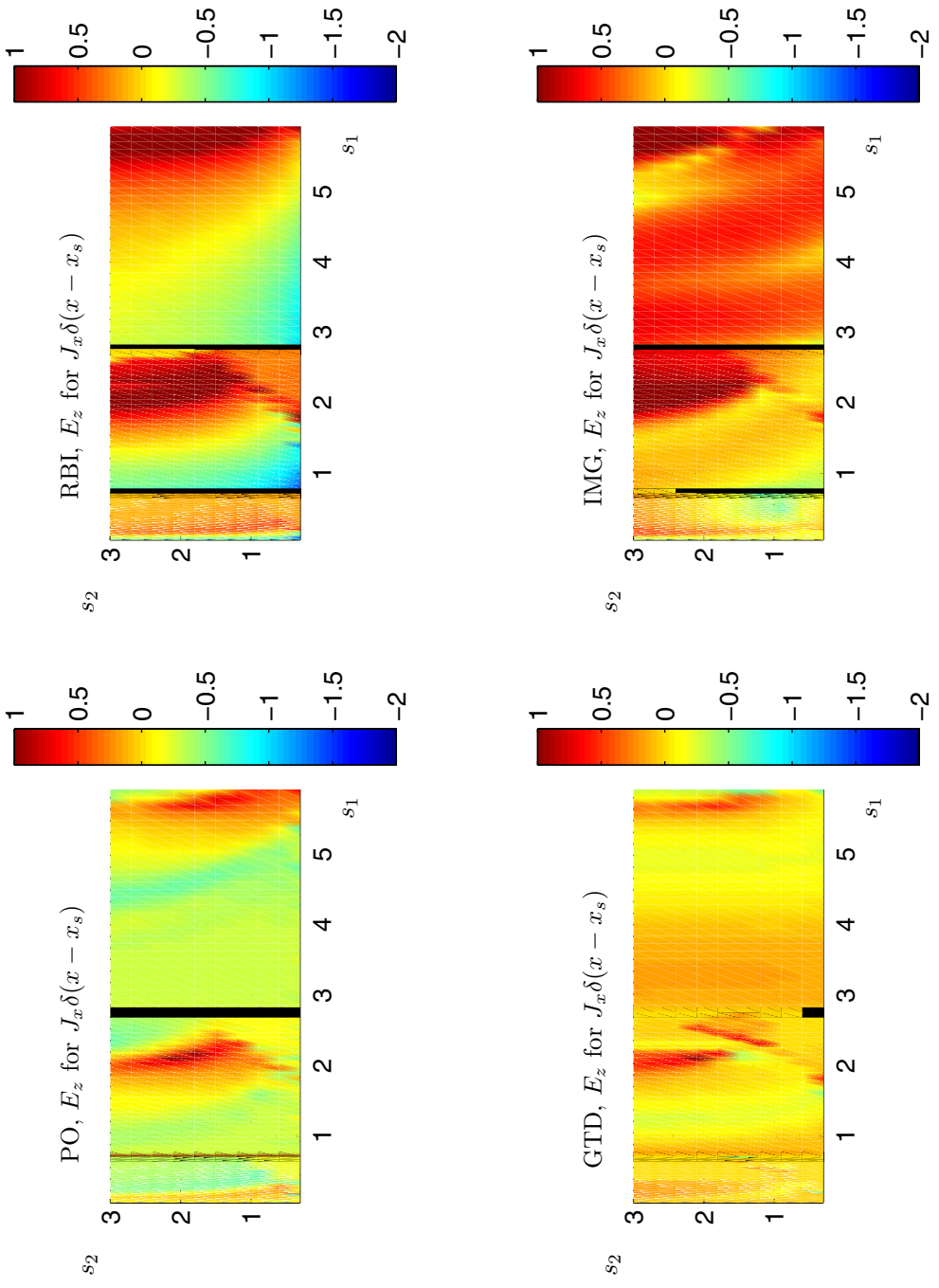

Figure 5.9: Cross-polar measure. Logarithm of relative error for the J_x- and E_z-polarization.

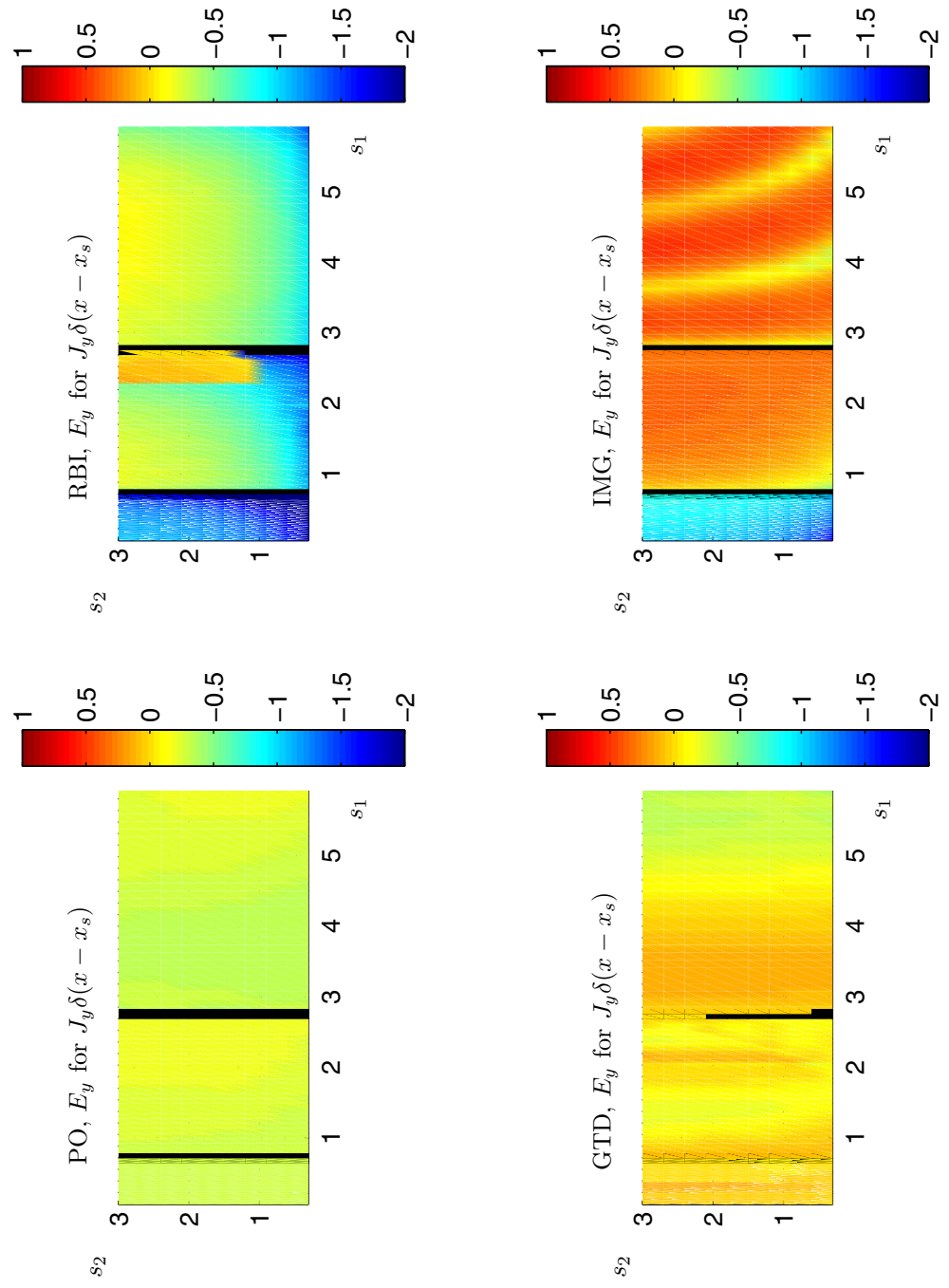

Figure 5.10: Co-polar measure. Logarithm of relative error for the J_y- and E_y-polarization.

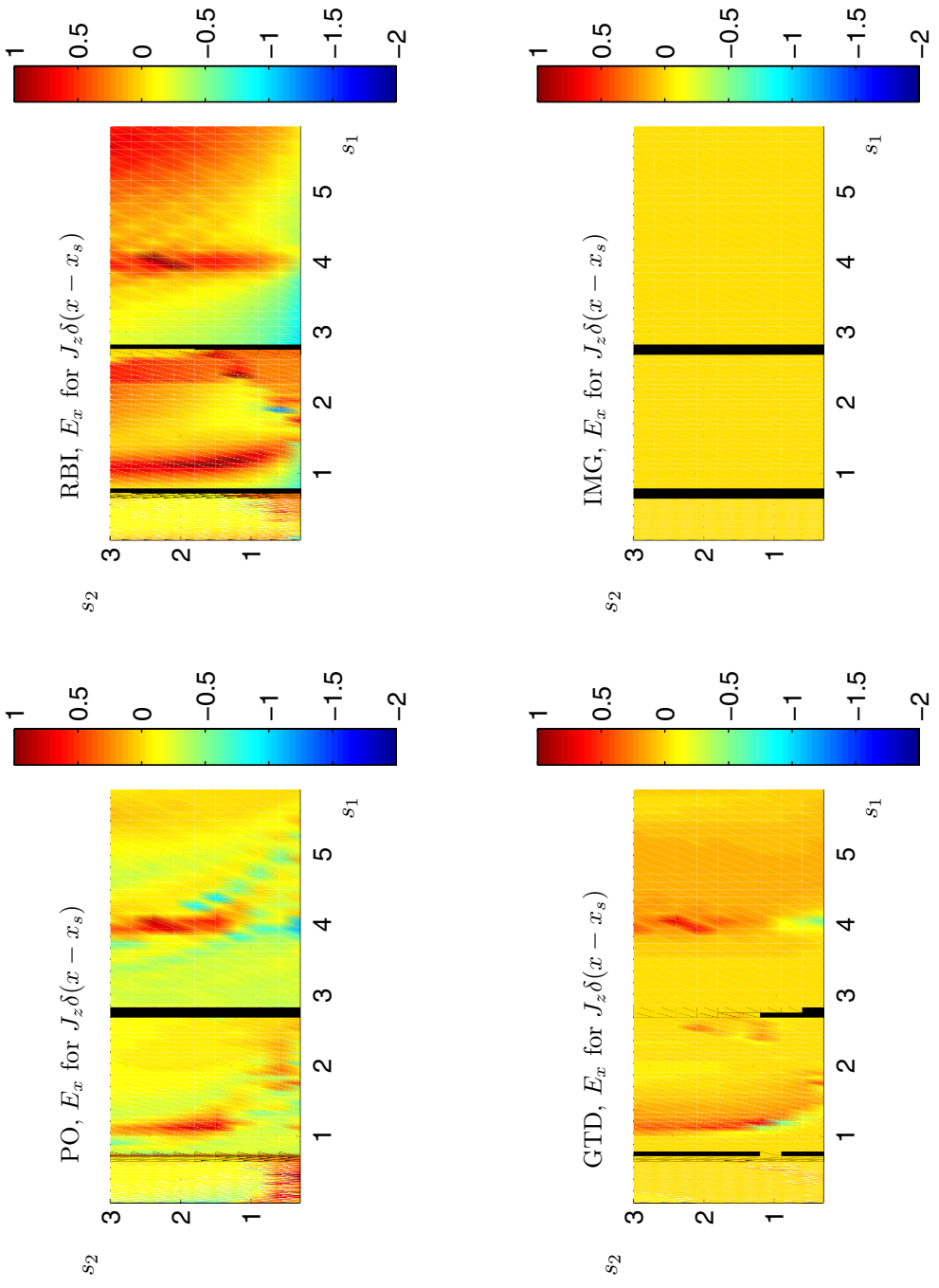

Figure 5.11: Cross-polar measure. Logarithm of relative error for the J_z- and E_x-polarization.

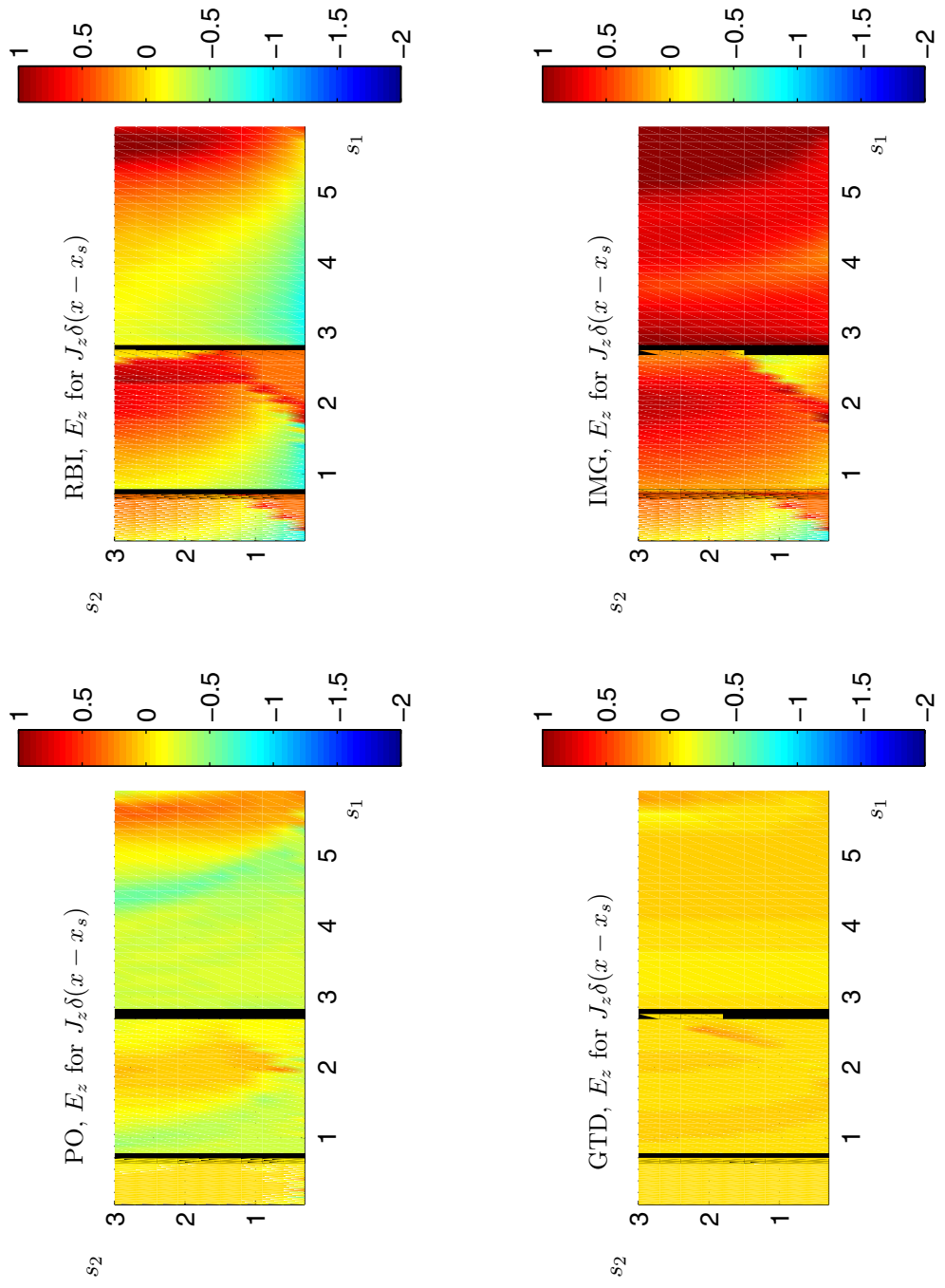

Figure 5.12: Co-polar measure. Logarithm of relative error for the J_z- and E_z-polarization.

field. However, since the Scatterer needs to be finite in the reference computation, we have used a truncated sphere, i.e. a closed northern hemisphere, where we hope that the smooth surface diffraction and edge diffraction may be negligible compared to the reflected field since the radius of the sphere is relatively large (5 λ).

We realize, by having the GTD in mind, that to each point in the (s_1, s_2)-diagram we can associate a reflection angle

$$\arccos\left(\frac{X_{rp} - x_s}{|X_{rp} - x_s|} \cdot \hat{n}_{rp}\right).$$

The closer s_1 gets to a discontinuity line the more obtuse will the reflection angle be. Each 4-plot visualize the errors for a polarization pair, (J^μ, E^ν). If $\mu = \nu$ we say that we analyze the co-polar component, other ways it is the cross-polar component. By inspecting the image theory we can in general say that the co-polar component is larger than the cross-polar. Hence, a large error in the co-polar component is more severe than in the cross-polar component since it will imply a large absolute error in the coupling. For the cross-polar component a small error is probably not serious.

The following observations can be made on the co-polar components:

- The performance of PO is about the same for all type of dipoles. Not very well but the errors are relatively bounded. C.f. PO-plots in Figure 5.8, 5.10 and 5.12.
- Referring to RBI-plots in Figure 5.8 and 5.10, RBI performs well for x- and y-components even for rather acute reflection angles. For J_z, c.f. Figure 5.12, the result is not as good.
- The GTD-method is only relatively successful for, to the ray, orthogonal components and large s_1. C.f. GTD-plots in Figure 5.8 and 5.10 for quite orthogonal components and Figure 5.12 for almost parallel component.
- Image method performs only well for field points with s_1 small. C.f. ANA-plots in Figure 5.8, 5.10 and 5.12.

The following observations can be made on the cross-polar components:

- PO performs rather bad in general. C.f. PO-plots in Figure 5.9 and 5.11.
- RBI is quite successful, as we hoped, for the (J_x, E_z) and (J_z, E_x) pairs, c.f. RBI-plots in Figure 5.9 and 5.11.
- The GTD-method probably underestimate most of the fields. C.f. GTD-plots in Figure 5.9 and 5.11.
- ANA underestimate the cross polar components in Figure 5.11. In Figure 5.9 we see that ANA overestimate the solution.

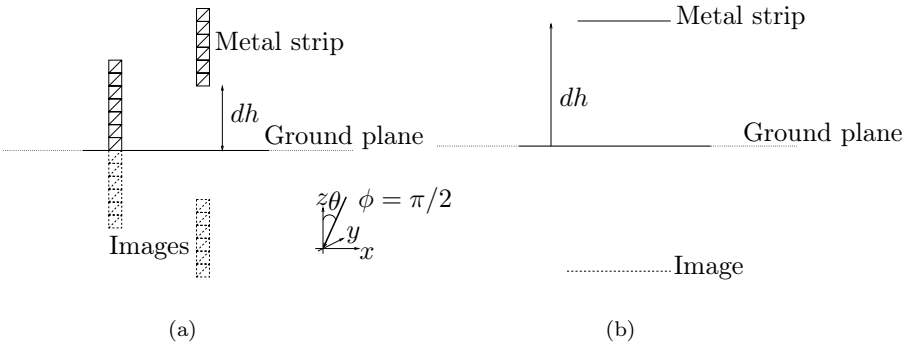

Figure 5.13: Horizontal and vertical perfect electric conducting strip 1.5 λ long

It is hard to explain or motivate all qualities in the the plots. However some statements can be made. We see that RBI is generally more successful when the dipole is close to the reflection point. All methods, accept for some polarizations for the GTD-method, fails for the case when the reflection phenomena approaches smooth surface diffraction, i.e. the reflection angle gets very obtuse. This error may be reduced with better GTD formulas. PO, although it is resolving the wave length in the Scatterer, is not as successful as RBI. We can only descry that the GTD-method improves for large S_{br}, but only for the *GTD components* that are orthogonal to the rays. Hence to visualize the benefits with the GTD-method we would need to increase S_{br}. It is of course not surprising that the analytical method fails for reflection points below the infinite ground plane.

Finally we want to point out that our test case is not impeccable. There is a risk that energy propagate around the hemisphere and then comes back. This is not a phenomena that we expect that our approximate methods are able to represent.

5.4.2 Numerical Error of Currents On a Scatterer

We now compute the currents on a perfect electric conducting strip. Since the strip is in the order of $\lambda/100$ thick we can think of it as a wire with currents only going in one dimension. The metal strip is placed above an infinite perfect electric conducting ground plane, c.f. Figure 5.13(a) and 5.13(b). With these test cases we want to investigate the errors by using the RBI method iteratively, i.e. by finding the Image Field Points (IFP), and, at least very approximately, get a feeling for which (s_1, s_2) the GTD-method is applicable.

The reference solution is produced by using the image technique presented in Section 2.6, i.e. removing the infinite ground plane in Figure 5.13 and adding the image strip and the image excitation below the xy-plane.

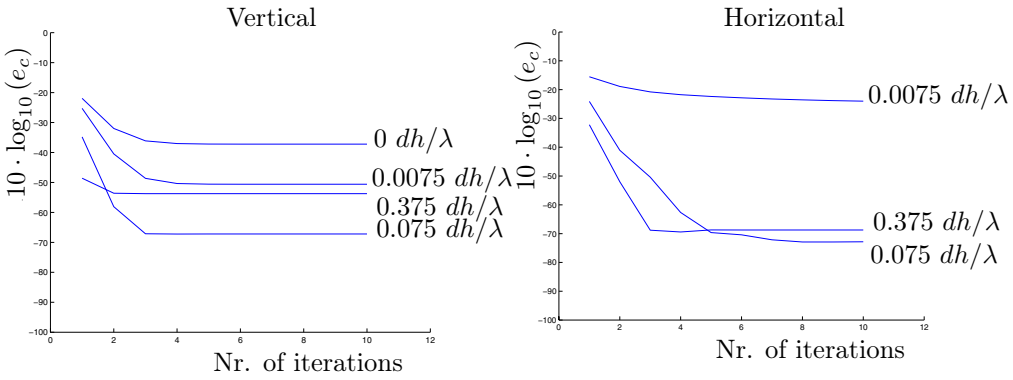

(a) Vertical strip at different positions.

(b) Horizontal strip at different positions.

Figure 5.14: Image field point test.

5.4.2.1 Image Field Point Test

The orientation of the strip is either horizontal or vertical and the position of the strip is changed in the z-direction.

In Figure 5.14(a) we see the convergence of surface current on a 1.5λ metal strip positioned vertically above a perfect electric conducting infinite ground plane. Since the strip was chosen as a multiple of $\lambda/2$ we see that even the strip with distance zero (no current in the center of the strip - image strip geometry) to the ground plane converge (however to a value with relatively larger error). This will not be the case if the strip length where chosen differently since then the very approximate estimation of expression (2.26) in the IFP technique, for boundary elements close to the image boundary elements, would be a very bad approximation.

In Figure 5.14(b) we see the convergence of surface current on a 1.5λ metal strip positioned horizontally above a perfect electric conducting infinite ground plane. When the strip is close to the ground plane we see a slow convergence. This is not surprising from a physical point of view. There will be a wave captured, bouncing back and forth several times between the strip and the ground plane. The current also seems to converge to a solution with a rather large error which can be explained with that IFP approximate the strip-image strip coupling poorly.

5.4.2.2 RBI-GTD Superposition Test

For terms of type (2.26), we know that the RBI will fail for large s_2 and, relative to the wave length, small radius of curvatures at the reflection point, since then the geometrical spreading of the wave front originating from the surface curvature, properly taken into account by the GTD-method, is disregarded. An interesting

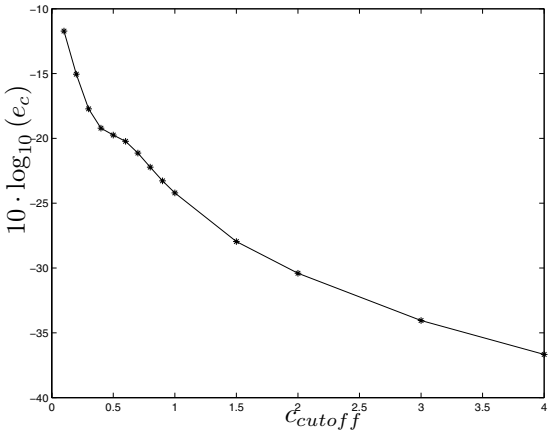

Figure 5.15: Error of currents, according to definition 5.7, for a vertically and attached metal strip with length $4/5\lambda$, versus c_{cutoff}.

test would then be to try to find out, for a certain geometry, for how small s_1 the GTD-method is applicable (within a certain error limit). For the sake of simplicity we assume linear interpolation of the two methods and try to find a c_{cutoff} for

$$(A_{11} - \beta * D_{12})\mathbf{J}_1^{n+1} = \mathbf{E}_1^{exc} + \bar{\mathbf{E}}_1^{exc} + \alpha * D_{12}\mathbf{J}_1^n \tag{5.17}$$

where

$$\begin{array}{lll} \alpha_{ij}(s_1) & = s_1^{ij}/c_{cutoff} & \forall s_1 < c_{cutoff} \\ \alpha_{ij}(s_1) & = 1 & \forall s_1 \geq c_{cutoff} \\ \beta_{ij}(s_1) & = 1 - \alpha_{ij}(s_1) & \forall s_1. \end{array} \tag{5.18}$$

In Figure 5.15 we see the error in the currents, after the iteration has converged, with respect to c_{cutoff}. Having in mind that the analysis may be very dependent on the geometry of the scatterer and the Scatterer we conclude that, at least for this specific BVP, $1 \leq c_{cutoff} \leq 2$ would be reasonable to use.

5.4.3 Numerical Error of the Scattered Field.

The mono-static scattered field from a plane wave hitting an infinite ground plane with normal $\hat{n}^{\varepsilon}$ is only different from zero when Poynting's vector $\hat{P}_{\varepsilon}$ is anti-parallel to the normal, i.e. $\hat{n}^{\varepsilon}\hat{P}_{\varepsilon} = -1$. Actually, according to the definition of radar cross section in the end of Section 2.5.1, the field will be infinite for $\hat{n}^{\varepsilon}\hat{P}_{\varepsilon} = -1$ since the scattered field has no attenuation with respect to distance from the Scatterer. By analyzing the mono-static scattered field for plane waves with $\hat{P}_{\varepsilon}$ non-parallel to $\hat{n}^{\varepsilon}$ we do not need to care about the scattered field from the Scatterer. I.e. the

mono-static scattered field from a metal strip installed on an infinite ground plane is equal to the reference case, scattered field from strip-image strip problem.

When the Scatterer is different from an infinite ground plane, will the reference solution be a little bit more tricky to compute. What we find with our hybrid method is the scattered field from the scatterer taking into account the interaction with the Scatterer. To achieve a reference solution, we therefore have to compute the scattered field from the boundary value problem where both the scatterer and the Scatterer is present and then subtract the scattered field from the boundary value problem when only the Scatterer is present. Asymptotically we then have

$$E^{\mu}_{scatt}(S-s) \sim E^{\mu}_{scatt}(S+s) - E^{\mu}_{scatt}(S). \tag{5.19}$$

The similarity sign has been used since we only take into account the Scatterer asymptotically in the hybrid solution $E^{\mu}_{scatt}(S-s)$.

5.4.3.1 Metal Strips Above a Ground Plane

In Figure 5.16 we see good agreement with the reference case with no iteration at all. That is, the coupling between the strip and the image-strip is negligible when the Scatterer and the scatterer are well separated.

In Figure 5.17 we see good agreement with the reference case after three iterations.

5.4.3.2 Small Metal Sphere Attached to a Large Sphere

The final numerical test, we will present, is the most composite one. We refer to Figure 5.18. The small sphere radius is $r = 2\lambda/3$ and the large sphere radius is $10\lambda/3$. $E^{\mu}_{scatt}(S+s)$ is computed by a direct numerical method solving for 18000 number of unknowns for each of 61 plane wave excitations. The fast multipole method implementation presented in [27] was then used and $E^{\mu}_{scatt}(S)$ was computed by using an analytic solution (Mie series). In the hybrid method, we used a 250 triangle mesh of the truncated sphere with 387 degrees of freedom. Using polar coordinates, with the small sphere attached to the north pole of the large sphere, we present the mono-static scattered field for $\theta = 0 \ldots 100$ degrees. The comparison between $\mathbf{E}^{\theta}_{scatt}(S-s) + \mathbf{E}^{\theta}_{scatt}(S)$ and $\mathbf{E}^{\theta}_{scatt}(S+s)$ is given in Figure 5.19(a). The comparison between the hybrid method $\mathbf{E}^{\theta}_{scatt}(S-s)$ and $\mathbf{E}^{\theta}_{scatt}(S+s) - \mathbf{E}^{\theta}_{scatt}(S)$ is pictured in Figure 5.19(b). We see good agreement of the hybrid method for $\theta = 20 \ldots 60$ degrees. From a physical viewpoint we believe that the discrepancy for other angles can be explained by that higher order phenomenons, such as Smooth Surface Diffraction, becomes non-negligible. However, the size of the Scatterer is moderate compared to the wavelength. We therefore believe that for increasing size of the Scatterer the discrepancy will asymptotically decrease.

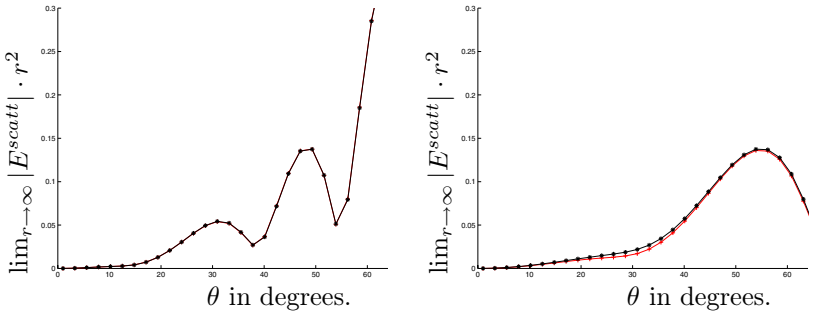

(a) (b)

Figure 5.16: A vertical strip $3\lambda/4$ long, $3\lambda/4$ (a) and $3\lambda/40$ (b) above a ground plane. 0 iterations. Hybrid method in red color and rigorous in black.

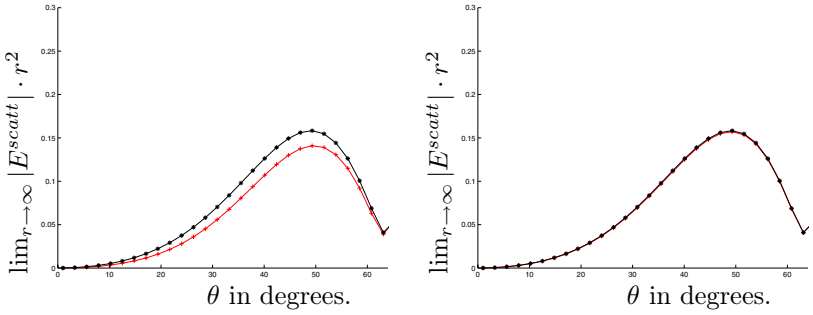

(a) (b)

Figure 5.17: A vertical strip $3\lambda/4$ long and $3\lambda/400$ above a ground plane. 0 iterations (a) and 3 iterations (b). Hybrid method in red color and rigorous in black.

5.4.4 Partition of Unity Error

To investigate the usefulness and generality of the partition of unity method discussed in Section 5.2.2, we mesh a sphere with two different sizes on the super triangles, producing different sizes of ϵ, and compare with a mesh where triangles are of $\mathcal{O}(\lambda/10)$. The radius of the sphere is $r = \frac{10}{3}\lambda$ and we used $\lambda = 0.3m$ in the test case. The results can be seen in figure 5.20. Depending on the application at hand, the errors may be too large for the λ- or 2λ-facet case.

For the λ-facet case, we choose the small triangle edge size to be 0.0296 m and

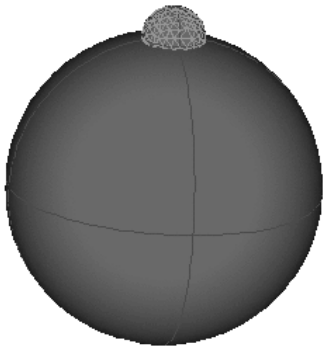

Figure 5.18: The most composite boundary value problem. The large sphere, numerically represented by NURBS, is taken into account by RBI and the, to the north pole, attached small sphere is taken into account with the boundary element method.

super triangle edge size to be 0.22 m. This produced 37632 number of unknowns, 25088 number of triangles and 392 number of super triangles. This will for example make the excitation $\frac{25088}{392 \cdot 1.5} = 43$ times faster than the reference case.

For the 2λ-facet case we choose the small triangle edge size to be 0.032 m and super triangle edge size to 0.22 m. This produced 27648 number of unknowns, 18432 number of triangles and 72 number of super triangles. This will make the excitation $\frac{18432}{72 \cdot 1.5} = 170$ times faster than the reference case.

For the reference case we had 22472 number of triangles and 33708 number of unknowns. The small triangle edge size was put to 0.0296 m.

We believe that, to achieve a successful partition of unity implementation, you need an efficient meshing algorithm that both take into account user given maximum triangle edge sizes *and* ϵ.

5.5 Hybrid Method 2 and 3, Theory

Previously, in the sections about the first hybrid method, we where able to approximate the interaction between the scatterer and Scatterer by using the RBI-method and the GTD-method. The access to RBI was crucial for our ability to approximate the currents that where close to the Scatterer. To be able to apply RBI, the Scatterer needed to be smooth close to the scatterer, and therefore locally similar to an infinite perfect electric conducting ground plane, or the currents needed to be a priori close to zero. What to do if the Scatterer is non-smooth close to the scat-

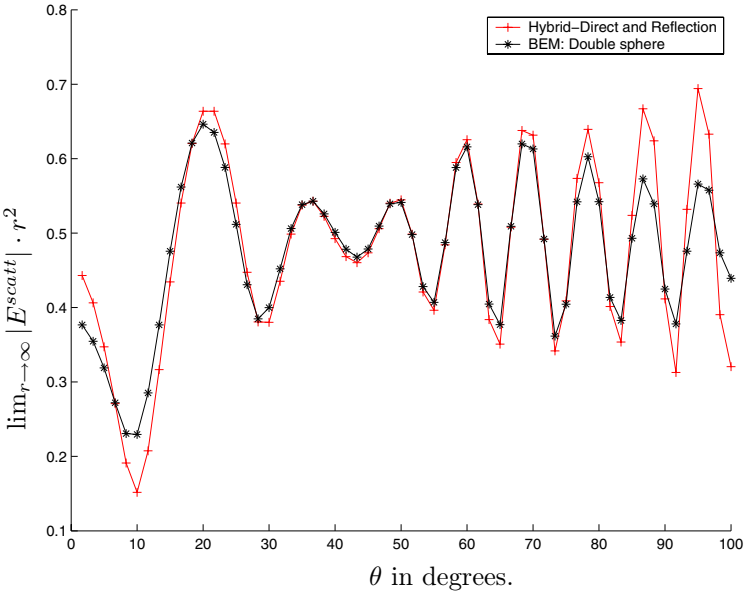

(a)

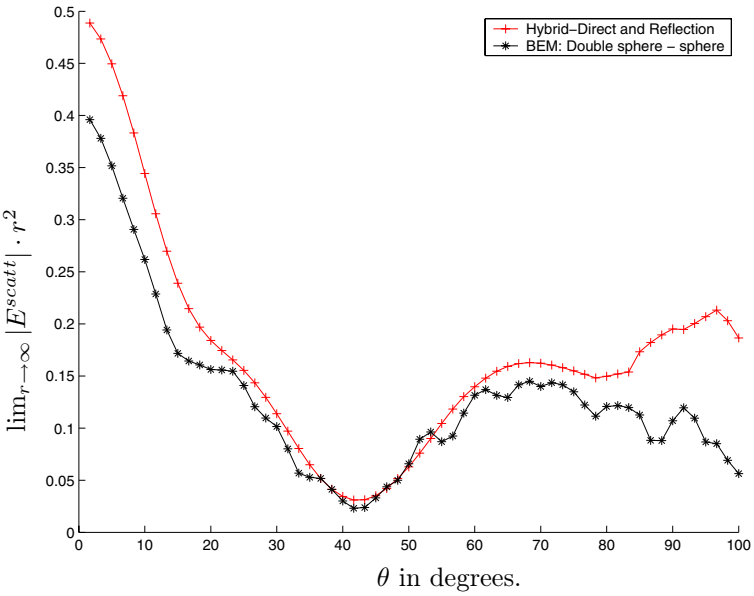

(b)

Figure 5.19: The sum 5.19(a) and difference 5.19(b) of mono-static scattered field from a small hemisphere $r = \frac{2}{3}\lambda$ attached to a large sphere ($r = \frac{10}{3}\lambda$) on the north pole. $|E_\theta^{inc}| = 1$.

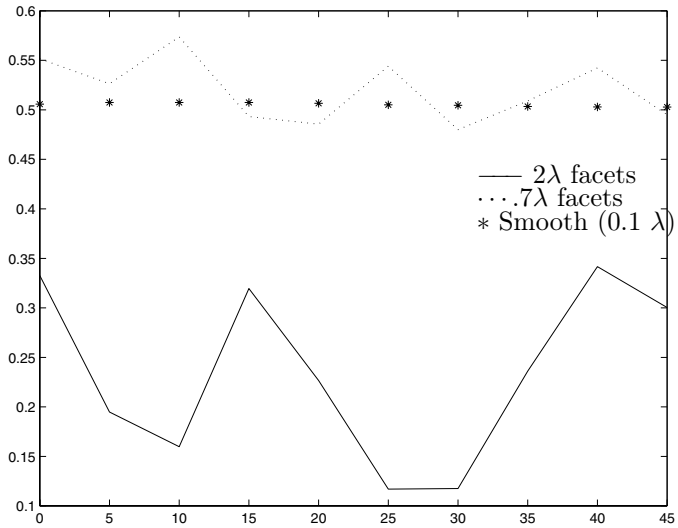

Figure 5.20: Scattered (mono-static) field from a sphere geometrically resolved at different levels.

terer? This problem has been treated in several publications. We refer the reader to [70] for the scalar problem and [71], [72], [60], and [73] for the electromagnetic problem. These methods mainly treat canonical Scatterers while we try to address problems with non-canonical Scatterers with our methods.

However, by way of introduction, let us consider an infinite ground plane to represent the large scales. Consider the boundary value problem discussed in Section 2.6. Namely $\hat{n}(x) \times \mathbf{E}(x) = 0$ for $\mathbb{R}^3 \ni x = 0$. How much will the scattered field from an incoming plane wave change if we drill a $r = \lambda$ hole in the perfect electric conducting geometry and put a metallic hemisphere, as in example 5.4.3.2? However, this time we use the southern hemisphere so that we get a protruded ground plane. Note that it is neither possible to mesh the entire problem, since we then end up with an infinite system of equations to solve, nor to apply image theory, since image theory is only applicable above the ground plane. We need to reduce the problem size! One way to proceed is to compute the scattered field from a, let say $r = 10\lambda$ un-protruded disc, while taking into account the rest of the ground plane as was done in previous sections. Then in a second step we can compute the scattered field from the 10λ-disc with the protrusion included where we also take into account the presence of the infinite ground plane. The scattered field can then be found by taking the difference of the scattered fields from the two steps. We refer to Figure 5.21 for a schematic picture of the example.

Let us call the ground plane minus the protruded $r = 10\lambda$ disc the Scatterer and and the protruded disc for the scatterer. Above we did not answer the following

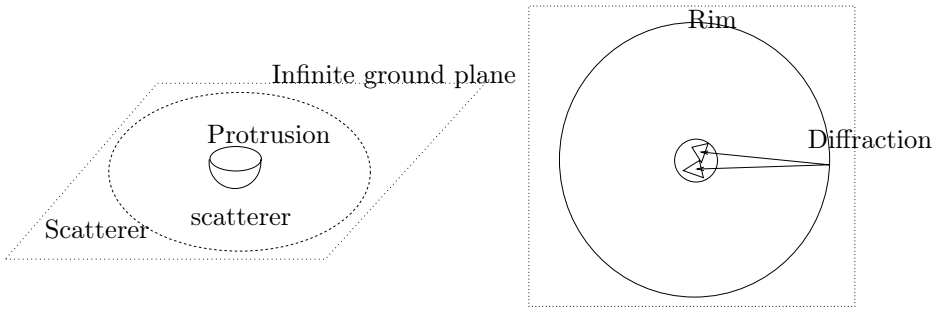

Figure 5.21: A protruded infinite ground plane.

question. How can we numerically compute the scattered field from the metallic disc in presence of an infinite ground plane? Note, that the problem resemble the limit of case B in Figure 5.2. The corner in two dimensions is represented by the $r = 10\lambda$ rim, which separates the Scatterer and the scatterer, in three dimensions. We know a priori that the currents will in general be large, approximately $2n \times H^{exc}$, along the rim since the plane wave is exciting currents all over the ground plane. Therefore it is important represent the currents close to the rim properly. Neither RBI can be used to compute the interaction between the small and the large scales, since we have no image theory for edges, nor can the GTD-method be used since the currents in the scatterer close to the rim will not produce a Ray-field at the edge. We see two ways to proceed and they are presented in Section 5.5.1 and 5.5.2.

To have a numerical method applicable to industrial problems, we have to insist on its ability to treat BVPs where the Scatterer is no longer an infinite ground plane, but something finite. In some cases it is very important to take into account the boundary conditions on the Scatterer even some wave lengths away from the scatterer. The first method, referred to method two in the introduction to this chapter, presented below is meant for these types of problems. The second method, referred to method three in the introduction to this chapter, which is more approximate in some sense, is meant for problems where it is only important to take into account that the disc does not end where the BEM-mesh ends but the currents are free to continuously cross the common rim. We can regard this feature as a kind of absorbing boundary condition for the scattered outwards propagating current.

Finally we want to remark two things. The analysis below is not developed as far as was done for the first hybrid method and it therefore needs further theoretical justification before a true implementation is advised. Secondly, we emphasize that the methodology developed for the GTD-method in Section 5.1 may still be used for boundary conditions that are relatively far from the S_2. That is, in this section we discuss methods that can be used for the the interaction between the small and large scales that are electrically close to each other.

5.5.1 Hybrid Using Basis Functions With Global Support

The ideas presented in this subsection were initiated by J. B. Keller [74]. See also Diffraction Theory in [75]. Below we very briefly give an idea how to implement these ideas in a boundary element setting for Maxwell's equations. To avoid the risk of occluding the principal ideas we keep the notation simple. We want to use the integral representation of the scattered field given in expression (2.17) and (2.18), but we want to split up the scattered solution in two terms, $\tilde{E}_{scatt} = E_{scatt} + E_{Mxw}$. We demand that E_{Mxw} solves Maxwell's homogeneous equations without boundary conditions and therefore that it may be represented by expression (2.17) and (2.18) on its own. Then we can write, with $j(x) = \hat{n} \times (H_{scatt} + H_{Mxw} + H_{inc})$,

$$\begin{aligned} &E_{scatt}(y) + E_{Mxw}(y) = L_{S\cup s}(j(x)) = \\ &i\omega\mu_0 \int_{S\cup s} G(x,y) j(x)\, dx - \frac{i}{\omega\varepsilon_0} \nabla_y \int_{S\cup s} G(x,y)\, \mathrm{div}_{S\cup s} j(x)\, dx, \end{aligned} \tag{5.20}$$

where the excitation (E_{inc}, H_{inc}) is an electromagnetic plane wave and $\mathrm{div}_{S\cup s}$ the surface divergence introduced in Chapter 2. Let us call the unperturbed scatterer s_u and the perturbed scatterer for s_p. Then we can represent the scattered field from both the perturbed and the unperturbed scatterer according to (5.20). For the unperturbed problem in Figure 5.21, we know from the image theory that

$$H = n \times H_{inc} + n \times H_{refl}$$

and

$$E = n \times E_{inc} + n \times E_{refl},$$

in the upper half space where H_{refl} is the image plane wave. At $x = 0$ we then fulfill the boundary condition that the surface tangential part of the scattered electric field is equal to minus the tangential incoming electric field. The image plane wave fulfill the free space Maxwell's equations and we may therefore let

$$\begin{aligned} E_{Mxw} &= E_{refl} \\ H_{Mxw} &= H_{refl}, \end{aligned} \tag{5.21}$$

for the unperturbed problem. Note that in our example the unperturbed geometry is an infinite ground plane. For a more general Scatterer (E_{refl}, H_{refl}) can be replaced by the GTD-solution for the unperturbed problem. We have, since $E^u_{scatt} = E_{refl}$,

$$\begin{aligned} &(E^p_{scatt}(y) + E_{refl}(y)) - E^u_{scatt}(y) = \\ &E^p_{scatt}(y) = L_{S\cup s_p}(j_p(x), y) - L_{S\cup s_u}(j_u(x), y), \end{aligned} \tag{5.22}$$

where $j_p = \hat{n} \times (H_{inc} + H_{refl} + H^p_{scatt})$ and $j_u = \hat{n} \times (H_{inc} + H_{refl})$. By canceling some terms we get more explicitly

$$\begin{aligned} &E^p_{scatt}(y) + \tilde{E}^p_{scatt}(y) = \\ &i\omega\mu_0 \int_{S\cup s_p} G(x,y) j_{scatt}(x)\, dx - \frac{i}{\omega\varepsilon_0} \nabla_y \int_{S\cup s_p} G(x,y)\, \mathrm{div}_{S\cup s} j_{scatt}(x)\, dx, \end{aligned} \tag{5.23}$$

where $j_{scatt}(x) = \hat{n} \times H^p_{scatt}$ and the function

$$\begin{aligned}
&\tilde{E}^p_{scatt}(y) = \\
&i\omega\mu_0 \int\limits_{s_u \setminus (s_u \cap s_p)} G(x,y)\hat{n} \times (H_{inc} + H_{refl})\, dx - \\
&\frac{i}{\omega\varepsilon_0}\nabla_y \int\limits_{s_u \setminus (s_u \cap s_p)} G(x,y)\, \mathrm{div}_{S \cup s} \left[\hat{n} \times (H_{inc} + H_{refl})\right] dx, - \\
&i\omega\mu_0 \int\limits_{s_p \setminus (s_u \cap s_p)} G(x,y)\hat{n} \times (H_{inc} + H_{refl})\, dx + \\
&\frac{i}{\omega\varepsilon_0}\nabla_y \int\limits_{s_p \setminus (s_u \cap s_p)} G(x,y)\, \mathrm{div}_{S \cup s} \left[\hat{n} \times (H_{inc} + H_{refl})\right] dx,
\end{aligned}$$

is considered to be known. Note that the way we have chosen the scattered field E^p_{scatt} and H^p_{scatt} imply that j_{scatt} and $\mathrm{div} j_{scatt}$ on the right hand side of (5.23) asymptotically decrease as $x \to \infty$. This suggests that we can truncate S to get an approximate estimate of $E^p_{scatt} + \tilde{E}^p_{scatt}$.

Using the boundary conditions on $S \cup s_p$ and variational formulation, as was done in equation (2.21), we get

$$\begin{aligned}
&E = \int\limits_{S \cup s_p} \left(\tilde{E}^p_{scatt}(y) - (E_{inc}(y) + E_{refl}(y))\right) j^{scatt}_t\, dy = \\
&i\omega\mu_0 \int\limits_{S \cup s_p} \int\limits_{S \cup s_p} G j^{scatt} j^{scatt}_t\, dxdy - \\
&\frac{i}{\omega\varepsilon_0} \int\limits_{S \cup s_p} \int\limits_{S \cup s_p} G\, \mathrm{div}_{S \cup s_p} j^{scatt}\, \mathrm{div}_{S \cup s_p} j^{scatt}_t\, dxdy.
\end{aligned}$$

Splitting up the integrals we get

$$\begin{aligned}
&E = i\omega\mu_0 \int\limits_S \int\limits_S G j^{scatt} j^{scatt}_t\, dxdy - \frac{i}{\omega\varepsilon_0} \int\limits_S \int\limits_S G\, \mathrm{div}_S j^{scatt}\, \mathrm{div}_S j^{scatt}_t\, dxdy + \\
&i\omega\mu_0 \int\limits_S \int\limits_{s_p} G j^{scatt} j^{scatt}_t\, dxdy - \frac{i}{\omega\varepsilon_0} \int\limits_S \int\limits_{s_p} G\, \mathrm{div}_S j^{scatt}\, \mathrm{div}_{s_p} j^{scatt}_t\, dxdy + \\
&i\omega\mu_0 \int\limits_{s_p} \int\limits_S G j^{scatt} j^{scatt}_t\, dxdy - \frac{i}{\omega\varepsilon_0} \int\limits_{s_p} \int\limits_S G\, \mathrm{div}_{s_p} j^{scatt}\, \mathrm{div}_S j^{scatt}_t\, dxdy + \\
&i\omega\mu_0 \int\limits_{s_p} \int\limits_{s_p} G j^{scatt} j^{scatt}_t\, dxdy - \frac{i}{\omega\varepsilon_0} \int\limits_{s_p} \int\limits_{s_p} G\, \mathrm{div}_{s_p} j^{scatt}\, \mathrm{div}_{s_p} j^{scatt}_t\, dxdy.
\end{aligned} \tag{5.24}$$

Assuming that $j^{scatt} \to 0$ as $|x| \to \infty$ it is natural to approximate j^{scatt} as follows

$$j^{scatt} = \sum_{\ell=1}^{N_L} J_\ell j^\mu_\ell + \sum_{\gamma=1}^{N_G} J_\gamma j^\mu_\gamma, \tag{5.25}$$

where j_ℓ^μ are local basis function, with support in s_p as defined in Section 2.5.1, and j_γ^μ are global basis functions with support in S mentioned in Section 2.5.2.

In our example it is also natural to assume that electromagnetic energy is propagating outwards, i.e. j_γ^μ fulfills approximately an outgoing radiation condition. We suggest that the orthonormal basis of *Vectorial Spherical Harmonics* are used to approximate

$$H_p^{scatt} = H - H_{inc} - H_{refl}, \tag{5.26}$$

in the exterior domain. Reference [2] provide an extensive analysis of this basis for Maxwell's equations and we will not give there explicit definitions here. Instead we choose to give the expansion schematically as

$$\begin{aligned} H_p^{scatt} &= \textstyle\sum_{\xi=1}^{\infty}\sum_{m=-\xi}^{\xi} a_\xi^m \frac{h_\xi^{(1)}(k|x|)}{h_\xi^{(1)}(|x|)} T_\xi^m(\theta,\phi) \\ &\frac{i\sqrt{\varepsilon_0}}{\mu_0}\textstyle\sum_{\xi=1}^{\infty}\sum_{m=-\xi}^{\xi} b_\xi^m \left(\frac{\xi+1}{2\xi+1}\frac{h_\xi^{(1)}(k|x|)}{h_{\xi-1}^{(1)}} I_\xi^m(\theta,\phi) + \frac{\xi}{2\xi+1}\frac{h_{\xi+1}^{(1)}(k|x|)}{h_\xi^{(1)}} N_\xi^m(\theta,\phi)\right), \end{aligned} \tag{5.27}$$

where $h_{\xi+1}^{(1)}$ is the $(\xi+1)$:th order Hankel function of first kind and the triplet $(T_\xi^m, I_\xi^m, N_\xi^m)$ can be deduced from a scalar function g_ξ^m, which in its turn can be found by applying some recursive formulas.

Remark that one of the important features with the so called *Multipole Expansion* in (5.27) is that the angular dependence and the radial dependence is split up in two parts.

Above we have suggested that the currents are expanded with local basis functions (compact support) on the scatterer and global basis functions (non-compact support) on the Scatterer. How is this done more specifically in a numerical implementation? Let us truncate expansion (5.27) and write the second term in expansion (5.25) as

$$\sum_{\xi=1}^{\tilde{N}_G}\sum_{m=-\xi}^{\xi} J_{\gamma(m,\xi)} j_{\gamma(m,\xi)}^\mu(|x|,\theta,\phi), \tag{5.28}$$

where we have

$$N_G = 2\left(2\tilde{N}_G + \tilde{N}_G^2\right), \tag{5.29}$$

and J_γ is an element in

$$J^S = \begin{bmatrix} a_1^{-1}, a_1^0, a_1^1, a_2^{-2}, a_2^{-1}, a_2^0, a_2^1, a_2^2, \dots \\ b_1^{-1}, b_1^0, b_1^1, b_2^{-2}, b_2^{-1}, b_2^0, b_2^1, b_2^2, \dots \end{bmatrix},$$

and correspondingly for $j_{\gamma(m,\xi)}^\mu$. Plugging in expansion (5.25) into (5.24) and collecting terms we get a linear system

$$\begin{pmatrix} Z^{ss} Z^{Ss} \\ Z^{sS} Z^{SS} \end{pmatrix} \begin{pmatrix} J^s \\ J^S \end{pmatrix} = \begin{pmatrix} E^s \\ E^S \end{pmatrix}, \tag{5.30}$$

where the elements in the final impedance matrix Z, will contain six types integrals. They are

$$z^{ss}_{\ell\gamma_t} = \int_{T_m}\int_{T_n} G j^{\mu}_{\ell} j^{\mu}_{\ell_t}\, dxdy, \tag{5.31}$$

$$z^{Ss}_{\ell\gamma_t} = \int_{S}\int_{T_n} G j^{\mu}_{\gamma} j^{\mu}_{\ell_t}\, dxdy, \tag{5.32}$$

$$z^{SS}_{\ell\gamma_t} = \int_{S}\int_{S} G j^{\mu}_{\gamma} j^{\mu}_{\gamma_t}\, dxdy, \tag{5.33}$$

$$z^{ss}_{\ell\gamma_t} = \int_{T_m}\int_{T_n} G\,\mathrm{div} j^{\mu}_{\ell}\,\mathrm{div} j^{\mu}_{\ell_t}\, dxdy, \tag{5.34}$$

$$z^{Ss}_{\ell\gamma_t} = \int_{S}\int_{T_n} G\,\mathrm{div} j^{\mu}_{\gamma}\,\mathrm{div} j^{\mu}_{\ell_t}\, dxdy, \tag{5.35}$$

$$z^{SS}_{\ell\gamma_t} = \int_{S}\int_{S} G\,\mathrm{div} j^{\mu}_{\gamma}\,\mathrm{div} j^{\mu}_{\gamma_t}\, dxdy, \tag{5.36}$$

where S indicate the Scatterer and T_n a boundary triangle in the scatterer. If we want to evaluate the elements, containing integrals over S, for our specific example with an infinite ground plane we need of course to truncate S. Naturally, we must assume that the size of the truncated S will be problem dependent.

Assume that we have access to a standard Boundary Element Solver that contain routines that numerically evaluate integral (5.31) and (5.34). We then need to develop and implement a quadrature to evaluate the matrix elements in (5.32), (5.33), (5.35) and (5.36). Is there a way to avoid this work if we have access to the GTD-solver used in the hybrid method one presented in Section 5.1?

5.5.2 Hybrid Using Edge Diffraction

We realize that, in the method presented in Section 5.5.1, the solution in the exterior domain is coupled to the solution in the perturbed part in matrix element (5.32) and (5.35). Differently stated, the two domains are rigorously coupled in the impedance matrix. This may be crucial in some cases and in others not.

We believe that it is possible to approximate (5.32), (5.33), (5.35) and (5.36), in many relevant engineering cases, by

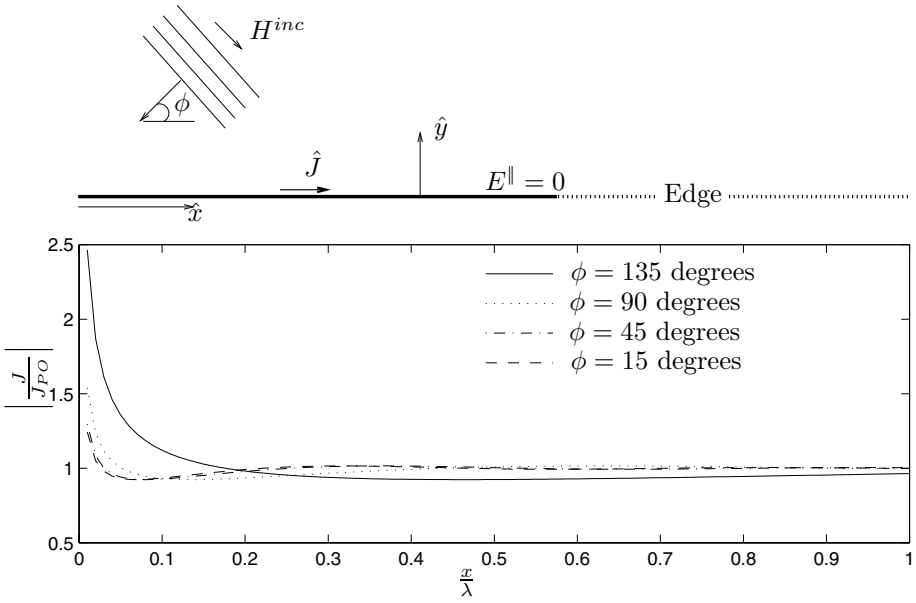

Figure 5.22: The electric currents close to a plane wave excited perfect electric conducting infinite edge. The plane wave propagates in the plane orthogonal to the edge and we plot the currents in the illuminated side of the edge. The currents are normalized against the Physical Optics currents, i.e. $J_{PO} = 2\hat{y} \times H^{inc}$. The results, which are analytical, has been derived from formulas given in [40].

- solving for the **difference** between the unknowns in the perturbed and unperturbed geometry respectively and
- by using **edge diffraction**, as was done in the iterative method presented in Section 5.1.

That is, if we omit the integrals over the Scatterer, when we build the integral equation, we will introduce *artificial edges* in the scatterer and improper edge currents are excited. The amplitude of the edge currents for a specific geometry can be seen in Figure 5.22. In the figure we relate a plane wave excited current to the so called physical optics approximation introduced in Section 5.4. The non-PO currents close to the edge can be seen to be quite large. To compensate for the artificial edge we suggest to apply GTD edge diffraction to the Scatterer and in this way let the diffracted field extinguish the scattered field from the artificial edges. However,

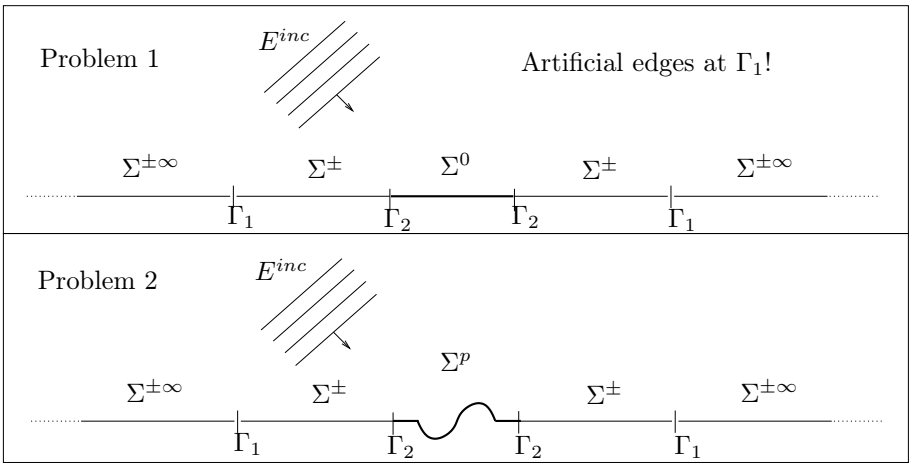

Figure 5.23: Picture of two scattering problems used to define the search scattered field E_2^s. $\Sigma^{\pm\infty}$ now correspond to the Scatterer and $\Sigma^{\pm} \cup \Sigma^0$ or $\Sigma^{\pm} \cup \Sigma^p$ to the scatterer. Γ_1 assigns $\Sigma^{\pm\infty} \cap \Sigma^{\pm}$ and Γ_2 assigns $\Sigma^{\pm} \cap \Sigma^0$ or $\Sigma^{\pm} \cap \Sigma^p$.

as we mentioned in Section 5.1 concerning the GTD-method given in Method 5.6, we need to have a Ray-field at the diffraction point. To achieve this we will, once more, solve for the difference between currents in the unperturbed and perturbed problem.

To explain the idea more in detail we must define two scattering problems. In each problem we also define a scattered field. Let us once more keep the notation simple and by referring to [70], which study a related mathematical problem, we skip the quite intricate, though important, mathematical questions of well posedness, raised by our method. We will present the method for the three dimensional Maxwell scattering problem with perfectly conducting boundaries. However, to explain the notation, we will use the two dimensional figures given in Figure 5.23. Let $E_j(x)$ be the total electric field in a point x for problem j and let Σ assign a PEC-boundary, i.e. $E^{\parallel} = 0$ where $\parallel$ indicate that it is the tangential component. Then define a scattered field for the problems according to the following

$$\begin{aligned} E_1^s &= E_1 - E^{inc}, \\ H_1^s &= H_1 - H^{inc} \end{aligned} \tag{5.37}$$

and

$$\begin{aligned} E_2^s &= E_2 - E^{inc} - E^{refl}, \\ H_2^s &= H_2 - H^{inc} - H^{refl}. \end{aligned} \tag{5.38}$$

We consider

$$\begin{aligned} E_1 &= E^{inc} + E_1^s = E^{inc} + E^{refl}, \\ H_1 &= H^{inc} + H_1^s = H^{inc} + H^{refl} \end{aligned} \tag{5.39}$$

to be known. If problem 1 correspond to an infinite conducting ground plane as indicated in the figure, image analysis may be used to compute H^{refl}. If it corresponds to something more general we demand that the scattered solution should, at least asymptotically, be possible to set. Let

$$\Sigma_1 = \Sigma^{\pm\infty} \cup \Sigma^{\pm} \cup \Sigma^0$$

and

$$\Sigma_2 = \Sigma^{\pm\infty} \cup \Sigma^{\pm} \cup \Sigma^p.$$

Note that the ∞-superscript does not indicate that the boundary *must* be infinite, just that it can be considered to be large relative to the wave length. We can write the boundary integral representation of the scattered fields in problem 1 and 2 as

$$E_1^s = ikc\mu_0 \int_{\Sigma_1} Gj_1 \, d\sigma + \frac{i}{kc\varepsilon_0} \nabla \int_{\Sigma_1} G \operatorname{div}_\Sigma j_1 \, d\sigma \tag{5.40}$$

and

$$E_2^s + E^{refl} = ikc\mu_0 \int_{\Sigma_2} Gj_2 \, d\sigma + \frac{i}{kc\varepsilon_0} \nabla \int_{\Sigma_1} G \operatorname{div}_\Sigma j_2 \, d\sigma, \tag{5.41}$$

where G is the fundamental solution to Helmholtz equation and $\operatorname{div}_\Sigma$ is the surface divergence introduced in Section 2.4. If we take the difference of (5.40) and (5.41) we get

$$\begin{aligned}
&\delta E_s = E_1^s - (E_2^s + E^{refl}) \\
&= ikc\mu_0 \left[- \int_{\Sigma^{\pm\infty}} Gj^s \, d\sigma - \int_{\Sigma^{\pm}} Gj^s \, d\sigma + \int_{\Sigma^0} G\hat{n} \times (H^{inc} + H^{refl}) \, d\sigma \right. \\
&\left. - \int_{\Sigma^p} Gj^s \, d\sigma - \int_{\Sigma^p} G\hat{n} \times (H^{inc} + H^{refl}) \, d\sigma \right] \\
&+ \frac{i}{kc\varepsilon_0} \nabla \left[- \int_{\Sigma^{\pm\infty}} G \operatorname{div}_\Sigma j^s \, d\sigma - \int_{\Sigma^{\pm}} G \operatorname{div}_\Sigma j^s \, d\sigma \right. \\
&+ \int_{\Sigma^0} G \operatorname{div}_\Sigma \left[\hat{n} \times (H^{inc} + H^{refl}) \right] \, d\sigma \\
&\left. - \int_{\Sigma^p} G \operatorname{div}_\Sigma j^s \, d\sigma - \int_{\Sigma^p} G \operatorname{div}_\Sigma \left[\hat{n} \times (H^{inc} + H^{refl}) \right] \, d\sigma \right],
\end{aligned} \tag{5.42}$$

where $j^s = \hat{n} \times H_2^s$. We can now use the boundary conditions

$$\begin{aligned}
&\hat{n}(x) \times E_1(x) = 0 \text{ for } x \in \Sigma_1 \\
&\hat{n}(x) \times E_2(x) = 0 \text{ for } x \in \Sigma_2,
\end{aligned} \tag{5.43}$$

to set up an integral equation. We have

$$\begin{aligned}
&\delta E_s^{\parallel}(x) = -\hat{n} \times \left(\hat{n} \times (E^{refl} + E^{inc}) \right) && \text{when } x \in \Sigma^p \\
&\delta E_s^{\parallel}(x) = 0 && \text{when } x \in \Sigma^{\pm} \\
&\delta E_s^{\parallel}(x) = 0 && \text{when } x \in \Sigma^{\pm\infty},
\end{aligned} \tag{5.44}$$

where we use the surface normal $\hat{n}$ to compute the surface tangential part of the vector field.

How can we solve (5.42), with boundary conditions according to (5.44), numerically? We propose that a method similar to the one presented in Section 2.5.1 is used. If we mesh $\Sigma_1 \cup \Sigma_2$ and assign basis- and test functions to the triangle edges according to Section 2.5.1 we can expand the unknowns in (5.42) with the basis functions j_e according to

$$y = \sum_{e=1}^{\infty} J_e j_e.$$

We may also use these basis functions to approximate known data according to

$$\begin{aligned} &ikc\mu_0 \left[\int_{\Sigma^0} G\hat{n} \times (H^{inc} + H^{refl})\, d\sigma - \int_{\Sigma^p} G\hat{n} \times (H^{inc} + H^{refl})\, d\sigma \right] \\ &\frac{i}{kc\varepsilon_0} \nabla \left[\int_{\Sigma^0} G \operatorname{div}_\Sigma \left[\hat{n} \times (H^{inc} + H^{refl}) \right] d\sigma - \right. \\ &\left. \int_{\Sigma^p} G \operatorname{div}_\Sigma \left[\hat{n} \times (H^{inc} + H^{refl}) \right] d\sigma \right] - \delta E_s^{\parallel}(x) = \sum_{e=1}^{\infty} E_e j_e. \end{aligned} \tag{5.45}$$

After expanding the known and the unknowns in (5.42) and multiplying the integrals with the test functions j_e^t we can finally integrate over each of them, i.e. forming an inner product. Let there be N^∞ unknowns in $\Sigma^{\pm\infty}$, $N^\pm$ unknowns in $\Sigma^\pm$, N^0 unknowns in Σ^0 and finally N^p unknowns in Σ^p. We then get an infinite, or very large, system of linear equations with each row according to the following

$$\begin{aligned} &\sum_{e=1}^{N^\infty} E_e \int_{T_{e'}} j_{e'}^t J_e \, dx_{e'} \\ &= ikc\mu_0 \left[\int_{T_{e'}} \int_{\Sigma^{\pm\infty}} j_{e'}^t G \sum_{e=1}^{N^\infty} J_e^{\pm\infty} j_e \, dx_e dx_{e'} + \int_{T_{e'}} \int_{\Sigma^\pm} j_{e'}^t G \sum_{e=1}^{N^\pm} J_e^\pm j_e \, dx_e dx_{e'} \right. \\ &\left. + \int_{T_{e'}} \int_{\Sigma^p} j_{e'}^t G \sum_{e=1}^{N^p} J_e^p j_e \, dx_e dx_{e'} \right] \\ &+ \frac{i}{kc\varepsilon_0} \nabla \left[\int_{T_{e'}} \int_{\Sigma^{\pm\infty}} j_{e'}^t G \sum_{e=1}^{N^\infty} J_e^{\pm\infty} \operatorname{div}_\Sigma j_e \, dx_e dx_{e'} \right. \\ &+ \int_{T_{e'}} \int_{\Sigma^\pm} j_{e'}^t G \sum_{e=1}^{N^\pm} J_e^\pm \operatorname{div}_\Sigma j_e \, dx_e dx_{e'} \\ &\left. + \int_{T_{e'}} \int_{\Sigma^p} j_{e'}^t G \sum_{e=1}^{N^p} J_e^p \operatorname{div}_\Sigma j_e \, dx_e dx_{e'} \right], \end{aligned}$$

where $T_{e'}$ is the domain where the basis function $j_{e'}$ is non-zero. We can further

rewrite the system to get

$$\begin{aligned}
&\sum_{e=1}^{N^\infty} E_e \int_{T_{e'}} j_{e'}^t J_e \, dx_{e'} \\
&= ikc\mu_0 \left[\sum_{e=1}^{N^\infty} J_e^{\pm\infty} \iint_{T_{e'},T_e^{\pm\infty}} G j_{e'}^t j_e \, dx_e dx_{e'} + \sum_{e=1}^{N^-} J_e^{\pm} \iint_{T_{e'},T_e^{\pm}} G j_{e'}^t j_e \, dx_e dx_{e'} \right. \\
&\left. + \sum_{e=1}^{N^p} J_e^p \iint_{T_{e'},T_e^p} G j_{e'}^t j_e \, dx_e dx_{e'} \right] \\
&- \frac{i}{kc\varepsilon_0} \left[\sum_{e=1}^{N^\infty} J_e^{\pm\infty} \iint_{T_{e'},T_e^{\pm\infty}} G \operatorname{div}_\Sigma j_{e'}^t \operatorname{div}_\Sigma j_e \, dx_e dx_{e'} \right. \\
&- \sum_{e=1}^{N^-} J_e^{\pm} \iint_{T_{e'},T_e^{\pm}} G \operatorname{div}_\Sigma j_{e'}^t \operatorname{div}_\Sigma j_e \, dx_e dx_{e'} \\
&\left. - \sum_{e=1}^{N^p} J_e^p \iint_{T_{e'},T_e^p} G \operatorname{div}_\Sigma j_{e'}^t \operatorname{div}_\Sigma j_e \, dx_e dx_{e'} \right].
\end{aligned} \tag{5.46}$$

By using the proper order of the rows and terms it is natural to define the infinite, or very large, sub-vector

$$J^S = \left[J_1^{\pm\infty}, \dots J_{N^\infty}^{\pm\infty} \right]$$

and the relatively small finite sub-vectors

$$J^p = \left[J_1^p, \dots J_{N^p}^p \right],$$

$$J^\pm = \left[J_1^\pm, \dots J_{N^-}^\pm \right]$$

and

$$J^s = \left[J^0, J^p, J^\pm \right].$$

Let us define E^S and E^s correspondingly. By calling the impedance matrix for A, we can write (5.46) as

$$\begin{pmatrix} A^{pp} & A^{p\pm} & \cdots & A^{sS} & \cdots \\ A^{\pm p} & A^{\pm\pm} & & & \\ \vdots & & & & \\ A^{Ss} & & & A^{SS} & \\ \vdots & & & & \end{pmatrix} \begin{pmatrix} J^p \\ J^\pm \\ \vdots \\ J^S \\ \vdots \end{pmatrix} = \begin{pmatrix} E^p \\ E^\pm \\ \vdots \\ E^S \\ \vdots \end{pmatrix}. \tag{5.47}$$

To solve (5.47), one can use the same technique as was used in Section 5.1.1. That is, one can solve for the unknowns in the scatterer only. Therefore, as before, let us write

$$A^{ss} J_{n+1}^s = E^s - A^{sS} \left(A^{SS} \right)^{-1} E^S + A^{sS} \left(A^{SS} \right)^{-1} A^{Ss} J_n^s, \tag{5.48}$$

where we defined

$$A^{ss} = \begin{pmatrix} A^{pp} & A^{p\pm} \\ A^{\pm p} & A^{\pm\pm} \end{pmatrix},$$

$E^s = [E^p, E^\pm]$ and $J^s = [J^p, J^\pm]$. Now we would like to, by using the GTD-method, estimate term two and three in iteration (5.48) containing infinite, or very large, matrices. This can be done by using the same physical reasoning as was done in Section 5.1.

Term two can be found with GTD as presented for Method 1. However, this time the largest GTD term will probably come from edge diffraction in the rim. To discuss the third term we need some further definitions. Let

$$\vartheta_1 = \frac{\min_{x\in\Gamma_1}\left[\min_{y\in\Sigma^0\cup\Sigma^p}|x-y|\right]}{\lambda}$$

and

$$\vartheta_2(y) = \frac{\min_{x\in\Gamma_1}|x-y|}{\lambda} \quad \text{with } y\in\Sigma^0\cup\Sigma^p\cup\Sigma^\pm.$$

Here, $\vartheta_1(y)$ tells us asymptotically how much a current element in y in the interior domain interacts with the exterior domain. Hence, for a current element in y with a large $\vartheta_1(y)$ the interaction with the large scales may be taken into account iteratively. This reasoning is supported by the fundamental solution in (2.10) and (2.11), i.e. the interaction between the large and the small scales in $\Sigma^{\pm\infty}$ and $\Sigma^0\cup\Sigma^p$ respectively, decreases asymptotically as ϑ_1 increases. It is also supported by the numerical experiments in Section 5.4.

By solving for the difference in current in $\Sigma^\pm$ it is natural to believe that both $\operatorname{div}_\Sigma j^s(y)\approx 0$ and $j^s(y)\approx 0$, when $y\in\Sigma^\pm$ is close to Γ_1, i.e. $\vartheta_1(y)$ is small. It is therefore natural to assume that the GTD-method defined in Method 5.6 (diffraction) may be used to estimate the interaction, between boundary elements in y_s (source) and y_r (receiver), in the iterative scheme (5.48), irrespective of the size of $\vartheta_2(y_{r/s})$. Differently stated may the GTD-method be used to compute all elements in the vector

$$A^{sS}\left(A^{SS}\right)^{-1}A^{Ss}J^s_n.$$

Previously in method 1, we were not able to use the GTD-method in the limit of Case B since the incoming field onto the edge where not a Ray-field. However, by solving for the difference in currents, we made the unknowns to be approximately equal to zero close to the edge. Since the unknowns are a priori approximately equal to zero their coupling to the large scales may therefore be disregarded as the right hand side in (5.48) is iteratively computed. We realize that as Γ_1 is moved further and further away from the small scales, or λ is decreased, the asymptotic error in the GTD-method will decrease and method 3 will probably produce more accurate solutions.

We would like to make two remarks.

- It is possible to approximate the incoming field to the edge much better than suggested in Assumption 5.5 and Method 5.6. As was also mentioned for method 1, may the transformations in [10] be used to decrease the size of $\Sigma_1 \backslash \Sigma^{\pm\infty}$ but still retain the same accuracy and convergence speed. We believe that this can be quite advantageous for at least two dimensional problems where the ray tracing is trivial.

- The fact that $\Sigma^{\pm\infty}$ and $\Sigma^{\pm}$ is made flat in Figure 5.23 was not meant to indicate that the method fails when they are non-flat. We only demand that the solution to problem 1 is known asymptotically.

The searched scattered E_2^s- or total $E_2^s + E^{refl}$ field can finally by computed by evaluating (5.42) with numerical quadrature. Plots similar to Figure 5.19(b) could then be produced.

5.6 Discussion

We have presented three hybrid methods to be used for scattering problems where both relatively large and small scales are present. Hybrid method 1 has been implemented in a Fortran 90 solver and shows good performance for a number of problems. The electromagnetic coupling between thin metal strips and a large smooth metallic Scatterer where well approximated with our method. In a more composite problem we tested the RBI method and achieved good results for excitations that did not excite creeping currents. To improve the performance in terms of complexity, a study on the Partition of Unity methodology suggested that great care has to be taken to the geometry meshing.

For the limit problem, where the small scales are close to non-smooth surfaces or boundary conditions, other methods has to be used. We therefore proposed two other more generally applicable hybrid methods. These two methods approximated the interaction between the large and small scales by using either global basis functions or GTD. By using Spherical Harmonics as global functions some more mathematical and numerical analysis needs to be done concerning the computation of the impedance matrix, before an implementation of a boundary element solver can be done. By using GTD, this analysis may be avoided. However, for both methods some more mathematical analysis needs to be done on the well posedness of the problems. Also, the overlapping basis functions between the domain, c.f. Γ_1 in Figure 5.23, must be chosen with care.

During the presentation above we had a scattering problem in focus. We emphasize however that it is trivial to adapt hybrid method one to a radiation problem. For hybrid method two and three other reference problems with known solutions have to be defined.

Chapter 6

Conclusions

This thesis has treated numerical methods for high frequency scattering problems. A numerical scheme has been developed with the purpose of computing the so called Smooth Surface Diffraction contribution to the scattered field. The scatterer where then assumed to only contain boundary conditions that can be treated accurately by Geometrical Theory of Diffraction (GTD). If parts in the geometry contained scales, too small for GTD to be applicable, we proposed that either of three new hybrid methods were to be used. These hybrid methods combined the Boundary Element Method (BEM) and asymptotic methods such as GTD and the Ray Based Image (RBI) method. The RBI-method was a new asymptotic method designed for our specific purposes.

6.1 Smooth Surface Diffraction

In Chapter 3 we introduced the analysis for Smooth Surface Diffraction and in Chapter 4 we developed, analyzed and tested a wave front construction technique applied to Smooth Surface Diffraction.

The standard numerical technique to compute the Smooth Surface Diffraction contribution was to propagate single rays representing the characteristics to the Surface Eikonal equation. This technique fails, or become quite inefficient, when rays deplete or when caustics forms. The wave front construction technique did not have these deficiencies. To be able to apply the wave front construction technique, we developed a new interpolation scheme for rays on faceted geometries.

Since we actually represented the solution along a generalized wave front it was possible to use well established techniques to compute the field in caustics, to keep track of phase shifts as the wave front passes through caustics and, by interpolation, achieve good efficiency as depletion of rays occurred.

To be able to get an implementation that could compute the smooth surface diffracted field in a robust, efficient and convergent manner we implemented a wave front solver in a hybrid geometry setting. The setting consisted of a triangular mesh

and a union of surface patches. Each surface patch was defined with Non-Uniform Rational B-Splines (NURBS). The intersection between the patches contained gaps which created topological errors. The triangle mesh did not have this deficiency.

By using a triangular mesh our numerical scheme became robust. A triangular mesh enabled us to solve the problems with gaps between NURBS by performing trivial jumps between triangles. With the help of the triangles, we were also able to find all shadow lines by using discrete shadow line data from the triangles as seeds to the shadow line algorithm applied to the NURBS setting.

With the NURBS we were able to achieve high accuracy in our scheme. By interpolating surface curvatures we were able to evaluate the GTD formulas more accurately. The geometrical information in the NURBS helped us achieve an almost mesh independent accuracy of the shadow lines which included occlusion. Since we built geometrical information from the NURBS data base we could propagate the field over geometries that contained true edges and corners. The NURBS also made it possible to assign geometrical data to the triangle nodes. The interpolated surface normals was then used to update the geodesic ray direction in such a manner that we managed to perform an order of convergence analysis.

Mathematical analysis suggested that the numerical error of the wave length dependent factors in the scattered field was of $\mathcal{O}(h)$. However, numerical results and mathematical analysis indicated that they were actually convergent with an error proportional to $\mathcal{O}(h^2)$ for many problems. Expressed in wave lengths, with element size of $\mathcal{O}(\sqrt{\lambda})$, the total error became constant as we decreased the wave length and mesh size. This meant that a surface curvature sensitive mesh could be used where the distance between the geometry and the mesh was bounded by $\mathcal{O}(\lambda)$. The complexity for such numerical computation can be seen to be of $\mathcal{O}(\lambda^{-1})$ which can be compared with FMM which is approximately of $\mathcal{O}(\lambda^{-2})$.

6.2 Hybrid Methods

In the second part of the thesis a methodology for hybrids between BEM and asymptotic methods were presented. Three new numerical methods were introduced. We justified one of the them by presenting extensive numerical results while the other two needed to be further analyzed and developed.

As mentioned in several sections of the text, our main objective of the hybrid methods was to provide electromagnetic engineers with more general hybrid tools in the frequency domain. The fact that the computational tools needed to be easy to use and relatively easy to develop guided us when we developed the methods.

Hybrid methods have existed for many years in the electromagnetic society both in terms of specific computational tools but also in forms of interactive ad hoc techniques that rests on each engineers individual skills. We hope that our work will make computational hybrid methods more popular and established, by achieving better accuracy, for a wider group of problems. The new methods will make a wider class of electromagnetic problems accessible to engineers in computational

electromagnetics and more specifically, for scattering computations. By having a more reliable method to compute the field from a sub-scatterer we also hope this will be more established.

In Chapter 2 and 3 we built the background for presenting and explaining three hybrid methods. By defining the Ray Based Image (RBI) method and the modified GTD-method we were able to formulate in Chapter 5 a methodology applicable to problems, where small and large scales did not have to be well separated in space, by blending two asymptotic methods (GTD and RBI).

When the large scales where non-smooth close to the small scales, we proposed two new techniques. The first one, initiated by J. B. Keller, represented the currents in the large scales with a Multipole expansion, while the second one, represented the currents in the large scales by using GTD edge diffraction and an auxiliary unperturbed problem.

The complexity of the first hybrid method was of $\mathcal{O}(n^2)$, with n as the number of unknowns in the small scale. This complexity could be compared with Physical Optics where the complexity will not only be dependent on n^2 but also the number of the unknowns in the large scales. The possibility to speed up the $\mathcal{O}(n^2)$ computations where also investigated by applying a partition of unity method to a boundary element problem. It was apparent that it was, at least in principle, possible to apply partition of unity methodology to the hybrid. We foresee however some unusual demands on the meshing tools to create an optimal mesh.

In the numerical examples, we tried to make it evident that the RBI-method actually served as an efficient method for problems with small scales close to smooth large scales. This was initially done by presenting a large number of error plots for a dipole-sphere problem. The RBI-errors were compared with three other established approximate methods and when the dipole were close to the spherical object, RBI were the best method. A blending parameter between GTD and RBI where also analyzed on an infinite ground plane problem.

Finally we demonstrated the RBI on a problem where the large scales where fairly small, thereby illustrating the lower bound for the scales in the large scale geometry.

Bibliography

[1] W. E, B. Engquist, X. Li, W. Ren and E. Vanden-Eijnden. The Heterogeneous Multiscale Method: A Review. Technical report, Princteon, PACM, http://www.math.princeton.edu/multiscale/.

[2] J.-C. Nédélec. *Acoustic and Electromagnetic Equations*. Springer Verlag, 2001.

[3] R. F. Harrington. *Field Computation by Moment Methods*. MacMillan, 1968. New York.

[4] S.M. Rao, D.R. Wilton and A.W. Glisson. Electromagnetic Scattering by Surfaces of Arbitrary Shape. *IEEE Trans. on Ant. Prop.*, 30:409–418, May 1982.

[5] A. Bendali. Numerical Analysis of the Exterior Boundary Value Problem for the Time-Harmonic Maxwell Equations by a Boundary Finite Element Method, Part 1: The Continuous Problem. *Mathematics of Computation*, 43(167):29–46, July 1984.

[6] A. Bendali. Numerical Analysis of the Exterior Boundary Value Problem for the Time-Harmonic Maxwell Equations by a Boundary Finite Element Method, Part 2: The Discrete Problem. *Mathematics of Computation*, 43(167):69–88, July 1984.

[7] P. A. Raviart and J. M. Thomas. A Mixed Finite Element Method for 2nd Order Elliptic Problems. In *Lecture notes in Math.*, volume 606, pages 292–315. Springer-Verlag, Berlin, New York, 1977.

[8] J. B. Keller. Geometrical Theory of Diffraction. *J. opt. soc. of Amer.*, 52(2):61–72, February 1962.

[9] M. G. Crandall and P.-L. Lions. Viscosity Solutions of Hamilton-Jacobi Equations. *Trans. Amer. Math. Soc.*, 277:1–42, 1983.

[10] J. -D. Benamou, F. Collino and O. Runborg. Numerical Microlocal Analysis of Harmonic Wavefields. *J. Comput. Phys.*, 199:717–741, 2004.

[11] V. Vinje, E. Iversen and H. Gjöystdal. Traveltime and Amplitude Estimation Using Wavefront Construction. *Geophysics*, 58:1157–1166, 1993.

[12] P. E. Hussar et al. An Implementation of the UTD on Facetized CAD Platform Models. *IEEE Ant. and Prop. Magazine*, 42:409–418, April 2000.

[13] J. Perez et al. Analysis of Antennas on Board Arbitrary Structures Modeled by NURBS Surfaces. *IEEE Trans. on Ant. and Prop.*, AP-45:1045–1052, June 1997.

[14] S. Fomel and J. A. Sethian. Fast-Phase Space Computation of Multiple Arrivals. *Proc. Natl. Acad. Sci. USA*, 99(11):7329–7334, May 2002.

[15] G. Farin. *Curves and Surfaces for Computer Aided Geometric Design.* Acad. Press, 1988.

[16] J. Edlund. *A Parallel, Iterative Method of Moments and Physical Optics Hybrid Solver for Arbitrary Surfaces.* Licentiate thesis, Uppsala University, 2001.

[17] F. Bergholm, S. Hagdahl and S. Sefi. A Modular Approach to GTD in the Context of Solving Large Hybrid Problems. In *AP2000 Millennium Conference on Antennas and Propagation*, 2000. Davoz, Switzerland.

[18] B. R. Levy and J. B. Keller. Diffraction by Smooth Objects. *Communications on pure and applied mathematics*, pages 159–209, 1959.

[19] S. Sefi. Ray Tracing Tools for High Frequency Electromagnetics Simulations. Licentiate thesis, Department of Numerical Analysis and Computer Science, May 2003.

[20] U. Andersson, F. Edelvik, J. Edlund, L. Eriksson, S. Hagdahl, G. Ledfelt, and B. Strand. GEMS-A Swedish electromagnetic suite of hybrid solvers-technical aspects. In *AP2000 Millennium Conference on Antennas & Propagation*, Davos, Switzerland, 2000.

[21] J. Edlund, S. Hagdahl and B. Strand. An Investigation of Hybrid Techniques for Scattering Problems on Disjunct Geometries. In *AP2000 Millennium Conference on Antennas & Propagation*, 2000. Davos, Switzerland.

[22] S. Hagdahl and B. Engquist. Numerical Techniques for Mixed High-Low Frequency EM-Problems. In *Proceedings RVK 02*, June 2002.

[23] S. Hagdahl. *Hybrid Methods for Computational Electromagnetics in the Frequency Domain.* Licentiate thesis No. 2003-018, Royal Institute of Technology, October 2003.

[24] S. Hagdahl. Tracking Wavefronts with Lagrangian Markers. Technical Report TRITA-NA-0122, Royal institute of technology, Department of Numerical Analysis and Computer Science, 2001.

[25] B. Engquist and S. Hagdahl. Computation of Smooth Surface Diffraction for Industrial Application. In *EMB04*, 2004. Göteborg, Sweden.

[26] C. A. Balanis. *Antenna Theory: Analysis and Design*. John Wiley and Sons, 1st edition, 1989.

[27] M. Nilsson. *Fast Numerical Techniques for Electromagnetic Problems in Frequency Domain*. PhD thesis, Uppsala University, 2004.

[28] A. Bendali and C. Devys. Calcul Numérique du Rayonnement de Cornets Electromagnetiques dont l'Ouverture est Partiellement Remplie par un Dielectrique. Technical report, CERFACS, Toulouse, 1996.

[29] E. Fatemi, B. Engquist and S. Osher. Finite Difference Methods for Geometrical Optics and Related Nonlinear PDEs Approximation the High Frequency Helmholtz Equation. Technical report, University of California, Department of Mathematics, 405 Hilgard Avenue, Los Angeles, CA 900024-1555, March 1995.

[30] O. Runborg. *Multiscale and Multiphase Methods for Wave Propagation*. PhD thesis, NADA, KTH, 1998.

[31] B. Engquist and O. Runborg. Computational High-Frequency Wave Propagation. *Acta Numerica*, 12, 2003.

[32] R. McOwen. *Partial Differential Equations, Methods and Applications*. Prentice Hall, 1996.

[33] J. B. Keller and R. M. Lewis. Asymptotic Methods for Partial Differential Equations: The Reduced Wave Equation and Maxwell's Equations. Course given at UCLA during winter quarter 1999.

[34] D.A. MacNamara. *Introduction to the Uniform Geometrical Theory of Diffraction*. Artech House, Norwood, Mars 1990.

[35] P. L. Lions. *Generalized Solutions of Hamilton-Jacobi Equations*. Pitman Advanced Pub., 1982.

[36] D. Peng, B. Merriman, S. Osher, H. Zhao and M. Kang. A PDE-Based Fast Local Level Set Method. *Journal of Computational Physics*, 155:410–438, 1999.

[37] J.A. Sethian. A Fast Marching Level Set Method for Monotonically Advancing Fronts. In *Proceedings of the National Academy of Science*, 1995.

[38] G.-S. Jiang and D. Peng. Weighted ENO Schemes for Hamilton-Jacobi Equations. Technical report, University of California, Department of Mathematics, 405 Hilgard Avenue, Los Angeles, CA 900024-1555, June 1997.

[39] S. Osher and R. Fedkiw. *Level Set Methods and Dynamic Implicit Surfaces*. Springer-Verlag, 2002.

[40] J. J. Bowman, T. B. A. Senior and P. L. E. Uslenghi., editor. *Electromagnetic and Acoustic Scattering by Simple Shapes*. Hemisphere Pub, 1987.

[41] H. Zhao. A Fast Sweeping Method for Eikonal Equations. *Math. Comp.*, 74:603–627, 2005.

[42] R. Kimmel and J. A. Sethian. Computing Geodesic Paths on Manifolds. *Proc. Natl. Acad. Sci. USA*, 95(15):8431–8435, July 1998.

[43] J. Steinhoff, M. Fan and L. Wang. A New Eulerian Method for the Computation of Propagating Short Acoustic and Electromagnetic Pulses. *Journal of Computational Physics*, 157:683–706, 2000.

[44] N. P. Weatherill and O. Hassan. Efficient Three Dimensional Delaunay Triangulation with Automatic Point Creation and Imposed Boundary Constraints. *Int. Journal for Numerical Methods in Ingeneering*, 37:2005–2039, 1994.

[45] S. C. Brenner and L. R. Scott. *The Mathematical Theory of Finite Element Methods*. Springer-Verlag, 2nd edition, 2002.

[46] C. Johnson. *Numerical Solutions of Partial Differential Equations by the Finite Element Method*. Cambridge University Press, 1987.

[47] P. Deuflhard and F. Bornemann. *Scientific Computing with Ordinary Differential Equations*. Springer-Verlag, 2002.

[48] N. C. Albertsen and P. L. Christiansen. Hybrid Diffraction Coefficients for First and Second Order Discontinuities of Two-Dimensional Scatterers. *SIAM J. Appl. Math*, 34:398–414, 1978.

[49] A. Michaeli. Transition Functions for High-Frequency Diffraction by a Curved Perfectly Conducting Wedge. I. Canonical Solution for a Curved Sheet. *IEEE Trans. on Ant. and Prop.*, 37(9):1073–1079, September 1989.

[50] A. Michaeli. Transition Functions for High-Frequency Diffraction by a Curved Perfectly Conducting Wedge. II. a Partially Uniform Solution for a General Wedge Angle. *IEEE Trans. on Ant. and Prop.*, 37(9):1080–1085, September 1989.

[51] D. J. Struik. *Lectures on Classical Differential Geometry*. Dover publications, Inc. New York, 1950.

[52] J. Choi, N. Wang and L. Peters, Jr. Near-Axial Backscattering from a Cone Sphere. *Radio Science*, 25(4):427–434, 1990.

[53] D. P. Bouche, et al. Asymptotic Computation of the RCS of Low Observable Axisymmetric Objects at High Frequency. *IEEE Trans. on Ant. and Prop.*, 40(10):1165–1174, Oct 1992).

[54] R. G. Kouyoumjian. The Geometrical Theory of Diffraction and Its Applications. In R. Mittra, editor, *Numerical and Asymptotic Techniques for Electromagnetics*, Applied Physics, pages 184–200. Springer-Verlag, 1975.

[55] T.B.A. Senior. The Backscattering Cross Section of a Cone Sphere. *IEEE Trans. on Ant. and Prop.*, 13:271–277, 1965.

[56] TrancenData. CADfix. http://www.cadfix.com.

[57] G. Lambaré. Computation of Multi-Arrival Travel Time Maps in Seismic Imaging by WaveFront Construction. Technical report, Centre de Recherche en Géophysique Ecoles des Mines de Paris, 2002. Proceedings at GO++ winter school on numerical methods for HL/HJB problems.

[58] G. A. Thiele and T. H. Newhouse. A Hybrid Technique for Combining Moment Methods with a Geometrical Theory of Diffraction. *IEEE Trans. on Ant. and Prop.*, 23:62–69, 1975.

[59] W. D. Burnside, C. L. Yu and R. J. Marhefka. A Technique to Combine the Geometric Theory of Diffraction and the Moment Method. *IEEE Trans. on Ant. and Prop.*, AP-33:551–558, 1975.

[60] H.-W. Tseng. *Hybrid Analysis of EM Radiation and Scattering by Composite Slot-Blade Cavity Backed Antennas on the Surface of Electrically Large Smooth Convex Cylinders*. PhD thesis, The Ohio State University, 1998.

[61] U. Jakobus and F. M. Landstorfer. Improved PO-MM Hybrid Formulation for Scattering from Three-Dimensional Perfectly Conducting Bodies of Arbitrary Shape. *IEEE Trans. on Ant. and Prop.*, 43(2):162–169, February 1995.

[62] R. P. Hodges. *A Current-Based Hybrid Method for Electromagnetic Modelling of Complex Structures*. PhD thesis, University of California, Los Angeles, 1996.

[63] M. Alaydrus et al. Hybrid2: Combining the Three-Dimensional Hybrid Finite Element-Boundary Integral Technique for Planar Multilayered Media with the Uniform Geometrical Theory of Diffraction. *IEEE Trans. on Ant. and Prop.*, 50(1):67–74, January 2002.

[64] L. N. Medgyesi-Mitschang and D.-S. Wang. Hybrid Methods for Analysis of Complex Scatterers. *Proceedings of the IEEE*, 77(5):770–779, 1989.

[65] PSCI. General ElectroMagnetic Solvers (GEMS). http://www.psci.kth.se/Programs/GEMS.

[66] F. Edelvik and G. Ledfelt. A Comparison of Time-Domain Hybrid Solvers for Complex Scattering Problems. *International Journal of Numerical Modeling*, 15(5-6):475–487, September/December 2002.

[67] M. Balabane. Boundary Decomposition for Helmholtz and Maxwell equations. I. Disjoint Sub-Scatterers. *Asymptot. Anal.*, 38(1):1–10, 2004.

[68] S. Hagdahl et al. MIRA I/O specification. Technical Report GEMS2/PSCI-2002.12, Royal institute of Technology, Department of Computer Science and Numerical Analysis, 2002.

[69] B. Strand et al. Randolph I/O specification. Technical Report GEMS2/PSCI-2002.11, Royal institute of Technology, Department of Computer Science and Numerical Analysis, 2003.

[70] S. N. Chandler-Wilde and A. T. Peplow. A Boundary Integral Equation Formulation for the Helmholtz Equation in a Locally Perturbed Half-Plane. *Zeitschrift für Angewandte Mathematik und Mechanik*, 56(2), 2005.

[71] J.S. Asvestas and R.E. Kleinman. Electromagnetic Scattering by Indented Screens. *IEEE Trans. on Ant. and Prop.*, 42:22 – 30, 1994.

[72] J.S. Asvestas. Scattering by an Indentation Satisfying a Dyadic Impedance Boundary Condition. *IEEE Trans. on Ant. and Prop.*, 44:28 – 33, 1997.

[73] H.-W. Tseng and P. H. Pathak. A Hybrid UTD-MM Analysis of the Radiation from a Composite Slot-Blade Cavity-Backed Antenna on Realistic Aircraft Configurations. *Radio Science*, 34(3):587–598, 1999.

[74] J. B. Keller. Scattering By a Localized Feature on a Plane. Unpublished Communication, UCLA, spring -99.

[75] J. D. Jackson. *Classical Electrodynamics*. Wiley, 3rd edition, 1998.